ALPHA-SYNUCLEIN AND ENHANCED GREEN FLUORESCENT PROTEIN IN TRIFLUOROETHANOL: PROTECTIVE FACTORS OPPOSE PROTEIN AGGREGATION

A Dissertation

Presented to the Faculty of the Graduate School

of Cornell University

In Partial Fulfillment of the Requirements for the Degree of

Doctor of Philosophy

by

Valerie Louise Anderson

August 2011

ALPHA-SYNUCLEIN AND ENHANCED GREEN FLUORESCENT PROTEIN IN TRIFLUOROETHANOL: PROTECTIVE FACTORS OPPOSE PROTEIN AGGREGATION

Valerie Louise Anderson, Ph.D.

Cornell University 2011

Protein aggregation, leading to the formation of amyloid fibrils, is associated with many human diseases, including Parkinson's disease, Alzheimer's disease and type II diabetes. 2,2,2-trifluoroethanol (TFE) is frequently used to induce amyloid conversion in biophysical studies, but the mechanisms underlying TFE-induced fibrillization are not yet well understood. We have measured secondary structural changes of the Parkinson's disease-associated protein α-synuclein (αS), and have discovered that TFE-induced aggregation is correlated with population of a partially structured state of the monomer protein. By investigating the pH- and temperature-dependences of the conformational transitions, we find evidence that loss of protein-solvent interactions drives both the structural changes and the fibril production. Furthermore, we used enhanced green fluorescent protein (EGFP) as a model system to examine the effects of sequence and tertiary structure in TFE-induced aggregation, and found that the behavior of acid-denatured EGFP is qualitatively similar to αS, while tertiary structure impedes aggregation. We conclude that initiation of protein aggregation in solutions containing TFE involves overcoming multiple protective factors, rather than stabilization of specific structural elements.

We identify three distinct structural states that contribute to the circular dichroism spectra of αS variants and acid-denatured EGFP. For both types of proteins, a partially α-helical conformation is populated at moderate TFE concentrations where aggregation is enhanced. The TFE-induced αS fibrils are β-sheet-rich, flexible, helical

structures, while the EGFP aggregates are flexible, uniform-width fibrils.

At low (<10-15% v/v) TFE, the αS variants and acid-denatured EGFP undergo loss of polyproline-II structure, which is suggestive of reduced protein-water interactions. At higher TFE, preferential solvation leads to TFE coating of the proteins, stabilizing α-helical structures. The temperature response of αS reveals distinct behavior for proteins in water-like vs. TFE-like local environments. Moreover, the intermediate-TFE conformations appear to be invariant with respect to temperature and pH, which indicates that the proteins experience reduced solvent interactions at moderate [TFE].

Our results suggest that TFE reduces solvation barriers in aggregation reactions. However, aggregation pathway selection may depend on details of protein structure, and the protein sequence affects the TFE concentrations required for dehydration-driven fibrillization.

BIOGRAPHICAL SKETCH

Valerie Anderson was born in Fairmont, MN and has lived in Kihei, HI, Pukalani, HI, Lafayette, CA, Mililani, HI, Bloomington, MN, Pasadena, CA, La Jolla, CA, San Francisco, CA, and Ithaca, NY. She obtained her bachelor's degree in physics from the California Institute of Technology in 1999 and worked as a software engineer at Sun Microsystems from 2000-2003. She received her Master's degree in physics from Cornell in 2006.

ACKNOWLEDGMENTS

I have been fortunate to be surrounded by very passionate and dedicated scientists at Cornell. My advisor, Prof. Watt Webb, has been a constant source of inspiration and good advice. Prof. David Eliezer of Weill Cornell Medical College and his group have also been extremely helpful and instructive. In particular, I thank Trudy Ramlall for all her protein expression work. I would also like to express gratitude to Prof. Warren Zipfel, Becky Williams, Mark Williams, Prof. Lois Pollack, Prof. Liz Rhoades, Ellen Keene, Huimin Chen, and numerous members of the CCMR and NBTC staffs for their assistance and instruction. I am especially indebted to John Grazul, Yuanming Zhang, and Prof. David Muller for their help with electron microscopy imaging and analysis.

I would also like to acknowledge the Zipfel and Webb lab members I have known, including Avtar, Johanna, Chris, Julian, Elaine, Kira, Ina, Jie, Jesse, Sally, Huizhong, Betsy, Evan, Pam, Josh, Paul, Lisa, Alex, and many others. I am especially appreciative of the encouragement and friendship I received from Laura, Heather, Jenn, Maura, Rebecca, Sarah, Autumn, Tom, Edwin, Terry, Marge, Anne, Alicia, Cindy, Nick, and Erica. I am very lucky to have had my amazing boyfriend Shawn in my life for the last three years. Finally, I am eternally grateful to Marion and Lois and their many friends. Thank you, Amy, for teaching me everything I know.

Collaborators and Contributors

Chapters 2-3: This research was performed in collaboration with Prof. David Eliezer of Weill Cornell Medical College. α–synuclein variant proteins were generously supplied by Trudy Ramlall and David Eliezer. Experimental design assistance was provided by David Eliezer and Carla Rospigliosi. I am also extremely

grateful to Prof. James Sethna for helpful conversations about data analysis.

Chapter 4: GFP variant proteins and vectors were a kind gift from Prof. David Piston and Dr. Gert-Jan Kremers at Vanderbilt University. Dr. Cynthia Kinsland of the Cornell University Life Sciences Core Laboratories Center Protein Production Facility performed the EGFP expression.

Appendix D: Prof. Bradley Hyman at Massachusetts General Hospital Medical School at Harvard University generously provided vectors for mammalian expression of the αS-EGFP construct. Transformation into a bacterial vector and subsequent protein expression was performed by Dr. Cynthia Kinsland. Trudy Ramlall of the Eliezer lab at Weill Cornell Medical College labeled and expressed αS variants tagged with Alexa Fluor 488.

Funding Sources

This research made use of the Hudson Mesoscale Processing facility of the Cornell Center for Materials Research with support from the National Science Foundation Materials Research Science and Engineering Centers program (DMR 0520404). Funding was provided by grants from the National Institutes of Health (5 R21 AG026650) and the National Science Foundation (STC program under agreement No. ECS-9876771).

Some of this material was based on work supported under a National Science Foundation Graduate Research Fellowship. Any opinions, findings, conclusions, or recommendations are those of the authors and do not necessarily reflect the views of the National Science Foundation.

TABLE OF CONTENTS

LIST OF FIGURES

LIST OF TABLES

LIST OF ABBREVIATIONS

αS, α–Synuclein

Aβ40, Amyloid β 1-40

AFM, Atomic Force Microscopy

CD, Circular Dichroism

EGFP, Enhanced Green Fluorescent Protein

GFP, Green Fluorescent Protein

HFIP, 1,1,1,3,3,3-Hexafluoro-2-propanol

MLE, Maximum Likelihood Estimation

NaPhos, Sodium Phosphate

NMR, Nuclear Magnetic Resonance

NRMSD, Normalized Root Mean Square Deviation

PBS, Phosphate Buffered Saline

PCA, Principal Component Analysis

PD, Parkinson's Disease

PPII, Polyproline Type II

RPM, Revolutions Per Minute

TEM, Transmission Electron Microscope/Microscopy

TFE, 2,2,2-Trifluoroethanol

Tris, Tris(hydroxymethyl)aminomethane

WT, Wild-Type

YFP, Yellow Fluorescent Protein

CHAPTER 1

OVERVIEW

1.1. Why use TFE to study protein aggregation?

Protein aggregation is implicated in over forty human diseases, including Alzheimer's disease, Parkinson's disease, type II diabetes, Huntington's disease, and amyotrophic lateral sclerosis (Chiti and Dobson, 2006). The proteins involved in these disorders include both globular proteins and natively disordered proteins and peptides. Additional proteins that are not associated with human diseases can be induced to aggregate *in vitro*, leading to the hypothesis that amyloid aggregation is a general property of polypeptides (Chiti, et al., 1999), although evolution has favored protective sequence elements (Monsellier and Chiti, 2007).

Biophysical investigations of protein aggregation aim to identify the fundamental interactions influencing these processes; this research may help identify potential drug treatments and preventative measures for human diseases. Chemical additives are often used in biophysical studies to reduce experimental variability, induce protein conformational changes, or simulate cellular conditions.

The fluorinated alcohol 2,2,2-trifluoroethanol (TFE) is one of the most common cosolvents used to induce amyloid conversion and accelerate protein aggregation (Otzen, 2010). TFE can increase experimental reproducibility and decrease lag times, resulting in controlled conditions conducive to comparisons of specific factors, such as protein sequences, that may affect aggregation reactions (Chiti, et al., 2000; Otzen, 2010). Moreover, TFE is able to induce conformational transitions in proteins, leading to the identification of potential intermediates in aggregation reactions (Anderson, et al., 2010; Fezoui and Teplow, 2002; Pallarès, et al., 2004; Williamson, et al., 2009). TFE can also populate unconventional aggregation

pathways. For example, TFE was used in studies that discovered that some globular proteins can associate in the absence of significant unfolding and later convert into β-sheet-rich, fibrillar structures (Plakoutsi, et al., 2004; Soldi, et al., 2005). The identification of new aggregation pathways is of particular interest to researchers in view of evidence that oligomeric or protofibrillar species, rather than mature amyloid fibrils, may be the toxic species in some diseases (Bucciantini, et al., 2002; Glabe, 2006). The clustering of TFE molecules in aqueous solution, in combination with the ability of TFE to populate structures that are similar to membrane-bound conformations of certain proteins, has also led some researchers to suggest that TFE may act as a membrane mimetic (Bychkova, et al., 1996).

However, the relationship between protein aggregation in solutions containing TFE and reactions that may occur *in vivo* is unclear. TFE stabilizes non-native protein structures and often promotes the formation of atypical aggregates. Additionally, the lack of a well-understood mechanism for TFE-induced aggregation complicates interpretation of experimental results. For example, in Chapter 2, we show that population of a specific secondary structural state, which appears partially α-helical, is correlated with α−synuclein (αS) aggregation, but it is not clear whether this conformation is truly aggregation-prone, or whether the observed structural changes are coupled to some solvent property that is the actual causative factor.

The effects of TFE on protein structure have been studied for decades, but the physical interactions underlying TFE-induced aggregation enhancement are not well-understood (Otzen, 2010). TFE can denature globular proteins, typically leading to the formation of non-native α-helical structure. Disordered proteins and peptides generally undergo a gradual coil-to-helix transition as TFE is added to a solution, reaching their maximally helical state by ~30-40% TFE. For both globular and disordered proteins, aggregation is usually maximized at an intermediate TFE

concentration (usually 10-40% v/v). Disruption of tertiary structure often, but not always, precedes aggregation for globular proteins.

In Chapters 2-4, we present our studies of the effect of TFE on the structures and aggregation properties of αS variants and enhanced green fluorescent protein (EGFP). Our results, in combination with a review of the literature related to fluoroalcohol effects on proteins and peptides (Section 1.4), suggest that desolvation is a likely explanation for the enhanced aggregation we observe at intermediate TFE concentrations. Low TFE conditions lead to dehydration, as evidenced by loss of polyproline type II (PPII) structure for disordered and denatured proteins and the rapid formation of aggregates under these conditions. Preferential solvation of proteins by TFE occurs above a threshold TFE concentration that depends on protein sequence. This partitioning of TFE into the protein solvation shell stabilizes α-helical structure and decreases aggregate production. Therefore, aggregation enhancement occurs at moderate TFE concentrations where water-protein interactions are disrupted and TFE-protein interactions are minimal.

We propose that TFE weakens or removes factors that protect against aggregation, rather than stabilizing aggregation-prone states. Intact tertiary structure, electrostatic repulsion, and protein-solvent interactions are crucial protective interactions. Protein-water interactions are an especially important stabilizing factor for disordered and denatured proteins; it is likely that natively disordered and weakly folded proteins have evolved sequence elements that increase their water accessibility in order to avoid toxic aggregation (Rauscher, et al., 2006; Uversky, et al., 2000). Our results have relevance for design and interpretation of experiments related to protein aggregation reactions. In particular, understanding natural protective factors may be useful in designing strategies aimed at prevention and treatment of amyloid diseases (Monsellier and Chiti, 2007).

1.2. Summary of our experimental results

We examine the effects of TFE on five variants of the Parkinson's disease-associated protein αS, as well as native and acid-denatured EGFP. By measuring circular dichroism (CD) spectra of sub-micromolar concentrations of proteins in various solution conditions, we characterize secondary structural transitions in the monomer proteins. We correlate these with aggregation by examining higher protein concentrations. Comparisons of proteins and solution conditions enable identification of general properties of TFE-induced aggregation reactions.

In Chapter 2, we report that short, flexible, β-sheet-rich fibrillar species result from incubation of the Parkinson's-disease associated protein αS in the presence of intermediate (10-20% v/v) concentrations of 2,2,2-trifluoroethanol (TFE). We demonstrate that enhanced fibril production is correlated with the formation of a monomeric, partly helical intermediate αS conformation. The intermediate exists in equilibrium with the natively disordered state at low TFE and with a highly α-helical conformation at high TFE. TFE-induced conformational changes in the monomer protein are similar for wild-type αS and three Parkinson's disease-associated mutants, as well as for the 1-102 C-terminal truncation mutant αS102. However, oligomerization rates differ substantially among the mutants. We initially concluded that the observed "intermediate" conformation is an intermediate in the fibrillization of αS, but we revisit this hypothesis in subsequent chapters.

Measurements of αS variant structure as a function of temperature, pH, and TFE concentration are presented in Chapter 3. By investigating the temperature dependence of the αS102 spectra at various TFE concentrations, we identify a clear crossover between "water-like" behavior at low TFE, which involves reduction of PPII structure with heating, and "TFE-like," helix melting behavior at high TFE. The

crossover point occurs at ~15% TFE, where the population of the TFE-induced intermediate is maximal. The similarities between the structural changes induced by heating and those observed for low concentrations of TFE suggest that TFE may cause loss of hydrogen bonds between water and the protein. The high-TFE behavior is suggestive of preferential solvation of αS by TFE; secondary structural changes level off above ~40% TFE, indicating that the protein environment is essentially TFE-like above this concentration. Solution pH affects the conformation of the protein in the TFE-rich environment, with reduced pH conditions resulting in an increase in α-helical structure. We also find that structural changes induced by pH at low TFE require the C terminal portion of αS, while temperature- and TFE-induced changes involve the N terminus. Therefore, αS can sample multiple partially structured states.

TFE- and heat-induced aggregation is associated with both loss of PPII structure and reduced α-helical structure. Because PPII structure is likely a signature of protein-water hydrogen bonding, while α-helical conformations reflect preferential solvation of proteins by TFE, we conclude that aggregation occurs where protective solvent interactions are minimized. However, we note that the aggregate morphology depends on temperature and the presence of the C terminal portion of αS, and so additional interactions are involved in aggregation pathway selection.

In the study described in Chapter 4, we use EGFP as a model protein to investigate the effects of tertiary structure and protein sequence on TFE-induced aggregation. We find that acid-denatured EGFP behaves very similarly to αS in the presence of 0-60% TFE. Loss of PPII structure occurs at low TFE, followed by helix induction at high TFE. The inferred CD spectrum of the EGFP intermediate conformation is similar to the intermediate structure for αS. However, the crossover from water-like to TFE-like behavior occurs at ~8% TFE for acid-denatured EGFP, in contrast to ~15% TFE for αS. This difference may be due to the presence of more

bulky hydrophobic residues in the EGFP sequence, which might favor solvent-shielded conformations or restrict water accessibility to the protein backbone. Little to no aggregation occurs within 24 hours for acid-denatured EGFP in 0-60% TFE. However, the addition of 75 mM NaCl to the solutions leads to significant aggregation at ~8-30% TFE, indicating that electrostatic repulsion limits aggregation of the acid-denatured protein. For native-state EGFP at pH 7.5, aggregation occurs at intermediate [TFE] following denaturation, but is reduced at high TFE where non-native α-helical secondary structure is favored. Denaturation is fastest at 30-60% TFE, suggesting that preferential solvation of proteins by TFE is involved in tertiary structure disruption. TFE-denatured EGFP behaves much like acid-denatured protein and likely samples a similar intermediate conformation, although the apparent helicity at high TFE is reduced at pH 7.5 compared to pH 2.4. Taken together, our results show that protein-solvent interactions, electrostatic repulsion, and intact tertiary structure protect against EGFP aggregation. In addition, solution conditions affect the aggregation pathway. The aggregates formed from EGFP at intermediate TFE appear to be flexible, sticky thin fibrils, while long incubations in the absence of TFE result in the formation of rigid, fibrillar aggregates for acid-denatured EGFP.

In sum, we demonstrate that all the αS variants and acid-denatured EGFP populate three secondary structural states in the presence of 0-60% (and higher) TFE, with a clear crossover between low-TFE and high-TFE behavior. The spectral changes in the two regimes are distinct, with a loss of PPII structure occurring at low TFE, followed by helix induction at high TFE. Aggregation is correlated with reduction of both PPII and α-helical structure, while tertiary structure has a protective role. Aggregate morphologies vary with solution conditions and protein sequence. Our results suggest that TFE removes solvation and structural barriers to protein aggregation, but additional factors affect aggregation pathway selection.

In the next section, we briefly review some physical properties of TFE-water mixtures. Then, in Section 1.4, we present a literature review of mechanisms that have been proposed to explain TFE-induced protein structural changes and aggregation behavior. We discuss our experimental results in the context of these models and conclude that protein dehydration and preferential solvation are the most likely explanations for our observations.

1.3. Some properties of TFE and TFE-water mixtures

TFE effects on protein structure are related to the properties of the TFE molecule (Figure 1.1). TFE is a good proton donor, but a poor acceptor, compared to water (Rajan and Balaram, 1996). The CF_3 group has a hydrophobic character and the fluorine atoms are not thought to participate in hydrogen bonds (Rajan and Balaram, 1996). The large size of TFE (~ 9 times larger than water), combined with its ability to participate in two hydrogen bonds rather than four, means that the hydrogen bonding capacity per unit volume of a TFE-water mixture decreases with increasing [TFE] (Van Buuren and Berendsen, 1993).

TFE is miscible with water in all proportions, but the excess molar Gibbs function, which measures the free energy of a mixture relative to an ideal solution of the same composition, is positive for TFE-water mixtures (Figure 1.1B). TFE-water mixtures also experience a volume contraction upon mixing (Figure 1.1C), which is probably due to water molecules forming solvation shells around the hydrophobic CF_3 groups (Rochester and Symonds, 1974). Note that the magnitude of the volume contraction is less than 1.5% of the total solution volume at its peak.

Additional properties of TFE-water mixtures are shown in Figure 1.1D-F. Some proposed models for TFE-protein interactions arise from these bulk properties,

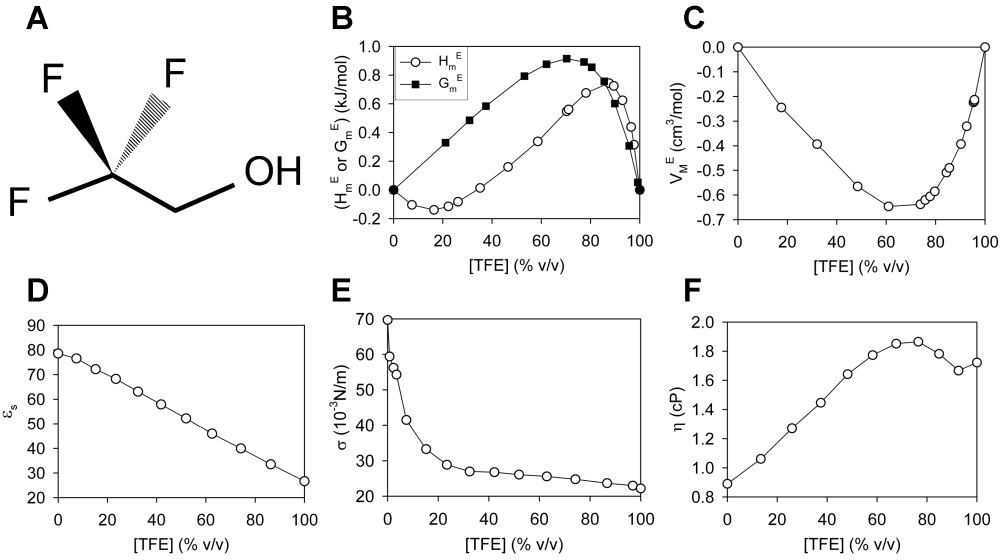

Figure 1.1. Some properties of TFE and TFE-water mixtures. The mixture properties are shown for 25 °C and the units of TFE concentration have been converted to % v/v in all cases. (A) Skeletal formula for the TFE molecule, CF_3CH_2OH. (B) The excess molar Gibbs function, G_m^E, and the excess molar enthalpy, H_m^E, for TFE-water mixtures, taken from (Cooney and Morcom, 1988). (C) Excess molar volumes, V_m^E, for TFE-water mixtures, from (Sassi and Atik, 2003). (D-F) The relative permittivity, ε_s, surface tension, σ, and viscosity, η, for TFE-water mixtures, taken from (Gente and La Mesa, 2000).

in particular the solvent's relative permittivity, while others relate to the excess molar quantities.

1.4. Review of models of TFE effects on protein structure and aggregation

A large number of proteins and peptides undergo fluoroalcohol-induced structural transitions and aggregation (Otzen, 2010). TFE is often used to stabilize α-helices, although it may also promote other types of structures (Rajan and Balaram, 1996). In the following section, we discuss some of the most common explanations for TFE-induced protein structural changes and aggregation. We consider our data in the context of each proposed model, and argue that protein dehydration in dilute TFE solutions, followed by preferential solvation at higher TFE concentrations, is the most likely explanation for our observations. We also believe that direct protein-TFE interactions may be involved in determining the conformation of a protein at high TFE. Therefore, our model combines several types of proposed TFE-protein interactions. TFE concentration, protein sequence, and other solution conditions determine which effect is dominant.

It is important to remark that the various models of fluoroalcohol-induced aggregation are interrelated. For example, protein conformational changes are likely to occur in parallel with changes in solvent properties or fluoroalcohol clustering, and it might be very difficult to separate correlation from causation in these processes (see also Chapters 3-4). Different mechanisms may also be involved in the fluoroalcohol-induced fibrillization of various proteins. Experiments and simulations that directly address the hydration status of proteins may help to distinguish causation vs. correlation in these processes (Rauscher, et al., 2006; Zhang and Yan, 2008).

Below, we identify and briefly summarize seven commonly cited models of TFE effects on protein structure. We contend that our experimental observations are

most consistent with two of the proposed mechanisms, and we explain our rationale for rejecting the other models. Because much of our evidence is indirect or circumstantial, we do not claim to have proven that our interpretation is correct. However, we believe that our model is a plausible explanation for our results, given the available information.

1.4a. Protein dehydration as a result of TFE-water mixture behavior

Many investigations, spanning decades, have proposed that alcohols and fluoroalcohols cause dehydration of the protein backbone (Cammers-Goodwin, et al., 1996; Conio, et al., 1970; Kentsis and Sosnick, 1998; Storrs, et al., 1992). Alcohol-induced protein dehydration has generally been studied in the context of protein folding, but recently has also been proposed as a potential mechanism underlying alcohol-induced protein aggregation (Zhang and Yan, 2008). Dehydration models involve changes in the solvation layer near the protein.

TFE-water interactions or bulk solution properties, rather than TFE-protein interactions, are generally implicated in dehydration. Kentsis and Sosnick proposed that TFE causes ordering of water molecules, which reduces their ability to form hydrogen bonds with proteins (Kentsis and Sosnick, 1998). This water structuring, or "kosmotropic", effect could destabilize unfolded or disordered protein conformations and enhance protein aggregation (Moelbert, et al., 2004). However, the sharp decrease in the surface tension for TFE-water mixtures at low TFE concentrations (Figure 1.1E) is inconsistent with a typical kosmotropic interaction (Chitra and Smith, 2002), although the protein-liquid interface may differ from the air-liquid interface. Alternatively, the reduced relative permittivity (dielectric constant) of TFE-water mixtures (Figure 1.1D) may favor the formation of solvent-shielded structures (Vila, et al., 2000). Or, TFE may simply compete with protein for water molecules. TFE-water

mixtures experience a volume contraction (Figure 1.1C), which is consistent with formation of a water cage around the CF_3 groups in the alcohol (Rochester and Symonds, 1974), and this TFE hydration could reduce water availability for protein solvation. The addition of a small amount of TFE to water will also increase the chemical potential of water as a result of the favorable entropy of mixing, increasing the cost of protein hydration. Moreover, the large size and partial hydrophobic character of TFE could displace water molecules from the protein surface or cause structural changes in the solvation shell.

In Chapter 3, we show that heat-induced changes in the CD spectrum of αS are qualitatively similar to those caused by adding small (<15%) amounts of TFE to the solution. The temperature-induced changes likely reflect reduced PPII secondary structure present in the ensemble of conformations for the disordered protein at elevated temperatures (Drake, et al., 1988; Tiffany and Krimm, 1972). Water-backbone hydrogen bonds, which are favorable at lower temperatures, are thought to unmask (Drozdov, et al., 2004) or promote (Poon, et al., 2000) PPII structure, while heating reduces these interactions. Therefore, our observation of reduction in PPII structure in the presence of small amounts of TFE is suggestive of backbone dehydration.

Low concentrations of TFE induce a similar structural change For EGFP (Chapter 4), although less TFE is needed to destabilize PPII structure for EGFP compared to αS. Notably, EGFP, which is globular in its native state, likely contains sequence elements that favor backbone dehydration and hydrophobic collapse.

We also demonstrate an increase in aggregation of αS variants (Chapters 2-3) and EGFP (Chapter 4) in solutions where PPII structure is diminished. Restriction of water availability via reverse micelles has been found to increase protein aggregation (Mukherjee, et al., 2009). In addition, dehydration coupled to aggregation has been

observed for proteins in ethanol-water mixtures (Zhang and Yan, 2008). Furthermore, the core of amyloid fibrils is dry, and therefore removal of solvent is likely a necessary step in the aggregation reaction (Balbirnie, et al., 2001). Indeed, sequences favoring peptide backbone hydration and PPII structure have been found to decrease amyloid formation (Rauscher, et al., 2006). Therefore, enhanced aggregation is consistent with dehydration.

Dehydration is thought to be a key step in protein folding, with removal of bound waters limiting folding rates (Hillson, et al., 1999; Liu and Chan, 2005; MacCallum, et al., 2007). Similar kinetic barriers may be involved in aggregation reactions. Or, TFE-induced destabilization of PPII structure might increase the average free energy of the monomer ensemble, leading to population of oligomeric or aggregated states. Loss of solvent-protein hydrogen bonds could also favor the formation of amyloid fibrils or other aggregates that contain intramolecular hydrogen bonds.

Zhang and Yan argued that the aggregation-promoting effects of TFE should be analogous to those for ethanol (Zhang and Yan, 2008), and our observations for dilute solutions of TFE are in agreement with their prediction. However, at higher TFE concentrations, aggregation is reduced, and therefore another type of interaction must occur. In addition, we find that electrostatic repulsion limits aggregation at low pH for both αS102 and EGFP, and the type of fibril produced depends on protein sequence, TFE concentration and temperature. Therefore, desolvation likely facilitates aggregation, but many other interactions contribute to the process.

1.4b. TFE as a hydrating agent

Grudzielanek, et al. propose that kosmotropic interactions enhance protein hydration, leading to destabilization of native insulin tertiary structure at moderate

TFE (Grudzielanek, et al., 2005). They hypothesize that low concentrations of TFE increase water structure, stabilizing hydrated, unfolded states. This unfolding leads to exposure of hydrophobic residues and aggregation.

Our data for EGFP at pH 7.5 also reveal TFE-induced tertiary structure disruption prior to aggregation (Chapter 4). However, we find that the denatured protein does not adopt PPII structure, but instead appears to sample non-native α-helical structures and a partially structured "intermediate" conformation. Significantly, PPII structure appears to be protective for acid-denatured EGFP. Moreover, our αS results (Chapter 2), as well as previous research on natively disordered peptides, indicate that PPII structure is correlated with solubility, while aggregation-prone conformations appear partially structured (Fezoui and Teplow, 2002; Williamson, et al., 2009). Therefore, although exposure of hydrophobic residues in the denatured state likely contributes to the aggregation process, the structure of the aggregation-prone state does not appear to be PPII-like. As we discussed in Section 1.4a, we believe that the aggregation-prone conformations are dehydrated, while the low-TFE, PPII-like state is stabilized by water-protein interactions.

In addition, dehydration is a more obvious promoter of aggregation than hydration. Removal of solvent molecules may present a kinetic barrier to aggregation, or loss of solvent interactions could increase the expected free energy of the monomer protein relative to the transition state and/or aggregated states (see also Section 1.4a). Hydration that leads to exposure of hydrophobic residues could be a plausible explanation for aggregation of globular proteins, but it does not explain the behavior of denatured or disordered proteins, which experience TFE-induced increases in aggregation propensity in the absence of tertiary structure. Our EGFP results show that subsequent to TFE-induced denaturation, EGFP behaves much like an intrinsically disordered protein and experiences solvation-related changes in aggregation

propensity. In addition, TFE can only denature EGFP when present in high concentrations, where PPII structure in the denatured state is minimal.

Notably, Grudzielanek, et al. do not measure the structure of the aggregation-prone states of insulin, and it may be that this conformation is indeed hydrated or PPII-like. It is possible that the properties of insulin are different from EGFP and αS, and that aggregation of these proteins proceeds via different mechanisms. Experiments to asses the conformation and hydration state of additional TFE-denatured globular proteins may help to clarify this issue.

1.4c. Preferential solvation of proteins by TFE

TFE has been hypothesized to affect protein structure as a result of preferential solvation (Fioroni, et al., 2002; Kundu and Kishore, 2004; Munishkina, et al., 2003; Roccatano, et al., 2002; Walgers, et al., 1998). Preferential solvation models involve TFE molecules partitioning into the solvation shell of a protein in order to reduce the free energy of the system. There is a significant amount of experimental (Chatterjee and Gerig, 2007; Diaz, et al., 2002; Kumar, et al., 2003; Othon, et al., 2009) and theoretical (Fioroni, et al., 2002; Roccatano, et al., 2002) evidence for coating of proteins by TFE, at least in >~30% TFE solutions.

TFE coating of proteins is often interpreted in terms of "chaotropic" effects (Grudzielanek, et al., 2005; Walgers, et al., 1998). The chaotropic mechanism implicates a breaking of water-water hydrogen bonds when TFE is introduced to a solution, leading to an unfavorable change in bulk water structure that drives TFE molecules into the protein solvation shell. Preferential solvation of proteins by TFE could also be related to the positive excess Gibbs function (Figure 1.1B), along with other thermodynamic properties of TFE-water mixtures (Marcus, 2001). Enthalpic TFE-protein interactions, if they occur, would contribute to preferential solvation

(Marcus, 1988). Hydrophobic interactions could also be a factor in protein solvation by TFE (Yamaguchi, et al., 2006; Yanagi, et al., 2011). Favorable changes in solvent free energy may occur when TFE displaces water from the protein solvation shell (Eggers, 2011). The large size of TFE compared to water might increase TFE-protein interactions because replacement of water molecules by a smaller number of TFE molecules would lead to a greater solvent entropy gain.

We find that the secondary structures of αS variants and acid-denatured EGFP vary between 0 ~30-40% TFE, above which the changes level off (Chapters 2-4). In Chapter 3, we show that the CD spectra of αS102 are very similar in the ~40% to >99% TFE range, indicating that the protein environment is essentially TFE-like under these conditions. Interestingly, many studies have demonstrated a similar ~30-40% TFE saturation in the helix induction curves for various proteins and peptides (Jasanoff and Fersht, 1994; Luo and Baldwin, 1997; Nelson and Kallenbach, 1986). Diaz et al. also observed complete coating of bombesin by TFE in ~30% TFE (Diaz, et al., 2002). These observations are consistent with preferential solvation resulting in TFE partitioning into the protein solvation shell above ~30% TFE, leading to the protein experiencing a local environment that is similar to bulk TFE.

Preferential TFE solvation may remove water interactions that destabilize helical structure relative to the coil state (Othon, et al., 2009; Walgers, et al., 1998). β-hairpin and other types of secondary structures may also be stabilized via a similar mechanism (Roccatano, et al., 2002). We find that EGFP and αS adopt highly α-helical structures above ~30-40% TFE. However, protein sequence and solution conditions (especially temperature and pH) affect the fraction of residues adopting helical conformations (Chapters 3-4), and so additional interactions must influence the protein conformation in the TFE-rich environment (see also Section 1.4f).

In addition, our results show that only the N terminus of αS experiences structural changes above ~15% TFE (Chapter 2). Because the CD signal from helical regions is much stronger than that from PPII-like or coil structures, it is possible that we fail to detect subtle structural changes in the C terminus at high TFE. However, it is also possible that preferential solvation affects only certain regions of the protein. Starzyk, et al. showed that complete dehydration affected only helical residues, while statistical coil sequences remained solvated in 40% TFE (Starzyk, et al., 2005). It is possible that TFE selectively displaces the highest-energy water molecules, which may be those surrounding sequences with a high helical propensity, in the protein solvation shell (Eggers, 2011; Walgers, et al., 1998). It is also possible that helical structure facilitates direct TFE-protein interactions (Section 1.4f), leading to preferential solvation of helical regions at relatively low TFE concentration. At sufficiently high TFE, coil regions must be completely dehydrated; such regions likely will remain in "statistical coil" or PPII states even in neat TFE (Kakinoki, et al., 2005; Rabanal, et al., 1993). It is not clear whether coil regions experience a gradual loss of water interactions, or whether they might undergo preferential solvation at higher TFE concentrations. Measurements of proline-rich peptides in neat TFE could be informative.

Preferential solvation may increase protein solubility because increased surface area for TFE accumulation is available for monomeric protein compared to aggregates (Moelbert, et al., 2004). Additionally, increased average solvent free energy, resulting from unfavorable TFE-water interactions, might decrease the energy difference between the protein solvation shell and bulk solvent. Such a change in solvent energy would reduce the free energy gain for freeing solvent molecules from protein surfaces that are buried during oligomerization, and therefore decrease the favorability of aggregated states (Eggers, 2011). TFE-protein interactions may also stabilize

monomer protein in a TFE-rich environment. In any case, the reduction in aggregation that is typically observed for proteins in high TFE solutions is consistent with preferential solvation. For example, Chiti, et al. find that aggregation diminishes above ~35% TFE for eight mutants of acylphosphatase, despite widely varying native state stabilities (Chiti, et al., 2000). Moreover, Grudzielanek, et al. (Grudzielanek, et al., 2005) suggest that preferential solvation occurs at >~30% TFE for insulin, where the aggregation propensity of that protein decreases. We similarly observe that αS and EGFP aggregation decreases above ~40% TFE, and agree that preferential solvation is likely contributing to this aggregation reduction.

However, it is not clear whether preferential solvation contributes to conformational changes and aggregation below ~10-15% TFE. We observe a crossover from more water-like (PPII) to more TFE-like (α-helical) CD spectra at ~15% for αS variants (Chapter 2) and at ~8% TFE for acid-denatured EGFP (Chapter 4). This crossover behavior is readily apparent as a shift in the position of isodichroic points for CD spectra and is also clear in transition diagram representations of the data. In addition, the variable-temperature behavior of the CD spectra shows a distinct crossover at a similar TFE concentration (Chapter 3).

In Section 1.4a, we argue that the behavior of our low-TFE CD spectra is suggestive of dehydration of αS and acid-denatured EGFP. It is possible that preferential solvation could contribute to dehydration, possibly as a result of displacement of water molecules by larger TFE molecules, leading to changes in the structure of the solvation shell or loss of protein-water hydrogen bonds. Alternatively, preferential solvation may be a minor effect below ~10-15% TFE, and other solvent properties may be primarily responsible for dehydration and aggregation enhancement at low TFE.

Preferential solvation is consistent with the saturation in helix induction and the decrease in protein aggregation that we and others observe above ~40% TFE. However, because no partitioning benefit is expected in 100% TFE solutions, preferential solvation cannot account for aggregation reduction at very high TFE. In addition, the stabilization of α-helices, as opposed to other types of structure, may be related to the properties of TFE or involve specific TFE-protein interactions. Therefore, we propose that preferential solvation leads to TFE coating of proteins, but additional factors affect the protein structure in the TFE-rich environment (see also Section 1.4f).

1.4d. Interactions between proteins and TFE clusters

The observation that fluoroalcohols associate in aqueous solution has led to the proposal that protein-TFE cluster interactions may cause or contribute to protein structural changes and aggregation (Hong, et al., 1999; Reiersen and Rees, 2000; Yamaguchi, et al., 2006) This hypothesis is supported by the fact that conformational changes and peak aggregation of certain proteins occur at ~30% TFE, where cluster formation is maximal (Hong, et al., 1999). The propensities of various alcohols to form clusters when mixed with water are also positively correlated with the abilities of these alcohols to induce α-helical structure in proteins (Hong, et al., 1999).

The amount of clusters present in TFE-water mixtures drops sharply between ~40-80% TFE (Gast, et al., 1999; Hong, et al., 1999). In contrast, protein conformational changes are usually rapid below ~30-40% TFE but level off at higher TFE concentrations (Gast, et al., 1999; Jasanoff and Fersht, 1994; Luo and Baldwin, 1997; Nelson and Kallenbach, 1986). We find that the secondary structure of αS (Chapter 2) and EGFP (Chapter 4) are essentially the same in ~40-60% TFE solutions. Therefore, it seems unlikely that protein structure is tightly coupled to clustering.

Gast et al. argue that, because no clustering occurs below ~20% TFE, while many proteins experience significant structural changes at lower TFE, cluster formation is a accompanying phenomenon, rather than the cause of structural transitions (Gast, et al., 2001). Similarly, we demonstrate that structural changes occur for αS variants and acid-denatured EGFP even at very low (2-5%) TFE. Furthermore, both EGFP and αS experience significant amounts of aggregation at ~10-15% TFE, which is below the ~20% TFE onset of clustering. Many other peptides and proteins show similar behavior (Chiti, et al., 2000; Fezoui and Teplow, 2002; Srisailam, et al., 2003; Zerovnik, et al., 2007). Therefore, cluster formation does not appear to be required for TFE-induced protein aggregation.

Increased water-water and cosolvent-cosolvent interactions (e.g. partitioning of TFE into the solvation shell of TFE molecules) may occur when the excess Gibbs function (Figure 1.1B), for a cosolvent-water mixture is positive (Marcus, 2001). Importantly, preferential solvation of additional solutes, for example proteins, can also occur when the excess Gibbs energy for a mixed solvent is positive (Marcus, 1988). Therefore, the formation of clusters may reflect solution conditions in which hydrophobic interactions among TFE molecules, and between TFE and proteins, are likely (Yamaguchi, et al., 2006). We believe that clustering and preferential protein solvation by TFE are probably manifestations of the same underlying thermodynamic effects, and that it is preferential solvation that directly impacts protein structure (see also Section 1.4c).

1.4e. TFE as a hydrogen bond enhancer

Luo and Baldwin observed that the hydrogen bond strength of a model compound (salicylic acid) in TFE is positively correlated with the propensity of alanine-rich peptides to form helical structure, and concluded that strengthening of

hydrogen bonds in the helix backbone may account for the dramatic structural changes induced by TFE (Luo and Baldwin, 1997). This effect can be partially explained by the reduction in the relative permittivity of TFE-water mixtures (Figure 1.1D) at high [TFE] (Hong, et al., 1999; Munishkina, et al., 2003).

However, as Gast et al. noted, if preferential solvation occurs for both proteins and salicylic acid, hydrogen bond strengthening could be an indirect effect of moving organic molecules into a relatively nonpolar local environment (Gast, et al., 1999). Preferential solvation may result in both the protein and the model compound experiencing a TFE-rich local environment (Section 1.4c), while hydrogen bond strengthening or other effects regulate the structure of the TFE-solvated protein. Notably, for many peptides, both hydrogen bond strengthening effects and helix induction plateau above ~40% TFE (Luo and Baldwin, 1997).

Hong, et al. showed that hydrogen bond strengthening for salicylic acid is greater in mixtures of simple alcohols and water compared to TFE, despite the fact that TFE is a better stabilizer of α-helices (Hong, et al., 1999). In addition, they observed that the salicylic acid hydrogen bonds were weaker in mixtures of 1,1,1,3,3,3-Hexafluoro-2-propanol (HFIP) with water, compared to TFE-water mixtures, for concentration ranges associated with helix formation (above ~10% alcohol), even though HFIP is a stronger helix inducer than TFE. Therefore, it seems that the marked effects of fluorinated alcohols on protein structure cannot be due to hydrogen bond strengthening alone.

Hydrogen isotope partitioning experiments also demonstrated that addition of 5% TFE to aqueous solution resulted in weakening of intramolecular hydrogen bonding for a coiled-coil peptide (Kentsis and Sosnick, 1998). Although helix formation is generally low at 5% TFE, this concentration range is associated with enhanced aggregation of some disordered or weakly structured proteins (Chiti, et al.,

2000; Munishkina, et al., 2003). In addition, this trend is inconsistent with increased β-structured aggregate production in ~10%-20% TFE for αS variants (Chapter 2); weakened intramolecular hydrogen bonds might be expected to destabilize such aggregates.

Considering these observations, we conclude that hydrogen bond strengthening, if it occurs, is likely an accompanying effect. Favorable intramolecular hydrogen bonds may increase protein helicity subsequent to preferential solvation (see also Section 1.4c and Section 1.4f).

1.4f. Hydrogen bonds between TFE and proteins

In Section 1.4c, we argued that preferential TFE solvation of proteins may contribute to reduced aggregation in solutions containing ~30-60% TFE. However, some proteins and peptides are highly soluble in neat TFE (Chin, et al., 1994; Malavolta, et al., 2006), although no partitioning benefit should occur in 100% TFE solutions, where all solvent molecules are equivalent. Therefore, additional TFE-protein interactions must be present to account for the stability of monomer proteins at very high TFE. Dispersive interactions and polar interactions are likely to occur, but protein-TFE hydrogen bonds may also form. TFE-protein interactions probably also affect the conformation of a protein in a TFE-rich environment.

Rajan and Balaram hypothesized that a TFE molecule might donate a hydrogen bond to a peptide carbonyl group; this bond could potentially form without disrupting a hydrogen bond between backbone amide hydrogen and carbonyl groups (Rajan and Balaram, 1996). They proposed that such bifurcated hydrogen bonds could stabilize secondary structural elements such as α-helices, and that direct interactions could therefore drive helix formation in TFE-water mixtures. However, a study of model compounds found that hydrogen bonds between TFE and the model substances were

not sufficient to account for helix induction, although some TFE-solute hydrogen bonding did occur at high (>~60%) TFE concentrations (Walgers, et al., 1998). Yang et al. also found evidence of direct interactions between proteins and alcohols (including TFE), but found that the strength of these interactions was not correlated with the ability of a given alcohol to induce protein structural transitions (Yang, et al., 1993). Additional studies of peptides and proteins in >40% TFE have found evidence of long-lived TFE-protein complexes of indeterminate nature (Chatterjee and Gerig, 2007), as well as hydrogen bonding between peptide backbone carbonyl groups and TFE (Iovino, et al., 2001; Rothemund, et al., 1996). Taken together, these studies indicate that TFE-protein hydrogen bonding may occur in a TFE-rich environment, but such hydrogen bonding likely does not initiate structural changes.

We observe that the protein conformation at high concentrations of TFE depends on protein sequence. For αS, we find that the helix induction involves the N terminus of the protein only (Chapter 2). The C terminal portion of αS contains >10% proline residues. Polyproline and proline-rich peptides typically adopt PPII structure in neat TFE (Kakinoki, et al., 2005; Rabanal, et al., 1993). A similar lack of helix formation at high TFE has been observed for proline-rich regions of the protein amelogenin (Ndao, et al., 2011). Hydrogen bonding between peptide amide hydrogens and carbonyl groups is precluded by the proline ring, and so intramolecular hydrogen bond strengthening (Section 1.4e) would not be expected to induce helix formation for proline-rich sequences. However, hydrogen bonds between TFE and carbonyl groups of polyproline peptides could contribute to increased population of relatively extended PPII conformations compared more compact structures (Strassmair, et al., 1969). Alternatively, a reduction in “solvophobic” and “solvophilic” behavior in TFE could also favor the extended conformation (Kinoshita, et al., 2000).

Heating leads to reduced helical structure for αS102 in ~20-99% TFE (Chapter 3). Increased temperatures could decrease helicity by favoring protein structures with greater conformational entropy. However, another explanation for this melting behavior might be loss of helix-stabilizing enthalpic solvent-protein interactions, potentially including TFE-protein hydrogen bonds. In addition, the relatively low fraction of residues in the helical conformation for EGFP at high TFE (Chapter 4), compared to αS variants (Chapter 3), could reflect differences in the interactions of these proteins with TFE.

Therefore, TFE-protein hydrogen bonding may account for some sequence- and temperature-dependent variations in protein structure in high-TFE solutions. As we discussed in Section 1.3, TFE forms significantly fewer hydrogen bonds per unit volume than water. In addition, TFE is a strong proton donor, but poor acceptor, compared to water, and this imbalance may limit protein-solvent hydrogen bonding. However, if a protein molecule is brought into close proximity with TFE by preferential solvation (Section 1.4c) or some other interaction, and both TFE and proteins have the capability to participate in hydrogen bonds, it seems likely that at least some such bonds would form. These bonds may the conformation of the protein in a TFE-rich environment and may also contribute to protein solubility in neat TFE.

1.4g. TFE as a structural switcher

Aggregation of many proteins in TFE is correlated with the formation of specific structural states, leading to the hypothesis that TFE acts as a "structural switcher", with moderate TFE concentrations stabilizing aggregation-prone protein conformations (Abedini and Raleigh, 2009a; Fezoui and Teplow, 2002; Pallarès, et al., 2004; Zerovnik, et al., 2007). Here, one or more of the mechanisms described above

(Sections 1.4a-1.4f) presumably causes the structural changes, but solvent-related effects are thought to be secondary to protein structure in the initiation of aggregation.

Many reports suggest that aggregation-prone intermediates are partially helical (Anderson, et al., 2010; Fezoui and Teplow, 2002; Liu, et al., 2004; Sen, et al., 2010; Williamson, et al., 2009; Zerovnik, et al., 2007). As a result, researchers have proposed that helix-helix interactions align neighboring disordered segments, facilitating aggregation (Abedini and Raleigh, 2009a; Williamson, et al., 2009). However, Calamai, et al. found that multiple conformational states can lead to similar aggregates, indicating that helical structure is not a prerequisite to aggregation (Calamai, et al., 2005) Also, short (5-6mer) peptides, which should not be capable of forming significant helical structure, show enhanced fibril formation in ~7-10% TFE (Chaudhary, et al., 2009). Investigation of additional proteins have revealed other types of aggregation-prone intermediates, particularly extended β-sheet conformations (Lim, et al., 2010; Pallarès, et al., 2004; Srisailam, et al., 2003), leading some researchers to suggest that TFE promotes the exposure of "sticky" unpaired β-sheet edges, leading to enhanced aggregation (Pallarès, et al., 2004; Srisailam, et al., 2003). Furthermore, TFE-induced aggregation can even occur in the absence of significant tertiary structure disruption (Plakoutsi, et al., 2004; Soldi, et al., 2005).

The diversity of aggregation-prone intermediates casts doubt on the hypothesis that particular structural elements directly cause aggregation. Of course, it is possible that multiple intermediates enhance aggregation and that various mechanisms contribute to this effect. However, a simpler explanation is that some solvent-dependent effect leads to reduced protein solubility, with structural transitions being coincidental.

Our αS data indicates that heat-induced aggregation near 15% TFE is correlated with loss of PPII structure (Chapter 3). We also observe loss of PPII signal

and aggregation for acid-denatured EGFP in ~8% TFE (Chapter 4). Other disordered proteins and peptides also show reduced PPII-like CD signals, along with aggregation enhancement, at low-to-moderate TFE (Fezoui and Teplow, 2002; Liu, et al., 2004; Yamaguchi, et al., 2006). In general, some helical structure is detected for these proteins prior to aggregation. However, we hypothesize that it is the loss of PPII structure, rather than the gain of α-helices or other types of secondary structure, that is important for TFE-enhanced aggregation.

As we discuss in Section 1.4a above, PPII structure is favored by hydrogen bond formation between water and the protein backbone, and so reduction of the PPII peak in the CD spectrum may indicate loss of these interactions. Weakening of water-protein interactions is likely to reduce solvation barriers to aggregation and to destabilize the monomer protein. Therefore, we believe that the protective nature of PPII structure is due to its solvent exposure.

Some "structural switcher" models propose that aggregation reduction at high TFE is due to the stability or other properties of the highly helical state (Fezoui and Teplow, 2002). It is quite plausible that helix stability could act as a barrier to aggregation. However, Chaudhary, et al., found that 5-6mer peptides, which should not be able to form α-helices, are soluble in neat TFE but form aggregates in solutions containing ~7-10% TFE (Chaudhary, et al., 2009). In addition, EGFP aggregation is reduced above similar TFE concentrations at pH 2.4 and 7.5, despite the fact that the pH 2.4, high-TFE conformation is approximately 50% more helical than the pH 7.5, high-TFE state (Chapter 4). For EGFP, it is possible that constraining a specific aggregation-promoting sequence is crucial, while the remainder of the helical structure is unimportant. However, it is more difficult to explain how helix stabilization could cause reduction in aggregation for very short peptides.

In Section 1.4c, we noted that preferential solvation could decrease aggregation in solutions containing moderate-to-high TFE. It is also possible that TFE-protein interactions (e.g. Section 1.4f) stabilize the monomer protein in neat TFE and/or the TFE-rich environment resulting from preferential solvation. Therefore, helix formation may be one of many factors that affect protein solubility at high TFE.

For globular proteins, loss of tertiary structure (a structural switch) often precedes aggregation at moderate TFE. In general, the stability of globular proteins is negatively correlated with the onset of TFE-induced denaturation (Chiti, et al., 2000; Gast, et al., 1999). In Chapter 4, we showed that little aggregation occurred when EGFP tertiary structure was intact, while aggregation increased sharply at 15% TFE subsequent to TFE-induced denaturation of EGFP. However, tertiary structure disruption was not sufficient to cause aggregation; aggregation of TFE-denatured EGFP was low above ~30% TFE. Indeed, once a globular protein is denatured, it behaves like a natively disordered protein in TFE, sampling various conformational states and experiencing reduced aggregation at high TFE (Chiti, et al., 2000). As we discussed in Section 1.4c, additional interactions, particularly preferential solvation, likely stabilize the high TFE conformation. Therefore, the "structural switcher" model does appear to have some validity for globular proteins, but it is the loss of a protective factor (tertiary structure), as opposed to the formation of a specific aggregation-prone conformer, that enables aggregation.

It is possible that aggregate morphology may be affected by the structure of intermediate states. In many cases, TFE promotes the formation of amyloid or other ordered, β-sheet-rich fibrillar species (Anderson, et al., 2010; Fezoui and Teplow, 2002; Srisailam, et al., 2003; Yamaguchi, et al., 2006). However, amorphous and granular species are also frequently observed (Bucciantini, et al., 2002; Chiti, et al., 1999; Zerovnik, et al., 2007). Very interesting chunky aggregates in which the tertiary

structure and function of the native protein is conserved can also be formed (Plakoutsi, et al., 2004; Soldi, et al., 2005). Therefore, TFE seems to act as a general-purpose aggregation enhancer, but additional factors influence the selection of a particular aggregation pathway.

Burial or constraint of certain residues could affect aggregation pathway selection. In particular, it appears very likely that native state stability does impact the aggregation pathway of globular proteins, leading to native-like aggregates in some cases (Plakoutsi, et al., 2004; Soldi, et al., 2005). However, there are many other mechanisms that may contribute to the diversity of TFE-induced aggregates, including details of protein sequence, electrostatic interactions, and stabilization of particular oligomeric conformations. In addition, protein aggregation may be subject to kinetic control (Hwang, et al., 2004; Pellarin, et al., 2010), and TFE may affect the relative rates of formation of various species.

We find that aggregation proceeds from very similar partially structured intermediate for αS variants and EGFP (Chapter 4). However, the resulting aggregate morphologies are different for the two proteins. For αS at 25-37 °C, β-sheet-rich, ordered, helical fibrils grow in solutions containing ~10-15% TFE (Chapter 2). For EGFP in >~7.5% TFE, flexible, smooth fibrils are observed (Chapter 4). Moreover, the C terminal tail of αS affects the aggregation pathway at 70 °C in the presence and absence of TFE (Chapter 3). Therefore, it appears that protein sequence elements and solution conditions can dramatically affect the aggregation pathway, even when a similar intermediate conformation is observed prior to the onset of aggregation.

A final issue to consider is the thermodynamic means by which stabilization of the intermediate state might increase oligomerization rates and enhance aggregate production. In Figure 1.2, we consider a dilute protein solution in the absence (black solid lines) or presence (red dashed lines) of a small amount of TFE. We assume that

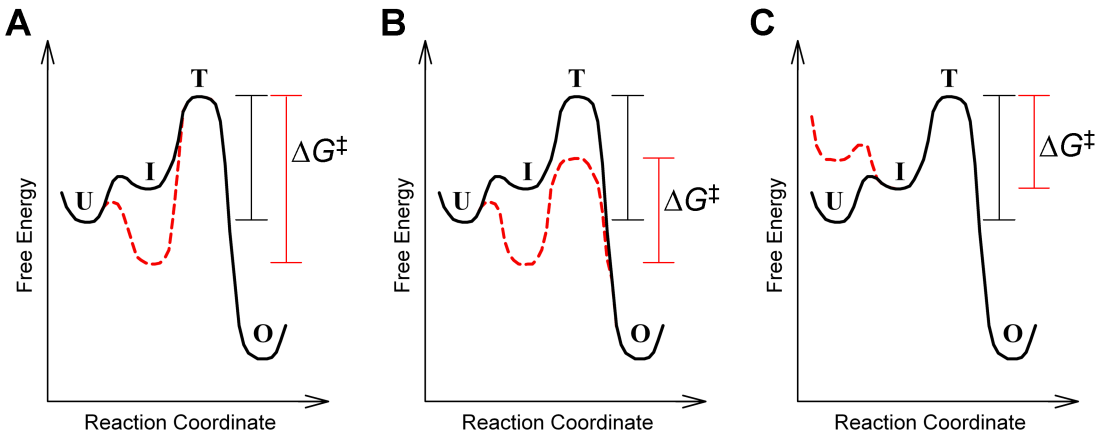

Figure 1.2. Free energy diagrams for an oligomerization reaction showing three possible TFE-induced modifications. The solid black lines show the hypothetical state of the system in the absence of TFE, while the putative TFE effects are illustrated by the dashed red lines. The U state corresponds to the monomer conformation that predominates in 0% TFE, the I state is the "intermediate" monomer structure favored in moderate [TFE], and the O state is a small oligomer. For the 0% TFE case, the activation energy, $\Delta G^{\ddagger}$, is equal to the difference between the transition (T) state energy and the U state energy (see the black measurement lines at the right of the diagrams). The activation energies $\Delta G^{\ddagger}$ for the proposed TFE-induced changes are shown via the red measurement lines. (A) Decreasing the free energy of the I state leads to an increase in the barrier height; $\Delta G^{\ddagger}$ is now equal to the difference in free energy between the T state and the stabilized I state. (B) Decreasing the free energies of both the T and I states decreases $\Delta G^{\ddagger}$. (C) Destabilizing the U state also decreases $\Delta G^{\ddagger}$.

the solution is dilute enough that we can consider only the formation of the earliest oligomer species ("O"). An example where this approximation is likely valid is the 2 μM αS samples we discuss in Chapter 2 (Figure 2.9); our data showed that αS variants populate the PPII-like "U" state at 0% TFE, while the addition of 15% TFE causes the monomer proteins to populate the intermediate "I" state and then convert to an oligomeric conformation. We also assume there is a kinetic barrier which prevents aggregation at 0% TFE, and we call the associated transition state "T". In transition state theory, quasai-equilibrium conditions are assumed to hold for reactants, and the reaction rate is proportional to the fraction of monomer protein having a thermal energy at or above the level of the transition state (Upadhyay, 2006). Thus, the reaction rate depends on the activation energy, $\Delta G^{\ddagger}$, which is equal to the difference between the free energy of the transition state and the lowest reactant state energy.

Figure 1.2A shows that simply decreasing the free energy of the intermediate state leads to an increase in $\Delta G^{\ddagger}$, and therefore causes a reduction in the aggregation rate (Creighton, et al., 1996). Moreover, if the energy of the O state remains constant, stabilizing the I state will reduce the total amount of oligomer produced after the system equilibrates because the free energy of monomeric protein is decreased. An increase in the reaction rate can result from stabilization of both the intermediate and the transition states (Figure 1.2B). This scenario might occur if, for example, the I and T states both contain specific structural elements that are favored in moderate [TFE]. However, the amount of oligomer produced will also be decreased, provided that the free energy of the O state remains unchanged. Only destabilizing the U state (Figure 1.2C) will both reduce the reaction rate and increase oligomerization, in the absence of a change in the O state energy.

An exception to the scenarios shown in Figure 1.2 might occur if the quasai-equilibrium assumption does not hold for the monomeric conformations. However, in

Chapter 2, we show that αS variant conformational changes occur faster than we can mix and load our samples onto the CD spectrometer (~1 minute), while oligomerization takes tens of minutes to hours for the 2 μM αS variant solutions (Chapter 2 and Figure 2.9). Structural rearrangements for acid-denatured EGFP are also rapid (Chapter 4). Therefore, at this time, we have no reason to expect that monomer rearrangements are rate-limiting for the aggregation of these proteins. Certainly, TFE may increase oligomer stability, in addition to decreasing kinetic barriers to aggregation, and the presence of multiple intermediates or diverse fibrillar species will complicate the diagram. However, the significance of stabilization of the I state, as opposed to changes in the free energies of the U, T, or O states, remains unexplained by our data.

In Section 1.4 a, we argued that the addition of small amounts of TFE to protein solutions may reduce water availability for protein solvation, destabilizing PPII structure. This scenario involves an increase in the free energy of the hydrated U state, and is equivalent to Figure 1.2C. Therefore, it seems likely that destabilization of the U state, rather than I state stabilization, leads to the increase in aggregation rates and fibril production that we observe for our proteins in TFE.

In sum, we believe that the secondary structural details of αS and EGFP are likely secondary to solvent interactions in TFE-induced aggregation reactions. For denatured or disordered proteins in low TFE solutions, loss of PPII structure is correlated with aggregation, while increased α-helical structure and reduced aggregation occur at high TFE. For globular proteins, tertiary structure stability determines the onset of aggregation for many proteins, and also is crucial in determining the aggregation pathway. However, once a globular protein is denatured, it behaves similarly to an unstructured protein, and TFE-protein interactions resist aggregation at high TFE. Therefore, it appears that removal of protective factors, such

as tertiary structure and protein-solvent interactions, are involved in initiating aggregation in solutions containing TFE, although secondary structural details may modify the aggregation pathway for some proteins.

1.5. Summary of our desolvation model for TFE-induced protein aggregation

We believe that dehydration (Section 1.4a) causes loss of PPII structure and increased aggregation at low TFE, while preferential solvation (Section 1.4c) leads to denaturation, α-helix induction and monomer stabilization at higher TFE. Direct TFE-protein interactions, which might include dispersion interactions, polar interactions, or hydrogen bonding (Section 1.4f), may affect the conformation of the protein in the TFE-rich environment. Aggregation is correlated with formation of a desolvated state in which both water-protein and TFE-protein interactions are minimized. Electrostatic repulsion and intact tertiary structure are also barriers to TFE-induced aggregation.

Although our data is consistent with dehydration and preferential TFE solvation of αS and EGFP, the precise molecular mechanisms underlying these phenomena are unclear. TFE has been proposed to act as a kosmotrope at low concentrations, leading to a reduction in solubility (Grudzielanek, et al., 2005; Kentsis and Sosnick, 1998). However, the strong decrease in surface tension for TFE-water mixtures compared to water (Figure 1.1E) is inconsistent with a typical kosmotropic interaction (Chitra and Smith, 2002). In addition, the molecular mechanisms underlying proposed kosmotropic and chaotropic interactions, which involve changes in bulk water structure, have been challenged (Eggers, 2011; Mancinelli, et al., 2007; Zhang, et al., 2005). Therefore, it is not clear whether it is strictly correct to interpret TFE effects in terms of changes in water structure. It is possible that bulk solvent properties, such as the reduced relative permittivity of TFE-water mixtures, lead to loss of protein-water interactions (see Section 1.4a). Or, thermodynamic properties of

TFE-water mixtures, along with possible direct TFE-protein interactions, could drive the cause dehydration and TFE coating of proteins (Eggers, 2011; Marcus, 1988).

Structural changes and aggregation in fluorinated alcohols are generally more marked than in simple alcohols. However, simple alcohols also can induce α-helical structure and enhance protein aggregation (Hirota, et al., 1997; Zhang and Yan, 2008). The extent of clustering of alcohol molecules in aqueous solution correlates with their ability to induce helical structure, and is greater for TFE and HFIP than for simple alcohols (Hong, et al., 1999). In Section 1.4d, we argue that clustering is likely a symptom of solution conditions that are conducive to preferential solvation. Therefore, relatively high concentrations of simple alcohols such as ethanol and methanol may be required for the protein to experience a fully alcohol-like local environment. It is not clear whether the ability of an alcohol to dehydrate a protein will be related to its propensity for preferential solvation. Munishkina, et al, found that αS oligomerization was correlated with the relative permittivity of simple alcohols (Munishkina, et al., 2003), and therefore dehydration may be due to changes in bulk solvent properties that occur prior to the onset of preferential solvation. Investigation of the impact of various alcohols on protein structure and aggregation may provide information about whether preferential solvation, solvent structure, or some other property, is responsible for dehydration.

Desolvation does not account for all of the features of our data. For both αS and EGFP, we find that low pH conditions increase helicity at high TFE. The interactions that determine the conformation of a protein in a TFE-rich environment are not well understood, and so it is difficult to propose a mechanism to account for these pH-dependent structural differences. In addition, the observed aggregate morphologies depend on protein sequence and solution conditions; the conformation of the protein may therefore impact aggregation pathway selection. We identify

electrostatic repulsion as an additional protective factor that reduces protein aggregation.

1.6. Relevance of our results to the study of amyloid diseases

Proteins have evolved various protective mechanisms to prevent abnormal aggregation. Hydration of disordered sequences may be among these defensive strategies. Our results suggest that TFE can be used to vary the strength of solvation barriers in protein aggregation reactions, enabling study of other factors influencing protein aggregation.

We find that loss of PPII structure in favor of partially structured states is correlated with aggregation at low TFE. These observations contradict the hypothesis that PPII structure is a killer conformation (Blanch, et al., 2000). The solvent accessibility of the PPII conformation is likely responsible for its aggregation-reducing qualities. We predict that more water-inaccessible, and therefore aggregation-prone, protein sequences will experience a sharper reduction in PPII structure in the presence of low concentrations of TFE. Measurements of these structural changes could potentially identify mutations that might increase or decrease the fibrillization of a disordered protein or peptide. Notably, in Chapter 2, we show that the Parkinson's disease-associated αS mutants A30P, E46K, and A53T, do not appear to differ in their structural responses to TFE, which indicates that other properties likely account for the variations in the mutants' aggregation rates. Moreover, our pH-dependent data show that TFE-induced dehydration is not strongly affected by protein charge, at least for αS variants (Chapter 3), and so it may be possible to use TFE to isolate and compare the contributions of electrostatic repulsion and hydration in aggregation reactions.

The solvation status of disordered proteins may also affect their interactions with chaperones. Heat shock proteins and other molecular chaperones, which bind to nascent chains and misfolded proteins to prevent their abnormal aggregation, often do not interact with natively disordered proteins (Hegyi and Tompa, 2008). For example, multiple studies have found that monomeric αS does not bind to Hsp70 chaperones, although these chaperones can inhibit αS aggregation by binding to small αS oligomers (Ahmad, 2010; Dedmon, et al., 2005; Hinault, et al., 2010). The hydration status (or low hydrophobicity) of natively disordered proteins likely contributes to their reduced chaperone binding (Hegyi and Tompa, 2008). However, it is possible that dehydration could trigger Hsp70 or other chaperone binding to disordered proteins, and so moderate TFE conditions may populate a species similar to a chaperone-associated conformation. Moreover, hydration may play a role in the abnormal oligomerization and aggregation of αS that has been found to be induced by Hsp90-type chaperones (Falsone, et al., 2009). Unlike Hsp70, Hsp90 binds to monomeric αS, and it is possible that nonspecific or accidental chaperone binding might actually induce dehydration and aggregation of the normal monomer. Of course, these ideas are speculative and much more evidence is needed to definitively link hydration status and TFE-induced conformations with chaperone activity.

In conclusion, we propose that TFE enhances aggregation by removing protective interactions, rather than by stabilizing specific aggregation-prone structural elements. Understanding natural defensive mechanisms may help identify potential interventions in amyloid diseases, and therefore TFE may be a useful tool for studying the role of solvation barriers in toxic aggregation processes.

CHAPTER 2

IDENTIFICATION OF A HELICAL INTERMEDIATE IN TRIFLUOROETHANOL-INDUCED ALPHA-SYNUCLEIN AGGREGATION*

2.1. Introduction

Parkinson's disease (PD) is one of a number of synucleopathies in which aggregation of the protein α-synuclein (αS) is linked to pathogenesis (Spillantini, 1999). αS is intrinsically disordered, but in the presence of lipid or detergent vesicles or micelles, adopts a highly helical structure in which its N-terminal region is membrane-bound and the C-terminal tail remains predominantly free and unstructured (Davidson, et al., 1998; Eliezer, et al., 2001). Although most PD cases are sporadic or idiopathic, three point mutations of αS– A53T, A30P and E46K– are associated with familial and early-onset PD (Kruger, et al., 1998; Polymeropoulos, et al., 1997; Zarranz, et al., 2004).

In addition to its free and membrane-bound states, αS adopts partially structured intermediate conformations under low-pH or high-temperature conditions (Uversky, et al., 2001). A folding intermediate has also been detected at low [TFE] (Munishkina, et al., 2003). Conditions favoring the formation of these intermediates also promote amyloid fibril growth, possibly implicating intermediate conformers as key species in the aggregation pathways.

Here, we examine TFE-induced monomer conformational changes, oligomerization, and fibrillization in detail for wild-type (WT) αS, C-terminally truncated WT αS (αS102), and the PD-associated αS mutants A30P, A53T, and

* Adapted with permission from: Anderson, V.L., Ramlall, T.F., Rospigliosi, C.C., Webb, W.W., and Eliezer, D. (2010). Identification of a helical intermediate in trifluoroethanol-induced alpha-synuclein aggregation. Proc. Natl. Acad. Sci. U. S. A. 107, 18850-18855.

E46K, expanding upon previous studies by Munishkina, et al. (Munishkina, et al., 2003) and Li, et al (Li, et al., 2002). This research also complements previous fluorescence correlation spectroscopy studies of αS membrane interactions (Rhoades, et al., 2006) and protein equilibrium structural dynamics (Chen, et al., 2007).

Helical intermediates have been reported to promote fibril formation of a number of amyloidogenic proteins (Abedini and Raleigh, 2009a; Abedini and Raleigh, 2009b; Booth, et al., 1997; Fezoui and Teplow, 2002; Williamson, et al., 2009; Yamaguchi, et al., 2006; Zerovnik, et al., 2007). We show that αS is likely to aggregate via such an intermediate in the presence of TFE, suggesting that membrane-induced αS aggregation may also involve the formation of a helical intermediate. Furthermore, TFE-induced fibrils are β-sheet rich and resemble previously reported aggregates formed by C-terminally truncated αS (Crowther, et al., 1998), as well as structures induced by detergent and lipid interactions (Broersen, et al., 2006; Giehm, et al., 2010), which may be linked to PD initiation and progression (Beyer, 2007; Li, et al., 2005; Michell, et al., 2007; Wakamatsu, et al., 2008).

2.2. Results

Ultrastructure of TFE-induced αS aggregates: Figure 2.1A-D shows transmission electron microscope (TEM) micrographs of various aggregates formed from WT αS after two weeks in a shaking incubator at 37 °C. Typical long, rigid amyloid fibrils form at 0% TFE (all percentages v/v). At 5% TFE, a combination of typical amyloid fibrils and shorter, flexible fibrillar structures are observed. When [TFE] is increased to 10-15%, classic amyloid fibrils disappear and only the flexible, short “TFE fibrils” are observed.

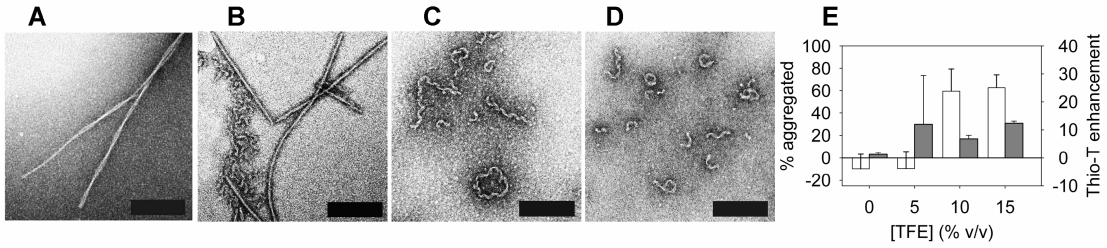

Figure 2.1. WT αS aggregate characteristics as a function of [TFE]. (A-D) TEM micrographs of structures grown from 50 μM WT αS, after two-week incubation at 37 °C with shaking in the presence of (A) 0%, (B) 5%, (C) 10%, and (D) 15% TFE. The scale bars are 200 nm. (E) For the samples in A-D, the percentage of total protein incorporated into large aggregates (white bars, left axis) and the thioflavin-T enhancement (gray bars, right axis). The error bars reflect the standard deviations for three samples and the uncertainty in volume due to evaporation.

Aggregate production for the samples in Figure 2.1A-D was quantified by centrifugation, UV absorbance and thioflavin-T fluorescence enhancement (Figure 2.1E). The amount of aggregate produced rises sharply at ≥10% TFE where TFE fibrils predominate.

Additional images of TFE-induced WT αS aggregates grown in a variety of solution conditions show that TFE fibrils can be grown at 25 °C even in the absence of shaking when [TFE] ≥ ~10% (Figure 2.2A). We have not observed classic amyloid fibril formation in the absence of shaking after incubations of up to 3 weeks in 0-20% TFE. Ultrastructurally, TFE fibrils appear to be helical, with a strand width of ~11 nm (Figure 2.3A). The overall fibril diameters are ~11-20 nm and appear to vary due to stretching or compression of the helical winding, while the minimum thickness of the strands is ~5-6 nm. Amyloid fibrils in our 0% TFE sample range in diameter from ~9-23 nm (the mean width is ~12 nm) and are thus similar in width to TFE fibrils, but are much longer and straighter. Structures that resemble closed, distorted rings can sometimes be found via TEM (Figure 2.1C, Figure 2.3B-C). Rings were most common in samples that were incubated at 37 °C with shaking, although we also observed them in some room-temperature samples (Figure 2.3C). It is not clear whether ring-like structures are actually closed loops or whether their appearance is accidental due to fibril flexibility and artifacts of drying onto the TEM grids. The extent of aggregation and thioflavin-T fluorescence emission enhancement varies as a function of [TFE] for αS samples incubated at room temperature under quiescent conditions (Figure 2.2B), with TFE fibril production occurring above ~10% TFE, and associated with some thioflavin-T binding. Similar TFE fibril production behavior at 25 °C is observed for the A30P, A53T, and E46K PD-associated αS mutants (Figure 2.2B). Qualitatively, the amount of aggregate produced is highest for the E46K mutant, while the extent of A30P aggregation is reduced. In addition, the C terminal

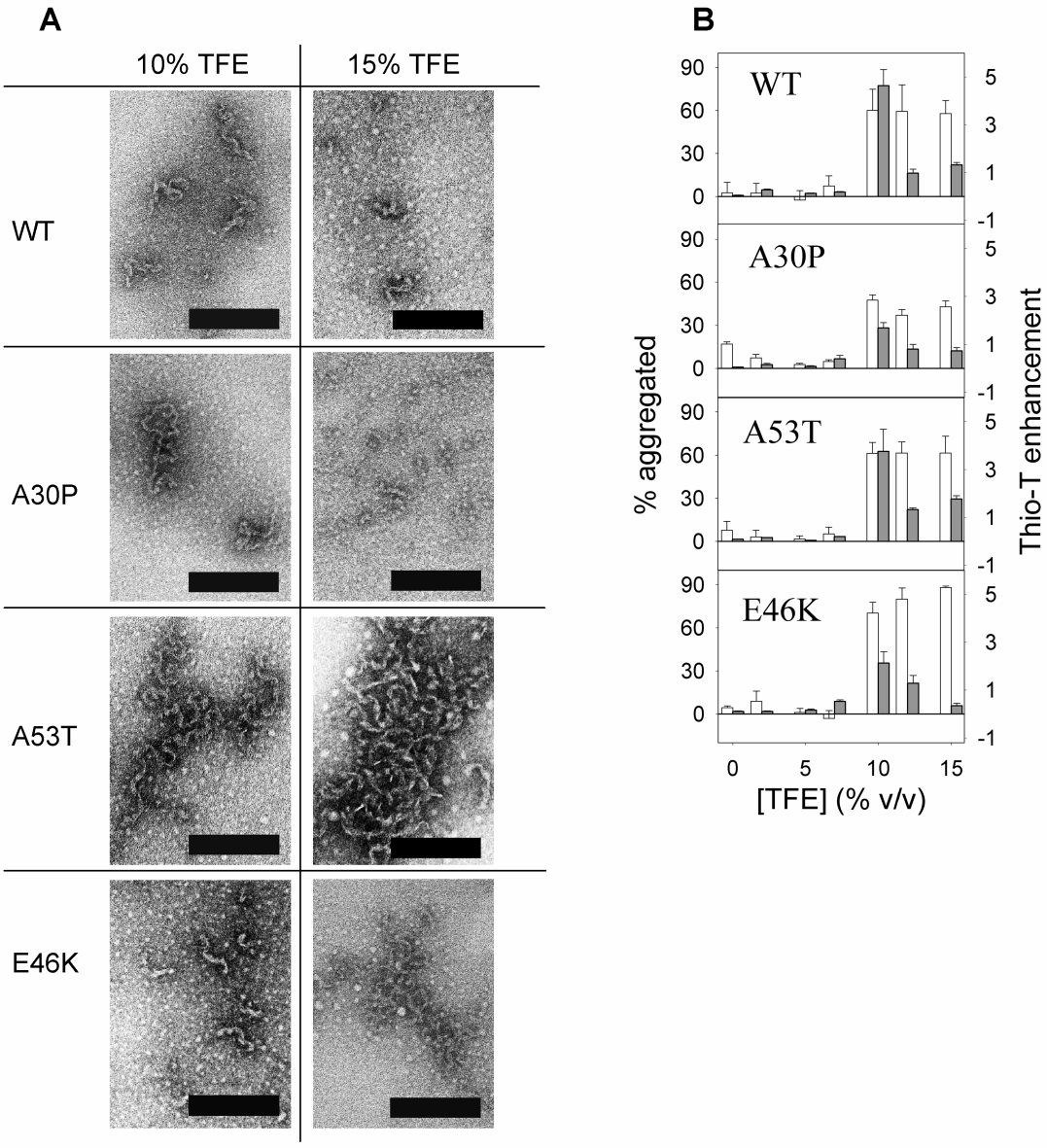

Figure 2.2. Aggregation of WT and PD-associated mutant αS at 25 °C in the absence of shaking (50 μM protein, two week incubation). (A) TEM micrographs (scale bar = 200 nm) of aggregates grown at 10-15% TFE for WT, A30P, A53T, and E46K αS. (B) Percentage of monomer protein incorporated into aggregates (white bars, left axis) and Thioflavin-T enhancement factor (gray bars, right axis) for WT, A30P, A53T, and E46K αS. The error bars represent the standard deviations for three identical samples.

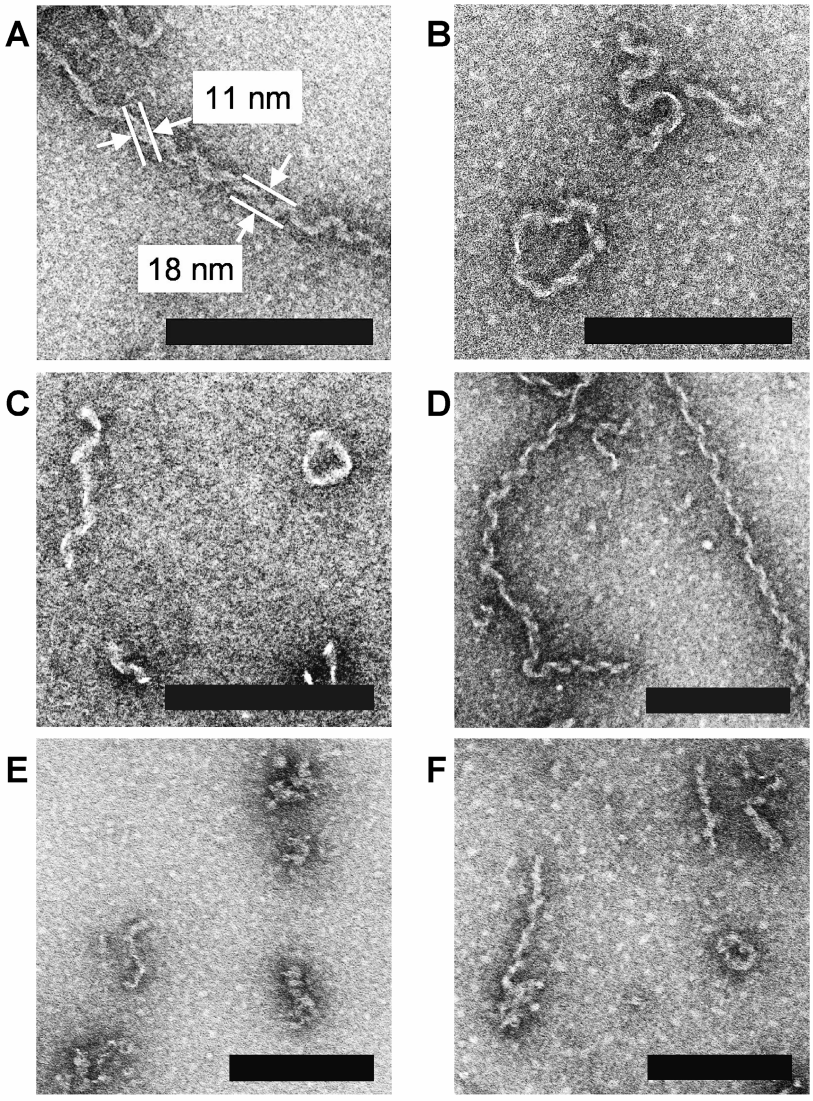

Figure 2.3. TEM images of TFE-induced aggregates grown from 50 μM of αS variants. Scale bars are 200 nm (note A-D and E-F have the same magnifications). (A) Straight TFE fibril, indicating fibril dimensions, grown from wild-type αS in the presence of 10% TFE, incubated with shaking at 37 °C for 2 weeks. (B) Ring-like and flexible structures found in the same sample as A. (C) Ring-like and fibrillar structures grown from wild-type αS in 15% TFE, incubated at room temperature in the absence of shaking for 2 weeks. (D) Straight and kinked TFE fibrils found in the same sample as images A-B. (E) Flexible TFE fibrils grown from αS102 in 10% TFE, after incubation for 2 weeks at room temperature in the absence of shaking. (F) Similar to E, but fibrils were grown in the presence of 15% TFE.

truncation mutant αS102 forms fibrillar aggregates when incubated in ~10-15% TFE (Figure 2.3E-F), indicating that the N terminal portion of the protein is sufficient for TFE-induced fibril formation.

TFE-induced secondary structural changes in monomeric αS: The far-UV circular dichroism (CD) spectrum of dilute (0.5 μM) WT αS in 0% TFE (Figure 2.4A) is relatively flat except for a deep minimum around 198 nm, consistent with a highly disordered protein. As [TFE] increases, the signal at 218-222 nm decreases, reflecting increased amounts of secondary structure. At 60% TFE, the spectrum has minima at 208 and 222 nm, indicating that αS adopts a highly α-helical conformation under these conditions. Surprisingly, sets of spectra for 0-14% and 17-60% TFE share isodichroic points (Figure 2.4A insets), consistent with coexistence of two distinct secondary structural conformations in each range of TFE concentrations. We have verified that the curves in Figure 2.4A are representative of monomeric protein by examining time- and concentration-dependent variations in the spectra (see Appendix A).

By plotting the mean residue ellipticities at 198 nm vs. 222 nm ($[\theta]_{222}$ vs. $[\theta]_{198}$), we can construct a transition diagram (Kuznetsova, et al., 2004) from the CD spectra in Figure 2.4A, enabling identification of structural transitions for the monomer protein (Figure 2.4B). Points derived from spectra corresponding to shifts in an equilibrium between two conformations appear as straight lines in this diagram; the spectra that share isodichroic points in Figure 2.4A form straight lines in our transition diagram. Our observation of two different, adjacent linear segments indicates that αS is sampling at least three secondary structure conformations: an unfolded conformation (U), which is approximated by the 0% TFE point, a well-folded, α-helical species (F), which is most similar to the 60% TFE point, and an intermediate secondary structural conformation (I) that is populated at moderate [TFE]. Along the

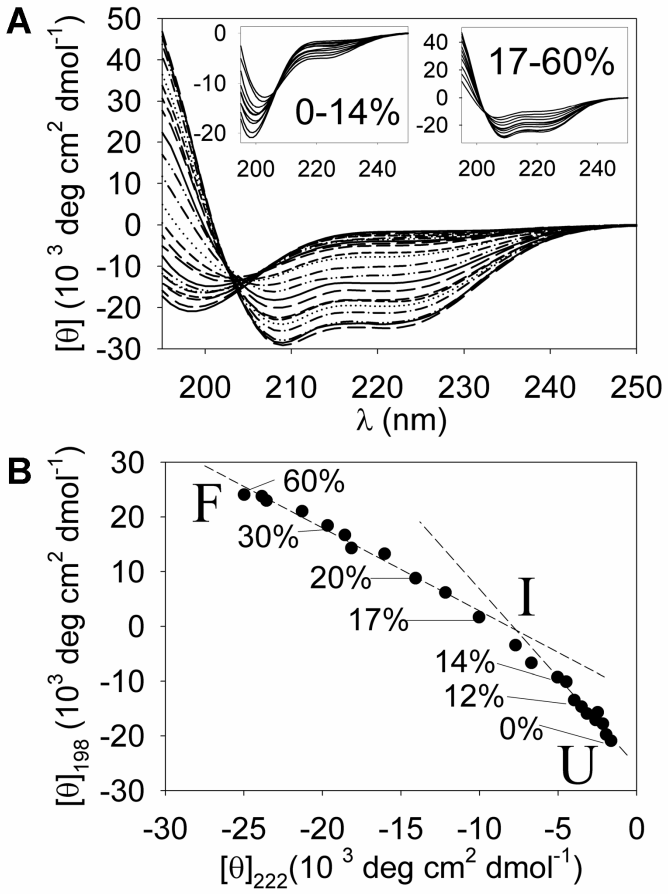

Figure 2.4. Secondary structural changes induced by TFE for WT αS at 25 °C. (A) Far-UV CD spectra for 0.5 μM WT αS in 0-60% TFE. The TFE concentrations for spectra with increasing negative ellipticity at 222 nm are 0, 2, 5, 8, 7, 9, 10, 12, 13, 14, 15, 16, 17, 18, 20, 22, 24, 26, 30, 40, 45, 50, and 60%. The insets show selected curves from the main plot, which correspond to TFE ranges where the spectra share an isodichroic point. (Inset axes units are the same as the main plot). (B) Transition diagram constructed from the ellipticity values at 222 nm and 198 nm using the data in A. For clarity, some points are labeled with their [TFE]. The dashed lines show linear fits to sets of points whose CD spectra share isodichroic points.

low-TFE line (bottom right of the plot), the U and I conformations coexist, while the I and F states are populated along the high-TFE line (top left).

Similar structural transitions are observed for αS102, as well as the A30P, A53T, and E46K αS mutants, with CD spectra showing a progression from a disordered conformation to α-helical secondary structure with increasing [TFE], and low- and high-TFE curves sharing isodichroic points (Figure 2.5A-D). The qualitative behavior of the αS102 mutant is very similar to WT, although the overall magnitude of the mean residue ellipticity for αS102 is increased at moderate to high TFE (Figure 2.5A,E, Figure 2.6A-B), indicating that a larger fraction of residues adopt secondary structure in the truncation mutant. Moreover, when transition diagrams are constructed for the three PD-associated mutants, their coexistence lines are nearly identical to those of WT αS (Figure 2.5F-H, Figure 2.6E). Therefore, the TFE-induced folding landscapes of the αS variants contain comparable structural transitions. Surprisingly, plots of $[\theta]_{222}$ and $[\theta]_{198}$ as a function of [TFE] for all the αS variants (Figure 2.6A-D) appear superficially to be sigmoidal, which is likely due to the fact that the intermediate spectrum $[\theta]_{222}$ and $[\theta]_{198}$ values lie in between the values for the U and F states. Thus, the transition diagrams reveal information about intermediate states that is hidden in these plots.

Table 2.1 shows the TFE concentrations and isodichroic points that correspond to U ↔ I and I ↔ F coexistence for all five αS variants. Note that, for a set of CD curves that share an isodichroic point, the ellipticity of all conformations that contribute to the spectra is the same at the isodichroic. Therefore, the I state ellipticity is equal to the values measured at these points. Additionally, the point at which the two straight lines in the transition diagrams intercept should correspond to the CD values for the pure I state; these values are also shown in Table 2.1.

Figure 2.5. Secondary structural changes induced by TFE for αS mutants. (A-D) Far-UV CD spectra for 0.5 μM αS variant proteins in 0-60% TFE. The insets show spectra from the main plot that share an isodichroic point. The inset axes have the same units as the main plot axes. (A) αS102 spectra. The TFE concentrations for spectra with increasing negative ellipticity at 222 nm are 1, 2, 0, 5, 7, 8, 10, 9, 11, 12, 13, 14, 15, 16, 17, 18, 19, 20, 22, 24, 26, 30, 35, 40, 50, and 60% TFE. (B) A30P αS spectra. The TFE concentrations for spectra with increasing negative ellipticity at 222 nm are 0, 2, 5, 7, 8, 10, 11, 12, 13, 14, 15, 16, 17, 18, 20, 22, 26, 30, 40, 50, and 60% TFE. (C) A53T αS spectra. The TFE concentrations for spectra with increasing negative ellipticity at 222 nm are 0, 2, 5, 7, 10, 11, 12, 13, 14, 15, 16, 17, 18, 19, 20, 22, 25, 30, 35, 40, 50, and 60% TFE.(D) E46K αS spectra. The TFE concentrations for spectra with increasing negative ellipticity at 222 nm are 0, 2, 5, 7, 9, 8, 10, 11, 12, 13, 14, 15, 16, 17, 18, 20, 22, 24, 30, 35, 40, 50, and 60% TFE. (E-H): Transition diagrams constructed from the mean residue ellipticity values at 222 nm and 198 nm using the data in A-C for (E) αS102 (F) A30P, (G) A53T, and (H) E46K αS. The ranges of TFE concentrations are as described for A-D above, and for clarity some points are labeled with their [TFE]. The dashed lines show linear fits to sets of points whose CD spectra share isodichroic points.

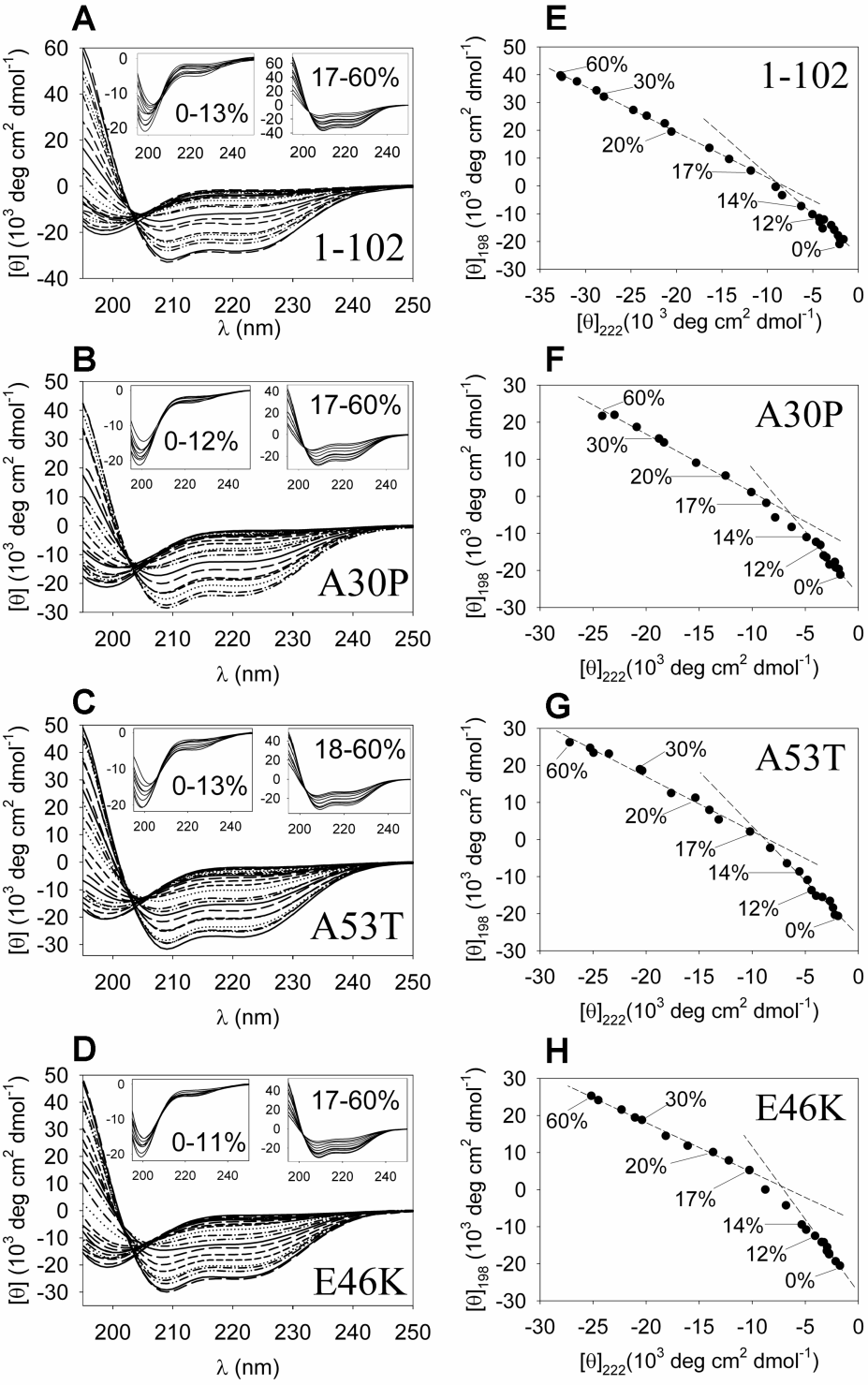
A
B
C
D
E
F
G
H
1-102
A30P
A53T
E46K
0-13%
0-12%
0-11%
17-60%
18-60%
60%
30%
20%
17%
14%
12%
0%
λ (nm)
[θ] (10^3 deg cm^2 dmol^-1)
[θ]198 (10^3 deg cm^2 dmol^-1)
[θ]222(10^3 deg cm^2 dmol^-1)

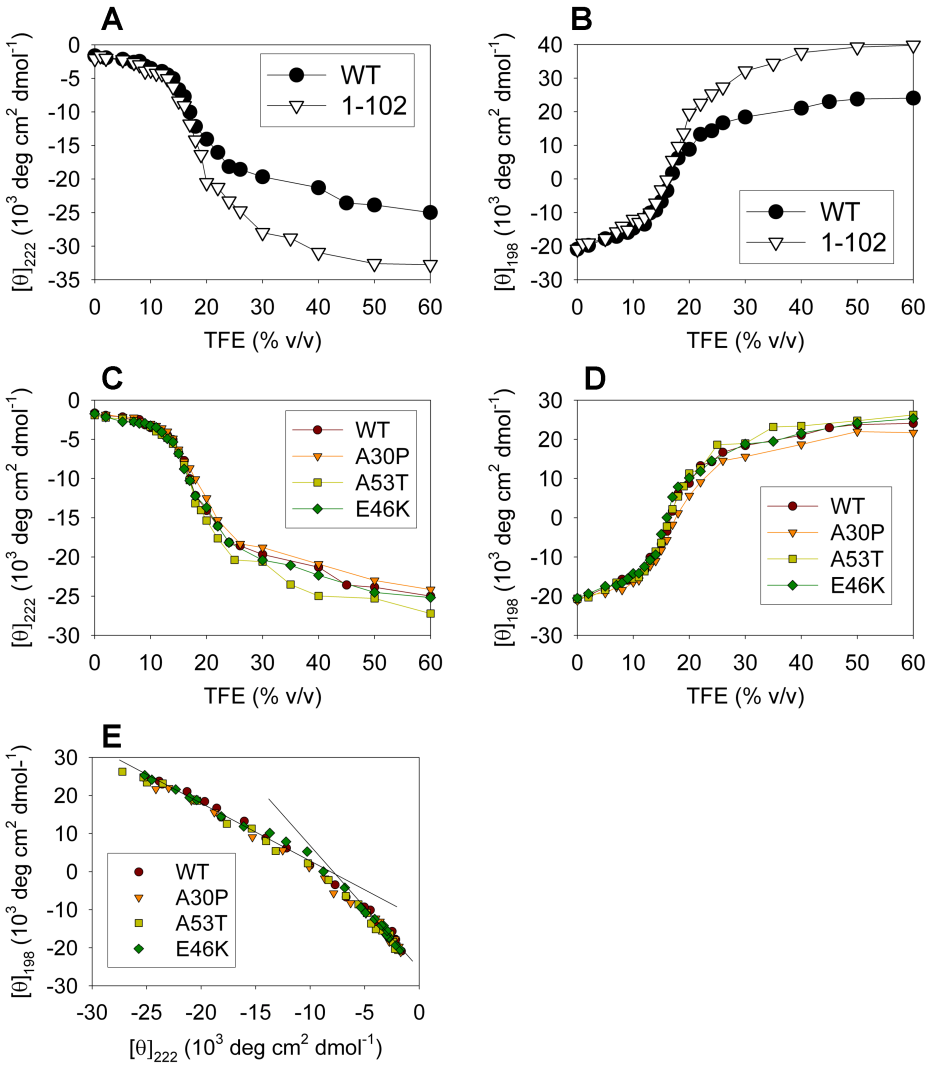

Figure 2.6. Comparisons of CD data for αS variants. (A) The mean residue ellipticity measured at 222 nm as a function of TFE concentration for WT αS vs. αS102 (B) Similar to A, except the ellipticity is measured at 198 nm.(C) The mean residue ellipticity measured at 222 nm as a function of TFE concentration for all WT αS compared to the disease-associated mutants. (D) Similar to C, except the ellipticity is measured at 198 nm.(E) The transition diagram data points from Figure 2.4B and Figure 2.5F-H are combined. The two lines show fits to the wild-type data for 0-14% and 17-60%, respectively.

Table 2.1. CD spectral data related to the intermediate state for the αS variants. The TFE ranges for which CD spectra share isodichroic points, the wavelength at which the curves coincide (λ_{iso}) in nm, and the ellipticity value at the isodichroic ($[\theta]_{iso}$) in units of 10^3 deg cm^2 dmol^{-1} are given for the two-state coexistence regions. The location of the intercept of the linear fits to the low- and high-TFE data points on the CD transition diagrams is also shown in units of 10^3 deg cm^2 dmol^{-1}. Uncertainties are estimated from experimental error.

	U ↔ I Coexistence			**I ↔ F Coexistence**			**Transition Diagram Intercept**	
	TFE range	λ_{iso}	$[\theta]_{iso}$	TFE range	λ_{iso}	$[\theta]_{iso}$	$[\theta]_{198}$	$[\theta]_{222}$
WT	0 - 14%	207 ± 1	-10.8 ± 1.2	17 - 60%	203 ± 1	-12.0 ± 3.9	0.7 ± 4.3	-7.7 ± 1.5
αS102	0-13%	205 ± 2	-12.6 ± 1.9	17 - 60%	203 ± 1	-11.1 ± 4.5	1.4 ± 6.3	-9.0 ± 3.2
A30P	0 - 12%	208 ± 1	-9.3 ± 1.4	17 - 60%	203 ± 1	-12.9 ± 3.5	-4.6 ± 5.7	-6.4 ± 2.0
A53T	0 - 13%	206 ± 1	-12.4 ± 1.3	18 - 60%	203 ± 1	-12.5 ± 4.1	0.9 ± 6.0	-9.1 ± 2.5
E46K	0 - 11%	208 ± 1	-9.4 ± 1.3	17 - 60%	202 ± 1	-7.4 ± 4.8	1.0 ± 3.9	-7.2 ± 1.1

Reconstructed I state spectrum: Table 2.1 shows ellipticity values for the pure I state at four points. However, a spectrum that covers a larger wavelength range is desirable to obtain information about the secondary structure of this conformer; therefore we reconstruct the I state curve for 195-260 nm using two methods. We use Principal Component Analysis (PCA) to reduce the dimensionality of our data sets, and then find the I state via fits (in the new coordinate system) to points whose spectra share isodichroics (see Appendix A). In addition, we use the information from Table 2.1, along with Maximum Likelihood Estimation (MLE), to find fractions of the U and F states as a function of [TFE], and then subtract these contributions from our measured spectra to reconstruct the I state spectrum (Appendix A). Results for both methods for WT αS are shown in Figure 2.7A. The spectra obtained from both methods are similar to one another and are also consistent with the values in Table 2.1. The PCA results for all the αS mutants are shown in Figure 2.7B; the MLE estimates are similar to the PCA results (Appendix A).

The reconstructed I state spectra for all the αS variants are similar to one another in that they all exhibit a minimum around 222 nm that is suggestive of α-helical secondary structure (Figure 2.7B). However, the accompanying minimum expected for pure α-helical structure at 208 nm is shifted to slightly shorter wavelengths. In addition, the magnitude of the signal at 222 nm is less than would be expected for fully helical structure for all five variants, indicating that the intermediate state is partially unstructured in all cases.

Using $[\theta]_{222}$, we estimate the fractional helicity (Luo and Baldwin, 1997) for the I and F states (Table 2.2). The percent helicity of both states is higher for αS102 compared to WT, but the number of residues in a helical conformation is similar, indicating that the N terminus of full-length αS is likely to be the region adopting structure in the presence of TFE. For all the variants, ~24 residues are predicted to be

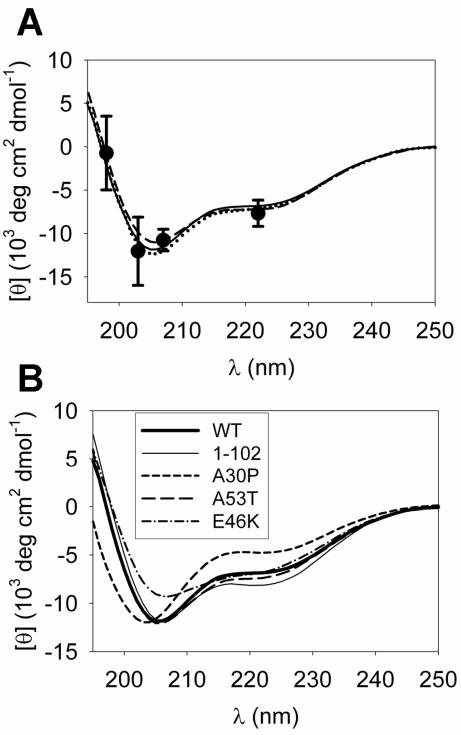

Figure 2.7. Reconstructions of the I state spectra for αS variants. (A) Predicted spectra for WT αS. The solid line shows the spectrum calculated via PCA. The dashed lines show results of MLE analysis, which were calculated using spectra that shared the low-TFE isodichroic points. The dotted line shows the MLE results calculated from spectra that shared the high-TFE isodichroic. The points (circles) show the I state reference points from Table 2.1 (B) Comparison of the results of the PCA calculations for all five αS variants.

Table 2.2. Estimates of the percentage of α-helical structure (Luo and Baldwin, 1997) for αS in the pure I and F states, based on the magnitude of the ellipticity at 222 nm. Note that the estimate is only defined for 0-50% TFE, but our CD spectra are nearly identical at 50%-60% TFE, and so we are able to use the 50% TFE parameters from (Luo and Baldwin, 1997) for the F state estimates. In addition, the 15% TFE parameters are used for the I state estimates. Error bars for the I state are due to uncertainties in our PCA estimate (see Appendix A) and errors for the F state are based on an experimental error.

	I state		**F state**	
	Percent helicity	# helical residues	Percent helicity	# helical residues
WT	17 ± 2	24 ± 2	61 ± 4	86 ± 5
αS102	20 ± 6	21 ± 6	83 ± 5	85 ± 5
A30P	11 ± 3	16 ± 4	59 ± 3	83 ± 5
A53T	18 ± 2	26 ± 3	68 ± 4	95 ± 5
E46K	17 ± 2	24 ± 3	62 ± 4	86 ± 5

in a helical conformation for the I state and ~86 residues are helical in the F state. Notably, helicity is slightly lower for the A30P I state. Deconvolution analysis of the CD spectra indicated that TFE does not lead to a significant increase in β-sheet content between the U and I states (see Appendix A).

Conformer populations for monomeric αS: The experimental CD data at all TFE concentrations are well fit by linear combinations of the reconstructed I state spectra, and the 0% and 60% TFE spectra (Figure 2.8A, see also Appendix A). The corresponding populations (Figure 2.8B), which are very similar for all five αS variants, show that the U state becomes depleted in favor of the I state as TFE is increased to ~ 15%, while at higher TFE, the F state population increases. The I state appears to be an intermediate in the TFE-induced conversion of U to F and in addition is significantly populated between ~10 to ~20% TFE, where TFE fibril formation is maximal.

Secondary structure of TFE-induced αS oligomers and fibrils: At protein concentrations of 2 μM in solutions that contain intermediate (~12-20%) amounts of TFE, the CD spectra change over time as oligomerization occurs, enabling an analysis of both secondary structure changes and kinetics (Figure 2.9A). The initial CD curves have double minima near 205 and 220 nm, and are consistent with partially unstructured protein. As time passes, a single minimum appears near 216 nm, signifying the formation of β-sheet-rich structure. Because the appearance of β-structure is both concentration- and time-dependent, we believe it reflects the formation of oligomeric species. Interestingly, the curves share isodichroic points at ~210 nm, suggesting that the systems are undergoing all-or-nothing transitions between two states. However, because oligomers with similar secondary structure could result in nearly identical far-UV CD curves, we may not be able to resolve conversions between oligomeric states, such as the association of smaller oligomers

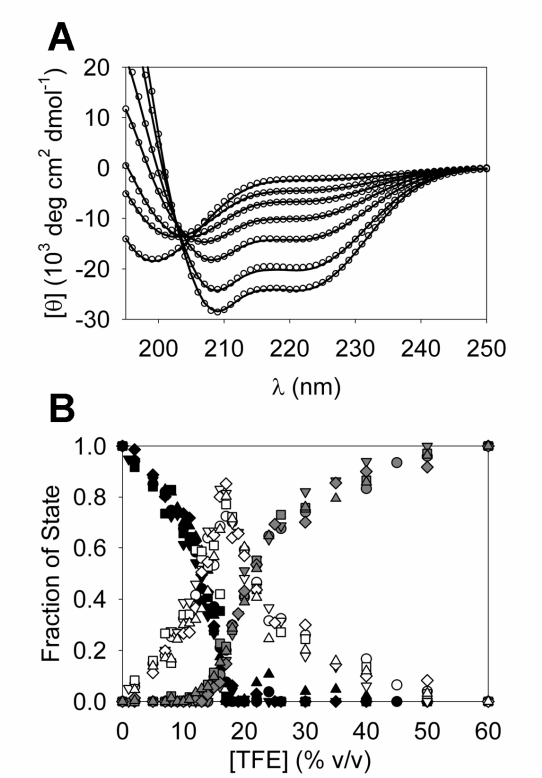

Figure 2.8. Protein spectra and conformer population calculations based on linear combinations of the pure U, I, and F states. (A) Fit results (black lines) for WT αS CD spectra (open circles, data as in Figure 2.4A), where the fitted curves were calculated from linear combinations of the 0%, 60% and the estimated I state spectra (see Appendix A). The TFE concentrations for spectra with increasing negative ellipticity at 222 nm are 5%, 13%, 15%, 17%, 20%, 30%, and 50% TFE. (B) Fractions of monomer protein in the three states U, I and F as a function of [TFE], obtained from fits of CD spectra to linear combinations of the pure states (see Appendix A). Black symbols: f_U. White symbols: f_I. Gray symbols: f_F. Data is shown for WT (circles), αS102 (down triangles), A30P (squares), A53T (diamonds) and E46K (up triangles) αS.

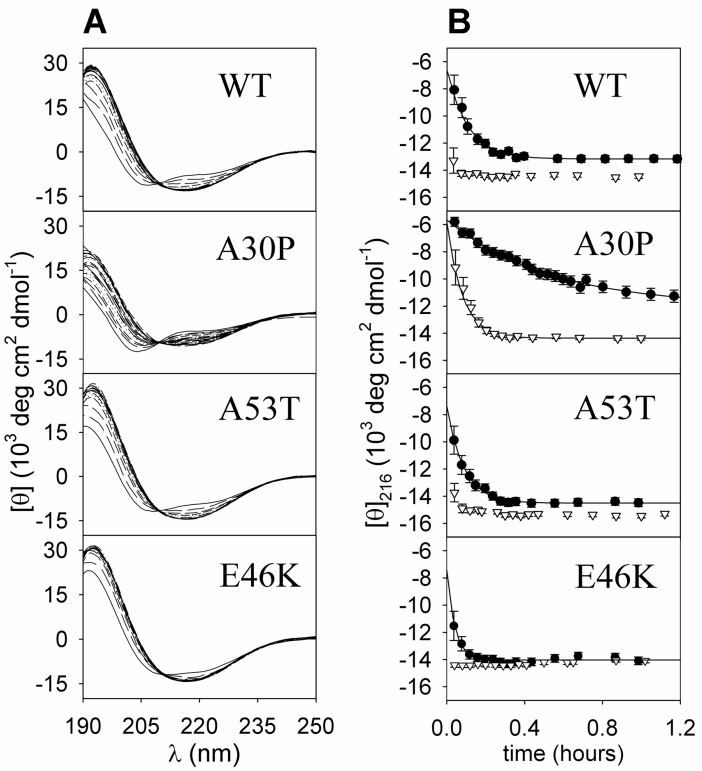

Figure 2.9. Oligomer formation kinetics in 15% TFE for αS variants. (A) Far-UV CD spectra taken at various time points for 2 μM WT, A30P, A53T, and E46K αS in 15% TFE at 25 °C. The initial time point for each plot has the least negative [θ] at 216 nm. (B) Kinetics of the oligomerization reaction for WT, A30P, A53T, and E46K αS. Filled circles: $[\theta]_{216}$ for the curves in A-D plotted vs. time. Open triangles: $[\theta]_{216}$ vs. time for 5 μM protein in 15% TFE. Lines: Results of fits to a single exponential model (see Appendix A). The error bars reflect the uncertainty in time due to mixing and experimental dead time, as well as signal fluctuations.

into larger species. We do not observe fibrils via TEM for samples incubated for ≤ 6 hours at 25 °C, even for αS concentrations as high as 50 μM; therefore we believe that the CD spectra changes for Figure 2.9 correspond to the formation of non-fibrillar oligomeric species.

Measurements at a higher protein concentration of 5 μM show that the appearance of the ellipticity minimum at 216 nm is nearly complete within the 1-3 minute mixing time for WT and the PD-associated mutants (excepting A30P), further confirming the concentration dependence of the initial oligomerization reaction (Figure 2.9B). Fits of the data to a single exponential model result in apparent rate constants k_{app} (Table 2.3, also see Appendix A). Visual inspection of the data in Figure 2.9A-B, in combination with the fit results (Table 2.3), reveals that the E46K mutant reaches steady-state fastest, while A30P is slowest. Therefore, oligomerization rates appear to follow a similar series (A30P < WT ≤≈ A53T < E46K) as the extent of aggregation data (Figure 2.2B), which indicated that the A30P mutant forms fibrils least readily and aggregation production is highest for E46K.

CD spectra for 50 μM WT αS solutions that were incubated for two weeks at room temperature (Figure 2.10A) demonstrate that mature TFE fibrils are also rich in β-strand structure. The presence of such fibrils in these solutions was confirmed by TEM (Figure 2.10B-C). Although the fraction of TFE fibrils was not measured for these samples, the data in Figure 2.2B, obtained for solutions incubated under identical conditions, indicates that a significant fraction of protein is incorporated into large aggregates. The ellipticity at 216 nm for samples containing TFE fibrils is within experimental error of the values measured for the rapidly formed oligomers, indicating that early- and late- aggregates contain similar secondary structure. The spectra are also similar to those obtained for typical amyloid fibrils (Ahmad, et al., 2006; El-Agnaf, et al., 1998; Serpell, et al., 2000).

Table 2.3. Rate constants for the oligomerization reactions shown in Figure 2.9B. Data is shown for 2 μM samples, unless otherwise indicated. See Appendix A for details of the fitting procedure.

	10^3 x k_{app} (1/sec)
WT	2.6 ± 0.3
A30P	0.53 ± 0.10
A30P (5 μM)	3.5 ± 0.4
A53T	3.1 ± 0.3
E46K	6.7 ± 1.2

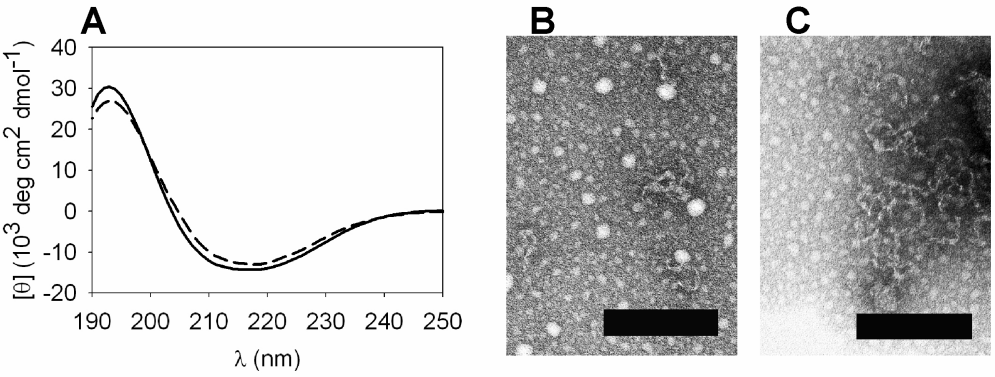

Figure 2.10. Solutions containing TFE fibrils possess β-sheet structure. (A) CD spectra of fibril-containing samples. 50 μM αS was incubated at room temperature for 14 days in solutions containing 10% (solid line) and 15% (dashed line) TFE prior to measurement. (B) TEM micrographs of the 10% TFE sample from A (scale bar = 200 nm). (C) Same as B, but for the 15% TFE sample.

2.3. Discussion

We have investigated TFE-induced conformational changes, oligomerization, and fibril production for WT human αS, C-terminally truncated αS, and three PD-associated αS variants. Our results demonstrate that the TFE-induced folding landscapes for the mutants are nearly identical to WT, but the kinetics of the oligomerization process vary among the disease-associated mutants. An intermediate conformational state, which has a far-UV CD spectrum that is consistent with the presence of significant α-helical structure, is highly populated at TFE concentrations where TFE fibril production is maximized. By examining the αS102 mutant, we verify that TFE-induced conformational changes involve the N terminal portion of the protein.

TFE induces short, flexible fibrils: CD data (Figure 2.10A) indicate that TFE-induced fibrils are β-sheet-rich, suggesting that they may represent a type of amyloid aggregate. TFE fibrils also exhibit a degree of thioflavin-T binding (Figure 2.1E). Nonetheless, our current data do not suffice to unequivocally establish whether these fibrils are a form of amyloid; only X-ray or electron diffraction experiments will be able to determine whether these species contain "cross-β" structure.

When imaged via TEM, TFE-induced fibrils have a flexible helical ultrastructure (Figure 2.1, Figure 2.2, Figure 2.3). As far as we know, these structures have not been extensively studied by TEM, although we found some images of possibly similar aggregates in the literature (Broersen, et al., 2006; Crowther, et al., 1998; Giehm, et al., 2010). Crowther, et al. (Crowther, et al., 1998) show micrographs of both typical amyloid fibrils and irregular fibrillar structures, which appear similar to TFE-induced species, for 1-120 C-terminally truncated αS and also report "small irregular wavey assemblies" formed from 1-130 truncation. In addition, Broersen, et al. (Broersen, et al., 2006) report images of aggregates induced by incubation of αS in

the presence of the polyunsaturated acids arachidonic acid and docosahexaenoic acid which are qualitatively similar to TFE fibrils. Also, a study was published which described detergent-induced formation of species that may be similar to our TFE fibrils (Giehm, et al., 2010). Although more research must be done to evaluate whether species produced by truncation mutations and/or lipid and detergent interactions are indeed related to TFE fibrils, the potential similarities with previously observed structures are particularly important in light of the hypothesis that intermediate or alternative oligomeric or fibrillar species are responsible for PD toxicity (Conway, et al., 2000), recent findings that C-terminal truncation of αS can led to neuron loss and increased susceptibility to stress in transgenic mouse models (Michell, et al., 2007; Wakamatsu, et al., 2008), and multiple lines of evidence that potentially link lipid interactions and metabolism with PD etiology (Beyer, 2007).

The "ring-like" structures we observed via TEM (Figure 2.1C and Figure 2.32B-C) may also be similar to annular structures imaged using atomic force microscopy (AFM) (Conway, et al., 2000; Pountney, et al., 2004). However, difficulties in comparing widths measured via TEM to heights measured via AFM prevent us from definitively verifying that these structures are comparable.

TFE induces a partially helical, monomeric intermediate: In contrast to previous studies by Li, et al (Li, et al., 2002) and Munishkina, et al. (Munishkina, et al., 2003), we investigated TFE-induced structural transitions in monomeric αS by examining relatively dilute solutions (0.5 μM compared to ~14 μM in Li et al. and ~35 μM in Munishkina, et al.). The higher concentrations used in these previous studies led to the conclusion that TFE stabilized an intermediate containing primarily β-sheet structure. Here, we demonstrate instead that the monomer protein samples three distinct conformations: an unfolded state, a partially structured intermediate, and a well-folded α-helical conformer (Figure 2.4, Figure 2.5, Figure 2.7). Increased

population of the partially α-helical intermediate state is correlated with formation of the β-sheet-rich, short flexible fibrils (Figure 2.8B). It is possible that changes in solution conditions may favor both structure formation and aggregation via separate mechanisms. However, because TFE fibril growth is strongly correlated with increasing population of the intermediate state for all WT αS variants, the simplest explanation implied by our data is that the intermediate conformer is on-pathway to TFE fibril formation, although such an assertion is very difficult to prove (Abedini and Raleigh, 2009b).

The TFE-induced structural intermediate we observe can be compared to previously reported αS folding intermediates. Qualitatively, our low-TFE CD spectra are similar to data reported for WT αS at high temperature and low pH (Uversky, et al., 2001). However, recent NMR studies show that decreased pH in fact leads to an increase in helical structure in the C-terminal tail of αS (McClendon, et al., 2009), while our data for the αS102 truncation mutant show that TFE-induced structural changes involve the N terminal portion of αS. Thus, the TFE and low pH intermediates differ in regards to the location of secondary structure. A more detailed comparison with the high temperature state awaits further characterizations.

Interestingly, far-UV CD spectra of detergent micelle bound and membrane-bound αS show a high degree of α-helical structure and appear similar to our F state curves (Bussell and Eliezer, 2003; Chandra, et al., 2003). The number of residues predicted to be in a helical conformation based on our CD data here (~85) is in good agreement with the number of residues that are known to be helical in the micelle- and membrane-bound structures (Bussell and Eliezer, 2003; Chandra, et al., 2003; Georgieva, et al., 2008; Ulmer, et al., 2005). In addition, our results for the C terminal truncation mutant show that TFE-induced structural changes involve the N terminal portion of the αS, which is consistent with data for membrane- and micelle- bound

conformations. If the TFE-induced F state does correspond to the highly helical membrane-bound state, then the partially helical I state, which we show is on the folding pathway to the F state, may also have a corresponding membrane-associated intermediate that could potentially be involved in membrane-induced aggregation *in vivo*. Indeed, evidence exists for such an intermediate; both ESR studies and recent NMR studies have reported observations of partially helical membrane-bound states of αS (Bodner, et al., 2009; Drescher, et al., 2008). Furthermore, the N terminus of αS contains a region with an elevated intrinsic helical propensity, which was proposed to nucleate helix formation upon membrane-binding by the protein (Bussell and Eliezer, 2003; Eliezer, et al., 2001). The length of this region was estimated to be around 32 residues (Eliezer, et al., 2001), which is fairly similar to our estimate of the number of helical residues (~24) in the TFE-induced I state, suggesting that the I state may be comprised of helical structure in this region. The slight drop in helical content of the intermediate for the A30P mutant (Table 2.2), which falls within this region, provides further support for this idea, although direct correspondence between membrane-associated conformations and the TFE-induced I state cannot be established based on our current data.

Although it was previously known that membranes or detergents can facilitate the aggregation of αS (Ferreon and Deniz, 2007; Necula, et al., 2003), and the protein is highly helical when bound to membranes or detergents as a monomer (Bussell and Eliezer, 2003; Chandra, et al., 2003; Eliezer, et al., 2001; Ferreon and Deniz, 2007; Georgieva, et al., 2008; Ulmer, et al., 2005), it has never previously been shown, to the best of our knowledge, that any helical αS conformations are directly involved in inducing the aggregation of this protein. Ahmad et al. (Ahmad, et al., 2006) found that sub-micellar detergent concentrations induced a partially helical ensemble of αS that was correlated with fibril elongation. However, a discrete helical intermediate was not

identified and their conditions could not support fibril formation in the absence of seeding. Past studies of TFE effects on αS structure, conducted at higher [αS], identified β-sheet-rich intermediates, likely corresponding to the rapidly formed oligomers that we observe, which obscured details of the helical I state conformation (Li, et al., 2002; Munishkina, et al., 2003).

The association of α-helical intermediates with amyloid fibril formation has been documented for a number of different amyloidogenic proteins or peptides, including the Aβ peptide and IAPP (Abedini and Raleigh, 2009a; Abedini and Raleigh, 2009b; Booth, et al., 1997; Fezoui and Teplow, 2002; Williamson, et al., 2009; Yamaguchi, et al., 2006; Zerovnik, et al., 2007). Our demonstration that TFE induces a significantly helical intermediate conformation of αS, which is strongly associated with fibril formation, adds αS to the list of proteins that aggregate via helical intermediates, at least under some conditions. The mechanism by which β-sheet-rich aggregates form from α-helical intermediates is currently unclear. One possibility involves helix-helix interactions leading to alignment of unstructured regions adjacent to helical segments, enabling oligomerization followed by β-sheet formation and propagation (Abedini and Raleigh, 2009b).

PD mutations alter TFE-induced aggregation kinetics, but not monomeric structural transitions: We find that the TFE-induced folding landscapes for the A30P, A53T, and E46K mutants are nearly identical to WT αS, which is in accordance with previous research that showed that the pH- and temperature- induced secondary structural conformations are similar for A30P, A53T and WT αS (Li, et al., 2001). All three mutants have also been observed to undergo similar structural transitions to WT αS in the presence of detergents or lipids (Bussell and Eliezer, 2004; Fredenburg, et al., 2007; Ulmer and Bax, 2005), although the A30P mutation may lead to a slight local reduction in helical structure. Thus, secondary structural transitions appear to be

largely similar among αS mutants. In contrast, oligomerization and fibrillization behavior vary significantly between PD-linked mutants, with amyloid fibril formation rates observed in the order A30P<WT<A53T/E46K (Conway, et al., 2000; Fredenburg, et al., 2007). Likewise, we find that TFE-induced oligomerization rates vary significantly among the αS variants despite their nearly identical monomer secondary structure landscapes. Interestingly, the rates of TFE-induced fibril formation (A30P<WT<A53T<E46K) follow the same order as that observed for amyloid formation in the absence of TFE, suggesting that similar properties may be controlling aggregation kinetics in both cases.

Whatever the effects of the PD mutations may be, they do not appear to significantly alter the TFE-induced conversion of the disordered free state to the TFE-induced intermediate. Thus, their effects may become important subsequent to this step, either during the initial formation of oligomeric species from the monomeric intermediate or during subsequent interconversions amongst oligomers and fibrillar species. An additional potential effect of disease-linked mutations may be to favor some aggregation pathways over others, rather than to accelerate a specific step during a single pathway. The existence of multiple types of fibrillar aggregates is clearly demonstrated both here and in previous studies (Crowther, et al., 1998; El-Agnaf, et al., 1998; Giehm, et al., 2010; Serpell, et al., 2000; Vilar, et al., 2008) but their relationship to each other, the degree of overlap in their formation pathways, and the influence of mutations on which type of aggregate is formed remain unclear at present and will require further investigation. In particular, it is unclear whether the TFE-induced αS intermediate is on-pathway to the formation of classical amyloid fibrils, in addition to TFE fibrils.

2.4. Conclusion

We have shown that intermediate concentrations of the fluorinated alcohol TFE led to rapid aggregation of the PD-linked protein αS into short fibrillar β-sheet aggregates. TFE-induced fibril formation is most efficient under conditions that cause residues in the N terminal portion of monomeric αS to populate a partially helical intermediate state, which is therefore likely to be on the pathway to TFE fibril formation. To our knowledge, this report is the best evidence to date for an αS aggregation pathway that involves a helical intermediate, and adds to indications that helical intermediates may be generally important in amyloid aggregation pathways. We propose that the TFE-induced αS intermediate may resemble membrane-associated conformations; therefore the TFE-induced aggregation pathway may be related to pathways of membrane-induced aggregation, which could be significant *in vivo*, where αS is known to bind to synaptic vesicles and possibly other membrane surfaces (Beyer, 2007). We demonstrate that the formation of the TFE-induced intermediate is not significantly affected by any of the three PD-linked αS mutations, but that all three mutations do influence the overall rate of TFE fibril formation, indicating that the mutations exert their effects subsequent to the formation of the intermediate state. TFE-induced fibrils are ultrastructurally similar to species detected for αS 1-120 and 1-130 truncation mutants (Crowther, et al., 1998), and may be related to aggregates produced by interactions between αS and lipids and detergents (Broersen, et al., 2006; Giehm, et al., 2010), potentially indicating that TFE fibrils may be relevant for understanding PD progression.

2.5. Materials and Methods

All solutions were buffered with 10 mM pH 7.5 sodium phosphate. Recombinant WT and mutant αS were produced and purified as previously described

(Bussell and Eliezer, 2001). Lyophilized αS variants were solubilized by dissolving at 1-2 mg/mL in buffer, followed by filtration through a 100 kDa (Microcon YM-100) centrifugal spin filter (Millipore).

Fibrils were grown by incubating 50 μM of αS variants for 14 days in solutions containing 0-15% TFE. Sodium azide (0.02% w/v) was added to the solutions as a preservative. After incubation, samples were fractionated via centrifugation at 16,000xg for 1h. UV absorbance at 275 nm of a ~10 fold dilution of the supernatant fraction was used to quantify the amount of soluble protein (which may include small oligomers) present in the samples after aggregation. The aggregated fraction was diluted to into a buffered, 20 μM thioflavin-T solution. Fluorescence emission spectra were measured using an excitation wavelength of 460 nm. Signals were compared by integrating the emission spectra from 475-485 nm, subtracting the baseline (20 μM thioflavin-T in buffer) emission from the sample value, and normalizing to the baseline, resulting in the "enhancement factor" by which the sample peak intensity exceeds the baseline value.

Far-UV CD data were obtained using a 1 nm bandwidth. Buffer-only baseline samples were measured and subtracted from all spectra and a noise-reducing option in the instrument software was used to smooth the data. Scan speeds of 1-2 seconds per nanometer were used (see Appendix A).

EM images were obtained with negative-staining TEM. A 5-10 μL droplet of a sample solution was placed onto a freshly glow-discharged, carbon-coated formvar, copper grid. After two min, the sample solution was wicked off with filter paper, the grid rinsed with deionized water, and a 5 μL droplet of 2% (w/v) phosphotungstic acid stain (pH 7) placed on the grid. After one min, the staining solution was wicked away and the grid air dried.

CHAPTER 3

SECONDARY STRUCTURE CHANGES INDUCED BY PH, TEMPERATURE, AND TRIFLUOROETHANOL SUGGEST THAT DESOLVATION PROMOTES ALPHA-SYNUCLEIN AGGREGATION*

3.1. Introduction

Parkinson's disease is characterized by dense Lewy body inclusions, which are primarily comprised of amyloid fibrils formed from the protein α-synuclein (αS). However, recent evidence suggests that amyloid fibrils may be protective, while smaller oligomers or alternate aggregate structures are responsible for dopaminergic cell death (Brown, 2010; Conway, et al., 2000). Solution conditions, including pH, temperature, or the presence of detergents, lipids, or alcohols, affect both the conformation of monomeric αS and the amount and type of aggregates that are produced; these various aggregate species may have disparate *in vivo* toxicities (Anderson, et al., 2010; Crowther, et al., 1998; El-Agnaf, et al., 1998; Giehm, et al., 2010; Serpell, et al., 2000; Vilar, et al., 2008). Observations of secondary structural changes for αS in aggregation-promoting solution conditions led to the hypothesis that "folding intermediates", or specific partially structured αS monomer conformations, initiate aggregation reactions (Uversky, et al., 2001).

We recently showed that the N terminus of αS adopts a partially helical conformation in the presence of moderate amounts of the fluorinated alcohol 2,2,2-trifluorethanol (TFE), and that population of this intermediate state is correlated with the formation of annular and fibrillar aggregates (Anderson, et al., 2010). Partially helical conformations are also detected when αS is incubated in the presence of

* This material will be submitted to J. Am. Chem. Soc. by V. L. Anderson, W. W. Webb, and D. Eliezer

detergents (Ahmad, et al., 2006), and flexible aggregates that may be similar to TFE-induced species can be grown such solutions (Giehm, et al., 2010). However, partially structured αS conformations observed in low-pH and high-temperature conditions have been hypothesized to contain β-sheet, rather than helical regions (Uversky, et al., 2001), although recent nuclear magnetic resonance (NMR) studies have indicated that reduced pH conditions lead to local collapse in the C-terminal domain of αS (Cho, et al., 2009; McClendon, et al., 2009; Wu, et al., 2009). Therefore, αS may adopt multiple conformations, which could potentially involve structure formation in disparate regions of the protein. Furthermore, the causal relationship between a particular "intermediate" state and an aggregation pathway is not fully established – solution conditions that promote aggregation may produce coincidental changes in protein structure, or a conformational state may be a true intermediate in a fibrillization pathway.

Here, we use circular dichroism (CD) spectroscopy to investigate the combined effects of various solution conditions on αS variant secondary structure. Our results suggest that loss of protective interactions, rather than the stabilization of specific conformational states, likely causes aggregation enhancement in TFE. In particular, we propose that low concentrations of TFE cause protein dehydration, while preferential solvation of protein molecules by TFE stabilizes α-helical structure at high [TFE]. Thus, the intermediate (~15% TFE) conformation is a desolvated state in which both protein-TFE and protein-water interactions are minimized.

Our evidence for desolvation includes the qualitative similarities between αS conformational changes induced by heating and by low [TFE], which are consistent with loss of polyproline-II (PPII) secondary structure as a result of decreased water-protein hydrogen bonding (Kelly, et al., 2001; Shi, et al., 2006). In addition, the CD spectra from αS102 solutions containing ~15% TFE, where the TFE-induced

intermediate is highly populated (Anderson, et al., 2010), appear to be invariant with respect to temperature. This suggests that the TFE-induced intermediate conformation is similar to the high-temperature state, in which enthalpic protein-solvent interactions are likely to be weakened (Kauzmann and Eyring, 1941; Kelly, et al., 2001). Moreover, we observe a distinct crossover at ~15% TFE, below which the CD spectra feature a negative peak near 200 nm that diminishes with increased temperature, and above which the spectra reflect α-helical structure that is disrupted by heating. Therefore, the local environment near αS molecules seems to be "water-like" at low TFE and "TFE-like" at high TFE, and protein-solvent interactions may be reduced at intermediate TFE concentrations. The aggregation enhancement near 15% TFE is also consistent with removal of desolvation barriers to fibrillization.

In addition, by comparing wild-type (WT) human αS and its 1-102 truncation mutant (αS102), we show that previously identified conformational intermediates actually reflect at least two distinct types of structure. Secondary structural changes observed at low pH require the C terminus of αS, while temperature- and TFE-dependent changes in αS secondary structure involve the N terminal portion of the protein.

Although TFE- and temperature-induced secondary structure changes are similar for full-length αS and αS102, the morphology of fibrils produced at elevated temperatures is affected by the presence of the C terminus. Reduced pH conditions also increase the helicity of the protein at high TFE. Therefore, a combination of electrostatic effects, solvent properties, and protein sequence contribute to the conformational rearrangements and aggregation behavior of αS.

Hydration is a protective factor that helps to stabilize disordered proteins (Uversky, et al., 2000). Sequence elements that enhance protein-backbone hydrogen bonding may have been selected by evolution in order to prevent abnormal

aggregation (Rauscher, et al., 2006). We find that the addition of small amounts (<~15%) of TFE to aqueous solution reduces hydration barriers to aggregation, but electrostatic repulsion limits association of the desolvated state. Therefore, αS aggregation in TFE likely involves overcoming multiple protective interactions, rather than the formation of specific aggregation-promoting structural elements.

3.2. Results

Effect of pH on WT αS and αS102 secondary structure: We measured CD spectra at various pH for WT αS and αS102 at 25 °C (Figure 3.1A-B). WT αS experiences a modest but definite drop in its mean residue ellipticity at 222 nm ($[\theta]_{222}$) at low pH, while changes in the αS102 spectra are below the noise in the measurement. Therefore, the C terminus of αS is necessary for the pH-induced secondary structural transition.

A fit of the curves in Figure 3.1C to a sigmoidal function results in transition midpoints of pH 5.7 ± 0.1 for WT αS and 5.6 ± 0.3 for αS102, although the fit is poor for the truncation mutant. The WT αS transition appears sharper and occurs at slightly higher pH than the titration curves reported by of Uversky, et al. (Uversky, et al., 2001), which may be a result of differences in ionic strength or other solution conditions. We observe that the magnitude of the pH-induced change in the WT αS CD spectrum is modest (~0.7 x 10^3 deg cm^2dmol^{-1} at 222 nm), which similar to the shift observed by Uversky, et al., but contrasts with the much larger changes in signal induced by TFE or heating (Anderson, et al., 2010; Munishkina, et al., 2003; Uversky, et al., 2001).

Temperature dependence of the WT αS and αS102 CD spectra: Figure 3.2 shows variable-temperature (*T*) CD curves for WT αS and αS102 at pH 7.5 and pH

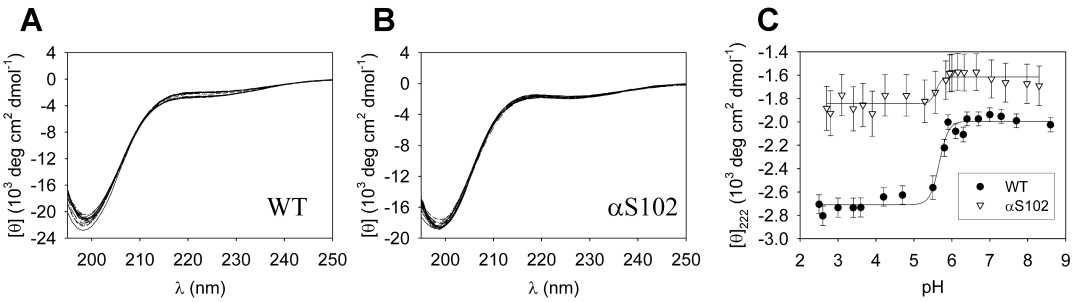

Figure 3.1. pH-induced changes in the secondary structure of αS variants. (A) CD spectra for WT αS between pH 2.5 and pH 8.6. (B) Spectra for αS102 for pH 2.7 to 8.3. (C) The ellipticity at 222 nm vs. pH for the spectra from A and B. The solid lines show sigmoidal fits to the data. The error bars show the standard deviation of three measurements of the same sample.

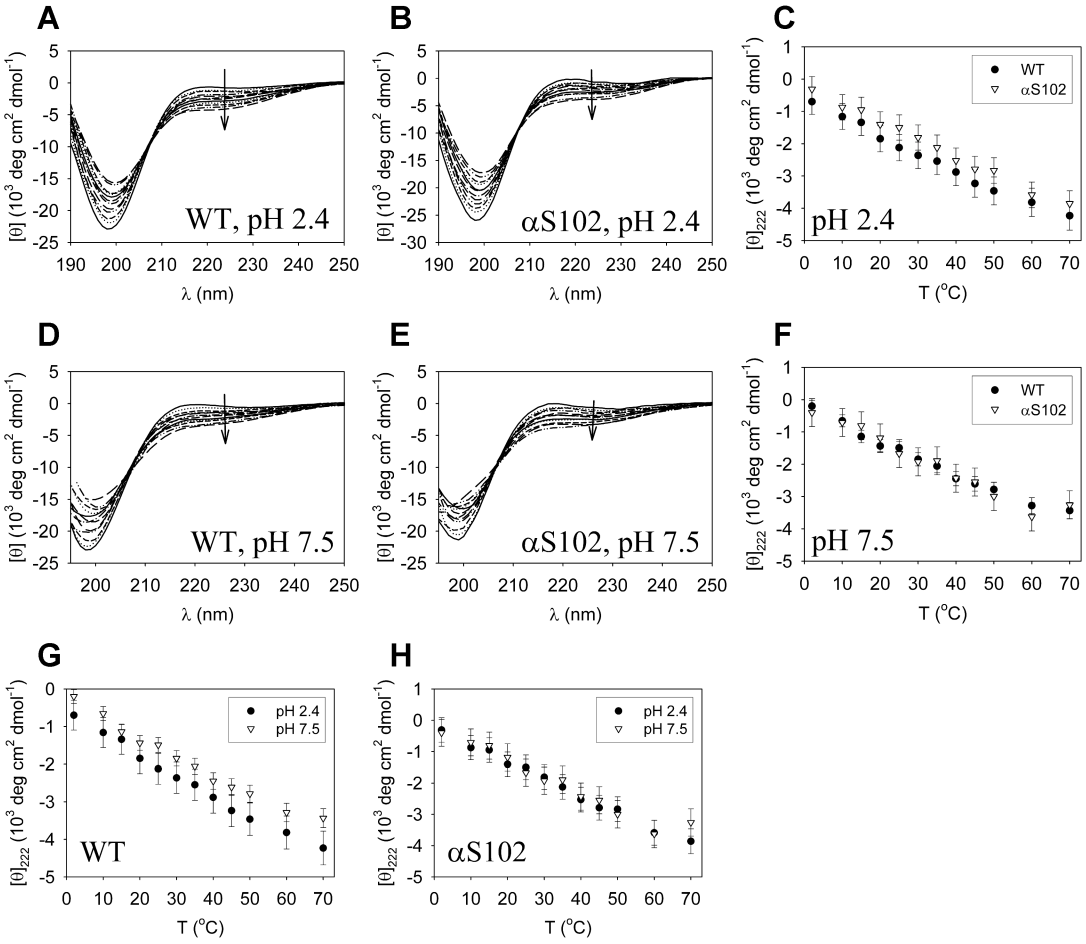

Figure 3.2. Variable-temperature CD measurements of 0.5 μM WT αS and αS102 at (A-B) pH 2.4 and (D-E) pH 7.5. Spectra were measured at 2, 10, 15, 20, 25, 30, 35, 40, 45, 50, 60, and 70 °C. The arrows show the general direction of increasing temperature. (C) and (F) show a comparison of the ellipticity at 222 nm for WT αS vs. αS102 at fixed pH, while (G) and (H) compare the values at pH 7.5 vs. pH 2.4 for each αS variant. The error bars reflect signal fluctuations and temperature-dependent drifts in the buffer baselines (see Appendix B).

2.4. We verified that temperature-dependent changes in αS structure were reversible by measuring the spectra at T=2 °C before and after heating (Figure B.1A-D), and we assume that the proteins remain monomeric in these dilute (0.5 μM) solutions when no significant hysteresis is observed (see Appendix B). At pH 7.5, the temperature-induced changes in the CD signal were similar for WT αS and αS102, and therefore pH-induced structural changes in αS differ from temperature-induced changes both in the magnitude of the ellipticity shift and in the region of the protein involved.

Both αS102 and WT αS undergo similar temperature-induced structural changes at pH 2.4. At both pH values, the spectra for both variants share isodichroics near 207 nm. However, for WT αS, $[\theta]_{222}$ appears to be slightly larger negative at pH 2.4 than at pH 7.5 over the entire temperature range. At 25 °C, the difference in $[\theta]_{222}$ between pH 7.5 and pH 2.4 is $0.63 \pm 0.45 \times 10^3$ deg cm^{2}dmol^{-1}, which is consistent with the pH-dependent spectral shift from Figure 3.1C, although the measurement uncertainty is large in the variable-temperature samples due to baseline drift during prolonged incubations (see also Appendix B). For αS102, the ellipticity appears similar at pH 7.5 and pH 2.4 over the entire temperature range, within the resolution of our measurements.

Temperature dependence of the CD spectra of αS and αS102 at 60% TFE: We also examined the variable-temperature spectra for αS102 and WT αS incubated in the presence of 60% TFE at pH 2.4 and pH 7.5 (Figure 3.3). Again, we verified that the temperature-dependent changes in αS variant structures were reversible (Figure B.1E-H). The samples appear highly α-helical under these conditions, and isodichroics point for the variable-temperature curves are observed at ~204 nm. The magnitude of the CD signal is larger for αS102 than for WT αS, which is consistent with TFE-induced helical structure involving the N-terminal portion of the protein (Anderson, et al., 2010).

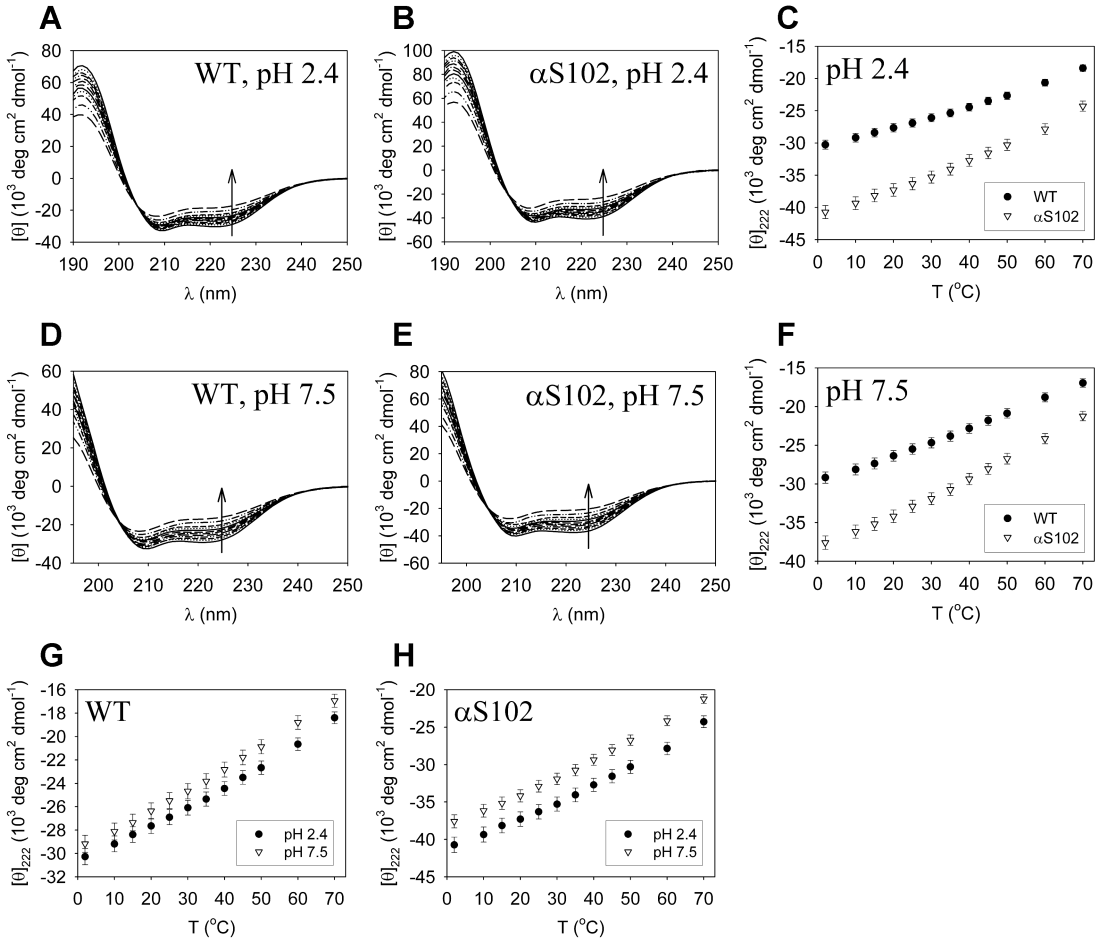

Figure 3.3. Variable-temperature CD measurements of 0.5 μM WT αS and αS102 in the presence of 60% TFE at (A-B) pH 2.4 and (D-E) pH 7.5. Spectra were measured at 2, 10, 15, 20, 25, 30, 35, 40, 45, 50, 60, and 70 °C. The arrows show the general direction of increasing temperature. (C) and (F) show a comparison of the ellipticity at 222 nm for WT αS vs. αS102 at fixed pH, while (G) and (H) compare the values at pH 7.5 vs. pH 2.4 for each αS variant. The error bars reflect signal fluctuations and temperature-dependent drifts in the buffer baselines (see Appendix B).

Interestingly, $[\theta]_{222}$ is slightly larger negative at pH 2.4 than at pH 7.5 for both αS102 and WT αS at 60% TFE. The ellipticity difference for WT αS at 25 °C is 1.41 ± 0.93 x 10^3 deg cm^2dmol^{-1}, while for αS102, it is 3.43 ± 1.24 x 10^3 deg cm^2dmol^{-1}.

Temperature, TFE and pH dependence of the CD spectra of A30P αS: We repeated the variable-temperature CD measurements for the A30P variant at pH 7.5 and pH 2.4 and 0% and 60% TFE (Figure B.3). The curves were identical to WT αS, within the uncertainty of our measurements.

Helicity estimates for αS variants: Using the method of Luo and Baldwin (Luo and Baldwin, 1997), we estimate the ensemble-averaged number of residues per protein molecule adopting a helical conformation at 60% TFE (Table 3.1). Notably, the number of helical residues is similar for αS102 and full-length αS, as is expected if helix formation involves the N terminal portion of the protein only. Moreover, ~10 additional residues are predicted to adopt a helical conformation at low pH compared to neutral pH for all the mutants.

Effects of temperature on the oligomerization state of αS102 for 0-60% TFE: We previously found that αS variants are aggregation-prone at intermediate [TFE] (Anderson, et al., 2010), and oligomerization may be accelerated at high temperatures. Therefore, we use the NRMSD parameter (Appendix A) to quantify changes in the CD spectra that occur during heating. Figure 3.4 shows NRMSD values for CD spectra that were measured before and after 0.5 μM αS102 samples were heated to a maximum temperature T_h for 20 minutes. We observe large spectral changes at pH 7.5 for ~10-30% TFE, but low and high [TFE], as well as lower temperatures and decreased solution pH, reduce the observed hysteresis. Therefore, we use Figure 3.4 as a starting point for finding conditions where αS102 probably remains monomeric, but we must quantify hysteresis for each sample individually because details of incubation time and heating and cooling rates impact oligomerization.

Table 3.1. The number of residues in the αS variants that adopt a helical conformation in the presence of 60% TFE, as estimated by the method of Luo and Baldwin using their 25 °C, 50% TFE parameters (Luo and Baldwin, 1997). The difference, Δ, between the pH 2.4 and pH 7.5 estimates is also calculated.

	pH 2.4	pH 7.5	Δ
WT	93 ± 3	88 ± 3	6 ± 4
αS102	95 ± 3	85 ± 3	10 ± 4
A30P	96 ± 3	86 ± 3	10 ± 5

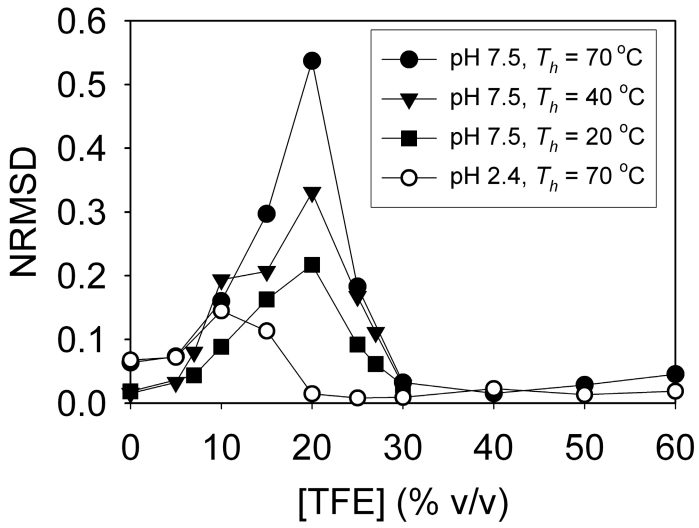

Figure 3.4. Spectral changes for 0.5 μM αS102 that occurred during a heating-cooling cycle (2 °C→ T_h →2 °C). The CD curves were measured at 2 °C before and after a 20 minute incubation at T_h, and the differences between the initial and final spectra are quantified using the NRMSD parameter. See Figure B.2 for the raw spectra used to calculate the NRMSD values.

Effects of temperature on the secondary structure of monomeric αS102 in the presence of TFE at pH 7.5: Figure 3.5 shows variable-temperature CD spectra for 0.5 μM αS102 samples in the presences of various [TFE] at pH 7.5. We quantify the amount of hysteresis during the measurements and verify that the NRMSD is < 0.15 for these samples, restricting our measurements to TFE and temperature ranges where the samples likely remain monomeric (Figure B.1M-R).

Spectra for the 5% and 7% TFE samples appear qualitatively similar to the 0% case, featuring a negative peak near 200 nm that is reduced by heating. In contrast, the 27-50% TFE spectra resemble the 60% TFE sample, showing α-helical structure that is more prominent at low temperatures. In addition, each set of curves shares an isodichroic point (Table 3.2A), and these isodichroics can be divided into two categories; at 0-7% TFE, the points are located near 207 nm and -9 x 10^3 deg cm^2 $dmol^{-1}$, while for 27-60% TFE, they occur near 204 nm and -20 x 10^3 deg cm^2 $dmol^{-1}$.

In Figure 3.6A, we plot the data from Figure 3.2E, Figure 3.3E, and Figure 3.5, along with the 25 °C, variable-TFE lines obtained previously (Anderson, et al., 2010), on a transition diagram (Kuznetsova, et al., 2004). As temperature increases, the conformations shift toward the point of intersection of the two lines, which we previously associated with the TFE-induced intermediate conformation. Transition diagrams constructed using the WT and A30P αS data show similar behavior (Figure B.4). Furthermore, $[\theta]_{222}$ vs. T plots (Figure 3.6B) for αS102 are approximately linear, and the 40-60% TFE curves appear to converge at low temperature.

CD spectra of αS102 in ≥ 60% TFE: We previously observed that TFE-dependent changes in the CD signal of αS appear to saturate at ~40-50% TFE (Anderson, et al., 2010).We verify that higher [TFE] does not lead to significant changes in the secondary structure of αS102 by investigating the CD spectra at 60->99% TFE (Figure 3.7). In order to avoid solubility issues with buffer salts, we

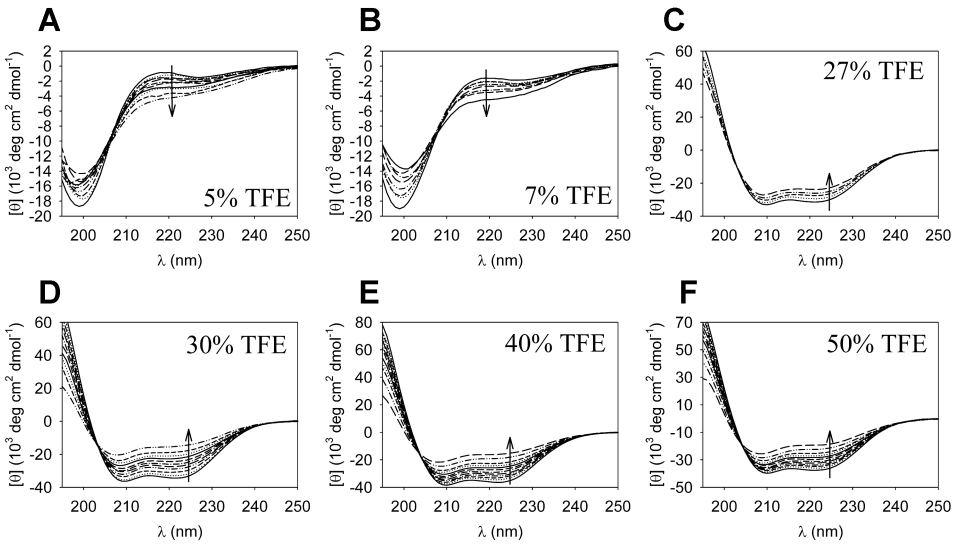

Figure 3.5. Variable-temperature CD spectra of ~monomeric, 0.5 μM αS102 samples at intermediate [TFE] and pH 7.5. The arrows show the general direction of increasing temperature (see also Figure 3.6B). The spectra were obtained for (A) 5% TFE, 2– 60 °C, (B) 7% TFE, 2 – 40 °C, (C) 27% TFE, 2 – 25 °C, (D) 30% TFE, 2 – 60 °C, (E) 40% TFE, 2– 70 °C, and (F) 50% TFE, 2– 70 °C.

Table 3.2. Variable-temperature isodichroic wavelengths (λ_{iso} in nm) and the CD signal at the isodichroics ($[\theta]_{iso}$ in units of 10^3 deg cm^2 dmol^{-1}) for αS102 (A) in pH 7.5 buffer (Figure 3.2E, Figure 3.3E, Figure 3.5), (B) in water (Figure 3.7A-C), and (C) in pH 2.4 solutions (Figure 3.2B, Figure 3.3B, Figure 3.8A-M). The uncertainties in $[\theta]_{iso}$ are due to experimental error, and the uncertainties in the wavelength measurements result from the CD spectrometer bandwidth and experimental error. Isodichroics for WT and A30P αS spectra can be found in Table B.1.

A

[TFE] (% v/v)	λ_{iso}	$[\theta]_{iso}$
0	207 ± 1	-9.2 ± 1.5
5	207 ± 1	-9.0 ± 1.4
7	208 ± 1	-8.5 ± 1.2
27	203 ± 1	-10.6 ± 6.3
30	203 ± 1	-13.0 ± 5.8
40	204 ± 1	-17.8 ± 5.6
50	204 ± 1	-18.5 ± 6.2
60	204 ± 1	-18.2 ± 6.3

B

[TFE] (% v/v)	λ_{iso}	$[\theta]_{iso}$
60	204 ± 1	-19.4 ± 6.5
80	204 ± 1	-20.4 ± 6.8
>99	204 ± 1	-23.7 ± 6.5

C

[TFE] (% v/v)	λ_{iso}	$[\theta]_{iso}$
0	207 ± 1	-10.2 ± 1.8
5	207 ± 1	-9.9 ± 1.5
7	208 ± 1	-9.5± 1.5
18	204 ± 1	-15.7 ± 1.8
20	204 ± 1	-16.2 ± 2.9
22	204 ± 1	-18.1± 3.8
25	204 ± 1	-17.5 ± 4.9
30	204 ± 1	-18.3± 5.8
60	204 ± 1	-20.6 ± 6.9

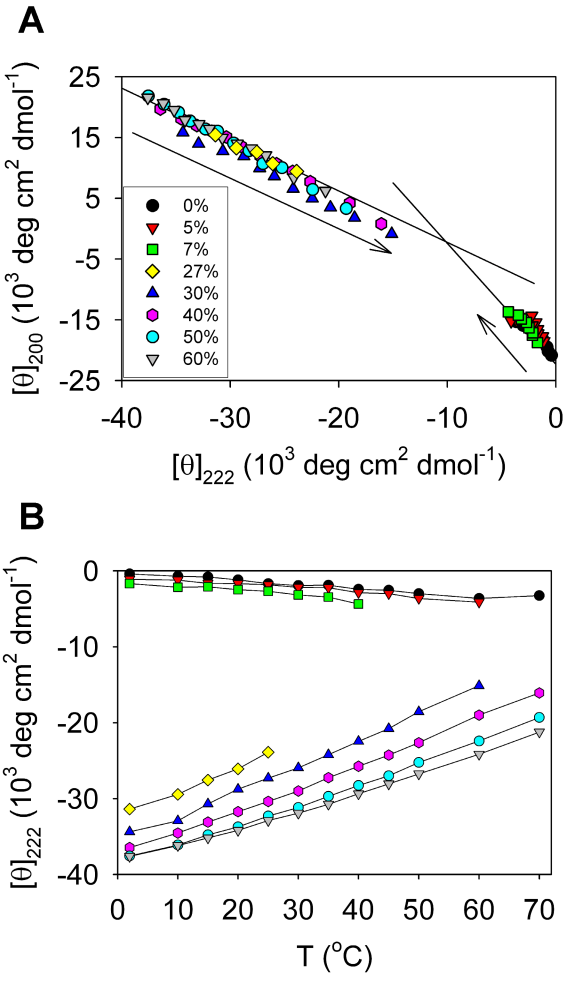

Figure 3.6. Transition diagram and $[\theta]_{222}$ vs. T plot for the variable-temperature, pH 7.5 αS102 CD data. (A) The transition diagram constructed from the data in Figure 3.2E, Figure 3.3E, and Figure 3.5 (colored symbols, [TFE] as in the legend). The arrows show the general direction of increasing temperature. The lower right (upper left) solid line shows a linear fit of the 0%-13% (17% - 60%) TFE data from (Anderson, et al., 2010). (B) The ellipticity at 222 nm vs. temperature for the spectra in Figure 3.2E, Figure 3.3E, and Figure 3.5. The [TFE] for each symbol is as described in the legend in A.

investigate ternary water-protein-TFE solutions. These high-TFE CD spectra are qualitatively similar to the 27-60% curves from Figure 3.5C-G, and the 60% TFE data in water is nearly identical to the pH 7.5 measurements (Figure 3.7D). Furthermore, the locations of the isodichroic points for these samples are similar to the 40-60% TFE, pH 7.5 points (Table 3.2B).

Effects of TFE and temperature on the secondary structure of αS102 at pH 2.4: The amount of hysteresis in αS102 secondary structure during heating and cooling cycles is significantly reduced at pH 2.4 compared to pH 7.5 (Figure 3.4), which likely reflects reduced oligomerization due to increased electrostatic repulsion between monomers. Therefore, we examine pH 2.4 solutions in order to obtain variable-temperature CD data at intermediate [TFE] (Figure 3.8A-M). We again restrict our measurements to temperature ranges for which the NRMSD of the spectra before vs. after heating is <= 0.15 (Figure B.1S-EE). The curves in Figure 3.8A-M are qualitatively similar to those measured at pH 7.5 (Figure 3.5). However, $[\theta]_{222}$ is significantly larger negative at pH 2.4 than at pH 7.5 for the 30% TFE sample, although the signals are similar at both pH values for the 5% and 7% TFE samples (Figure 3.8N).

The transition diagram constructed from the spectra from Figure 3.2B, Figure 3.3B, and Figure 3.8A-M is similar to the constant-temperature lines from (Anderson, et al., 2010), although the points are slightly offset, particularly at low [TFE] (Figure 3.9A). The differences are mostly due to reduced $[\theta]_{200}$ for pH 2.4 samples compared to pH 7.5 samples. It is unclear whether this difference is due to increased signal from the pH 7.5 baseline buffer at low wavelengths or whether it reflects a slight pH-dependent shift in the disordered conformation. The pH 2.4 transition diagram points also appear to be slightly more collinear than those for the pH 7.5 samples (Figure 3.6A). However, the existence of two distinct isodichroics at different wavelengths

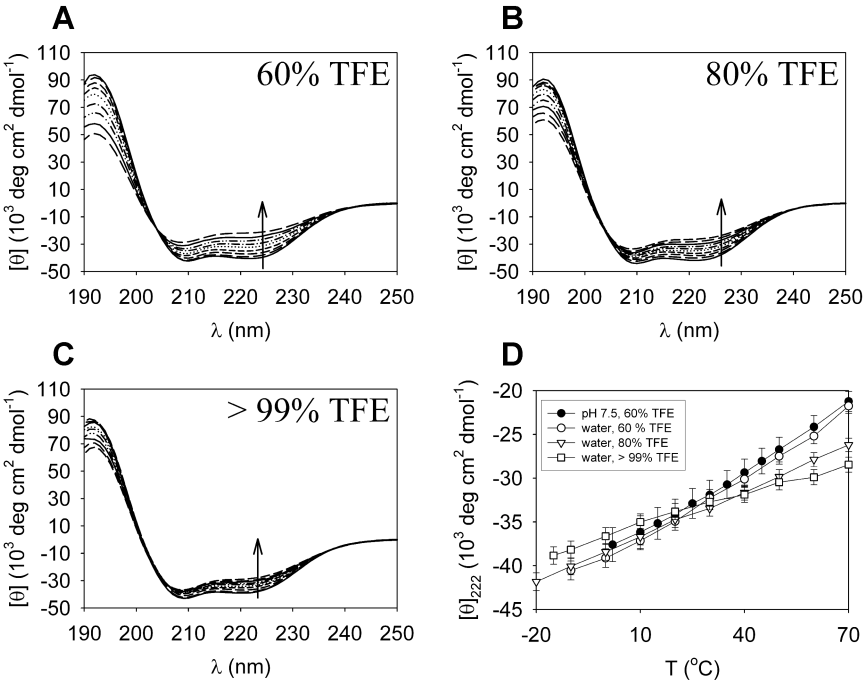

Figure 3.7. CD measurements in TFE-water-protein ternary systems. (A) Far-UV CD spectra for 0.5 μM αS102 in 60% TFE taken from -10 °C (largest negative signal at 222 nm) to 70 °C (smallest negative signal at 222 nm). The arrow shows the general direction of increasing temperature. (B) Same as A, except data was measured for 80% TFE from -20 °C to 70 °C. (C) Same as A, except data was measured for >99 % TFE from -15 °C to 70 °C. (D) The ellipticity at 222 nm vs. temperature for the samples in A-C (white symbols), along with the 60% TFE, pH 7.5 data from Figure 3.3E (black circles).

Figure 3.8. (A-M) Variable-temperature CD spectra for ~monomeric, 0.5 μM αS102 samples at intermediate [TFE] and pH 2.4. The arrows show the general direction of increasing temperature when trends are apparent (see also Figure 3.9B). The spectra were obtained for (A) 5% TFE, 2 – 70 °C, (B) 7% TFE, 2 – 50 °C, (C) 10% TFE, 2 – 25 °C, (D) 12% TFE, 2 – 25 °C, (E) 14% TFE, 2 – 25 °C, (F) 15% TFE, 2 – 25 °C, (G) 16% TFE, 2 – 25 °C, (H) 17% TFE, 2 – 40 °C, (I) 18% TFE, 2 – 40 °C, (J) 20% TFE, 2 – 50 °C, (K) 22% TFE, 2 – 60 °C, (L) 25% TFE, 2 – 70 °C, and (M) 30% TFE, 2 – 70 °C. (N) Comparison of the ellipticity at 222 nm for these samples (black circles) with data obtained at pH 7.5 (white triangles, see also Figure 3.6B).

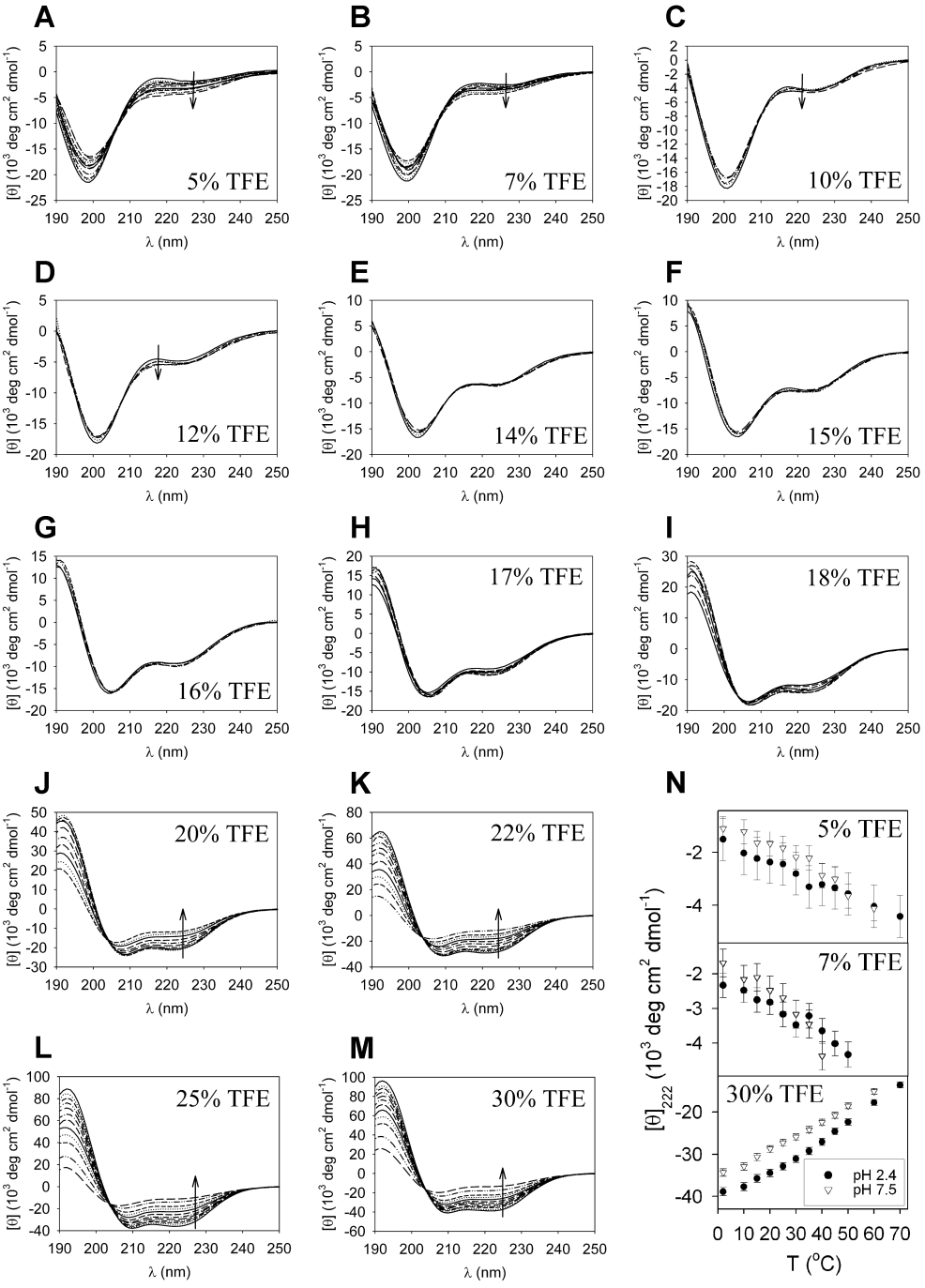
A
B
C
D
E
F
G
H
I
J
K
L
M
N
5% TFE
7% TFE
10% TFE
12% TFE
14% TFE
15% TFE
16% TFE
17% TFE
18% TFE
20% TFE
22% TFE
25% TFE
30% TFE
λ (nm)
[θ] (10^3 deg cm^2 dmol^-1)
[θ]222 (10^3 deg cm^2 dmol^-1)
T (°C)
pH 2.4
pH 7.5

(Table 3.2C), along with the qualitative differences in the behavior of the high- and low-TFE samples, confirms that the protein is sampling at least three conformations.

Figure 3.9B shows $[\theta]_{222}$ vs. T curves for the pH 2.4 spectra. The temperature-dependent behavior at low (< 10%) and high (> 20 %) TFE is similar to the pH 7.5 samples (Figure 3.6B). However, near 10-15% TFE, the signals changes very little with temperature, and at 17-20% TFE, the curves are non-monotonic.

When plotted as a function of [TFE], the $[\theta]_{222}$ curves appear sigmoidal (Figure 3.9C). However, the data for all temperatures appear to overlap or approach similar values in the ~12-16% TFE range. In addition, a comparison of the plots for pH 2.4 samples with the pH 7.5 data (Figure 3.9D) reveals that the curves are similar at low TFE, but diverge above ~20% TFE. However, when the data is rescaled so that the maximum and minimum values coincide (Figure 3.9D inset), the curves are similar at both pH values.

CD spectra of αS102 samples undergoing oligomerization: We now relax the requirement that CD spectral changes induced by heating should be irreversible and examine pH 7.5, intermediate [TFE] samples from 2 °C to 70 °C (Figure 3.10). Near 20% TFE, the high-temperature curves possess the single minima near 216 nm that is characteristic of β-sheet secondary structure. The insets in Figure 3.10 show that significant hysteresis (NRMSD > 0.15) occurs for these samples, and the final 2 °C spectra for the 17 and 20% samples also have a shape that is characteristic of partial β-sheet formation. These observations are consistent with heating leading to the production of β-sheet-rich oligomers or aggregates.

The transition diagram for these samples (Figure 3.11A) differs significantly from the constant-temperature, variable-TFE data. The region of the diagram that is associated with the oligomeric conformation appears to occur somewhere to the upper

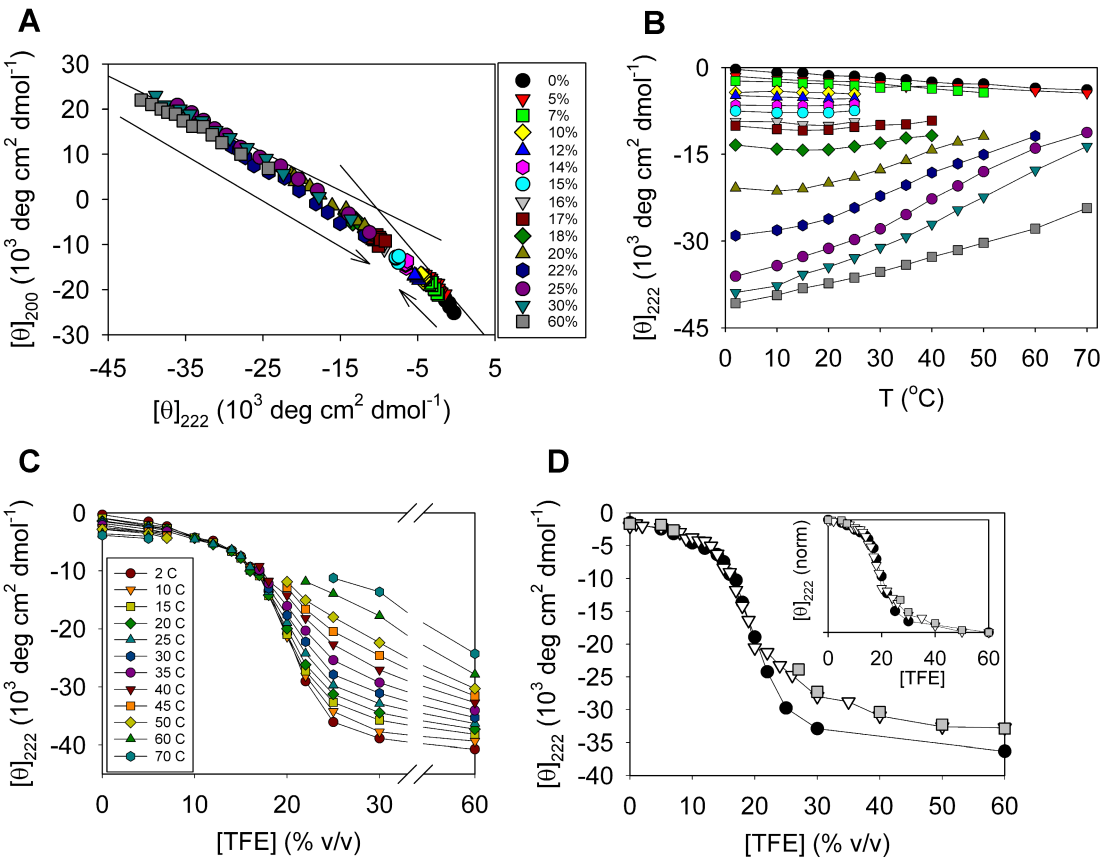

Figure 3.9. Transition diagram and $[\theta]_{222}$ plots of the variable-temperature, pH 2.4 CD data for αS102. (A) The transition diagram constructed from the pH 2.4 data in Figure 3.2B, Figure 3.3B, and Figure 3.8A-M (colored symbols, [TFE] as in the legend). The arrows show the general direction of increasing temperature. The lower right (upper left) solid line shows a linear fit of the 0%-13% (17% - 60%) TFE data from (Anderson, et al., 2010). (B) The ellipticity at 222 nm vs. temperature for these samples. The [TFE] for each symbol is as described in the legend in A. (C) The ellipticity at 222 nm vs. [TFE] for these samples. The temperature (in °C) is noted in the legend. (D) A comparison of the 25 °C ellipticity as a function of TFE concentration for the pH 2.4 data (black circles), the pH 7.5 data from (Anderson, et al., 2010) (white triangles), and the pH 7.5 data from Figure 3.2E, Figure 3.3E, and Figure 3.5 (gray squares). The inset shows the main plot curves normalized by subtracting the lowest-magnitude point and dividing by the absolute value of the ellipticity of the 60% TFE sample. The inset x-axis units are the same as the main plot.

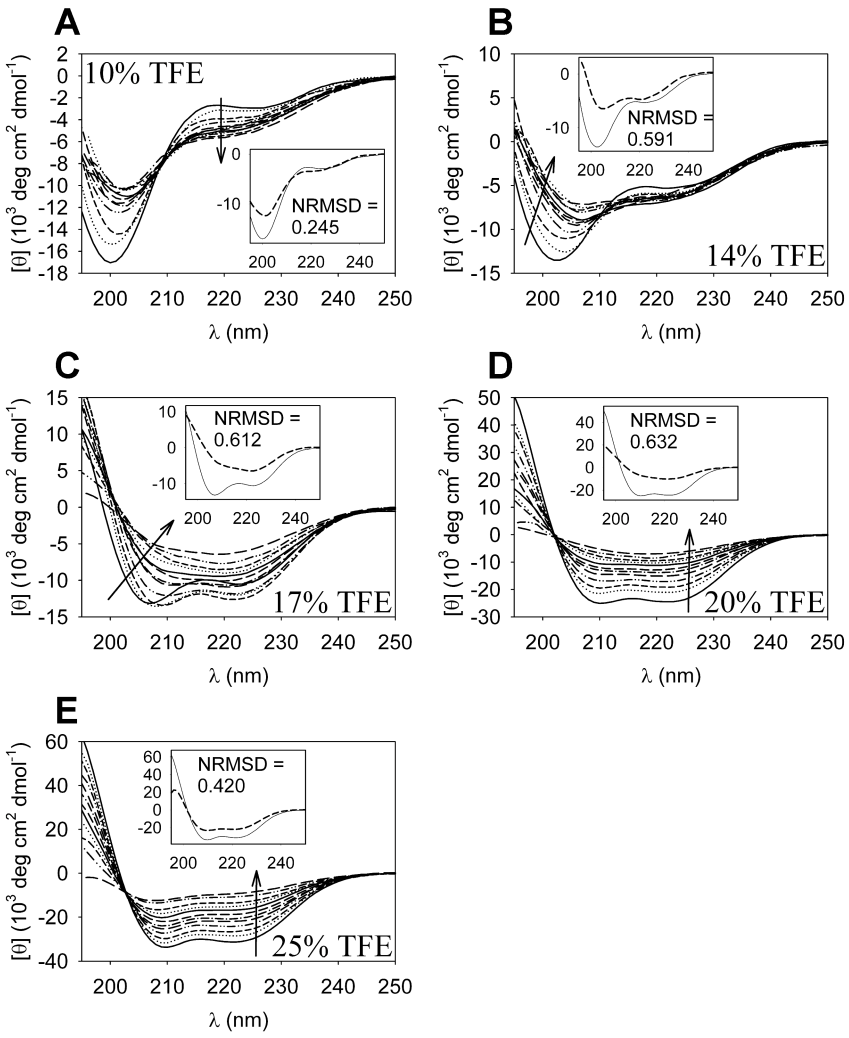

Figure 3.10. Variable-temperature CD spectra of 0.5 μM αS102 at pH 7.5 and 10-25% TFE. Spectra are measured for 2 °C to 70 °C and the arrows show the general direction of increasing temperature (see also Figure 3.11B). The insets show the spectra, and their NRMSDs, taken at 2 °C before (solid line) and after (dashed line) the heating cycle. The inset axis units are the same as those for the main plot. The spectra are obtained for (A) 10% TFE, (B) 14% TFE, (C) 17% TFE, (D) 20% TFE, and (E) 25% TFE.

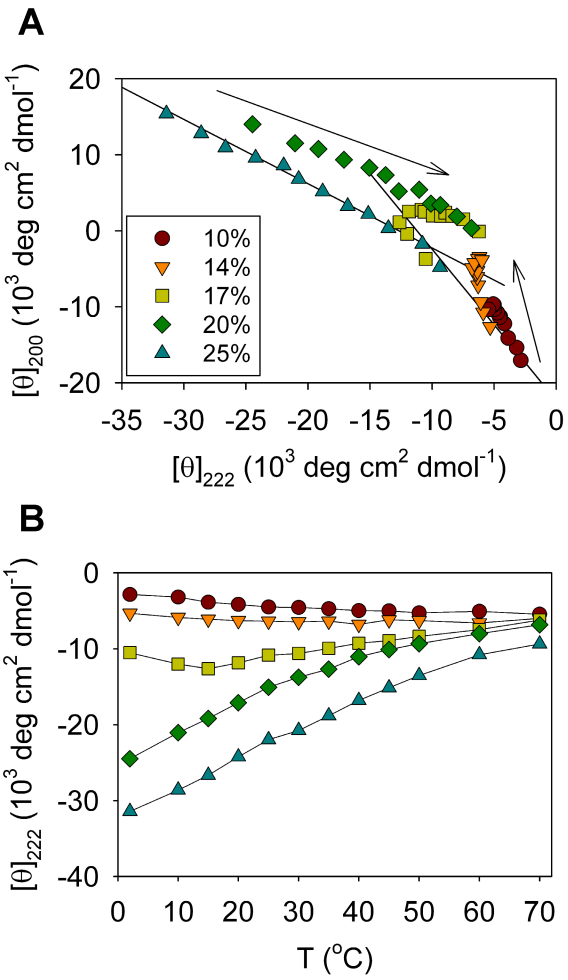

Figure 3.11. Transition diagram and $[\theta]_{222}$ vs. *T* plot of the variable-temperature CD data for pH 7.5, αS102 samples in 10-25% TFE. (A) The transition diagram constructed from the data in Figure 3.10A-E (colored symbols, [TFE] as in the legend). The lower right (upper left) solid line shows a linear fit of the 0%-13% (17%-60%) TFE data from (Anderson, et al., 2010). The arrows show the general direction of increasing temperature. (B) The ellipticity at 222 nm vs. temperature for the spectra in Figure 3.10A-G. The [TFE] for each symbol is as described in the legend in A.

right of the lines representing monomer transitions. Plots of $[\theta]_{222}$ as a function of temperature (Figure 3.11B) show the data converging onto an intermediate value at high temperatures.

Ultrastructure of αS and αS102 aggregates produced by elevated temperatures: Figure 3.12 shows images of WT αS and αS102 fibrils grown in pH 7.5 buffer containing 0% and 15% TFE after three days incubation at 70 °C under quiescent conditions. In the absence of TFE, rigid, linear fibrils are observed for both WT αS and αS102 (Figure 3.12), although αS102 samples tend to contain more and thicker fibrils, which often clump together. For WT αS in 15% TFE, large quantities of "TFE fibrils" similar to those observed previously (Anderson, et al., 2010) are produced and no classic amyloid is observed. However, αS102 samples in 15% TFE tend to contain linear fibrils, while a few flexible, helical TFE fibrils are observed as a minor fraction. Therefore, the presence of the C terminus affects fibril morphology, even in identical solution conditions.

3.3. Discussion

We have examined the effects of pH, temperature, and TFE on αS variant secondary structure in order to determine the relationships among conformational rearrangements induced by various aggregation-promoting conditions. We find that pH-dependent effects require the C terminal portion of αS, while TFE- and temperature-induced changes involve the N terminus. Aggregation is correlated with a crossover between TFE-like and water-like behavior with respect to temperature. We propose that desolvation is likely to play a role in the formation of both the TFE-induced and the high-temperature intermediate states.

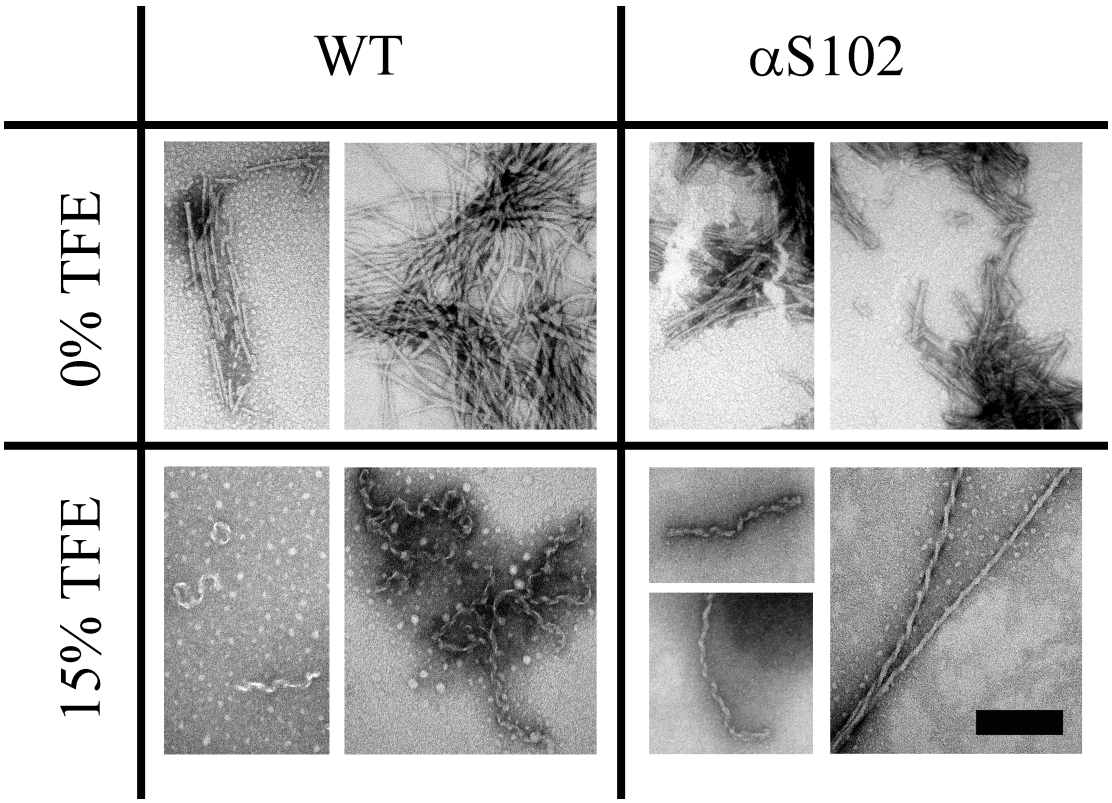

Figure 3.12. TEM images of aggregates grown from 50 μM WT αS (left column) and αS102 (right column) incubated at 70 °C for 3 days in pH 7.5 buffer with 0% (top row) or 15% (bottom row) TFE. The scale bar is 200 nm, and all images are shown at the same magnification.

The pH-induced secondary structural transition is distinct from the TFE-induced conformational rearrangements: By comparing WT αS to the C-terminal truncation mutant αS102, we show that the final 38 residues of the protein are required for the pH-induced secondary structural transition (Figure 3.1). Thus, our CD data corroborates multiple NMR studies that have shown that only the C terminus of WT αS undergoes structural changes at low pH (Cho, et al., 2009; McClendon, et al., 2009; Wu, et al., 2009). In contrast, we previously found that the TFE-induced conformational changes involve the N terminal portion of the protein and can be observed for both αS102 and WT αS (Anderson, et al., 2010).

Temperature-induced conformational changes involve the N terminal portion of αS and are consistent with loss of PPII structure: Uversky et al. first observed temperature-induced changes in the CD signal of WT αS (Uversky, et al., 2001). We reproduce these results and also examine A30P αS and αS102. All the variants undergo nearly identical secondary structural transitions between 2 °C and 70 °C in the absence of TFE (Figure 3.2, Figure B.3A-B). The αS102 data shows that the structure of the N terminal portion of αS changes with temperature, but the similarity in the magnitude of the mean residue ellipticity change for αS102 and WT αS indicates that the C terminus of αS is probably also affected by heating (Figure 3.2C).

Temperature-induced changes in the CD spectra of disordered peptides were initially observed decades ago (Tiffany and Krimm, 1972). A decrease in the ellipticity near 222 nm and concurrent weakening of the ~200 nm negative peak are typical for multiple proteins and peptides at elevated temperatures. These changes are generally thought to reflect loss of PPII structure from the ensemble of disordered conformations (Bochicchio and Tamburro, 2002). Given the extensive literature on the effects of temperature on the structure of intrinsically disordered proteins and peptides, we feel that it is safe to assume that heating-induced structural changes in αS

reflect a similar phenomenon. Loss of solvent interactions at high temperatures may shift the equilibrium distribution of disordered conformations toward a truly "random-coil" ensemble (Kjaergaard, et al., 2010). Alternatively, breaking protein-solvent hydrogen bonds may increase intramolecular hydrogen bonding, leading to the formation of secondary structure such as α-helices, β-sheets, or β-turns (Ma and Wang, 2003; Nettels, et al., 2009; Shi, et al., 2002; Yang, et al., 2003).

The TFE-induced intermediate may be similar to the high-temperature state: The CD spectral changes induced by addition of small amounts of TFE (Anderson, et al., 2010) are qualitatively similar to those observed during heating (Figure 3.2). In addition, both transitions involve the N terminal portion of the protein. With CD data alone, it is impossible to be certain that the protein is sampling the same structures in different solution conditions. However, the behavior of our spectra provides some indirect evidence that the TFE-induced and high-temperature intermediate conformations are related.

Inspection of our variable-temperature CD curves reveals two distinct types of spectra. Below ~15% TFE, the curves show the large negative peak near 200 nm that is characteristic of PPII structure and the spectra share isodichroic points at 207-208 nm. Above ~15% TFE, the spectra are distinctly α-helical and isodichroic points are located near 204 nm. The crossover behavior is also apparent in plots of $[\theta]_{222}$ as a function of temperature (Figure 3.6B and Figure 3.9B); below ~15% TFE, these curves have negative slopes, while above ~22% TFE, the slopes are positive (the complexities in the ~17-20% data at pH 2.4 are discussed in a later section). The fact that crossover behavior occurs in conditions in which the TFE-induced intermediate is expected to be highly populated (Anderson, et al., 2010) and oligomer production increases (Figure 3.4) indicates that there is likely to be some relationship between the high-temperature and intermediate-TFE conformations. Notably, the CD spectra of

αS102 near 15% TFE do not change significantly with temperature, at least in the 2-25 °C range (Figure 3.8E-G, Figure 3.9B).

Furthermore, plots of $[\theta]_{222}$ as a function of [TFE] for pH 2.4 samples (Figure 3.9C) show that the curves approach similar values near ~15-16% TFE for all temperatures measured, which suggests that the TFE-induced intermediate structure may be invariant with respect to temperature. The $[\theta]_{222}$ vs. T curves (Figure 3.6B and Figure 3.9B) also appear to approach intermediate-TFE values at high temperatures, which is consistent with heating leading to increased population of a conformation similar to the TFE-induced intermediate.

The transition diagram representations of our CD data also reveal significant overlap between temperature- and TFE-induced transitions. At pH 7.5, points derived from CD spectra for various [TFE] and temperatures collapse onto the two straight lines that characterize the constant-temperature, TFE-induced structural transitions we identified previously (Figure 3.6A). Increasing the temperature causes a shift toward the region of the diagram that corresponds to the TFE-induced intermediate conformation. Transition diagrams for samples at lower pH are qualitatively similar (Figure 3.9A).

For constant-temperature (25 °C), variable-TFE samples, we previously detected three factors via PCA, which were readily identifiable as reflecting the disordered state, the intermediate conformation, and a highly α-helical state (Anderson, et al., 2010). However, the combined temperature- and TFE-dependent PCA results are more difficult to interpret. The total number of significant factors is estimated to be at least four for our pH 2.4 data, and at least three for our pH 7.5 data (Appendix B and Figure B.6A-B). Some of the variations appear to be due to differences in the relative magnitudes of the CD signal at 208 vs. 222 nm for the highly helical conformation (Appendix B and Figure B.5), which may be expected for

helical proteins and peptides (Wallimann, et al., 2003). Therefore, although PCA reveals additional components that are associated with temperature-induced spectral changes, it is unclear whether these changes are artifacts, reflect temperature-dependent changes in the signals from the three previously-identified conformations, or represent distinct states.

Dehydration may cause loss of PPII structure and enhanced aggregation for αS in 0-15% TFE. The potential similarities between the heat- and TFE-induced αS structural changes suggest that a common mechanism may involved in both transitions. As we discussed above, characteristic heat-induced loss of PPII structure in the disordered states of peptides and proteins is thought to result from disruption of hydrogen bonds between backbone amide groups and water (Adzhubei and Sternberg, 1993; Kelly, et al., 2001; Rucker, et al., 2003). Alcohols may also dehydrate the peptide backbone (Conio, et al., 1970; Kentsis and Sosnick, 1998).

Recent studies have implicated dehydration in protein aggregation processes. Zhang and Yan demonstrated aggregation coupled to dehydration for proteins in the presence of ethanol, and they suggested that similar effects should occur in TFE (Zhang and Yan, 2008). In addition, aggregation enhancement was observed when reveres micelles were used to limit water availability (Mukherjee, et al., 2009). Furthermore, structural studies of amyloid fibrils suggest that the fibril cores are dehydrated, implying that removal of water from the protein backbone is a necessary step in the aggregation reaction (Balbirnie, et al., 2001). Dehydration is thought reduce kinetic barriers in protein folding (Hillson, et al., 1999; Liu and Chan, 2005; MacCallum, et al., 2007), and similar effects could impact aggregation reactions.

Therefore, the similarities between temperature- and TFE-induced changes in the αS spectra, as well as the aggregation enhancement observed in low TFE solutions, are consistent with dehydration leading to protein aggregation. The PPII

peak in the CD spectra may be a signature of protein-water interactions, and weakening of this peak may reflect loss of these interactions.

Kentsis and Sosnick proposed that kosmotropic effects lead to protein dehydration in the presence of low concentrations of TFE (Kentsis and Sosnick, 1998). In this model, TFE causes an increase in solvent structure, leading to destabilization of unfolded or disordered protein conformations. However, the addition of TFE to aqueous solutions causes a reduction in surface tension, which is inconsistent with typical kosmotropic "salting out" behavior (Chitra and Smith, 2002), although the protein-water interface may differ from the air-water interface. Dehydration could result from other bulk solution properties. One molecule of TFE is about nine times the size of a water molecule, but TFE can participate in only two hydrogen bonds (Van Buuren and Berendsen, 1993). Therefore, TFE-water mixtures have a reduced hydrogen bonding capacity compared to pure water, which might favor solvent-shielded conformations in which backbone exposure is reduced. Water-TFE interactions may also reduce water availability for protein solvation. Or, incorporation of a minor fraction of TFE into the protein solvation layer could cause structural changes in the solvation shell.

Although the precise nature of the molecular interactions underlying TFE-induced dehydration is uncertain, our experimental evidence is consistent with loss of water-protein interactions in dilute TFE solutions. However, at high TFE, aggregation decreases and highly α-helical structures are observed. Additional interactions must be present to account for these effects.

Preferential solvation may explain decreased αS aggregation at high TFE: The CD spectra of our 40-60% TFE, pH 7.5 αS102 samples (Figure 3.3E, Figure 3.5) are very similar to those for 80-99% TFE (Figure 3.7). Also, plots of $[\theta]_{222}$ vs. [TFE] show saturation behavior at high TFE (Figure 3.9B-C). Therefore the protein

environment appears TFE-rich above ~40% TFE. Preferential solvation at this relatively low TFE concentration (40% v/v is less than 15 mole % TFE) is consistent with the report that complete TFE coating of the protein bombesin occurs in solutions containing 30% TFE (Diaz, et al., 2002).

Previous studies have suggested that preferential solvation leads to TFE-induced protein structural changes (Fioroni, et al., 2002; Kundu and Kishore, 2004; Munishkina, et al., 2004; Roccatano, et al., 2002; Walgers, et al., 1998). TFE may partition into the protein solvation layer as a result of the free energy costs of TFE-water mixing relative to ideal solutions (Marcus, 1988; Marcus, 2001). Moreover, TFE might selectively replace the highest energy water molecules in the protein solvation layer (Eggers, 2011), potentially resulting in local coating of helical regions (Starzyk, et al., 2005; Walgers, et al., 1998). Alternatively, chaotropic effects resulting from disruption of water structure leading to TFE repulsion from bulk solvent could lead to preferential solvation of proteins by TFE (Grudzielanek, et al., 2005). Once a protein is in a TFE-rich environment, the decreased relative permittivity (dielectric constant) may favor the formation of intramolecular hydrogen bonds, leading to helix induction. TFE-protein interactions may also affect the conformation of the TFE-coated protein (Rajan and Balaram, 1996).

Partitioning of TFE molecules into the protein solvation shell may decrease aggregation because more surface area is available when all protein molecules are monomeric (Moelbert, et al., 2004). Direct TFE-protein interactions might also help stabilize monomeric protein in a TFE-like environment. In addition, the solvent entropy contribution to oligomerization reactions, whereby feeing solvent molecules upon binding helps to promote association, may also be decreased as a result of the relatively large size of the TFE molecule and the decreased free energy difference

between the solvation layer and the bulk solvent for TFE-water mixtures (Eggers, 2011).

The observation that fluoroalcohols, but not simple alcohols, form clusters when mixed with water has led researchers to hypothesize that protein-cluster interactions may be responsible for protein structural transitions and aggregation in fluoroalcohol solutions (Hong, et al., 1999; Reiersen and Rees, 2000). However, clustering and preferential solvation could be independent manifestations of the same solution properties. Gast, et al. demonstrated that the onset of cluster formation is ~20% TFE, while protein structural changes often occur below this threshold (Gast, et al., 2001). Similarly, we observe αS structural changes and maximal aggregation below 20% TFE. Also, clustering decreases at high TFE, but αS structures remain constant above ~40% TFE. Therefore, αS structure does not seem to be tightly coupled to cluster formation. Interestingly, conditions that are conducive to preferential solvation also may also lead to clustering of solvent molecules. Thermodynamic models predict that both preferential solvation and clustering (i.e. preferential solvation of TFE by TFE) may occur when the excess Gibbs function of water-cosolvent mixtures is positive and when protein-cosolvent interactions are favorable (Marcus, 1988; Marcus, 2001). In addition, cluster formation could reflect the hydrophobicity of the cosolvent, and hydrophobic forces could drive both TFE-TFE and TFE-protein interactions (Yamaguchi, et al., 2006). Therefore, we believe that it is likely that preferential αS solvation and cluster formation are coincidental effects resulting from the properties of TFE and TFE-water mixtures.

Loss of protective interactions, rather than the formation of aggregation-prone structural elements, may cause increased αS aggregation in solutions containing ~15% TFE: We previously demonstrated that aggregation is correlated with increased population of a partially-structured αS intermediate state (Anderson, et al., 2010).

However, it is not clear whether this protein conformation actually promotes aggregation, or whether solvent properties or other interactions cause both structural changes and fibrillization.

The structure of a flexible, disordered protein may be tightly coupled to solvent properties. Therefore, structural changes and solvation variations are likely to occur in tandem, and it may be very difficult to separate causation from correlation in the aggregation process. However, the literature provides some guidance. We note that increased aggregation in intermediate [TFE] occurs for many proteins and peptides (Otzen, 2010). Helical structures are often detected prior to aggregation (Anderson, et al., 2010; Fezoui and Teplow, 2002; Liu, et al., 2004; Sen, et al., 2010; Williamson, et al., 2009; Zerovnik, et al., 2007). However, β-sheet-rich intermediates have also been observed (Lim, et al., 2010; Pallarès, et al., 2004; Srisailam, et al., 2003). Calamai, et al. also found that multiple partially structured intermediate conformations are correlated with aggregation of human muscle acylphosphatase (Calamai, et al., 2005). In addition, 5-6mer peptides, which should not be able to form α-helical structure, experience enhanced aggregation in ~7-10% TFE (Chaudhary, et al., 2009). TFE can even induce the formation of aggregates from globular proteins in the absence of significant tertiary structure disruption (Plakoutsi, et al., 2004; Soldi, et al., 2005).

It is possible that multiple structural intermediates promote aggregation via different mechanisms. For helical intermediates, helix-helix interactions are thought to align neighboring disordered regions, enabling their association (Abedini and Raleigh, 2009b; Williamson, et al., 2009), while β-structured intermediates may aggregate in order to bury "sticky" unpaired β-sheet edges (Pallarès, et al., 2004; Srisailam, et al., 2003). However, a simpler explanation for the diversity of fibrillogenic intermediates is that removal of protective interactions, rather than stabilization of specific structural states, leads to aggregation enhancement.

As we discussed above, dehydration can cause CD spectral changes similar to those induced by low concentrations of TFE, while α-helical structure likely reflects the protein experiencing a TFE-rich local environment. Both water-protein interactions and preferential TFE solvation are likely to stabilize monomer protein. Therefore, loss of protein-solvent interactions, rather than details of protein structure, may responsible for aggregation enhancement near ~15% TFE. The apparent protective natures of PPII and/or α-helical structures could reflect their solvent accessibilities.

Water-protein interactions lead to solvation barriers in protein folding (Hillson, et al., 1999; Liu and Chan, 2005; MacCallum, et al., 2007). Hydration of disordered and denatured states could also inhibit aggregation. In fact, dehydration has been found to increase aggregation for proteins in the presence of simple alcohols and reverse micelles (Mukherjee, et al., 2009; Zhang and Yan, 2008). Protein sequences that favor hydration also tend to show reduced amyloid aggregation (Balbirnie, et al., 2001). Hydration may be particularly important for natively disordered and weakly folded proteins, and evolution may have favored solvent-accessible sequence elements for such proteins (Uversky, et al., 2000).

Desolvation is a straightforward explanation that can account for several features of our data. However, we cannot definitively establish that dehydration occurs for our samples. Higher-resolution experiments and examination of additional αS mutants will be necessary to determine whether structural changes, dehydration, or some other interaction initiates aggregation. It also remains unclear whether desolvation in TFE might be related to dehydration in biological environments. The formation of structural intermediates may be less important than solvent interactions for alcohol-water mixtures, but structural intermediates may still be involved in aggregation in aqueous solutions and *in vivo*. It is possible that fluoroalcohol-induced

conformations have biological relevance, even if they do not directly drive aggregation in the solutions examined. Moreover, desolvation alone cannot account for all of our observations. In the following sections we discuss some unexplained aspects of our data.

Solution conditions affect the conformation of αS in the TFE-rich environment: The TFE concentration (~15%) at which the CD spectra of αS102 cross over from water-like to TFE-like behavior is similar at pH 2.4 and pH 7.5 (Figure 3.9D). In addition, the TFE concentration at which the structural changes level off is similar at both pH values. Therefore, protein charge does not seem to significantly affect the transfer of the protein into the TFE-rich environment. However, the protein structure at high TFE varies with pH (Figure 3.3H, Figure 3.8N). We observe similar pH-dependent spectral changes for WT and A30P αS in the presence of 60% TFE (Figure 3.3G and Figure B.3G-H). For all the αS variants, the ensemble-averaged helicity of the low pH samples at 60% TFE is increased by an amount equivalent to ~10 residues per protein molecule (Table 3.1).

Some studies have proposed that short- or medium-range electrostatic interactions impact helix formation in fluoroalcohol solutions. For example, Fan and Mayo show that a lysine residue interacts with a glutamate residue located 11 amino acids away on a model peptide, leading to decreased flexibility and a reduction in helical structure near neutral pH and 40% TFE (Fan and Mayo, 1995). Similarly, contacts between oppositely charged groups separated by 7 residues may limit helix formation for the Aβ40 peptide in the presence of 70% 1,1,1,3,3,3-Hexafluoro-2-propanol (HFIP) (Valerio, et al., 2008). Short- and long- range contacts have been detected for αS (Bertoncini, et al., 2005; Rospigliosi, et al., 2009), and some of these may be responsible for observed pH-dependences. Helix stop signals and amino acid helix propensities also might be altered by pH in solutions containing TFE (Lawrence

and Johnson, 2002; Rohl, et al., 1996). Higher-resolution information will be necessary to identify the precise interactions responsible for the pH-dependence of the high TFE structures of the αS variants.

αS fibril morphology is not determined solely by N terminal secondary structure: Intermediate-TFE and high-temperature conditions appear to induce similar changes in the CD spectra of αS variants. We previously found that solutions containing ~15% TFE promote the formation of flexible "TFE fibrils" (Anderson, et al., 2010), but we demonstrate here that at 0% TFE and 70 °C, classical amyloid structures are formed (Figure 3.12). Notably, at 25 °C, classic amyloid was formed in solutions containing 5% TFE (Anderson, et al., 2010), so a relatively low population of the intermediate state may promote amyloid fibrillization. However, other temperature-related effects, such as strengthened hydrophobic forces, may play a role in aggregation pathway selection, or aggregation may be under kinetic control. In addition, we observe differences in fibril morphology for WT αS and αS102 in 15% TFE (Figure 3.12), despite the fact that their N termini undergo similar TFE-induced (Anderson, et al., 2010) and temperature-dependent (Figure 3.2 and Figure 3.3) conformational rearrangements. Thus, the precise roles of TFE and temperature in determining fibril morphology remain unclear. Studies that examine additional truncation mutants and the pH and ionic strength dependences of aggregate morphology could potentially be informative.

Some of the αS102 helix induction curves are non-monotonic: At ~17-20% TFE and pH 2.4, the $[\theta]_{222}$ vs. temperature plots are convex (Figure 3.9B). These curves appear similar to low-HFIP curves for model peptides that were reported previously (Andersen, et al., 1996). However, Andersen, et al. showed clear spectral evidence that their peptides sampled three distinct conformations during heating, while our 20% TFE spectra (Figure 3.8J) share a distinct isodichroic point near 204 nm,

which is consistent with only two conformations being present over the entire temperature range. The situation is likely to be similar at 17-18% TFE; although the CD curves for these samples (Figure 3.8I,J) are nearly invariant over the temperature range we examine, points derived from these spectra lie on the high-TFE lines in the transition diagram (Figure 3.9A), and so the non-monotonic behavior observed for these samples probably does not involve significant sampling of the hydrated, PPII conformation. Therefore, the mechanism of cold denaturation for αS102 in ~20% TFE is likely to be different from that reported by Andersen, et al. for model peptides in ~8% HFIP. It is possible that heat-induced changes in the properties of fluoralcohol-water mixtures, changes in fluoralcohol-protein interactions, or α-helix melting contribute to the observed behavior.

3.4. Conclusion

We have measured pH, TFE, and temperature-dependent changes of the secondary structure of WT αS, A30P αS, and αS102. We demonstrate a distinct ~15% TFE crossover between water-like and TFE-like behavior in the CD spectra. We hypothesize that, as TFE is titrated into an aqueous solution containing αS, water-protein interactions are weakened, leading to population of a dehydrated intermediate state. As additional TFE is added, preferential TFE solvation of protein molecules leads to the formation of α-helical structure.

Aggregation is enhanced at moderate TFE and high temperatures, where the CD spectra show minimal amounts of both PPII and α-helical structure. Because PPII structure is likely a signature of protein-water hydrogen bonding, while α-helical conformations reflect preferential solvation of proteins by TFE, we propose that aggregation occurs where protective solvent interactions are minimized. However, we note that the final fibril morphology depends on solution conditions and on the

presence of the C terminal portion of αS, and so additional interactions are involved in aggregation pathway selection.

We also demonstrate that αS can populate at least two distinct structural intermediates. The pH-induced intermediate involves structural changes in the C terminus of αS and is distinct from TFE- and temperature-induced conformations. By examining combined effects of TFE and temperature on αS102, we find inconclusive but suggestive evidence that the secondary structure of the protein is similar at intermediate TFE and at elevated temperatures. Therefore, caution must be employed in investigating aggregation-prone structures, as αS flexibility enables the formation of multiple distinct conformations.

Moreover, we hypothesize that aggregation enhancement in TFE may result from removal of protective factors, rather than from stabilizing specific aggregation-prone states. Therefore, studying defensive mechanisms may be more useful than examining aggregation-prone conformations in increasing understanding amyloid diseases. Disordered proteins have likely evolved sequence elements that facilitate backbone hydration in order to protect against amyloid aggregation (Rauscher, et al., 2006). It may be possible to use TFE to vary the strength of protein-solvent interactions, enabling study of the effects of hydration on protein aggregation processes.

3.5. Materials and Methods

Reagents and solutions: Acros Organics brand 99.8% pure 2,2,2-Trifluoroethanol (TFE) was purchased from Fisher Scientific. All chemicals were reagent grade and all solutions were prepared using MilliQ (≥ 18.2 MΩ cm) or HPLC grade water.

Protein expression and purification: Recombinant WT and mutant αS were produced and purified as previously described (Bussell and Eliezer, 2001). Lyophilized αS variant protein was solubilized by dissolving at 1-2 mg/mL in pH 7.5 buffer for the variable-temperature experiments and 2 mM NaOH for the acid titrations. Insoluble material was removed by filtering each stock solution through a 100 kDa (Microcon YM-100, Millipore) centrifugal spin filter.

Circular dichroism (CD) spectroscopy: An Aviv 400 Circular Dichroism Spectrometer (Aviv Biomedical, Inc.) was used to obtain far-UV CD data. All samples were measured using a 1 cm path length, a strain free quartz cuvette, and a bandwidth of 1 nm. A noise-reducing option in the instrument software was used to smooth the data. Three scans with a speed of 1 sec / nm were averaged to obtain each curve.

pH-dependent spectra were obtained using a Microlab syringe pump (Hamilton) to titrate 0.1 N sulfuric acid (Mallinckrodt Baker) into a solution containing 1 μM protein in 10 mM dibasic sodium phosphate (Sigma). The curves were corrected for changes in concentration due to dilution. A buffer-only baseline was subtracted from the CD spectra, and errors in the measurement were calculated from the standard deviations of three measurements (see Appendix B for more details of the baselining procedures).

For variable-temperature experiments at pH 7.5, the solutions contained 10 mM sodium phosphate buffer (Sigma), while the pH 2.4 samples contained 10 mM phosphoric acid (Mallinckrodt Baker). The pH values we report refer to the pH of solutions in the absence of TFE; TFE-induced pH shifts for buffer and water ionization constants are expected to be minimal at low to neutral pH and so we ignore these effects (Espinosa, et al., 2002; Zagorski and Barrow, 1992). Each sample was prepared by mixing the protein, water, and buffer salts or acid, chilling these solutions to ~4 °C, and then adding room-temperature TFE to the aqueous protein solutions on

ice. Then, these samples were placed in the CD spectrophotometer and cooled to 2 °C. CD spectra were obtained starting 2 °C and heating to the maximum temperature. After the heating cycle, the solutions were cooled and a final measurement was performed at 2 °C to quantify hysteresis. The baselining procedure averaged over temperature-related drifts but accounted for some solvent expansion and contraction due to temperature changes (see also Appendix B). Errors in the measurements were estimated from the standard deviations of three measurements and from uncertainties due to temperature drifts in the baseline signals.

The procedure for measuring the high-TFE, (approximately) ternary water-TFE-protein samples (Figure 3.10) was similar to that for the pH 7.5 and 2.4 samples, except that hysteresis was not quantified and the minimum temperatures measured were lower than 0 °C. Our highest TFE sample was prepared by diluting 4.2 μL of the stock solution of protein in aqueous buffer into 3 mL of the 99.8% pure TFE so that the final TFE concentration was ~99.6%. Note that these solutions contained residual (~10 μM) concentrations of buffer salts.

Transmission electron microscopy (TEM) imaging: 50 μM αS variant solutions in 10 mM pH 7.5 sodium phosphate buffer were incubated at 70 °C for three days in quiescent conditions prior to examination. 0.02% sodium azide (Sigma) was added to these solutions as a preservative. TEM images of fibrils were obtained as described previously (Anderson, et al., 2010).

CHAPTER 4

ENHANCED GREEN FLUORESCENT PROTEIN CONFORMATIONAL CHANGES AND AGGREGATION INDUCED BY TRIFLUOROETHANOL: A GENERAL ROLE FOR DESOLVATION-DRIVEN FIBRIL FORMATION?*

4.1 Introduction

Proteins experience various structural rearrangements in the presence of fluorinated alcohols, including loss of tertiary structure, stabilization of non-native secondary structure, and aggregation (Otzen, 2010). Helix induction at moderate to high concentrations of 2,2,2-trifluoroethanol (TFE) is thought to result from preferential solvation or chaotropic effects, which lead to TFE enrichment near protein molecules (Diaz, et al., 2002; Fioroni, et al., 2002; Walgers, et al., 1998). However, preferential solvation should stabilize monomeric protein, while lower concentrations of TFE promote aggregation. Many researchers have hypothesized that TFE increases aggregation by stabilizing fibrillogenic structural intermediates. Alternatively, interactions between proteins and clusters comprised of TFE molecules have been hypothesized to promote protein aggregation (Yamaguchi, et al., 2006). Observations of desolvation-initiated aggregation for proteins in the presence of simple alcohols also suggest that dehydration might enhance fibrillization in solutions containing TFE (Zhang and Yan, 2008).

We previously (Chapters 2-3) examined TFE-induced secondary structural transitions for the Parkinson's disease-associated protein α–synuclein (αS). We identified three distinct αS conformational states, the relative populations of which varied with TFE concentration (Anderson, et al., 2010). In the absence of TFE, αS is natively disordered, featuring a far-UV CD spectrum similar to that of a polyproline-II

* This material will be submitted to Biopolymers by V. L. Anderson and W. W. Webb

(PPII) helix. The addition of low (<~15% v/v) concentrations of TFE causes the protein to populate an "intermediate" state. The similarities between TFE- and temperature-induced structural changes, and the apparent protective nature of PPII structure, led us to hypothesize that the αS intermediate conformation is a desolvated state in which protein-water interactions are weakened (Chapter 3). Moreover, enhanced aggregation is correlated with population of the intermediate conformation, as might be expected if this state is indeed desolvated (Balbirnie, et al., 2001; Mukherjee, et al., 2009; Zhang and Yan, 2008). We also found that higher (>~15%) concentrations of TFE led to preferential TFE solvation of αS variants, resulting in a TFE-rich local environment that decreased αS aggregation and induced the formation of α-helical structure.

If our explanation for the TFE-induced conformational changes and aggregation behavior of αS is correct, a natural question to ask is whether desolvation might play a role in the fibrillization of other proteins. Indeed, enhanced aggregation in the presence of moderate amounts of TFE has been observed for numerous proteins and peptides (Otzen, 2010). The TFE concentration at which aggregation is maximal (typically 10-30%) varies among proteins, suggesting that sequence plays some role in the process (Zerovnik, et al., 2007). However, in most cases, little or no fibrillization occurs for very low and very high [TFE], a result that is qualitatively similar to our observations for αS. Needless to say, different proteins may undergo fluoroalcohol-induced fibrillization via different mechanisms. However, the protective nature of low and high TFE conditions is suggestive.

Here, we investigate TFE-induced structural rearrangements and aggregation using enhanced green fluorescent protein (EGFP) as a model system. Near physiological pH, EGFP possesses "β-can" tertiary structure, while low and high pH conditions denature the protein, leading to readily-detectable loss of green

fluorescence (Bokman and Ward, 1981; Ward and Bokman, 1982). Thus, EGFP is a nearly ideal system for examining the roles of tertiary vs. secondary structure in TFE-induced conformational rearrangements. In addition, comparing αS and EGFP may help us to separate the contributions of protein sequences and solvent properties in these aggregation processes.

We find that acid-denatured EGFP populates three secondary structural states in 0-60% TFE. These conformations are analogous to those observed for αS (Anderson, et al., 2010). However, the protein sequence appears to affect the relative populations of the states at a given [TFE]. Solution conditions that favor an intermediate conformation are roughly correlated with increased aggregate production, although electrostatic repulsion limits association in low pH, low ionic strength solutions.

Near neutral pH, EGFP tertiary structure prevents aggregation below ~15% TFE, but higher TFE concentrations lead to denaturation in favor of partially and highly helical conformations. Aggregation of TFE-denatured EGFP is correlated with reduction of α-helical structure in favor of a partly structured state that is likely similar to the pH 2.4 intermediate conformation.

Our results indicate that desolvation may play a general role in TFE-induced protein aggregation. Intact tertiary structure and electrostatic repulsion also appear to inhibit EGFP aggregation. Therefore, loss of protective interactions, rather than the formation of specific aggregation-promoting structural elements, is likely to be responsible for enhanced aggregation at moderate TFE concentrations. Moreover, the TFE concentration at which fibrillization is maximized appears to depend on sequence-related factors. The natively disordered αS protein is more resistant to desolvation-driven structural changes and aggregation than acid-denatured EGFP, which is in accordance with evidence that evolution might have selected well-solvated

sequences for natively disordered proteins (Rauscher, et al., 2006; Uversky, et al., 2000).

4.2 Results

Tertiary structure of EGFP in the presence of TFE: Figure 4.1 shows the fluorescence signal from EGFP as a function [TFE] for pH 2.4 and 7.5 solutions. As expected, low pH solutions are dark; EGFP tertiary structure is disrupted below pH ~3 (Patterson, et al., 1997). At pH 7.5, TFE decreases EGFP fluorescence in a concentration- and time-dependent manner. We interpret fluorescence decreases as reflecting disruption of native EGFP tertiary structure, which leads to solvent quenching and of the removal of barriers to non-radiative relaxation pathways (Craggs, 2009). Although loss of fluorescence can occasionally occur for natively folded green fluorescent protein (Hsu, et al., 2009), our circular dichroism studies (below) verify that TFE- and acid-induced dark states involve a dramatic structure change.

Secondary structure of EGFP at various [TFE]: Figure 4.2A shows CD spectra of 0.3 μM EGFP in the presence of 0-60% TFE at pH 2.4. These curves do not change significantly during the ~20 minute (per sample) experimental duration (Appendix C and Figure C.1). The 0% TFE spectrum features the negative peak near 200 nm that is characteristic of a PPII-like or statistical coil state. As [TFE] increases, the ellipticity near 222 nm becomes larger negative and the 200 nm peak becomes less prominent. At high TFE, the spectra show the double minima at 208 and 222 that are expected for α-helical structure. Isodichroic points are immediately apparent for two subsets of the spectra (Figure 4.2A insets). The wavelength positions of these points are ~209 nm for the 0-8% TFE samples and ~203 nm for the 11-60% TFE samples (Table 4.1).

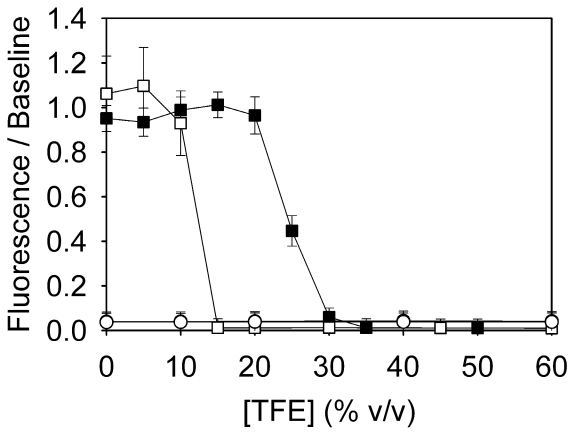

Figure 4.1. EGFP fluorescence at pH 7.5 (squares) and pH 2.4 (circles) as a function of TFE concentration. The emission signal from 0.3 μM protein was measured 2.0 ± 0.5 minutes (solid symbols) or 24 ± 2 hours (open symbols) after the samples were heated to 37 °C. The error bars show the standard deviations of measurements of three identical samples.

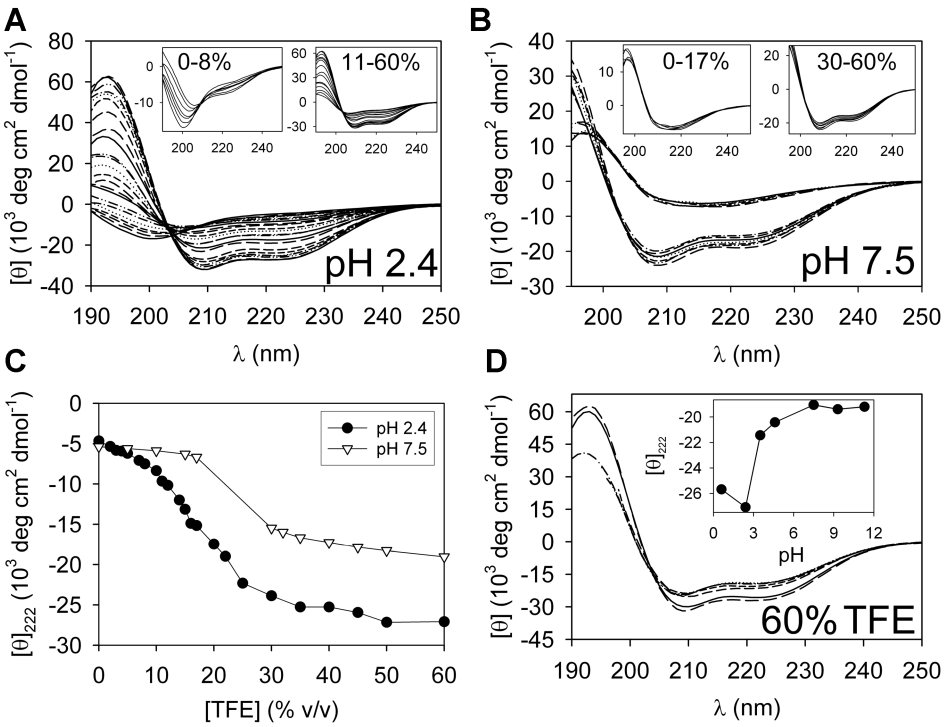

Figure 4.2. Secondary structural transitions for EGFP induced by TFE. (A-B) Far-UV CD spectra for 0.3 μM EGFP in 0-60% TFE, which were obtained ~10 minutes after the samples were mixed and heated to 37 °C. The insets show selected spectra from the main plot, and the inset axes' units are the same as those for the main plots. (A) Data for EGFP at pH 2.4. The TFE concentrations for spectra with increasing negative ellipticity at 222 nm are 0, 2, 3, 4, 5, 7, 8, 10, 11, 12, 14, 15, 16, 17, 20, 22, 25, 30, 35, 40, 45, 60, and 50 % TFE. The figure insets show spectra that share isodichroic points. (B) Data for EGFP at pH 7.5. The TFE concentrations for spectra with increasing negative ellipticity at 222 nm are 0, 5, 10, 15, 17, 30, 32, 35, 40, 45, 50, and 60 % TFE. The left inset shows low-TFE spectra that are nearly invariant. The right inset shows high-TFE spectra that share an isodichroic point. (C) The mean residue ellipticity measured at 222 nm as a function of TFE concentration for the spectra in A-B. (D) The CD spectra of EGFP in 60% TFE at various pH. The solution conditions for spectra with increasing negative ellipticity at 222 nm are 10 mM sodium phosphate (pH 7.5), 2 mM NaOH (pH 11.3), 10 mM borax (pH 9.3), 10 mM citrate-phosphate buffer (pH 4.6), 10 mM citrate-phosphate buffer (pH 3.5), 10 mM phosphoric acid (pH 2.4), and 0.25 N sulfuric acid (pH 0.6). The inset shows the ellipticity at 222 nm as a function of pH, and the units for $[\theta]_{222}$ are the same as those for the main plot.

Table 4.1. Isodichroic points observed in the EGFP CD spectra (Figure 4.2A-B insets). The TFE ranges for which CD spectra share isodichroics, the wavelength at which the curves coincide (λ_{iso}) in nm, and the ellipticity value at the isodichroic ($[\theta]_{iso}$) in units of 10^3 deg cm^2 dmol^{-1}, are reported. Uncertainties in wavelengths reflect the CD spectrometer bandwidth and experimental error, while errors in the ellipticity reflect experimental variations and the uncertainty in the wavelength measurement.

pH	TFE range	λ_{iso}	$[\theta]_{iso}$
2.4	0 – 8 %	209 ± 1	-10.3 ± 0.7
	11 – 60%	203 ± 1	-10.7 ± 4.7
7.5	0 – 17% *	202 ± 3	6.7 ± 7.6
	30 – 60%	203 ± 1	-11.4 ± 4.2

* The existence of the pH 7.5, low TFE isodichroic point is uncertain.

CD spectra for similar samples at pH 7.5 are shown in Figure 4.2B. We report only spectra that do not vary significantly during our measurements; samples containing ~20-30% TFE undergo unfolding in the experimental time frame and so are omitted (see also Appendix C and Figure C.1). The 0-17% TFE spectra (Figure 4.2B, left inset), are consistent with the expected signal from β-can structure (Visser, et al., 2002). There may be an isodichroic near 200 nm for the 0-17% TFE data, but we cannot be certain of this because these spectra are very similar to each other. In contrast, above 30% TFE, the spectra appear α-helical, and an isodichroic point is immediately apparent (Figure 4.2B right inset). The position of this point appears similar to that observed for the pH 2.4, 11%-60 TFE samples (Table 4.1).

Plots of the ellipticity at 222 nm ($[\theta]_{222}$) vs. [TFE] for both pH values show roughly sigmoidal behavior (Figure 4.2C), but at high TFE, the signal for pH 7.5 samples is weak compared to pH 2.4 samples. The estimated number of helical residues, based on $[\theta]_{222}$, is ~50% higher in the acidic solution (Table 4.2). Examination of additional solution conditions reveals that the helicity is stable at high pH, but drops rapidly below pH ~3.5 (Figure 4.2D).

A "transition diagram" (Kuznetsova, et al., 2004) plot of the pH 2.4 CD data shows two linear segments that correspond to sets of spectra that share isodichroic points (Figure 4.3). The existence of two isodichroics and two linear segments indicates that EGFP is likely sampling at least three secondary structure conformations, which include a low-TFE, PPII-like state ("U"), a high TFE, helical state ("F") and an intermediate conformation ("I"). The point corresponding to the 10% TFE sample is located slightly above the point of intercept of the two lines.

Points derived from the 0-17% TFE, pH 7.5 spectra are clustered in a region of the transition diagram that corresponds to the native β-can fold ("N"). These points may lie along a straight line, although the low variability among these spectra makes

Table 4.2. Estimates of the number of EGFP residues adopting helical structure in the presence of 60% TFE, calculated using the method of Luo and Baldwin with their 50% TFE parameters (Luo and Baldwin, 1997). The difference, Δ, between the estimates at pH 2.4 and pH 7.5 is also shown. The errors reflect experimental uncertainties.

	# helical residues
pH 2.4	161 ± 9
pH 7.5	106 ± 6
Δ	55 ± 11

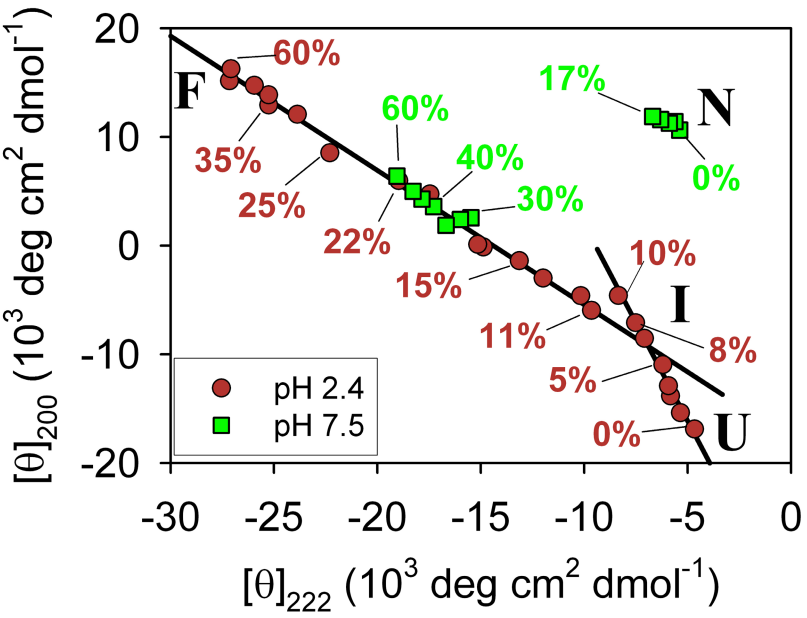

Figure 4.3. Transition diagram (Kuznetsova, et al., 2004) constructed from the EGFP CD spectra in Figure 4.2A-B. For clarity, some points are labeled with their [TFE] and the labels are color coded to show pH. The solid lines show fits to the pH 2.4 points whose spectra share isodichroic points (Figure 4.2A insets).

this uncertain. We previously found that EGFP remains fluorescent immediately after heating at pH 7.5 and below ~20% TFE (Figure 4.1), and so it seems likely that any conformational changes that occur at low TFE affect loop regions, rather than the core β-can. In contrast, the loss of fluorescence observed for >30% TFE, pH 7.5 samples is associated with the formation of significant amounts of non-native helical structure (Figure 4.2B), and points derived from the 30-60% TFE spectra lie along the middle portion of the I ↔ F transition line.

We analyze our CD data using principal component analysis (PCA) to obtain more information about the conformations being sampled (Figure 4.4). A Scree plot (Cattell, 1966) constructed from the pH 2.4 curves reveals two significant factors, i.e. three distinct conformational states (Figure 4.4A). Projection of the CD data onto the first two PCA basis vectors (Figure 4.4B) results in a full-spectral transition diagram, which is analogous to Figure 4.3 (Anderson, et al., 2010). Additional PCA results, including discussion of the basis vectors and analysis of the pH 7.5 data from Figure 4.2B, can be found in Appendix C. Notably, our pH 7.5 PCA results were also consistent with the protein sampling 3 conformational states, within the resolution of our data.

The point of intersection of the two straight line fits shown in Figure 4.4B provides an estimate of the CD spectrum of the intermediate state (Anderson, et al., 2010). This inferred I state spectrum (Figure 4.4C) has double minima which are suggestive of α-helical structure, but the low overall signal magnitude and the shift of the lower-wavelength peak from the expected 208 nm to ~204 nm indicates that the protein is partially disordered. Deconvolutions of the U and I state spectra via several algorithms are consistent with an increase in helicity for the I state compared to the pH 2.4, 0%TFE conformation (Appendix C and Table C.1). However, the deconvolution results are somewhat unreliable, especially for the disordered and partially structured

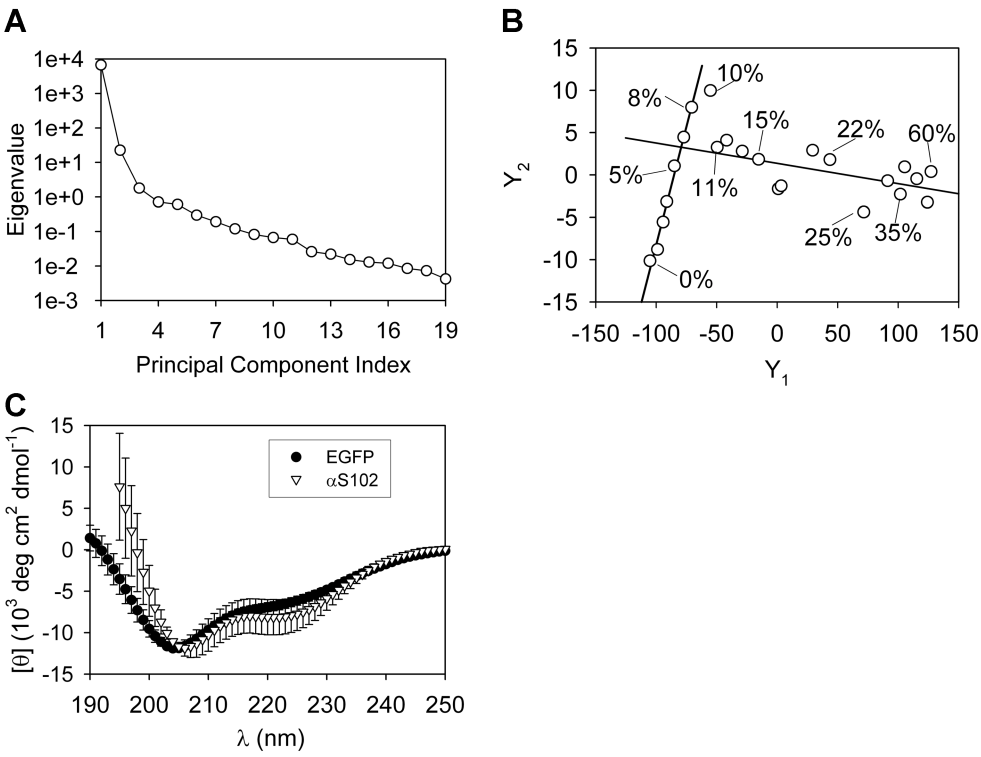

Figure 4.4. Analysis of the EGFP CD data in Figure 4.2A using PCA. (A) Scree plot (Cattell, 1966) showing the eigenvalue magnitudes for the transformation. (B) Projection of the CD spectra onto the first two principal component axes (Y_i denotes the i^{th} principal component). The solid lines show linear fits to points whose curves share isodichroics (Figure 4.2A insets). For clarity, some points are labeled with their [TFE]. (C) Reconstruction of the I state spectrum for EGFP, compared to the αS102 results from (Anderson, et al., 2010).

cases. Intriguingly, the reconstructed EGFP intermediate state curve is very similar to the I state spectrum for αS102 (Figure 4.4C), which also may be partly helical (Anderson, et al., 2010).

By fitting our CD data to a linear combination of the inferred intermediate state spectrum and the low and high TFE curves, we can obtain an estimate of the population of the protein in each state as a function of [TFE] (Figure 4.5A symbols). Note that these plots tend to underestimate the I state population (Anderson, et al., 2010). The data is noisy at high TFE, which likely reflects the similarities between the U and I spectral shapes. When we fit to only two conformations (U and I for 0-8% TFE, and I and F for 10-60% TFE), the data appears smoother (Figure 4.5A lines). The intermediate conformation appears to be maximally populated near 8% TFE. Both the 3-state and the 2-state fits are very good (NRMSD < 0.05) for the 0-5% and the 11-60% TFE data, but are somewhat poor (NRMSD ~ 0.1 to 0.25) for the 8-10% TFE samples (Figure 4.5B). The observation that points derived from the ~8-10% TFE spectra appear above the intersection of the U↔I and I↔F lines in Figure 4.3 and Figure 4.4B, along with the fact that these spectra do not fit well to a linear combination of the U, I, and F states, indicates that there may be additional subtle structural changes occurring for EGFP. These rearrangements may reflect the presence of multiple "intermediate" conformations. Alternatively, these anomalies may be a result of a small degree of protein oligomerization in these samples, experimental noise or fitting errors.

Moderate TFE concentrations promote EGFP aggregation, but tertiary structure and electrostatic repulsion are barriers to fibrillization: In Figure 4.6A, we show light scattering data for EGFP incubated for 24 hours at 37 °C in various solution conditions. The scattering intensities reflect relative amounts of aggregate production. At pH 2.4, with no added salt, aggregation is minimal over the entire

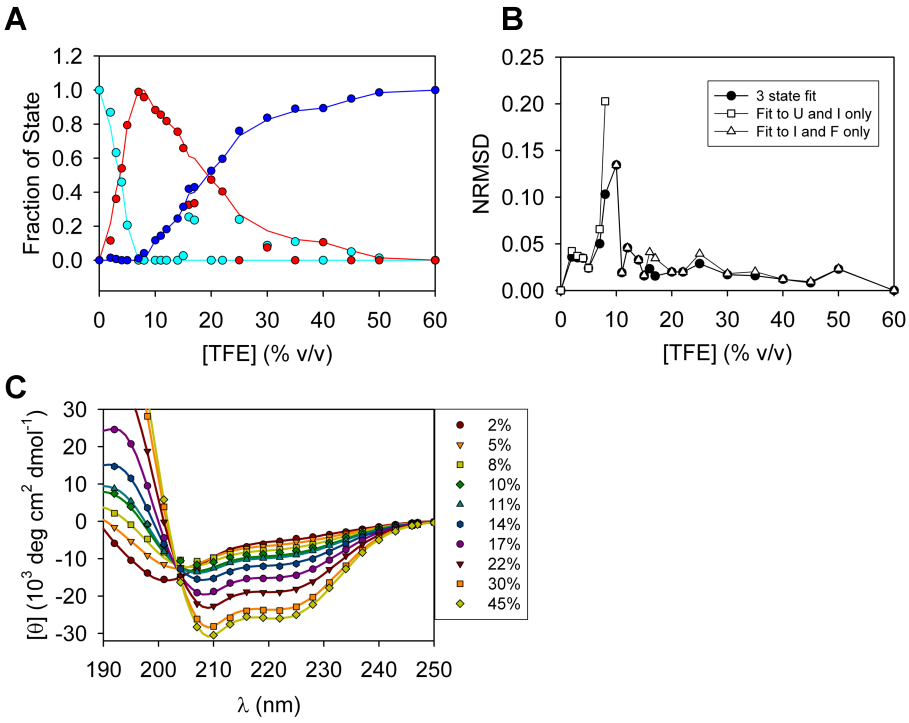

Figure 4.5. Results of fits of the pH 2.4 CD spectra (Figure 4.2A) to linear combinations of the 0% TFE ("U"), 60% TFE ("F"), and inferred I state spectra. (A) Fractions of EGFP in the three states U (cyan), I (red) and F (dark blue) as a function of [TFE], resulting from the fits, assuming the presence of three (symbols) or two (lines) states. For the two-state fits, the fraction of the F state is assumed to be zero for the 0-8% TFE samples, while the fraction of the U state is assumed to be zero for the 10-60% TFE data. (B) The NRMSD deviations between the experimental spectra and the fits used to obtain A. (C) A comparison of the experimental spectra (symbols) to the fit results (lines) for some samples. The TFE concentrations of the selected samples are shown in the legend.

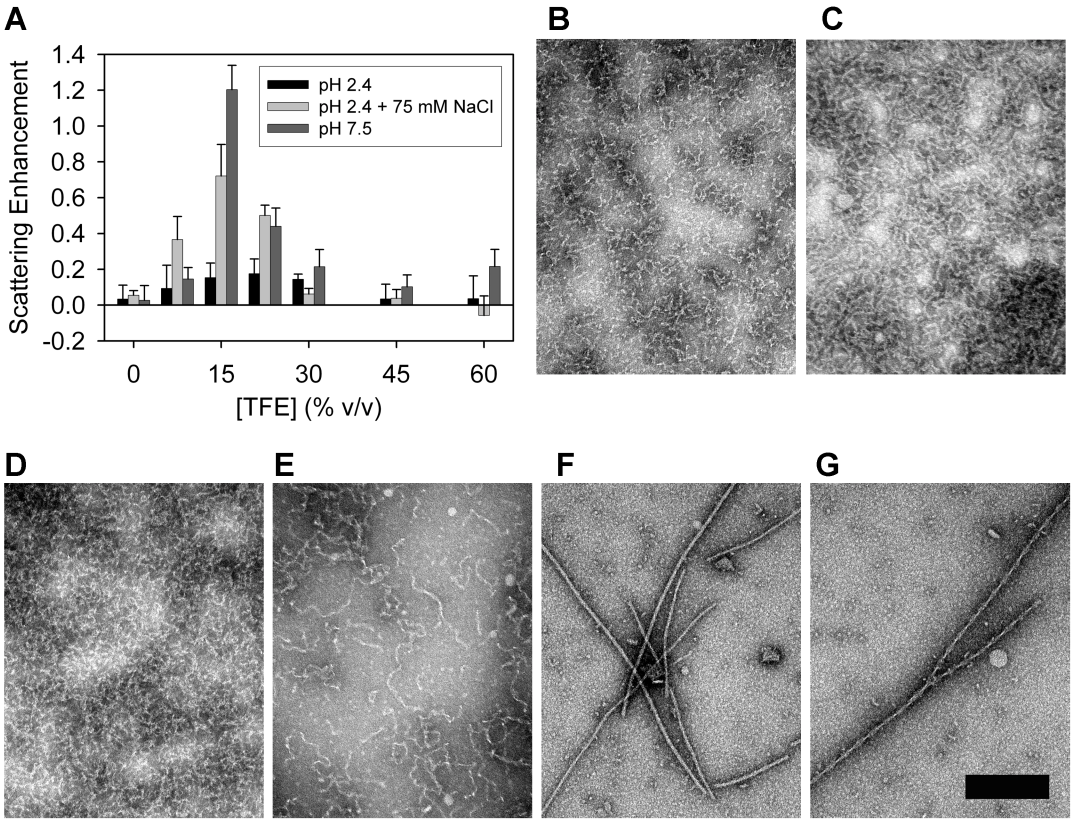

Figure 4.6. EGFP aggregation vs. [TFE]. (A) Visible (600 nm) light scattering signal from 50 μM EGFP at pH 2.4, pH 7.5, and pH 2.4 with 75 mM NaCl. The samples were incubated for 24 hours at 37 °C in the presence of 0, 7.5, 15, 22.5, 30, 35, and 60% TFE. (B-G) TEM images of EGFP aggregates gown at 37 °C in various solution conditions. The scale bar is 200 nm wide and all images are shown at the same magnification. (B) Flexible thin fibril aggregates observed after 24 hours incubation in quiescent conditions for 50 μM EGFP at pH 2.4, with 15% TFE and 75 mM NaCl. (C) Flexible thin fibrils observed after 24 hours incubation in quiescent conditions for 50 μM EGFP at pH 7.5 with 15% TFE. (D) Similar to B, except the solution contained 7.5% TFE. (E) Similar to C, except the solution contained 45% TFE. (F-G) Rigid, amyloid-like aggregates found after incubating 50 μM EGFP for 7 weeks with shaking at pH 2.4 in the absence of TFE or added salt.

0-60% TFE range. However, the addition of 75 mM NaCl to the pH 2.4 solution leads to aggregation enhancement for samples containing 7.5-30% TFE.

Aggregation at pH 2.4 and 75 mM NaCl appears to be roughly correlated with increased population of the I state (Figure 4.5A, Figure 4.6A). The maximal scattering signal may be slightly shifted rightward to ~15% TFE, compared to the ~8% TFE maximum we predict for the I state population, although the differences are within the measurement uncertainties.

For pH 7.5 samples, aggregation is low for 0-7.5% TFE samples, increases sharply at 15% TFE, and then decreases at higher TFE. In Figure 4.1, we showed that tertiary structure disruption occurred above 15% TFE for samples in these solution conditions. Therefore, EGFP aggregation at low-to-moderate TFE appears to be associated with tertiary structure disruption. However, very high TFE conditions stabilize monomeric protein.

The morphology of EGFP aggregates depends on solution conditions: Figure Figure 4.6B-E shows Transmission Electron Microscope (TEM) images of EGFP aggregates from identical solutions as those examined in Figure 4.6A. Solutions containing TFE typically showed thin fibrillar aggregates, which often clumped together. Rigid, amyloid-like fibrils were sometimes observed after extended incubations (Figure 4.6F-G), although fibril growth in these solutions was somewhat sporadic and often required very long (> 1 month) incubations. Additional images of EGFP aggregates grown in various solution conditions can be found in Figure C.4. Amyloid-like fibril growth most frequently occurred in pH 2.4 samples without added salt or TFE, but a combination of thin flexible fibrils and rigid, amyloid-like fibrils could be observed in some samples containing TFE at pH 7.5 (Figure C.4K-L).

4.3 Discussion

We find that TFE-induced EGFP aggregation requires tertiary structure disruption and is also correlated with secondary structural changes of the denatured protein. For acid-denatured EGFP, we detect three secondary structural conformations via CD. Increased aggregation roughly coincides with population of a partially structured intermediate state. For pH 7.5 samples, aggregate production is peaked at TFE concentrations where the native tertiary structure is disrupted but the helicity remains relatively low. Our observations for acid-denatured EGFP are qualitatively similar to studies of the natively disordered protein αS (Chapters 2-3), although the TFE concentrations at which structural changes and aggregation occur are different for the two proteins. We hypothesize that desolvation may initiate the conformational changes and aggregation at moderate TFE that are observed for numerous proteins and peptides. However, details of protein sequence and solution conditions will also affect aggregation reactions. We discuss our EGFP data in the context of our previous αS experiments and the extensive literature on fluoroalcohol-induced protein and peptide aggregation.

Population of an intermediate secondary structural state is correlated with aggregation for acid-denatured EGFP: The far-UV CD spectrum of EGFP at pH 2.4 shows the negative, PPII-like peak near 200 nm that is typical for disordered proteins (Figure 4.2A). The existence of two distinct isodichroics in the pH 2.4 CD spectra for EGFP, along with the transition diagram representation of our data (Figure 4.3) and our PCA results (Figure 4.4), indicates that the protein samples at least three conformational states (on a residue-by-residue basis) in the presence of 0-60% TFE. Increasing [TFE] from 0% to ~ 8% results in loss of PPII-like signal in favor of the formation of an intermediate conformation. Above ~11% TFE, we observe two-state

coexistence between the intermediate and a highly α-helical state. The population of the intermediate is maximal near 8% TFE (Figure 4.5A).

We previously observed similar conformational changes for αS, including the formation of a partially structured intermediate at moderate TFE (Anderson, et al., 2010). However, the population of the intermediate state was peaked near 15% TFE for αS, as opposed to ~8% TFE for EGFP. Although we initially measured αS structural transitions at 25 °C and pH 7.5 (Anderson, et al., 2010), our variable-temperature data indicated that the TFE concentration at which the αS intermediate conformation is maximally populated is independent of temperature and is similar at low and neutral pH (Chapter 3). Therefore, effects other than electrostatic repulsion or temperature are probably responsible for the differences in relative populations of the three conformations between the two proteins.

The fraction of EGFP in the PPII-like U state falls off rapidly at low TFE (Figure 4.5A), compared to the previous observation for multiple αS variants (Anderson, et al., 2010). This difference is also apparent in the low-TFE behavior of the CD signal near 200 nm (Figure 4.7). For simplicity, we compare $[\theta]_{200}$ for EGFP with the signal for the human αS C terminal truncation mutant αS102 (Chapters 2-3). The ~200 nm EGFP peak diminishes rapidly with TFE addition, while the αS102 signal is more stable at low TFE, even when the pH and temperature of the solution is varied.

At pH 2.4, both αS102 and EGFP are unfolded and they have a similar net charge per residue (approximately +0.14*e* for αS102 and +0.15*e* for EGFP) (Putnam, 2006). In addition, they contain a comparable fraction of nonpolar amino acids (41% for αS102 and 37% for EGFP). However, αS102 contains a relatively large proportion of alanine residues, while EGFP has more phenylalanine, tyrosine, leucine and isoleucine residues. As we discussed in Chapter 3, the PPII conformation is thought to

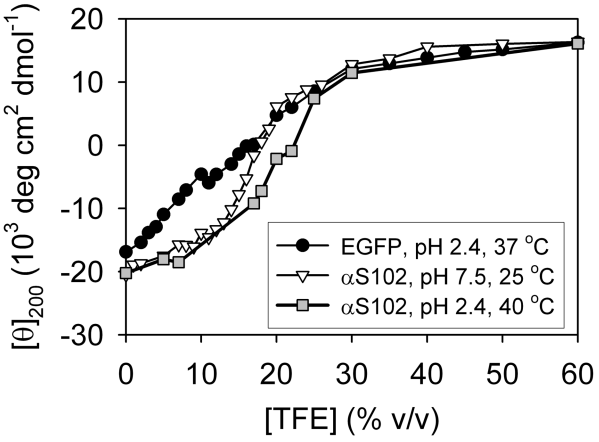

Figure 4.7. A comparison of the 200 nm negative peak signal for EGFP with the αS102 data from (Anderson, et al., 2010) and Chapter 3**.**

be stabilized by water-protein hydrogen bonding, in particular water-backbone hydrogen bonds (Adzhubei and Sternberg, 1993; Rucker, et al., 2003). The addition of low concentrations of TFE may reduce protein-solvent interactions leading to structural changes and aggregation. It may be that bulky nonpolar residues in EGFP restrict water access to the protein backbone, or the high surface areas of these residues might favor adoption of a more solvent-shielded conformation at low TFE. The sequence context of nonpolar residues could also affect a protein's propensity to adopt PPII structure.

Aggregation of acid-denatured EGFP is minimal in low ionic strength solutions (Figure 4.6A). However, the addition of 75 mM NaCl enables significant aggregation in solutions containing ~7.5-30% TFE. It is likely that electrostatic repulsion limits aggregation for the pH 2.4 samples. The magnitude of the net charge on the EGFP is predicted to be +36*e* pH 2.4, compared to -7.7*e* at pH 7.5 (Putnam, 2006). Charge-charge repulsion might act as a kinetic barrier to aggregation, and could also destabilize oligomeric conformations. Salt can partially screen these repulsive forces.

We predict that the I state population is maximal near 8% TFE (Figure 4.5A). However, peak aggregation in pH 2.4, 75 mM NaCl solutions may be shifted slightly rightward to ~15% TFE (Figure 4.6A), although the differences in scattering signals are within the measurement uncertainties. Changes in the viscosity and dielectric constant of the TFE-water mixtures (see Chapter 1) may affect oligomerization rates for proteins in aggregation-prone states. It is also possible that the kinetic barrier to aggregation arising from water-protein interactions is larger than the barrier due to interactions that occur in a TFE-rich environment.

Native EGFP tertiary structure is protective against aggregation: At pH 7.5 and 37 °C, EGFP native structure remains intact for ~1 day below 15% TFE (Figure

4.1). We find that aggregate production is relatively low for 0-7.5% TFE samples during this time period (Figure 4.6A), but fibril production increases sharply for ~15-30% TFE samples. Therefore, tertiary structure appears to protect against EGFP aggregation.

Tertiary structure disruption is required for TFE- induced aggregation of many proteins (Chiti, et al., 1999; Grudzielanek, et al., 2005). In general, the TFE concentrations needed for denaturation depend on solution conditions and the stability of the native fold. Chiti et al. observed that mutations that destabilize the native state of acylphosphatase reduce the TFE concentration required to induce aggregation (Chiti, et al., 2000). Similar effects have been observed for α-Chymotrypsin, which aggregates at relatively low TFE concentrations when the native fold of the protein is destabilized by low pH, high salt, or elevated temperature conditions (Rezaei-Ghaleh, et al., 2007). For EGFP, we find that denaturation requires higher TFE concentrations for samples at room temperature compared to 37 °C (Figure C.3A), and therefore we predict that lower temperatures should shift the EGFP aggregation peak toward higher [TFE].

Denaturation rates in TFE appear to be strongly dose-dependant. Loss of EGFP fluorescence occurs within seconds above 35% TFE, while tertiary structure is stable for >20 minutes below 17% TFE (Figure 4.1, Figure 4.2). Unfolding of 15-20% TFE samples occurs over a period of several hours to one day (Figure 4.1 and Figure C.3B). We also observed by eye that pH 7.5 EGFP samples containing 5% TFE appeared bright green for > 9 weeks, while 10% TFE samples became clear after 2 week incubations at 37 °C.

At high TFE, preferential solvation likely leads to a complete coating of the protein by TFE (see Chapter 3). The fact that tertiary structure disruption is rapid above 30% TFE where the F state population is nearly maximized (Figure 4.5A),

suggests that preferential solvation increases the unfolding rate. The native state may be destabilized in the TFE-rich environment, or kinetic barriers to unfolding may be decreased.

Studies of protein unfolding at high (>~30%) TFE concentrations have suggested that native state destabilization drives denaturation. Mutations and solution conditions that lessen the native state stability facilitate unfolding (Chiti, et al., 2000; Rezaei-Ghaleh, et al., 2007). Moreover, Kumar, et al. found evidence of TFE molecules penetrating into the core of β-lactoglobulin, possibly leading to loosening of the protein's tertiary structure (Kumar, et al., 2003). In addition, a TFE-solvated protein is not likely to be stabilized by hydrophobic forces because water is excluded from the surface of the protein, and this may tend to destabilize the native state compared to transition states or folding intermediates. The reduced surface tension for TFE compared to water may also reduce the free energy gain for formation of a compact native state (Del Vecchio, et al., 2003).

However, denaturation alone is not sufficient for EGFP aggregation. Both pH 7.5 and pH 2.4 samples show reduced aggregation at high TFE (Figure 4.6A). As we discussed in chapter 3, preferential solvation of protein molecules by TFE might stabilize monomeric protein because of increased surface areas available for TFE accumulation (Moelbert, et al., 2004). Or, changes in solvent free energy may reduce the solvent entropy gain for release of solvent molecules from the protein solvation layer during oligomerization (Eggers, 2011). TFE-protein interactions may also inhibit aggregation in the TFE-rich environment.

The helicity of the high TFE state is pH-dependent: We previously found that, in the presence of >~30% TFE, the helicity of αS variants is slightly increased in acidic conditions (Chapter 3). EGFP shows similar but more dramatic behavior, experiencing a sharp increase in the magnitude of its CD spectrum below pH ~3.5

(Figure 4.2D), which is consistent with a ~50% increase in helical content (Table 4.2). The ellipticity shift coincides roughly with the pKa of acidic residues, although presence of the fluoroalcohol may slightly modify buffer and protein ionization constants (Espinosa, et al., 2002; Zagorski and Barrow, 1992). As discussed in Chapter 3, pH-dependent changes in helicity may be due to short- or long-range electrostatic interactions that reduce flexibility and favor compact structures (Fan and Mayo, 1995; Valerio, et al., 2008). Helix stop signals might also be altered by pH in solutions containing TFE (Lawrence and Johnson, 2002; Rohl, et al., 1996).

It is unlikely that an α-helix can propagate through the EGFP chromophore, which involves a covalent bond between Thr65 and Gly67 backbone groups (Reid and Flynn, 1997). At pH 2.4, ~160 residues are helical (Table 4.2), and therefore structure formation cannot involve only the portion of the protein N terminal to the chromophore. It is possible that the C terminal 172 residues are involved in helix formation. However, a second helix could form in the N terminus, or multiple short segments could form in various parts of the protein. The EGFP protein is not natively helical and so it seems unlikely that a single contiguous helix would be stable even at high TFE. It is possible that the pH-dependent differences in helicity involve changes in the number or length of various helical segments. Higher-resolution information will be necessary to identify the precise interactions responsible for the pH-dependence of the high TFE structures.

The reduction in aggregation at high TFE appears fairly similar for both pH 7.5 and pH 2.4 solutions, although the helicity of the high-TFE, pH 2.4 state is much greater than that for pH 7.5 solutions (Table 4.2). Preferential solvation and TFE-protein interactions could reduce aggregation in the absence of secondary structure formation. Alternatively, it is possible that the most aggregation-prone regions of the protein are buried in both pH conditions. Additional information regarding the

locations of helical structure for EGFP could be helpful in determining the factors responsible for the solubility in high TFE solutions.

TFE induces the formation of flexible fibrils: The TFE-induced aggregation behavior for acid-denatured EGFP is qualitatively similar to that for αS (Anderson, et al., 2010). In the absence of TFE, EGFP can form classic amyloid-like fibrils after long incubation periods (Figure 4.6E-F), while moderate [TFE] leads to the immediate formation of flexible, thin fibrillar aggregates (Figure 4.6B,D). At pH 7.5, ~15-30% TFE also causes the rapid formation of thin, fibrillar aggregates (Figure 4.6C,F). However, the ultrastructures of TFE-induced aggregates is different for EGFP and αS. EGFP fibrils are thinner (~9 nm compared to ~ 18 nm), and their ultrastructures appear less helical than αS fibrils'. They also seem to be shorter and to clump together more often.

TEM and atomic force microscopy images of TFE-induced aggregates from additional proteins reveal a variety of species, including rigid amyloid, flexible fibrils, annular structures and amorphous aggregates (Anderson, et al., 2010; Chaudhary, et al., 2009; Fezoui and Teplow, 2002; Grudzielanek, et al., 2005; Pallarès, et al., 2004). Therefore, aggregate morphology appears to be strongly sequence-dependent.

EGFP is frequently used as a label in biological experiments. The EGFP aggregation pathways we report here require extreme solution conditions and are not likely to interfere with most studies. However, the ability of EGFP to form fibrils could complicate interpretation of some experiments that use fluorescent protein tags to study amyloid aggregation reactions, especially in potentially denaturing conditions (see also Appendix D).

Desolvation may be a general mechanism underlying TFE-induced protein aggregation: In Chapter 3, we proposed that desolvation may drive both the conformational changes and the aggregation behavior of αS in TFE. We hypothesized

that water-protein interactions stabilize PPII structure at low TFE, while α-helix induction at high TFE involves transfer of the protein into a TFE-rich environment as a result of preferential solvation. At intermediate [TFE], we suggested that both TFE-protein and water-protein interactions are minimized, leading to desolvation-driven fibril formation. Our basis for this hypothesis included our measurements of the secondary structure of αS in >99% TFE, which revealed that the protein environment is basically "TFE-like" above ~30% TFE, where aggregation is reduced, as well as our observation that αS conformational changes induced by low TFE are very similar to heat-induced transitions, which are thought to reflect loss of protein-water hydrogen bonds, leading to PPII destabilization (Adzhubei and Sternberg, 1993; Kelly, et al., 2001; Rucker, et al., 2003). Moreover, we drew on multiple literature sources which suggest that TFE coats or binds to proteins at higher concentrations (Diaz, et al., 2002; Fioroni, et al., 2002; Walgers, et al., 1998). Solvation barriers are also known to affect aggregation reactions, and therefore desolvation is a plausible explanation for TFE-induced fibrillization (Balbirnie, et al., 2001; Mukherjee, et al., 2009; Rauscher, et al., 2006; Zhang and Yan, 2008).

Our data for acid-denatured EGFP is consistent with our αS results. In particular, we detect a crossover between PPII-like structure at low TFE and helical states at high TFE. The low TFE behavior, featuring loss of PPII structure, is consistent with dehydration leading to loss of water-protein interactions. Acid-denatured EGFP appears to be dehydrated more readily than αS, which may be due to decreased water accessibility to the protein backbone as a result of EGFP's higher proportion of bulky, nonpolar amino acids. The high number of phenylalanine and leucine residues may also decrease the number of water contacts per unit surface area for EGFP, facilitating dehydration.

Molecular dynamics simulations have found that proteins that adopt PPII conformations are more strongly hydrated and less likely to form amyloid aggregates (Rauscher, et al., 2006). It is unclear whether destabilization of PPII structures involves steric barriers that decrease water accessibility to the protein backbone, or whether large nonpolar residues favor collapsed states. In any case, the position of the aggregation peak for unfolded proteins is likely to correlate with backbone hydration. Sequences favoring more extended, water-accessible conformations should experience maximal aggregation at higher TFE concentrations.

Preferential solvation of EGFP and αS likely occurs at >~30% TFE, but the conformation of a protein in the TFE-rich environment depends on pH and temperature (Figure 4.2, see also Chapter 3). Stabilization of helical structure at high TFE may involve direct TFE-protein interactions, which could also resist aggregation. Chatterjee and Gerig observed long-lived TFE-peptide interactions, which were consistent with either TFE-peptide hydrogen bonding or hydrophobic contacts (Chatterjee and Gerig, 2007). They also found that increasing temperature reduces the lifetime of peptide-fluoroalcohol complexes (Chatterjee and Gerig, 2006; Chatterjee and Gerig, 2007), and we similarly observed that TFE-induced helical structure is disrupted by heating for αS (Chapter 3). However, the precise structure of the protein in the TFE-rich environment appears to have little to no effect on aggregation reduction at high TFE.

We find that EGFP tertiary structure impedes aggregation, but once tertiary structure is disrupted, pH 7.5 EGFP behaves qualitatively like acid-denatured protein and αS. In particular, aggregate production is correlated with reduced α-helicity, which indicates that aggregation-prone, pH 7.5 conformations are not fully coated by TFE molecules. Therefore, multiple protective interactions, including intact tertiary structure and solvation barriers, must be overcome to initiate aggregation.

Our previous αS results (Chapters 2-3) and our EGFP data indicate that desolvation is a plausible mechanism for TFE-induced aggregation of these proteins. However, we do not directly measure protein-solvent interactions. Because changes in solvent structure and protein conformation are likely to occur in parallel, it may be difficult to separate correlation from causation in the aggregation reaction (see also Chapters 1 and 3). Investigation of simple alcohols, which may cause dehydration but not preferentially solvate the protein to the same extent as fluoroalcohols, could be instructive. Experiments and simulations that directly address the hydration status of proteins might also help isolate the primary factors driving aggregation in the presence of TFE (Rauscher, et al., 2006; Zhang and Yan, 2008). Finally, we note that the aggregation pathway in solutions containing TFE may be different than the pathway in physiological conditions. It is not clear whether TFE-induced dehydration may be similar to *in vivo* processes. Structural intermediates may also play a more significant role in aqueous solutions than in the presence of alcohols.

4.4 Conclusion

We have observed a correlation between TFE-induced secondary structural transitions and aggregation for EGFP, and we hypothesize that changes in protein-solvent interactions underlie both phenomena. The structural changes for acid-denatured EGFP are qualitatively similar to those for αS, and are consistent with dehydration leading to loss of PPII structure at low TFE. High concentrations of TFE induce the formation of α-helical structure as a result of preferential solvation. We propose that removal of these solvation barriers to aggregation initiates the formation of fibrillar aggregates.

Protein-solvent interactions impede aggregation, whether the local environment near the protein molecule is water-like or TFE-rich. In addition,

electrostatic repulsion and intact tertiary structure reduce fibrillization. We propose that fluoroalcohol-induced protein aggregation involves removal of multiple protective factors, rather than the formation of particular aggregation-prone conformations.

4.5 Materials and Methods

Reagents and solutions: All chemicals were reagent grade and were as described in Chapter 3. Our pH measurements refer to aqueous samples; we did not correct our measurements to account for TFE effects on ionization constants of protein, water, or buffer components. These changes are likely to be small at low pH but can be significant at higher pH (Espinosa, et al., 2002; Zagorski and Barrow, 1992). Samples labeled pH 2.4 contained 10 mM phosphoric acid, while samples labeled pH 7.5 contained 10 mM sodium phosphate buffer, which was pH 7.5 at room temperature in the absence of TFE. Additional solutions conditions are specified in the text.

EGFP expression and purification: Enhanced GFP derived from wild-type *A. Victoria* GFP (GFPmut1) with substitutions F64L and S65T (Cormack, et al., 1996) was synthesized by Cynthia Kinsland and the Cornell University Life Sciences Core Laboratories Center Protein Production Facility. Briefly, the plasmid pEGFPcasp6.XF1, a T7lac driven expression plasmid encoding an N-terminal hexahistidine tag and a Caspase 6 cleavage site on EGFP, was transformed into BL21Star(DE3) (Invitrogen), a plasmid containing the rare tRNA accessory plasmid from Rosetta2 (Novagen). Cells were grown in 1 L of ZY505 under dual ampicillin and chloramphenicol selection at 37°C. Once the OD600 had reached 0.6, overexpression was induced with 1 mM IPTG and growth was continued for another 3 hours before the cells were harvested by centrifugation. Cells were resuspended in an IMAC binding buffer (20 mM Tris, pH 8.0, 30 mM imidazole, 500 mM NaCl) and

lysed by passage through an Avestin C3 homogenizer at 20-25 kpsi. Cell debris was removed by centrifugation and the cleared lysate was loaded onto a 5 mL HisTrap HP column (GE Healthcare). The column was extensively washed with IMAC binding buffer and IMAC wash buffer (as binding buffer except the concentration of imidazole was raised to 100 mM) before being eluted (as binding buffer except the concentration of imidazole was 500 mM). Fractions were analyzed by SDS-PAGE and the fractions containing the protein of interest were combined and concentrated. The protein was further purified by gel filtration on a Superdex 200 column, using 20 mM Tris, 150 mM NaCl, pH 7.5. The protein eluted as essentially one sharp peak with a slight leading shoulder. SDS-PAGE analysis showed that the leading shoulder contained a variety of contaminants, so this area was excluded when pooling fractions. All combined fractions were dialyzed against PBS with 5% glycerol, followed by buffer exchange into water or 1 mM pH 7.5 NaPhos buffer using Amicon YM-10 spin filters (Millipore). Protein stock solution concentrations were obtained via absorbance spectroscopy following the procedures described in Appendix D.

Fluorescence emission and light scattering measurements: Fluorescence scattering experiments were performed using a QuantaMaster fluorescence spectrofluorometer (Photon Technology International). Correction for lamp fluctuations was automated by the vendor-supplied software. The sample temperature was maintained during fluorescence measurements using a NesLab Endocal RTE-110 chiller/circulator (Thermo Scientific).

Fluorescence emission measurements were obtained using 0.3 μM EGFP samples. The fluorophores were excited at 460 nm and emissions were collected from 480 to 580 nm. The emission spectra were integrated and normalized to the integrated signal from 0.3 μM pH 7.5 EGFP solutions in PBS (10 mM NaPhos, 154 mM NaCl)

at 25 °C. In each case, three identical samples were measured and their standard deviations calculated in order to determine the measurement variability.

For scattering measurements, 600 nm light was used in order to avoid EGFP absorption. The scattering angle was 90° and the same quartz cuvette was used to obtain all the data. Prior to measurement, 50 μM EGFP samples, along with baseline solutions containing identical ingredients excepting the protein, were maintained under quiescent conditions for 24 ± 2 hours in a 37 °C incubator. For each measurement we report, data was taken for three identical samples and three baseline solutions. The sample signals were normalized to the baseline signals and the uncertainties in the measurements were based on the standard deviations of the sample and baseline signals.

Circular dichroism (CD) spectroscopy: Far-UV CD measurements were performed using an Aviv 400 Circular Dichroism Spectrometer (Aviv Biomedical). Data was collected at 1 nm intervals with a scan speed of one second per nanometer, using a 1 nm bandwidth. Spectra for 0.3 μM EGFP were obtained in 1 cm quartz cuvettes. Buffer-only baseline samples were measured and subtracted from the protein spectra and noise was reduced using a smoothing routine in the instrument software.

CD samples were mixed at room temperature. Immediately prior to the measurement, TFE was added and the samples were placed into the instrument sample holder at 37.0 ± 0.1 °C. Temperature equilibration took approximately one minute. Two sets of three spectra each were obtained and averaged to verify that the CD signals were stable during the measurement interval (see Appendix C). Principal component and other analysis of the CD data was performed as described in Appendix A and (Anderson, et al., 2010).

Transmission electron microscopy (TEM) imaging of EGFP aggregates: Samples requiring quiescent conditions were maintained at 37 °C using an incubator,

while agitated samples were incubated using a benchtop orbital shaker operating at 200 RPM and 37°C. Sodium azide (0.02 % w/v) was added to solutions incubated for longer than one day. Images were obtained as described previously (Anderson, et al., 2010). In order to prevent grid damage, samples containing >15% TFE or high concentrations of aggregates were diluted with water or buffer prior to placement on the TEM grids.

APPENDIX A

VERIFICATION AND ANALYSIS OF CIRCULAR DICHROISM DATA FOR SUB-MICROMOLAR CONCENTRATIONS OF ALPHA-SYNUCLEIN

Verification that the 0.5 μM CD spectra are representative of monomeric α-synuclein (αS)

We investigate time- and concentration- dependent differences in CD signals to verify that the curves we report in Figure 2.4A and Figure 2.5A-D are appropriate estimates of the αS monomer spectra. We use the normalized root mean square deviation (NRMSD) parameter (Brahms and Brahms, 1980; Mao, et al., 1982; Whitmore and Wallace, 2008) to quantify differences in CD data. The NRMSD of sample 1 vs. sample 2 is given by:

$$NRMSD = \left\{ \frac{\sum_{i=1}^{N} \left[[\theta]^{S1}(\lambda_i) - [\theta]^{S2}(\lambda_i) \right]^2}{\sum_{i=1}^{N} \left[[\theta]^{S1}(\lambda_i) \right]^2} \right\}^{1/2} \quad \text{(A1)}$$

where λ is wavelength, $[\theta]^{S1}(\lambda)$ and $[\theta]^{S2}(\lambda)$ are the experimental CD spectra for samples 1 and 2, and N is the number of data points in the spectrum. The NRMSD parameter is generally used to measure goodness of fit in CD data deconvolution, rather than to compare experimental curves. NRMSD values below 0.1 are generally thought to indicate good agreement for fitting purposes (Whitmore and Wallace, 2008). However, we observe NRMSD values of 0.01 – 0.03 for repeated measurements of identical, stable samples under our standard experimental conditions. Furthermore, uncertainties in protein concentration and baseline offsets contribute additional errors. Therefore, when the NRMSD is used to compare experimental data sets, values slightly higher than 0.1 may occur for similar samples.

Because the distribution of monomer vs. oligomer protein in solution is concentration-dependent, we first investigate oligomerization by comparing the CD spectra we measure at 0.5 μM to spectra for 5 μM αS. Below ~ 10% and above ~24% TFE, the shapes of the CD spectra are similar at both protein concentrations, and the NRMSD deviations between these samples are relatively low (< 0.15) (Figure A.1A). Since oligomerization is expected to result in secondary structure changes, we conclude that no oligomerization is detected by this method at low or high TFE. However, for ~12-23% TFE, we observe concentration-dependent differences in the CD spectra, indicating that oligomerization is likely occurring at the higher concentration, and necessitating further evaluation at the lower concentration.

In order to assess whether our data at 0.5 μM protein concentration represent a good approximation of the monomer curve over the full TFE range, we also consider time-dependent changes in the CD spectra. First, we note that the αS mutants we study show a wide range of of oligomerization rates (Table 2.3 and Figure 2.9B), but experience similar structural transitions at 0.5 μM. Also, we showed that at 15% TFE, oligomerization takes place on a time scale of minutes to hours for 2 μM αS variant samples (Table 2.3 and Figure 2.9B), and we expect the oligomerization rate to be slower at lower concentrations. To verify this, we measure time-dependent changes in our CD signal for our 0.5 μM samples, comparing spectra measured 5 minutes vs. 15 minutes after sample preparation (Figure A.1B). The NRMSD values are all fairly low, although they tend to show a peak at ~12-22% TFE. For WT, A30P, A53T, and E46K αS, the maximum deviations occur at 15-16% TFE, while the low-TFE values are large for αS102, which is probably due to the reduced CD signal magnitude from the disordered conformer of this smaller protein compared to full-length αS. In addition, the NRMSD values near 15% TFE are largest for E46K αS and smaller for A30P αS and αS102. However, because we observe nearly identical structural

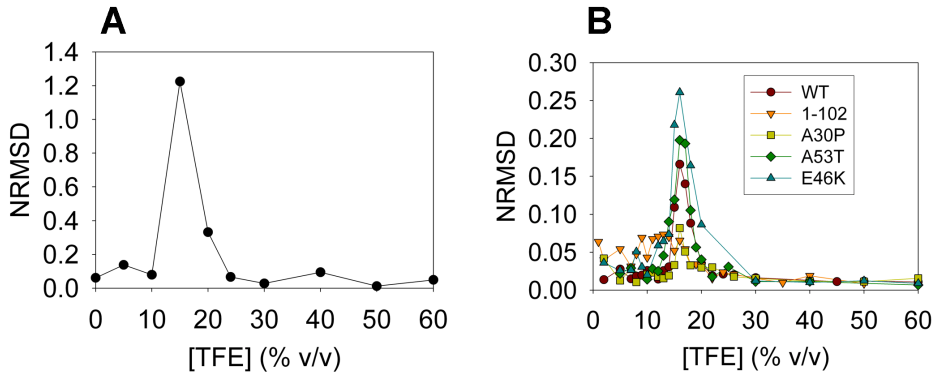

Figure A.1. Comparisons of αS variant CD data using the NRMSD parameter. (A) NRMSD values for 0.5 μM vs. 5 μM WT αS, as a function of TFE concentration. The curves were taken ~5 minutes after the samples were mixed. (B) NRMSD vs. [TFE] for spectra measured 5 minutes vs. 15 minutes after TFE is added to the solutions for the five αS variants.

transformations for all the αS variants (Figure 2.4, Figure 2.5, Figure 2.6), including the slowly-associating A30P mutant, it is unlikely that oligomerization contributes significantly to our signal at 0.5 μM.

Reconstruction of the intermediate state CD spectrum

Principal Component Analysis (PCA) is frequently used to reduce redundancy and extract the minimal basis for a given data set. For CD data, this method is often used to estimate the information content in measured spectra and to compare deconvolution methods (Lees, et al., 2006; Miles, et al., 2005; Pribic, 1994). Here, we use PCA to verify that our minimal basis set consists of three spectra; therefore we are observing only three distinct secondary structural conformations for our protein. In addition, we use PCA to reconstruct the spectrum of the intermediate state over all wavelengths.

The I state ellipticity at 198 and 222 nm can be found by noting the crossover points in the transition diagram in Figure 2.4B (Figure 2.5E-H for the mutants). However, we can use PCA to determine the I state ellipticity at all measured wavelengths. We express each CD spectrum as a point in *N*-dimensional space, where each dimension corresponds to one wavelength. We measure our spectra from 195-260 nm at 1 nm intervals; therefore *N*=66. For PCA, we transform this *N*-dimensional space onto a set of principal components, in which the basis consists of orthogonal vectors for which the variations in the data have been minimized. The first principal axis is the best straight line fit (in the 66-dimensional space) to the data, the second principal axis is the best linear fit to the data in a direction orthogonal to the first component, the third principal axis is the best linear fit in a direction orthogonal to the first two, etc. Therefore, we have transformed our vector into a new orthonormal basis in which each component contains a descending amount of information.

We perform the transformation for the sets of CD curves in Figure 2.4A. We visualize the 66-dimensional vector in 3D by projecting it onto the first 3 principal component axes (Figure A.2A). All our data appears to lie on a plane, and the three axes we have chosen show the maximal variations about this plane for any 3D projection.

We verify that the dimensionality of our data can be reduced from 66 to 2 by plotting the eigenvalues of our transformation on a scree plot (Figure A.2B). The first two eigenvalues appear prior to the "elbow" in the plot; therefore the first and second principal components are sufficient to describe our data (Cattell, 1966). Note that the PCA method involves subtracting the mean spectrum for our data. Thus, a 2D projection expresses all our CD data as a linear combination of the mean spectrum and the two principal component basis spectra. Therefore, the fact that our data lies on a plane indicates that we detect only three conformational states in our solutions.

We project our data onto the plane of the first two principal components and show the result in Figure A.2C. This plot is entirely analogous to Figure 2.4B, except that a point on this diagram provides corresponds to a complete spectrum. Now, by finding the location of the crossover point for the straight line fits to the data that share isodichroics, projecting this crossover point onto the basis vectors for the two principal components, and adding the mean spectrum, we are able to determine the I state spectrum over the full range of 195-260 nm (Figure 2.7A). We repeat this analysis for the αS102, A30P, A53T, and E46K αS variants using the data in Figure 2.5A-D.

We corroborate the I state spectra we determine via PCA by reconstructing them using a different, independent method. First, we note that, for the U $\leftrightarrow$ I coexistence regime (e.g. 2-14% TFE for wild-type αS), a measured CD spectrum $[\theta]$ is a linear combination of the spectrum of the pure U state, $[\theta]^U(\lambda)$, and the spectrum of the pure I state, $[\theta]^I(\lambda)$:

Figure A.2. Analysis of the αS variant CD data using PCA. (A) Projection of the curves for the WT αS data from Figure 2.4A onto the first three principal component axes. The data is shown as blue dots, and the graph is rotated to show the data at three different angles. Y_i denotes the i^{th} principal component axis, and the $Y_3 = 0$ plane is shown in green. The Y_3 range is reduced to better show variation of the data around the plane. (B) Scree plot (Cattell, 1966) showing the eigenvalue magnitudes for the transformation for all αS variants. (C) Projection of the WT αS data from A onto the plane of the first two principal components. The dashed lines show linear fits to points whose curves share isodichroics. (D-G) Comparisons of PCA prediction with MLE and transition diagram intercept data for the αS mutants (D) αS102, (E) A30P, (F) A53T, and (G) E46K. The solid lines show the spectra calculated via PCA. The dashed lines show results of MLE analysis, which were calculated using spectra that shared the low-TFE isodichroic points. The dotted line shows the MLE results calculated from spectra that shared the high-TFE isodichroic. The points (circles) show the I state reference points from Table 2.1

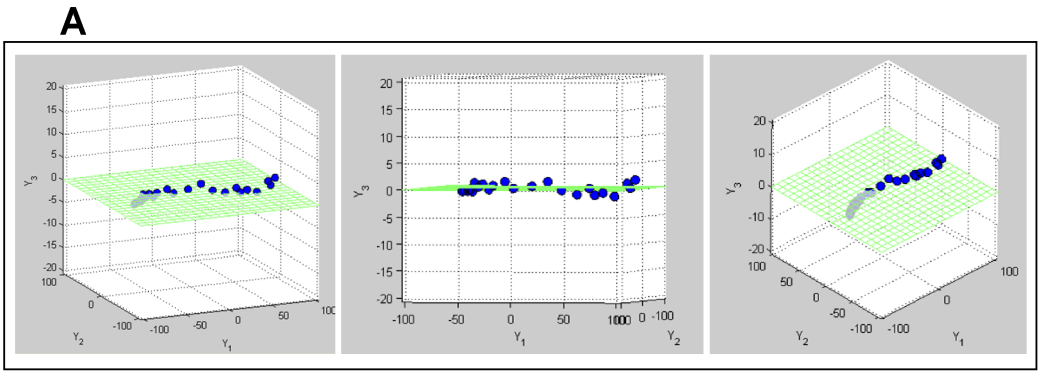
A
B
Eigenvalue
Principal Component Index
WT
1-102
A30P
A53T
E46K
C
Y_1
Y_2
14%
17%
18%
22%
12%
15%
30%
10%
45%
7%
0%
60%
D
1-102
E
A30P
F
A53T
G
E46K
[θ] (10^3 deg cm^2 dmol^{-1})
λ (nm)

$$[\theta](\lambda) = f_U [\theta]^U(\lambda) + f_I [\theta]^I(\lambda) \quad \text{(A2)}$$

where f_U is the fraction of the protein in the U state and f_I is the fraction of the protein in the I state. Note that f_U and f_I are functions of TFE concentrations, while $[\theta]^U$ and $[\theta]^I$ are functions of wavelength only. Because the total amount of protein is conserved, we also have:

$$f_U + f_I = 1 \quad \text{(A3)}$$

Combining Equations A2 and A3, we can find f_U:

$$f_U = \frac{[\theta](\lambda) - [\theta]^I(\lambda)}{[\theta]^U(\lambda) - [\theta]^I(\lambda)} \quad \text{(A4)}$$

In order to solve Equation A4, we need CD data for the U and I states for at least one wavelength. The isodichroic points observed at low- and high-TFE and the intercept of the two lines on the transition diagrams (Table 2.1) provide estimates of the I state ellipticity at four wavelengths. However, Equation A4 is undefined at the low-TFE isodichroic point, where $[\theta]^U = [\theta]^I$; therefore we use the three remaining reference wavelengths. In addition, we use the mean residue ellipticity values for our 0% TFE sample for $[\theta]^U$. For each αS variant, we solve Equation A4 at each of our reference wavelengths, and then use Maximum Likelihood Estimation (MLE) analysis to obtain the best estimate of f_U (therefore, $f_I = 1 - f_U$).

Having found f_U for low-TFE data, we can calculate the full I state spectrum over the entire wavelength range by rearranging Equations A2 and A3 to solve for $[\theta]^I(\lambda)$:

$$[\theta]^I(\lambda) = \frac{[\theta](\lambda) - f_U [\theta]^U(\lambda)}{1 - f_U} \quad \text{(A5)}$$

Essentially, we are subtracting the U state (0% TFE) spectrum from a curve that contains some fraction of the I state and renormalizing. We perform this calculation for each spectrum in the U ↔ I two-state coexistence regime and use maximum likelihood to average the results. We then follow an analogous procedure for the I ↔

F coexistence regime data (17-50% TFE for wild-type αS), using the 60% TFE data as an estimate of the F state spectrum at the reference wavelengths. Our inferred I state spectra, and comparisons to the spectra obtained via PCA and to the reference wavelength data points from Table 2.1 are shown in Figure 2.7A and Figure A.2D-G. The I state curves calculated using the low- and high-TFE data are similar to each other, and are also consistent with the values from Table 2.1 and the results of the PCA calculation.

Calculations of the populations of the U, I and F states

We estimate state populations and check our reconstructed I state curve by fitting all CD data to linear combinations of the U, I and F state spectra. We start with the system of equations that describe the mean residue ellipticity of any sample that contains three distinct conformations:

$$[\theta](\lambda) = f_U[\theta]^U(\lambda) + f_I[\theta]^I(\lambda) + f_F[\theta]^F(\lambda)$$
$$f_U + f_I + f_F = 1 \qquad \text{(A6)}$$

Again, the 0% and 60% TFE curves are used to represent $[\theta]^U(\lambda)$ and $[\theta]^F(\lambda)$, while $[\theta]^I(\lambda)$ is taken to be the I state spectrum inferred from PCA (Figure 2.7B). Thus, Equations A6 have two free parameters; we fit for f_U and f_I. Figure 2.8A shows our calculated vs. experimental curves for WT αS, demonstrating that these spectra are nearly identical. The results are very similar for the mutant αS (Figure A.3A-D). For WT αS and the disease-associated mutants, the NRMSD for the experimental vs. calculated curves is less than 0.06 over the entire range of [TFE] (Figure A.3E). The NRMSD is increased at low [TFE] for αS102, which probably reflects the relatively low CD signal magnitude, and therefore increased experimental uncertainty, for this smaller protein in its disordered conformation. For all the variants, the predicted curves reproduce key qualitative features of the experimental data, including the low-

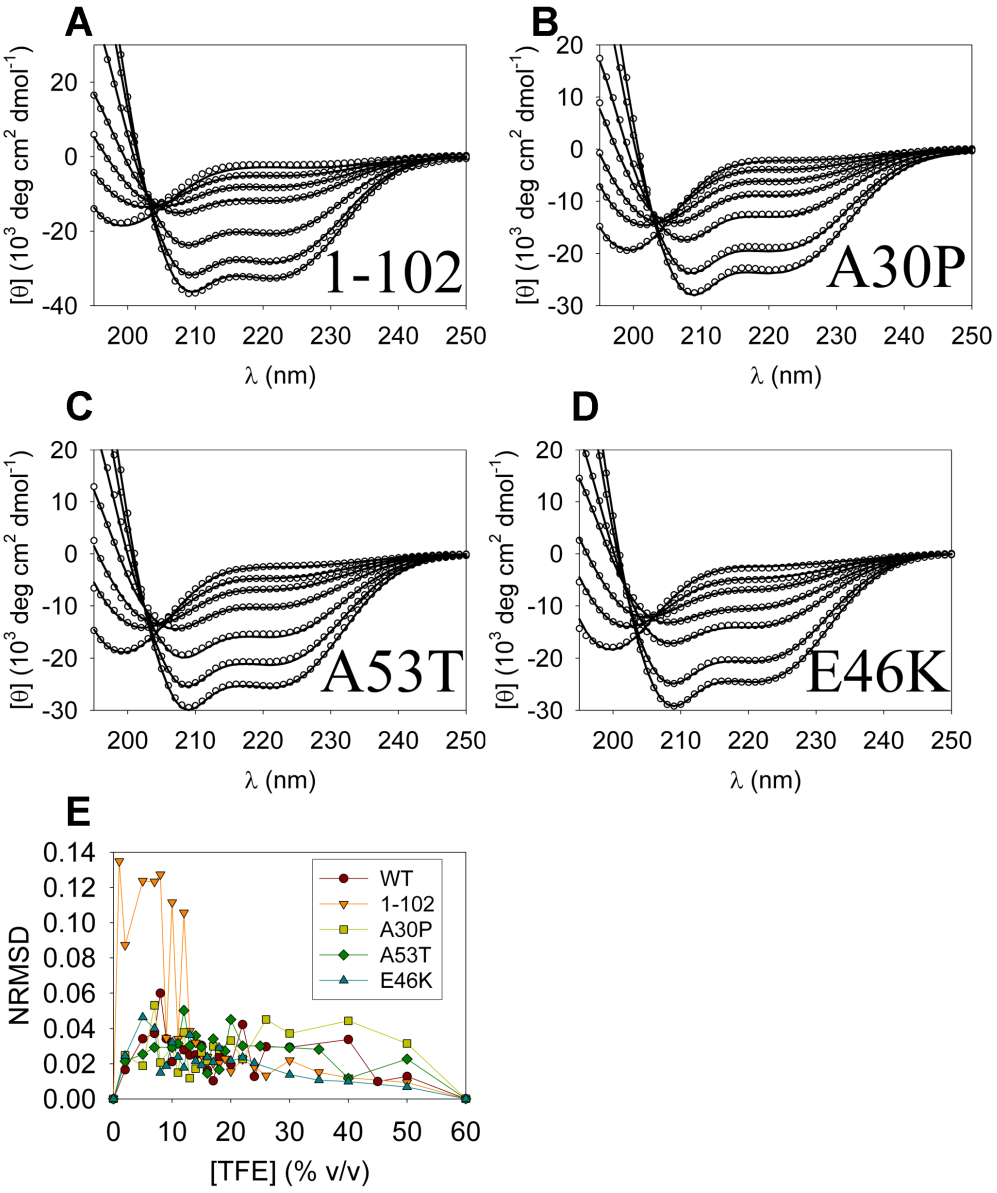

Figure A.3. Goodness of fit for αS variant CD spectra fit to a linear combination of three states (see also Figure 2.8A). (A-D) Comparison of experimental spectra (open circles, data as in Figure 2.5A-D) and curves calculated from linear combinations of the 0%, 60% and the estimated I state spectra using Equations A6 (black lines) for (A) αS102, (B) A30P, (C) A53T, and (D) E46K αS. The TFE concentrations for spectra with increasing negative ellipticity at 222 nm are 5%, 13%, 15%, 17%, 20%, 30%, and 50% TFE. (E) NRMSD values for the experimental data vs. calculated spectra over the full range of [TFE] for the αS variants.

and high-TFE isodichroic points. Thus, our experimental CD data can be reconstructed from linear combinations of the 0% TFE, 60% TFE, and estimated I states, which verifies that the spectra from Figure 2.7 are plausible estimates of the intermediate CD curves, and also that we are observing no more than three secondary structural conformations. In addition, the fit parameters f_U and f_I (and $f_F = 1 - f_U - f_I$) provide estimates of the conformational state populations as a function of [TFE] (Figure 2.8B).

Oligomerization kinetics data fitting

We fit the data in Figure 2.9B to a single exponential model:

$$[\theta]_{216}(t) = a + b \cdot \exp(-k_{app} t) \qquad \text{(A7)}$$

where t is time, and a, b, and k_{app} are coefficients that are found via the fits. Because the changes in signal are small for fast-associating mutants and high protein concentrations, fit results to the data tend to be uncertain. We overcome this limitation by assuming that the t=0 signals for the 2 μM and 5 μM protein samples should be the same as the 0.5 μM protein data obtained in the same buffer conditions (Figure 2.4A and Figure 2.5A-D), with an uncertainty of 1 x 10^3 deg cm^2 $dmol^{-1}$ due to signal fluctuations, baselining errors and uncertainty in protein concentration. The rate constant k_{app} resulting from of fits of the data in Figure 2.9B, along with these t=0 data points, are shown in Table 2.3.

Although the single exponential model should not be sufficient to describe an oligomerization reaction, it fits our data quite well. We attempted fits to other functions, including a double exponential model, the exact solution for two-state dimerization reaction (Milla and Sauer, 1994), and various hyperbolic functions, but comparisons using the adjusted R^2 value or the Akaike Information Criterion showed that none of these models was superior to the single exponential function for our data. Therefore, we conclude that the relatively long dead time, poor time resolution, and

noise in our data prevent us from discriminating among possible kinetic models. Hence, we can estimate the overall "speed" of the reaction, as measured by k_{app}, but we have insufficient information to determine what type of oligomers form under these conditions.

Software for MLE, PCA, and kinetics data analysis

MLE, PCA, and kinetics data analysis were done using MATLAB 7.1. PCA analysis was performed via the MATLAB princomp() function, while fminsearch() was used to fit our measured CD spectra to Equations A6. The MATLAB function fit() was used for fits to Equations A7.

CD Data Deconvolution

We performed deconvolution of the αS variant U, I, and F state CD spectra (Figure 2.4, Figure 2.5, Figure 2.7) using k2d2 (Andrade, et al., 1993; Perez-Iratxeta and Andrade-Navarro, 2008). In all cases, the estimated maximum total error (Perez-Iratxeta and Andrade-Navarro, 2008) reported by the software was ≤ 0.4.

For all five αS variants studied, k2d2 predicted that the U (0% TFE) state is 9.45 % α-helical and 30.04% β-strand. In aqueous solution, αS and its variants are known to be disordered (Bussell and Eliezer, 2001; Eliezer, et al., 2001; Fredenburg, et al., 2007), and so these predictions are likely to be inaccurate. However, we are able to use the U state k2d2 results as a baseline; we compare results for the PCA-estimated I state and the F (60% TFE) state spectra to the 0% TFE prediction in order to obtain information about changes in secondary structure.

k2d2 predicts that the WT αS I state is 20.89% α-helical and 25.48% β-strand, which is a significant increase in predicted α-helical content, and a slight decrease in predicted β-strand content, compared to the U state. The F (60% TFE) state is

predicted to be 69.46% α-helical and 1.85% β-strand, which is consistent with a highly helical conformation at high [TFE].

For αS102, the I state is predicted to be 25.60% α-helical and 19.93% β-strand, and the F state is predicted to be 78.05% α–helical and 1.62% β-strand. Hence, the truncation mutant experiences an increase in predicted α-helical structure for the I and F states compared to the U state, and these changes are greater in magnitude than those predicted for WT αS, as might be expected if structure formation involves the N terminal portion of the full-length protein.

Structure predictions for the A53T and E46K mutants are similar to WT αS. For A53T, the I state prediction is 25.51% α-helix and 20.71% β-strand, while the F state prediction is 69.61% α-helix and 1.77% β-strand. For E46K, the I state result is 19.92% α-helix and 27.52% β-strand, while the F state prediction is 69.46% α-helix and 1.85% β-strand. Therefore, the I states for these mutants show a significant increase in predicted α-helical structure and a modest decrease in predicted β-sheet structure, compared to the U state.

For the A30P mutant, the I state is predicted to be 7.74% α-helical and 34.08% β-strand, while the F state prediction is 69.46% α-helix and 1.85% β-strand. Hence, the A30P I state is predicted to be less helical and contain more β-sheet structure than the other αS variants studied. However, differences in β-strand and α-helical content between the U and I states for A30P are modest and probably are within the error of the method. We conclude that the A30P mutant I state likely contains less secondary structure than the other variants' I states, as might be expected due to the helix-breaking nature of the proline residue and the data in Figure 2.7B and Table 2.2.

APPENDIX B

ANALYSIS AND SUPPORTING INFORMTION RELATED TO TEMPERATURE- AND PH- DEPENDENT CIRCULAR DICHROISM MEASUREMENTS OF ALPHA-SYNUCLEIN

Baseline subtraction and concentration corrections for variable-pH and variable-temperature CD spectra

Prior to the variable-pH measurements shown in Figure 3.1, we performed the sulfuric acid titration into buffer and measured these baseline spectra as a function of pH. These curves did not change significantly during the titration; the pH-dependent baseline variations were < 5% of the protein signal at 222 nm, and <1% of the signal at 200 nm. Therefore, we averaged the buffer spectra over the full pH range in order to obtain a single baseline for each protein. In addition, we corrected our data for changes in concentration that occurred during the titration (the initial protein concentration was 1.0 μM and the final concentration was 0.88 μM). Errors in the measurements were calculated from the standard deviations of three spectra.

Measurements of temperature-dependent CD spectra (Figure 3.2, Figure 3.3, Figure 3.5, Figure 3.7, Figure 3.8, Figure 3.10, and Figure B.3) required incubation times ranging from ~40 minutes to 3 hours, depending on the temperature interval being examined. Heating and prolonged incubations led variability in the baseline spectra. In general, the *y*-position of the baseline drifted over time, and the shape of the baseline spectrum changed slightly with temperature. The details of the heating rates and incubation time affected the baseline measurements, and it was difficult to directly subtract the baseline for a given temperature. Therefore, we used a simpler approach to estimate the baseline signal and its uncertainty. First, we subtracted a constant from all our CD data in order to correct for drifts, so that the ellipticity was

zero when averaged from 255-260 nm. Then, we averaged baselines taken at various temperatures and subtracted the averaged, rescaled curve from our protein data. The deviations of the baselines measured at various temperatures was calculated and included in our estimates of the experimental errors of our measurements.

Our CD data is reported in units of mean residue ellipticity, accurate determinations of which depend on knowledge of the protein concentration. Therefore, because the protein concentration depends on the sample volume, we corrected our variable-temperature CD data to account for thermal expansion and contraction. Between 2 °C and 70 °C, the volume of water changes by ~2% (Weast, 1988), while TFE expands by ~10% (Malhotra and Woolf, 1991). We calculate the expected volume of a TFE-water mixture using density vs. temperature data for the pure substances, assuming that the total volume is simply the volume of the water component at a given temperature plus the volume of the TFE component at the same temperature.

TFE-water mixtures experience volume contraction upon mixing, and so the assumption that the mixture volume is the sum of the component volumes is incorrect. The excess molar volume is peaked near 60% TFE (see Figure 1.1C), where a ~2%-reduction in volume may be observed at 25 °C (Minamihonoki, et al., 2007; Palepu and Clarke, 1989; Rochester and Symonds, 1974; Sassi and Atik, 2003). However, measurements of this volume contraction in the literature tend to contradict one another and do not cover a wide temperature range. Therefore, we are unable to apply this correction over the entire TFE and temperature range studied, and so we ignore this effect. As a result, we may overestimate the magnitude of the spectra of our ~50-60% TFE samples.

Verification of reversibility for heating and cooling cycles

We previously found that NRMSD values of ~0.02 are typical for multiple measurements of identical, stable samples (Anderson, et al., 2010). In addition, as discussed above, we observe temperature-dependent changes in baseline signals, which contribute variability to our data. Temperature drift can lead to NRMSD values of ~0.05-0.15, especially at 0-15% TFE where the CD signals are relatively weak. Therefore, we use a NRMSD value of 0.15 as a cutoff below which we consider our samples to remain monomeric or mostly monomeric during heating. We calculate NRMSD values over the entire wavelength range for which data is available, i.e. 195-260 nm for pH 7.5 samples and 190-260 nm for pH 2.4 samples, except for the data shown in Figure 3.4, which were obtained for the 195-260 nm range at both pH values. Note that oligomerization is not the only potential source of irreversibility – changes in the properties of TFE-water mixtures or other effects may also contribute to hysteresis in the signal. However, we assume that absence of hysteresis is likely to indicate that the amount of oligomerization is low, regardless of other potential sources of irreversibility.

We obtained our variable-temperature CD spectra starting from the lowest temperature and heating. For the data we report in Figure 3.2, Figure 3.3, Figure 3.5, Figure 3.8, Figure 3.10, and Figure B.3, we measured an initial spectrum at 2 °C, heated the samples to the next desired temperature and measured a spectrum, repeated until the maximum temperature was obtained, and then returned the samples to 2 °C and measured a final spectrum. The initial and final 2 °C spectra for the "mostly monomeric" samples are shown in Figure B.1. For Figure 3.10, the initial and final measured spectra are shown in the inset graphs. The NRMSD between the initial and final 2 °C spectra was examined; note that baseline subtractions and volume corrections (see above) were applied prior to the NRMSD calculations.

Figure B.1. CD spectra measured at 2 °C before (solid black lines) and after (dashed red lines) the heating cycle for the data sets in Figures 3.2, 3.3, 3.5, 3.8, and 3.10, as well as Figure B.3A-D. The y-axes show mean residue ellipticity in units of 10^3 deg cm^2 dmol^{-1}, while the x axes plot wavelength in nm. The NRMSD for the initial vs. final samples is indicated on the graphs. The samples were heated to a maximum temperature, T_h, of 70 °C, unless otherwise indicated. Data is shown for the samples from (A) Figure 3.2A (WT αS, 0% TFE, pH 2.4), (B) Figure 3.2B (αS102, 0% TFE, pH 2.4), (C) Figure 3.2D (WT αS, 0% TFE, pH 7.5), (D) Figure 3.2E (αS102, 0% TFE, pH 7.5), (E) Figure 3.3A (WT αS, 60% TFE, pH 2.4), (F) Figure 3.3B (αS102, 60% TFE, pH 2.4), (G) Figure 3.3D (WT αS, 60% TFE, pH 7.5), (H) Figure 3.3E (αS102, 60% TFE, pH 7.5), (I) Figure B.3A (A30P αS, 0% TFE, pH 2.4), (J) Figure B.3B (A30P αS, 0% TFE, pH 7.5), (K) Figure B.3C (A30P αS, 60% TFE, pH 2.4), (L) Figure B.3D (A30P αS, 60% TFE, pH 7.5), (M) Figure 3.5A (αS102, 5% TFE, pH 7.5, T_h=60 °C), (N) Figure 3.5B (αS102, 7% TFE, pH 7.5, T_h=40 °C), (O) Figure 3.5C (αS102, 27% TFE, pH 7.5, T_h=25 °C), (P) Figure 3.5D (αS102, 30% TFE, pH 7.5, T_h=60 °C), (Q) Figure 3.5E (αS102, 40% TFE, pH 7.5), (R) Figure 3.5F (αS102, 50% TFE, pH 7.5), (S) Figure 3.8A (αS102, 5% TFE, pH 2.4), (T) Figure 3.8B (αS102, 7% TFE, pH 2.4, T_h=50 °C), (U) Figure 3.8C (αS102, 10% TFE, pH 2.4, T_h=25 °C), (V) Figure 3.8D (αS102, 12% TFE, pH 2.4, T_h=25 °C), (W) Figure 3.8E (αS102, 14% TFE, pH 2.4, T_h=25 °C), (X) Figure 3.8F (αS102, 15% TFE, pH 2.4, T_h=25 °C), (Y) Figure 3.8G (αS102, 16% TFE, pH 2.4, T_h=25 °C), (Z) Figure 3.8H (αS102, 17% TFE, pH 2.4, T_h=40 °C), (AA) Figure 3.8I (αS102, 18% TFE, pH 2.4, T_h=40 °C), (BB) Figure 3.8J (αS102, 20% TFE, pH 2.4, T_h=50 °C), (CC) Figure 3.8K (αS102, 22% TFE, pH 2.4, T_h=60 °C), (DD) Figure 3.8L (αS102, 25% TFE, pH 2.4), and (EE) Figure 3.8M (αS102, 30% TFE, pH 2.4).

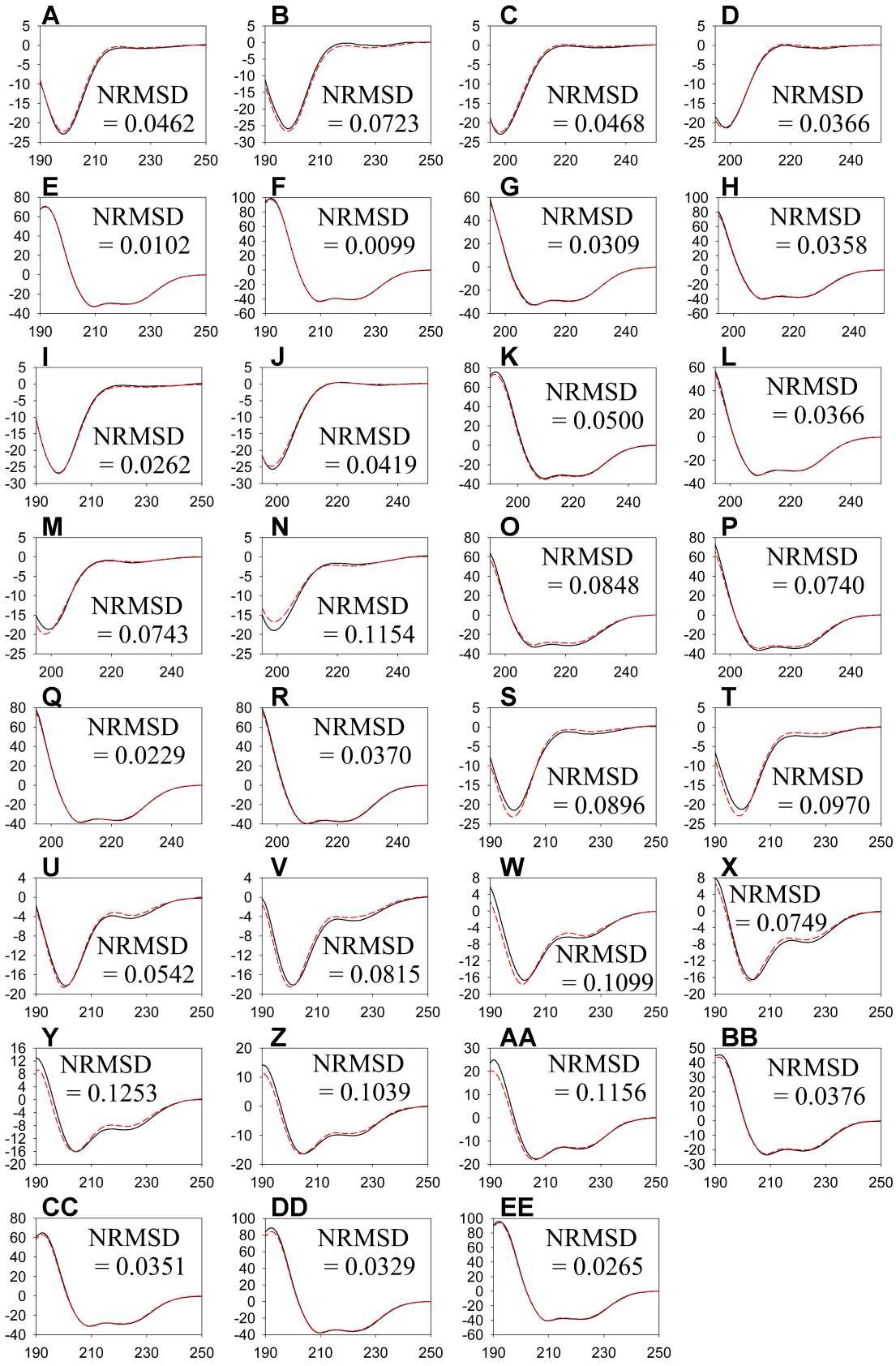
A
NRMSD = 0.0462
B
NRMSD = 0.0723
C
NRMSD = 0.0468
D
NRMSD = 0.0366
E
NRMSD = 0.0102
F
NRMSD = 0.0099
G
NRMSD = 0.0309
H
NRMSD = 0.0358
I
NRMSD = 0.0262
J
NRMSD = 0.0419
K
NRMSD = 0.0500
L
NRMSD = 0.0366
M
NRMSD = 0.0743
N
NRMSD = 0.1154
O
NRMSD = 0.0848
P
NRMSD = 0.0740
Q
NRMSD = 0.0229
R
NRMSD = 0.0370
S
NRMSD = 0.0896
T
NRMSD = 0.0970
U
NRMSD = 0.0542
V
NRMSD = 0.0815
W
NRMSD = 0.1099
X
NRMSD = 0.0749
Y
NRMSD = 0.1253
Z
NRMSD = 0.1039
AA
NRMSD = 0.1156
BB
NRMSD = 0.0376
CC
NRMSD = 0.0351
DD
NRMSD = 0.0329
EE
NRMSD = 0.0265

We also quantified oligomerization for simple heating cycles (Figure 3.4) in order to obtain information about the solution conditions where oligomerization might occur. The CD spectra used to generate Figure 3.4 are plotted in Figure B.2. For these samples, we did not perform a baseline subtraction and simply compared the raw ellipticity signals before and after the heating cycle.

We did not quantify hysteresis for these samples shown in Figure 3.7A-C because cooling below 0 °C was slow. However, we found that >≈30% TFE samples do not oligomerize significantly, at least for 0.5 μM αS variants (Figure 3.4), and we also observe a single isodichroic during heating for all the samples in Figure 3.7A-C. Therefore we assume that ≥ 60% TFE αS102 samples likely remained monomeric during the measurements.

Temperature, TFE and pH dependence of the CD spectra of A30P αS

We performed temperature-dependent measurements for A30P αS at pH 7.5 and pH 2.4 and 0% and 60% TFE (Figure B.3A-D). As discussed above, we verified that heating-induced spectral changes for these samples were minimal (NRMSD < 0.15); the initial and final 2 °C spectra are shown in Figure B.1I-L. The A30P αS spectra and $[\theta]_{222}$ vs. T curves (Figure B.3E-H) were identical to WT αS, within the uncertainty of our measurements.

Figure B.4 shows that the variable-temperature transition diagrams constructed for the A30P and WT αS data collapse onto the variable-TFE, 25 °C lines from (Anderson, et al., 2010).

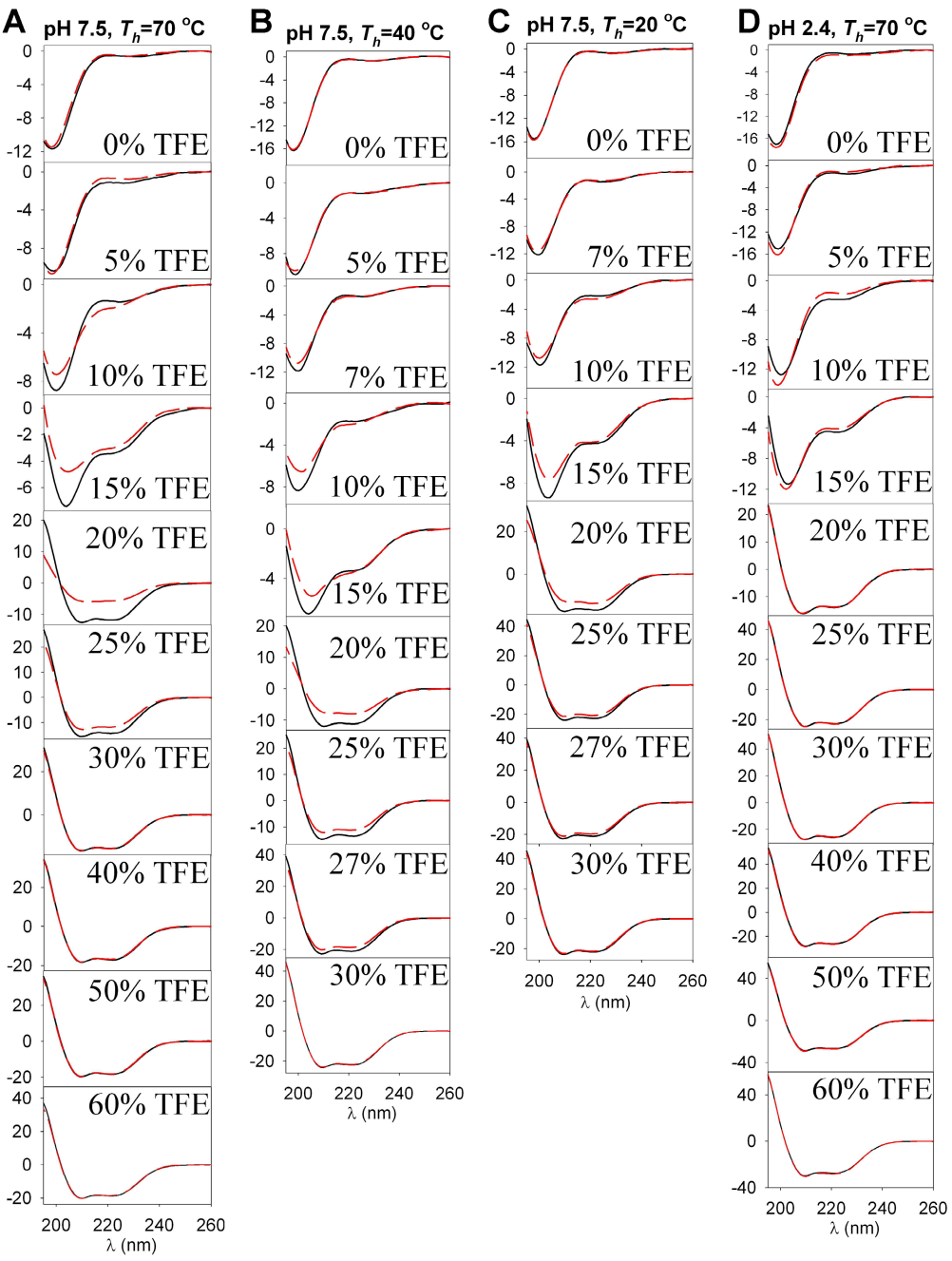

Figure B.2. The CD spectra used to calculate the NRMSD values in Figure 3.4. The initial (solid black lines) and final (dashed red red lines) spectra, both obtained at 2 °C, are shown. The y-axis values are the raw CD ellipticity in mdeg. The TFE concentrations at which data was obtained are indicated in the plots. Data is shown for each of the four curves in Figure 3.4, which correspond to (A) pH 7.5 and T_h= 70 °C, (B) pH 7.5 and T_h= 40 °C, (C) pH 7.5 and T_h= 20 °C, and (D) pH 2.4 and T_h= 70 °C.

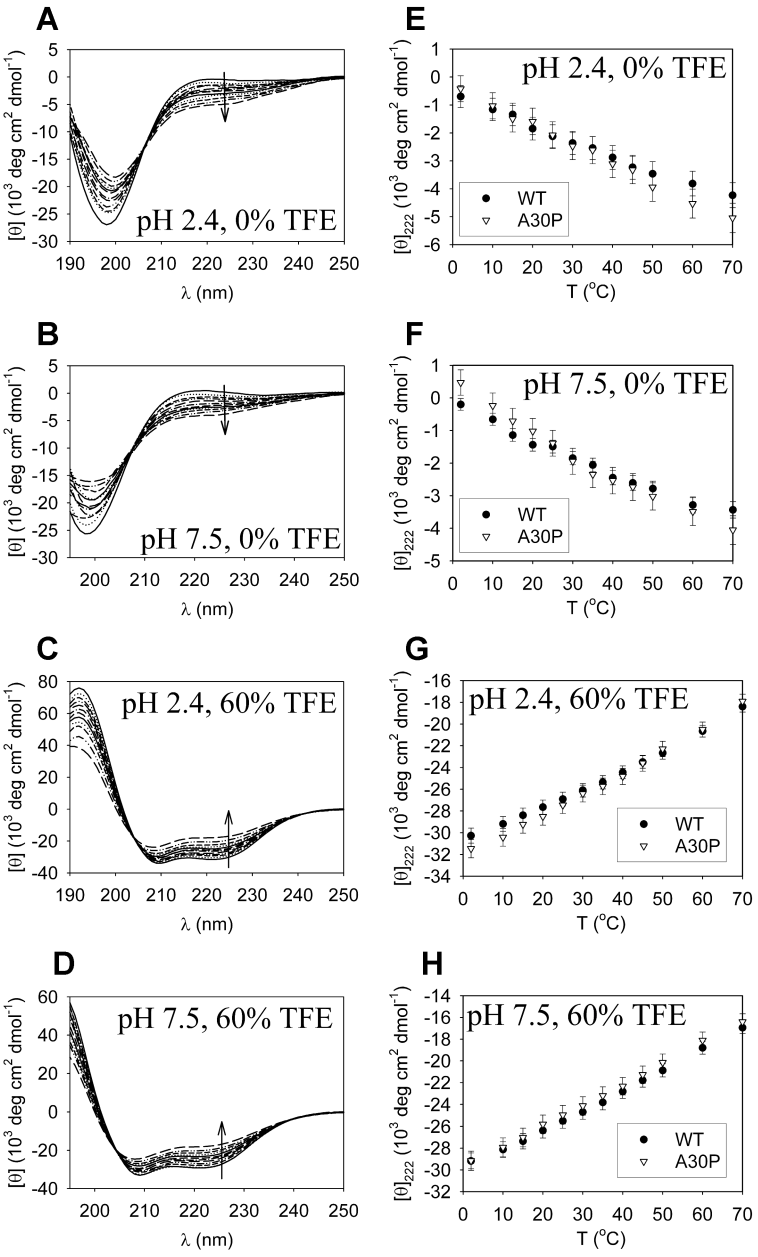

Figure B.3. (A-D) Variable-temperature CD spectra for A30P αS. The spectra were measured at 2, 10, 15, 20, 25, 30, 35, 40, 45, 50, 60, and 70 °C, and the arrows show the general direction of increasing temperature. The solution conditions examined were (A) pH 2.4, 0% TFE, (B) pH 7.5, 0% TFE, (C) pH 2.4, 60% TFE, and (D) pH 7.5, 60% TFE. (E-H) Comparisons of the A30P data to WT αS (see Figure 3.2 and Figure 3.3).

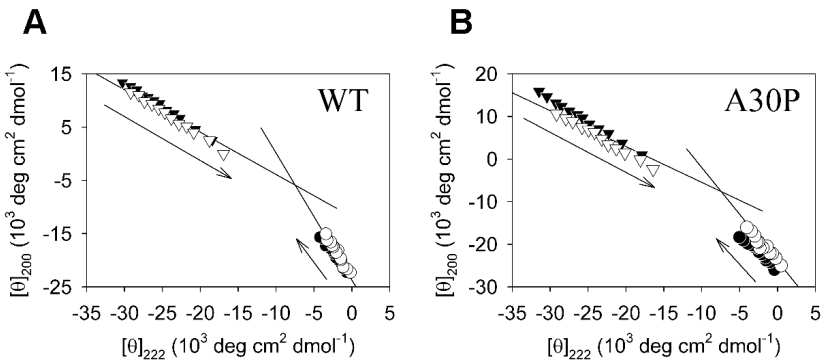

Figure B.4. Comparisons of variable-temperature, 0% and 60% TFE data with the 25 °C, variable-TFE transition diagrams for WT and A30P αS. The black symbols show the pH 2.4 data and the white symbols show the pH 7.5 data, with circles and triangles corresponding to 0% and 60% TFE, respectively. The arrows show the general direction of increasing temperature. The solid lines show fits to the low- and high-TFE data from (Anderson, et al., 2010). (A) Data for WT αS (derived from Figure 3.2A,D and Figure 3.3A,D), with the lower right (upper left) solid line showing a fit of the 25 °C, 0%-14% (17% - 60%) TFE, WT αS data from (Anderson, et al., 2010). (B) Data for A30P αS (derived from Figure B.3A-D), with the lower right (upper left) solid line showing a fit of the 25 °C, 0%-12% (17% - 60%) TFE, A30P αS data from (Anderson, et al., 2010).

Isodichroic points for WT and A30P αS CD spectra

Table B.1 shows isodichroics for WT αS and A30P αS spectra from Figure 3.2, Figure 3.3, and Figure B.3A-D. These points are compared to the αS102 data and the variable-TFE data points from (Anderson, et al., 2010).

We found two distinct isodichroic points for CD spectra of αS variants at pH 7.5 and 25 °C in the presence of 0-60% TFE (Anderson, et al., 2010). We similarly observe two types of isodichroics in the variable-temperature data (Table 3.2, Table B.1). The variable-temperature, 0% TFE isodichroic measurements agree with the previous 25 °C, low-TFE points, within the experimental uncertainties in the measurements (Table B.1A), but those for the 5-7% TFE αS102 samples have slightly shifted ellipticities at pH 7.5 (Table 3.2A). In addition, although the > 20% TFE isodichroic positions are within experimental uncertainties of the 25 °C, high TFE isodichroics, there is a tendency toward larger negative values for the variable-temperature samples as [TFE] increases.

Variations in spectral shapes for high-TFE αS102 samples

When all the pH 2.4, αS102 CD spectra from Figure 3.2B Figure 3.3 B, and Figure 3.8A-M are combined (Figure B.5A), we see that spectra with same ellipticity at 222 nm do not always overlap at all wavelengths (e.g., the green and orange curves in Figure B.5A). In particular, the relative depths of the 222 and 208 nm peaks vary slightly with TFE concentration regardless of temperature. The combined pH 7.5 curves (Figure B.5B) reveal similar behavior.

Transition diagram plots of the CD signals at 208 nm vs. 222 nm show that there is a possible trend toward slightly larger negative $[\theta]_{208}$ for a given $[\theta]_{222}$ when the TFE concentration is increased, although the observed differences are well within the experimental uncertainties (Figure B.5C-D). Volume contraction for TFE-water

Table B.1. Isodichroics for variable-temperature, 0% and 60% TFE CD spectra of 0.5 μM WT and A30P αS. The units for the wavelength position of the isodichroics (λ_{iso}) are nm and the units for the mean residue ellipticity at the isodichroics ($[\theta]_{iso}$) are 10^3 deg cm^2 dmol^{-1}. The uncertainties in $[\theta]_{iso}$ are due to experimental error, and the uncertainties in the wavelength measurements result from to the CD spectrometer bandwidth and experimental error. (A) Isodichroic point locations for 0% TFE samples at pH 2.4 and pH 7.5. (B) Isodichroic point locations for 60% TFE samples at pH 2.4 and pH 7.5.

A

	pH 2.4		pH 7.5		Const-Temp*	
	λ_{iso}	$[\theta]_{iso}$	λ_{iso}	$[\theta]_{iso}$	λ_{iso}	$[\theta]_{iso}$
WT	207 ± 1	-10.0 ± 1.5	207 ± 1	-10.4 ± 1.5	207 ± 1	-10.8 ± 1.2
αS102	207 ± 1	-10.2 ± 1.8	207 ± 1	-9.2 ± 1.5	205 ± 2	-12.6 ± 1.9
A30P	207 ± 1	-13.3 ± 1.7	207 ± 1	-11.2 ± 1.6	208 ± 1	-9.3 ± 1.4

B

	pH 2.4		pH 7.5		Const-Temp*	
	λ_{iso}	$[\theta]_{iso}$	λ_{iso}	$[\theta]_{iso}$	λ_{iso}	$[\theta]_{iso}$
WT	204 ± 1	-17.2 ± 4.8	204 ± 1	-18.1 ± 4.5	203 ± 1	-12.0 ± 3.9
αS102	204 ± 1	-20.6 ± 6.9	204 ± 1	-18.2 ± 6.3	203 ± 1	-11.1 ± 4.5
A30P	204 ± 1	-17.9 ± 5.0	204 ± 1	-18.9 ± 4.2	203 ± 1	-12.9 ± 3.5

* Constant-temperature (25 °C) isodichroic points from Table 2.1 and (Anderson, et al., 2010). For A (B), the isodichroics for the low-TFE, U ↔ I (high-TFE, I ↔ F) coexistence are shown.

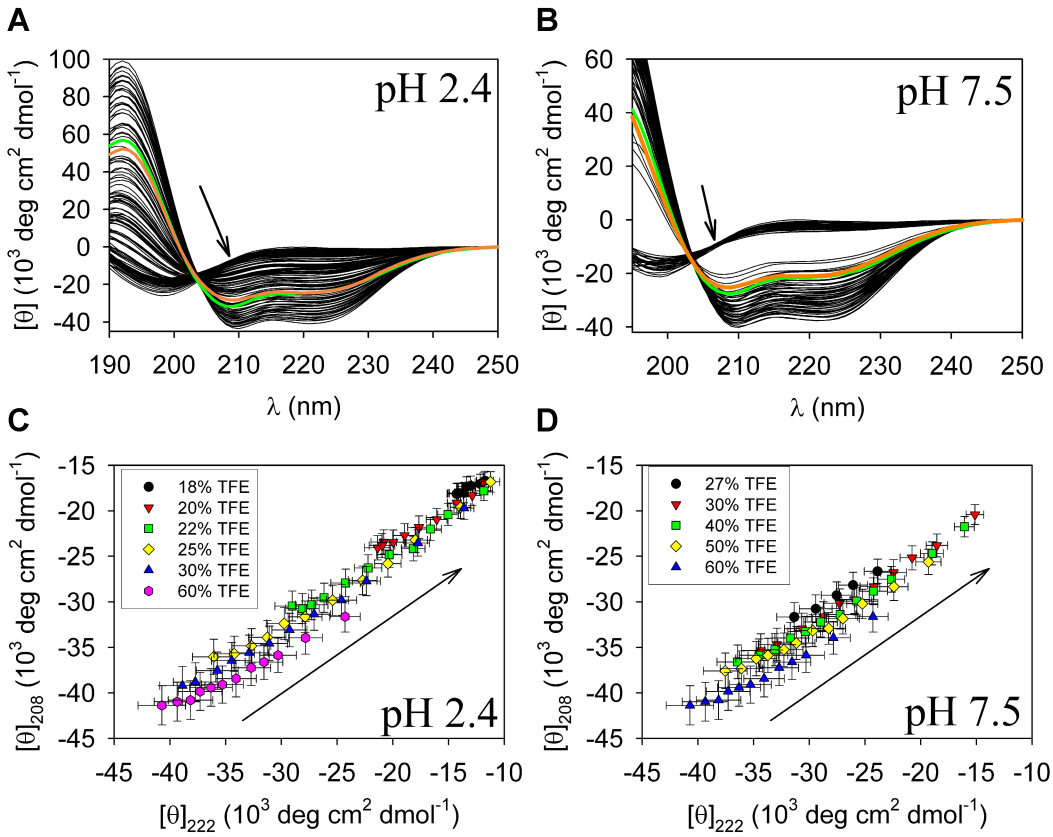

Figure B.5. Changes in CD spectral shapes at high TFE. (A-B) Combined data sets for the variable-temperature αS102 data at (A) pH 2.4 and (B) pH 7.5. Two curves are highlighted in green and orange to highlight systematic differences in the signals at 208 nm compared to 222 nm. The 60% TFE, 70 °C spectra are shown in green, while for pH 2.4 (7.5), the 22% TFE, 25 °C (30% TFE, 45 °C) curve is shown in orange. An arrow indicates the location of the low-TFE, variable-temperature isodichroic points. (C-D) Transition diagrams constructed for high TFE data, showing the ellipticity at 208 vs. 222nm. The error bars reflect experimental uncertainties, and the arrows show the general direction of increasing temperature.

mixtures (see above) could contribute to the observed discrepancies by tending to displace the ~40%-60% TFE data toward the lower left corner of the plots. Furthermore, CD spectral shape variations of this sort are often observed for alanine-rich and other peptides and are thought to be due to changes in the CD signal from an α-helix (Wallimann, et al., 2003). Therefore, it is not clear whether these differences in the CD spectra reflect actual differences in secondary structure or whether they are artifacts.

Principal Component Analysis (PCA) of the CD spectra at various temperatures and TFE concentrations

PCA can be used to estimate the number of independent factors in a data set (Appendix A). We apply this analysis to two data sets: (1) the set consisting of all the pH 2.4, αS102 spectra from Figure 3.2B, Figure 3.3B, and Figure 3.8A-M, and (2) the set of all the pH 7.5, αS102 curves in Figure 3.2E, Figure 3.3E, and Figure 3.5. These two data sets are shown in Figure B.5A-B. For the pH 2.4 data set, we analyze the complete wavelength range from 190-260 nm, while for the pH 7.5 data set, we use only the 200-260 nm range because of issues with buffer absorbance at low wavelengths, which were particularly problematic at high temperatures and 0-7% TFE.

Scree plots (Cattell, 1966), resulting from PCA applied to these two data sets, reveal that both sets contain more than two factors, implying we are sampling more than three distinct secondary structure conformations when we vary both [TFE] and temperature (Figure B.6A-B). For the pH 2.4 samples, the number of factors above the Scree baseline is at least four, while for pH 7.5, at least three factors are significant. The basis vectors corresponding to the most significant factors are plotted in Figure B.6C-D.

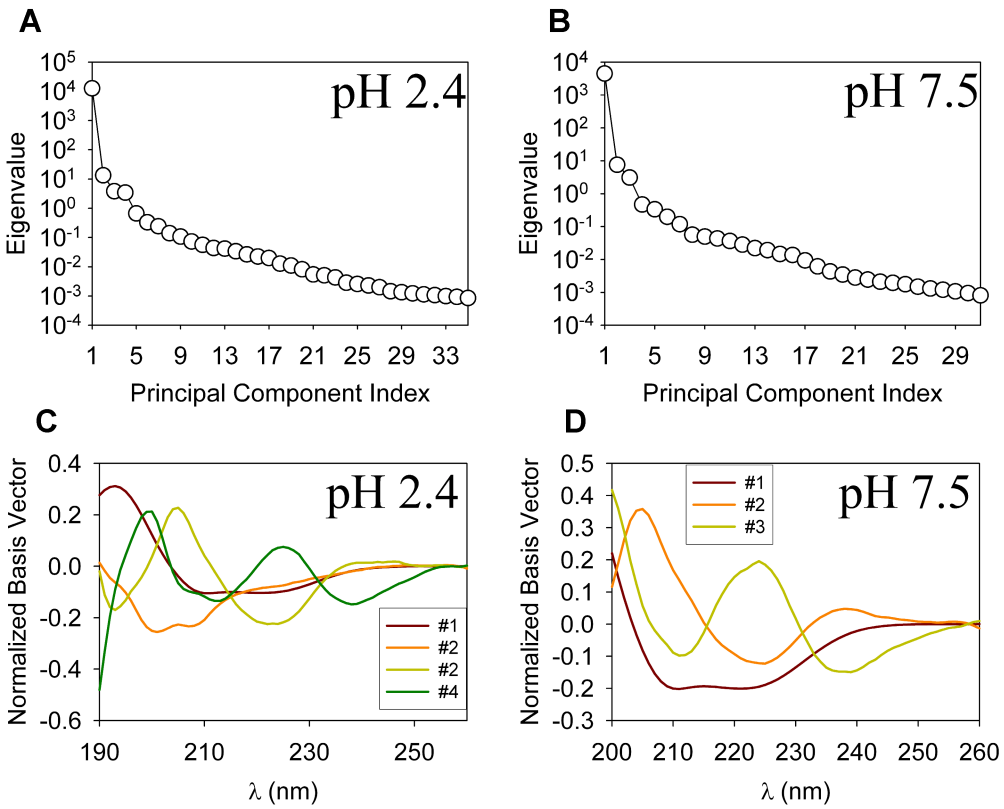

Figure B.6. PCA results for the αS102 data shown in Figure B.5A-B. (A-B) Scree plots (Cattell, 1966) for the (A) pH 2.4 and (B) pH 7.5 data. (C-D) The significant PCA basis vectors for the (C) pH 2.4 and (D) pH 7.5 data sets.

Over 99.7% of the variance in the data sets is due to the first principal component, which is associated with the overall coil-to-helix transition (Table B.2). Plots of the PCA scores as a function of temperature (Figure B.7A-B) demonstrate that the first principal components for each data set reflect the overall helicity of the samples; these plots are similar to Figure 3.6B and Figure 3.9B, with the sign of the *y*-axes reversed. These curves also clearly show the non-monotonic behavior of the pH 2.4 samples at ~17-20% TFE.

Plots of the next few principal component scores (Figure B.7C-G) are much noisier. Component #3 for the pH 2.4 data set appears to be analogous to component #2 for the pH 7.5 data set, while component #4 for the pH 2.4 data may correspond to component #3 at pH 7.5. It is tempting to associate pH 2.4 component #4 and pH 7.5 component #3 with a "high temperature" intermediate state because these components are populated at elevated temperatures for all [TFE]. However, component #3 (for pH 2.4) is nearly the inverse of component #4, and for the low-TFE samples, the contribution from component #3 will tend to cancel out the contribution from component #4. (Similar behavior is observed for components #2 and #3 for the pH 7.5 case). Therefore, the combined effects of components #3 and #4 for the pH 2.4 data (#2 and #3 for the pH 7.5 data) appear to involve changes in the magnitudes of the 222 nm peak compared to the 208 nm peak for high [TFE] samples. These TFE-dependent differences in the magnitudes of the 222 nm signal vs. the 208 nm for the highly helical state were discussed above (see also Figure B.5).

At constant temperature, we previously found that two significant factors (i.e. three states) contributed to the 0-60% TFE data (Anderson, et al., 2010). The variable-temperature case appears to be more complex and may involve four to five conformations. The overall helix-coil transition dominates the signal, and contributions from other components involve subtle changes in the shapes of the CD

Table B.2. The variance in the pH 2.4 and pH 7.5 αS102 data sets (Figure B.5A-B) that is accounted for by each of the first five principal components (Figure B.6C-D).

Principal Component #	% Variance	
	pH 2.4	pH 7.5
1	99.822	99.732
2	0.106	0.168
3	0.030	0.068
4	0.027	0.010
5	0.005	0.007

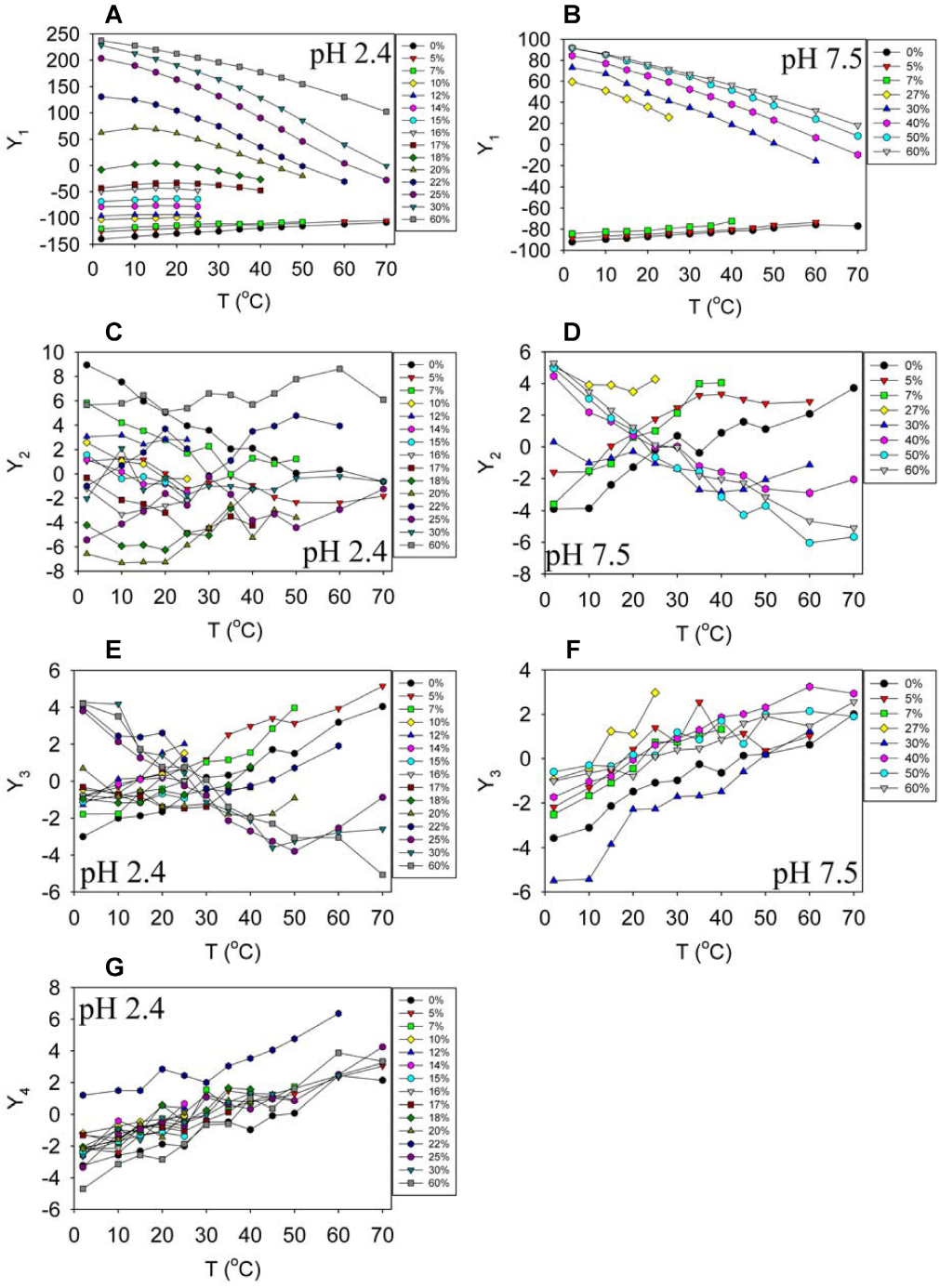

Figure B.7. The PCA scores, Y_i, vs. temperature for the significant factors for the data sets from Figure B.5A-B, where *i* is the principal component index. The [TFE] for each curve is shown in the legends. Scores are plotted for (A) pH 2.4, *i*=1, (B) pH 7.5, *i*=1, (C) pH 2.4, *i*=2, (D) pH 7.5, *i*=2, (E) pH 2.4, *i*=3, (F) pH 7.5, *i*=3, and (G) pH 2.4, *i* = 4.

spectra. Some of these changes may be a result of temperature-dependent variations in the spectra of ideal α-helices and other types of secondary structure (Wallimann, et al., 2003). Therefore, we conclude that PCA reveals temperature-related contributions to the data, which are distinguishable from TFE-induced structure, but it is unclear whether these factors correspond to a definite temperature-related "intermediate" conformation or whether they are artifacts of some sort. And, if the CD spectra of the disordered, polyproline-II-like conformation, the highly α-helical state, or the TFE-induced intermediate are temperature-dependent, it is not immediately obvious whether it makes sense to call such spectral changes an additional "state" or just consider them to be variations within a state.

APPENDIX C

SUPPORTING INFORMATION RELATED TO EGFP STRUCTURE AND AGGREGATION EXPERIMENTS

Stability of 0.3 μM EGFP samples during CD measurements

We use the NRMSD parameter (Appendix A) to quantify changes in the CD spectra during the experimental time frames. For the samples shown in Figure 4.2A-B, we verified that the spectra did not change significantly for 5 min. vs. 10 min. after TFE addition and heating (Figure C.1). Note that we omitted samples for pH 7.5 and ~20-30% TFE from Figure 4.2 and Figure C.1 because the CD spectra for these samples change rapidly with time as a result of EGFP tertiary structure disruption.

Additional principal component analysis results for EGFP CD spectra

We performed principal component analysis (PCA) on the two sets of CD spectra shown in Figure 4.2A-B (see also Chapter 4 and Figure 4.4). The first three PCA basis vectors obtained for these spectra are shown in Figure C.2A-B. For both pH values, the first and second basis vectors show smooth variations over wavelength scales that make sense for CD data, while the third basis vector appears noisy. The Scree plot (Cattell, 1966) corresponding to the pH 7.5 plot is shown in Figure C.2C. The pH 7.5 plot is somewhat ambiguous and could reflect either two or three significant factors. In contrast, the pH 2.4 Scree plot (Figure 4.4A) is consistent with the presence of two significant factors.

Plots of PCA scores as a function of TFE for each of the first three principal components are shown in Figure C.2D-I. At both pH values, the first component corresponds to the overall helical transition. For the pH 2.4 data, the second component appears to mostly reflect variations at low (<~10% TFE), and may

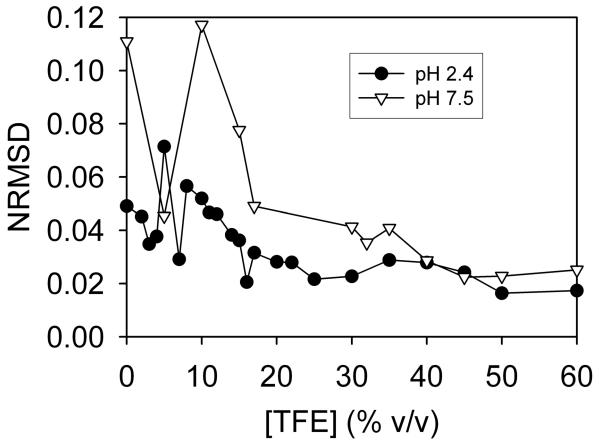

Figure C.1. NRMSD vs. [TFE] for spectra measured 5 minutes vs. 10 minutes after TFE addition and the initiation of heating for 0.3 μM EGFP samples (see also Figure 4.2A-B).

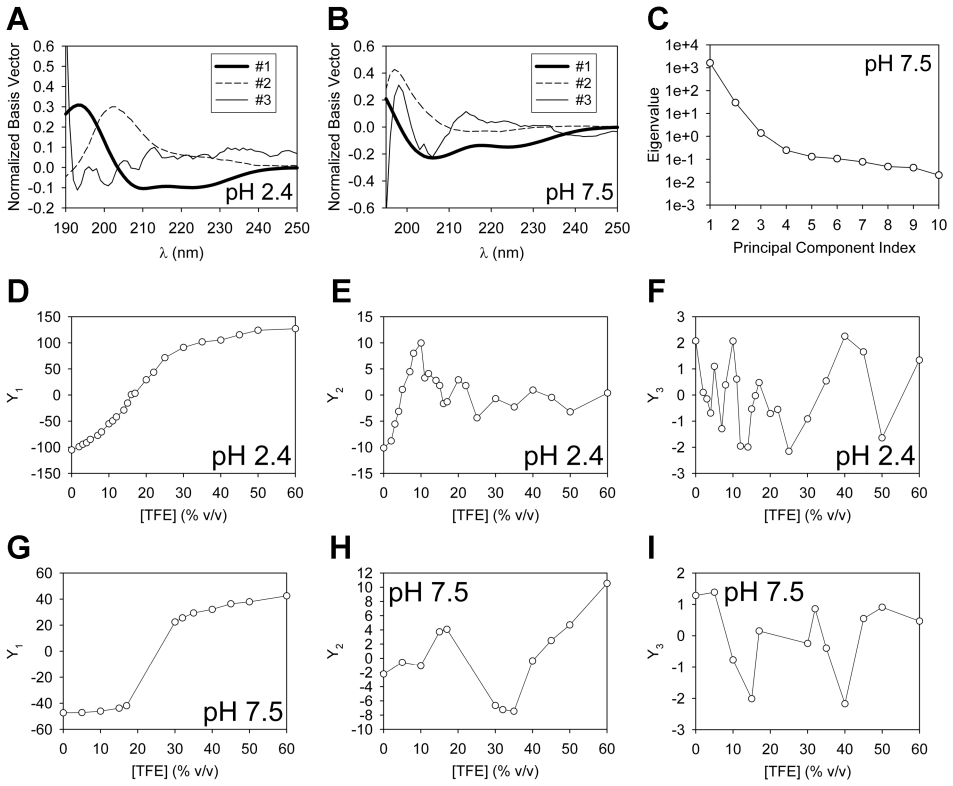

Figure C.2. Additional PCA results for EGFP CD spectra. (A-B) The first three PCA basis vectors for (A) the pH 2.4 CD spectra from Figure 4.2A, and (B) the pH 7.5 spectra from Figure 4.2B. (C) Scree plot (Cattell, 1966) showing the eigenvalue magnitudes for the PCA transformation of the pH 7.5 data (the pH 2.4 plot is shown in Figure 4.4A). (D-F) The PCA scores Y_i, reflecting the projection of the pH 2.4 spectra from Figure 4.2A onto the i^{th} PCA basis vector, for the first three PCA components. (G-I) Similar to D-F, but for the pH 7.5 spectra from Figure 4.2B.

correspond to population of the 0% TFE polyproline-II-like conformation. At pH 7.5, the second component seems to reflect intermediate-TFE variations in the shape of the spectra. For both pH values, the third component shows no definite trend with respect to TFE concentration.

Given the noisiness of the third principal component basis vectors and the lack of meaningful trends in the principal component score vs. TFE plots for this component, it seems likely that only the first two components in each case are meaningful, at least within the resolution of our CD data. However, experimental noise, low sensitivity of CD spectra to slight structural changes, or other factors could obscure additional transitions.

Temperature dependence of TFE-induced EGFP tertiary structure disruption

Figure C.3A shows the fluorescence emission from freshly-prepared EGFP solutions at room temperature (~22 °C), compared to the 37 °C data. It appears that increased amounts of TFE are required for tertiary structure disruption at lower temperatures. Notably, the 37 °C emission curves are time-dependent (Figure 4.1, Figure C.3B), and so the discrepancies are probably at least partially due to differences in unfolding rates at room temperature vs. 37 °C.

When EGFP is incubated for more than 2 days at 37 °C (in pH 7.5 PBS buffer), samples containing 5% TFE remain fluorescent and are nearly identical to 0% TFE solutions, while ≥ 10% TFE samples become dark (Figure C.3B). It is unclear whether there is a threshold below which TFE-induced tertiary structure disruption does not occur, or whether 5% TFE samples simply unfold very slowly.

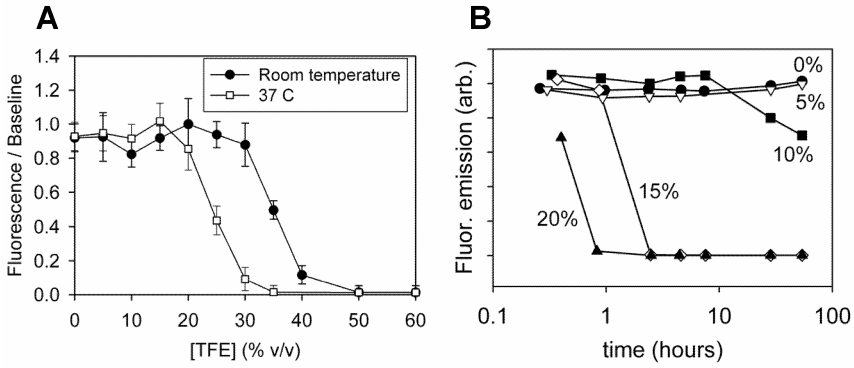

Figure C.3. TFE-induced disruption of EGFP tertiary structure is dependent on temperature and time. (A) The fluorescence emission from 0.3 μM EGFP in pH 7.5 NaPhos 2 ± 0.5 minutes after TFE was added to the samples and the samples were either incubated at room temperature (~22 °C) or placed into a 37 °C incubator. The 37 °C data is identical to that shown in Figure 4.1. (B) EGFP fluorescence emission at 507 nm vs. time after the protein was heated to 37 °C, for 25 μM protein in pH 7.5 PBS buffer (10 mM NaPhos with 154 mM NaCl). The TFE concentration for each sample is noted on the plot.

Deconvolution of EGFP CD data

We obtained estimates of secondary structural content for some of our CD spectra using the k2d (Andrade, et al., 1993), CDSSTR (Compton and Johnson, 1986; Sreerama and Woody, 2000), and CONTINLL (Provencher and Glockner, 1981; Van Stokkum, et al., 1990) algorithms, as they were implemented in the DichroWeb software package (Whitmore and Wallace, 2011; Whitmore and Wallace, 2004; Whitmore and Wallace, 2008). We compared these results to the CDSSTR and CONTINLL predictions provided by the CDPro software package (Sreerama, 2004; Sreerama and Woody, 2000). For the DichroWeb CDSSTR and CONTINLL analyses, the SP175 reference data set (Whitmore and Wallace, 2008) was used, while the SDP48 basis set (Sreerama, et al., 2000) was employed in the CDPro runs.

Both software packages required CD data for 190-240 nm. Our pH 2.4 data (Figure 4.2A) satisfied this requirement, and we examined the 0% TFE, pH 2.4 spectrum ("U" state), the inferred "I" state (Figure 4.4C), and the 60% TFE ("F" state) curves. Our 0.3 μM, pH 7.5 data (Figure 4.2B) was only reliable to 195 nm, and so we measured the pH 7.5, 0% TFE ("N" state) and 60% TFE ("F2" state) spectra for 3 μM EGFP in order to obtain data to 190 nm. The 3 μM curves matched the 0.3 μM data very well in the 260-195 nm range (NRMSD < 0.1).

Our deconvolution results are shown in Table C.1. k2d provides an estimate of only α-helical (α), β-sheet (β), and disordered (U) content, while the other algorithms resolve regular (R subscript) and distorted (D subscript) β-sheets and α-helices, and also provide estimates of turn (T) content. We also report the NRMSD value for the measured vs. predicted spectra for all the fitting methods.

The U and N state estimates in Table C.1 provide some information about the reliability of the deconvolutions. All the algorithms predict that the U state contains significant amounts of secondary structure, although EGFP is likely completely

Table C.1 Deconvolution results for EGFP CD spectra. See the text for definitions of symbols.

		pH 2.4			pH 7.5	
		U	**I**	**F**	**N**	**F2**
k2d (DichroWeb)	α	0.11	0.16	0.92	0.17	0.74
	β	0.29	0.28	0.00	0.35	0.02
	U	0.60	0.56	0.08	0.48	0.24
	NRMSD	*0.128*	*0.121*	*0.094*	*0.280*	*0.174*
CDSSTR (DichroWeb)	α_R	0.05	0.09	0.62	0.08	0.47
	α_D	0.11	0.12	0.23	0.11	0.20
	β_R	0.11	0.12	0.01	0.23	0.02
	β_D	0.11	0.09	0.00	0.11	0.01
	T	0.18	0.16	0.05	0.10	0.09
	U	0.45	0.42	0.08	0.36	0.22
	NRMSD	*0.012*	*0.021*	*0.007*	*0.015*	*0.013*
CDSSTR (CDPro)	α_R	0.032	0.101	0.591	0.085	0.538
	α_D	0.047	0.095	0.306	0.097	0.310
	β_R	0.068	0.066	0.021	0.222	0.024
	β_D	0.043	0.048	0.014	0.122	0.010
	T	0.094	0.122	0.037	0.229	0.028
	U	0.713	0.569	0.025	0.240	0.083
	NRMSD	*0.061*	*0.063*	*0.023*	*0.108*	*0.042*
CONTINLL (DichroWeb)	α_R	0.045	0.065	0.555	0.084	0.390
	α_D	0.109	0.110	0.199	0.099	0.182
	β_R	0.107	0.117	0.002	0.236	0.012
	β_D	0.109	0.103	0.000	0.113	0.023
	T	0.170	0.155	0.094	0.103	0.115
	U	0.460	0.450	0.150	0.365	0.278
	NRMSD	*0.020*	*0.098*	*0.056*	*0.128*	*0.033*
CONTINLL (CDPro)	α_R	0.027	0.099	0.603	0.097	0.462
	α_D	0.039	0.098	0.306	0.089	0.277
	β_R	0.062	0.046	0.000	0.243	0.000
	β_D	0.038	0.049	0.031	0.115	0.055
	T	0.114	0.147	0.041	0.200	0.135
	U	0.720	0.561	0.019	0.256	0.071
	NRMSD	*0.017*	*0.019*	*0.016*	*0.025*	*0.010*

denatured at pH 2.4 in the absence of TFE. CDPro appears to provide a slightly better estimate for the U state structure, as might be expected given that the SDP48 basis set includes denatured proteins, although even these predictions probably overestimate the secondary structural content. In addition, our measured N state spectrum is highly consistent with the expected CD curve for a "β-can" fluorescent protein (Visser, et al., 2002), but deconvolutions of this spectrum underestimate its β-sheet content and overestimate disordered and helical structure. Interestingly, the CDPro SDP48 basis set contains the green fluorescent protein, while the DichroWeb SP175 basis set does not, but the CDPro structure predictions appear to be only slightly better than the DichroWeb fits, and the NRMSD value for CDPro's CDSSTR prediction is actually increased relative to the DichroWeb CDSSTR result. When we used reference sets containing green fluorescent protein with the DichroWeb program, we obtained predictions that were very similar to the CDPro results, including the increase in NRMSD for the CDSSTR algorithm. Therefore, the NRMSD parameter is of limited value in comparing fit results, which is consistent with previous reports that agreement between the calculated and actual CD spectra is a poor measure of the reliability of structure estimations (Greenfield, 1996). Given these observations, we use the information in Table C.1 to identify trends in the predictions, but we cannot definitively resolve the secondary structural content of the protein, and we cannot determine which estimate is most accurate.

All the deconvolution algorithms predicted an increase in α-helical structure for the I state compared to the U state, while the amount of β-sheet and turn content was reported to decrease or to increase very slightly. The CDPro estimates predict relatively large amounts of helical content for the I state, and we believe these predictions are probably more reliable than the DichroWeb results, based on the U

state estimates from both software packages. The 60% TFE states (F and F2) were estimated to be highly helical, as expected from inspection of these curves.

In sum, our EGFP spectra deconvolution results are consistent with an increase in helicity for the I state compared to the U state, but the absolute predictions of structural content are unreliable. Higher resolution techniques are necessary to definitively identify structural features of partially structured conformations.

Figure C.4. TEM images of EGFP aggregates grown in various solution conditions. The scale bar is 200 nm and all images are shown at the same magnification. The pH 7.5 samples contained 10 mM NaPhos buffer, the pH 2.4 samples contained 10 mM phosphoric acid, and the pH 9.3 sample containeded 10 mM borax. Unless otherwise specified, 50 μM EGFP samples were incubated at 37 °C in quiescent conditions. (A) Flexible thin fibril aggregates grown at pH 2.4 with 75 mM NaCl and 15%TFE after 24 hrs incubation (see also Figure 4.6B). (B-C) Thin fibrils grown at pH 7.5 with 30% TFE after 24 hrs. (D) Similar to B, but the sample contained 60% TFE. (E-F) Rigid fibrils grown in pH 2.4 solutions containing no TFE, after 3 weeks incubation with shaking. (G) Flexible fibrils grown from a sample similar to E, but with 154 mM NaCl. (H-J) Similar to E, but after 7 weeks incubation (see also Figure 4.6F-G). (K) Rigid and flexible fibrillar aggregates grown from 150 μM EGFP at pH 7.5 with 15% TFE, after 3 weeks incubation with shaking. (L-M) Rigid and flexible fibrillar aggregates found after 2 weeks incubation with shaking, in pH 7.5 solutions with 15% TFE that had been seeded by adding a small fraction (~6%) of neutralized solution from the sample shown in H. (N-O) Thin fibrils grown at pH 7.5 with 15% TFE, after three weeks incubation with shaking. (P) Similar to N, but for pH 9.3.

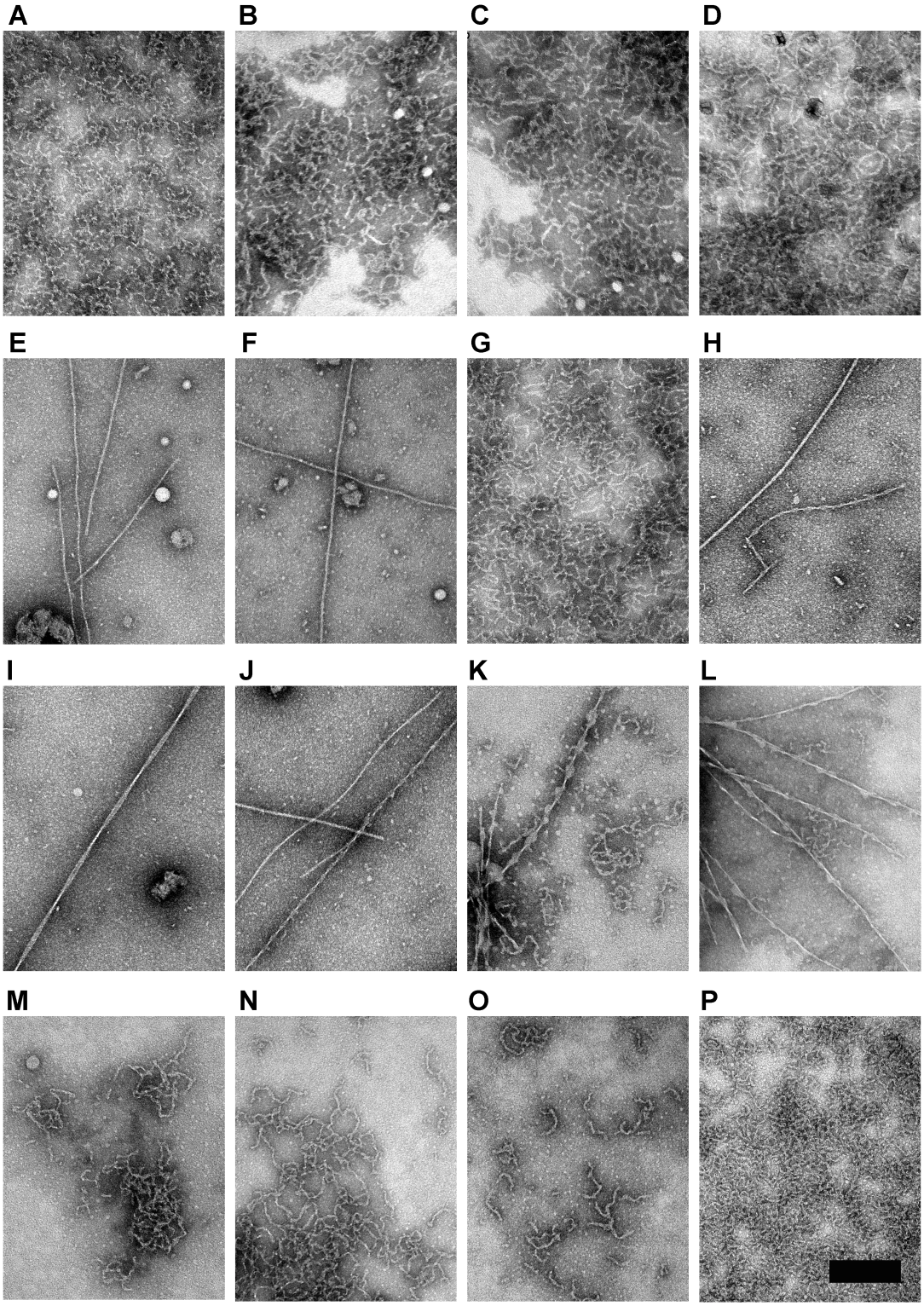
A
B
C
D
E
F
G
H
I
J
K
L
M
N
O
P

APPENDIX D

CHARACTERIZATION OF FLUORESCENT TAGS FOR USE IN AMYLOID PROTEIN AGGREGATION STUDIES

Motivation and Summary

Fluorescent tags are commonly used to monitor proteins and peptides in microscopy and spectroscopy experiments. In the context of amyloid aggregation, it is necessary to investigate potential perturbations of the aggregation pathway due to the presence of the label. In this Appendix, I present fluorescence and transmission electron microscope (TEM) characterization of fluorescently-labeled amyloid β 1-40 (Aβ40) peptide and α-synuclein (αS) protein. For Aβ40, three extrinsic fluorophores (AMCA, TAMRA, and Hilyte Fluor 488) were examined, while αS was labeled with both a small organic dye (Alexa Fluor 488) and enhanced green fluorescent protein (EGFP). Fibrils were grown in diverse solution conditions in order to determine whether the presence of the fluorophore precludes adoption of a significant subset of the wide array of possible amyloid fibril ultrastructures for these proteins/peptides (Anderson, et al., 2010; El-Agnaf, et al., 1998; Giasson, et al., 1999; Giehm, et al., 2010; Kodali and Wetzel, 2007; Pedersen and Otzen, 2008; Wetzel, et al., 2007).

My TEM images show that several extrinsic fluorescent labels do not preclude the formation of amyloid deposits of varying morphologies for Aβ40 and αS. These results are in accordance with previous studies of Amyloid β 1-42, which showed that extrinsic fluorophore labeling does not prevent the formation of classic amyloid aggregates (Chafekar, et al., 2008; Jungbauer, et al., 2009; Saavedra, et al., 2007; Webster, et al., 2001). Furthermore, I measured the two-photon action cross section of the Hilyte Fluor 488-labeled Aβ40 peptide and verified that this construct is suitable for two-photon microscopy and spectroscopy applications.

In contrast, fluorescent protein labeling of αS appears to favor the formation of two types of rigid aggregates when protein solutions are incubated near physiological pH. Notably, a previous paper demonstrated that a yellow fluorescent protein (YFP) label did not prevent the formation of at least one type of αS amyloid fibril (Van Ham, et al., 2010). However, it is unclear whether the EGFP tertiary structure remains intact in the αS-EGFP fibrils. In addition, my preliminary experiments suggest that filtering solutions to remove oligomers and insoluble material may prevent aggregation of αS-EGFP, and therefore fibrillization may be nucleation-dependent. Additional investigations will be required to fully understand the fibril structures and aggregation pathways for the αS-EGFP construct.

Moreover, the tertiary structure of EGFP can be disrupted by incubation in acidic or basic solutions (Bokman and Ward, 1981) or via the addition of the fluorinated alcohol TFE (2,2,2-trifluoroethanol) (see Chapter 4). I find that disruption of the EGFP tag modifies the aggregation properties of the αS-EGFP construct, as might be expected. When αS-EGFP is incubated in acidic (pH 2.4), low ionic-strength solutions, long, rigid fibrils are formed. The addition of 154 mM NaCl to these acidic solutions results in the formation of both flexible and rigid fibrils. Flexible fibrils are also formed in solutions containing ~10-15% (all TFE percentages v/v) TFE. Therefore, although the EGFP tag does not prevent aggregation of the αS-EGFP construct, the fibrillization pathway is affected by the conformation of the fluorescent protein label. Also, some αS-EGFP fibrils formed under denaturing conditions are similar to those observed for EGFP alone (Chapter 4), implying that properties of the fluorescent protein tag may dominate the aggregation reaction at low pH and/or moderate-to-high TFE. Thus, caution must be used when employing fluorescent protein tags to study αS aggregation reactions in potentially denaturing conditions.

Materials and Methods

Solutions and Reagents: Acros Organics brand 99.8% pure TFE was purchased from Fisher Scientific. MilliQ or HPLC grade water was used to prepare all solutions. Trizma brand pre-set pH 7.7 crystals (Sigma) were used to prepare Tris buffers that were pH ~7.4 at 37 °C. Temperature-dependent changes in the pH of other buffer solutions were ignored. Sodium azide (Sigma) at ~0.02% w/v was added to all solutions incubated at ≥ 20 °C for over 24 hours. A benchtop orbital shaker operating at 200 RPM was used to agitate some samples during incubation.

Aβ40 Preparation / Solubilization: The three tags for the Aβ40 peptide that are discussed in this appendix are Hilyte Fluor 488, TAMRA (5-carboxytetramethylrhodamine), and AMCA (7-Amino-4-methylcoumarin-3-acetic acid). N-terminally fluorophore-labeled, synthetic Aβ40 peptides were purchased from Anaspec. The subsequent preparation roughly followed the protocol from (Bitan and Teplow, 2005). Briefly, the lyophilized peptides were dissolved at ~1 mg/mL in 2 mM NaOH, and then these solutions were flash-frozen in liquid nitrogen and re-lyophilized. Final solubilization was accomplished by dissolving the powder into 10 mM, pH 10 carbonate buffer and filtering through YM-30 or YM-50 Microcon filters (Millipore). An exception to this procedure is shown in Figure D.1A; for this sample, 0.1 mg of Hilyte Fluor 488-labeled Aβ40 was dissolved directly into water.

Alexa Fluor 488 labeled αS Preparation / Solubilization: Alexa Fluor 488 was purchased from Invitrogen, and labeling was generously performed by Trudy Ramlall and Prof. David Eliezer of Weill Cornell Medical College, using previously described procedures (Rhoades, et al., 2006). However, serine-to-cysteine mutations and labeling at position 9 were performed on A30P and A53T, in addition to WT αS. Furthermore, C-terminal labeling of WT and A30P αS was also investigated via a glutamate-to-cysteine mutation at position 130. Free dye was removed from the

samples by dialysis vs. 10 mM pH 7.5 sodium phosphate (NaPhos) buffer using Slide-A-Lyzer 10,000 MW cutoff dialysis cassettes (Thermo-Fisher Scientific).

αS-EGFP Expression: Vectors for mammalian expression of the αS-EGFP construct were a kind gift from Professor Bradley Hyman of Massachusetts General Hospital Medical School at Harvard University; information about this construct can be found in (McLean, et al., 2001). Transformation into a bacterial vector and subsequent protein expression was performed by Dr. Cynthia Kinsland and the Cornell University Life Sciences Core Laboratories Center Protein Production Facility.

Plasmid DNA was purified with the Qiagen Miniprep kit. E. coli strain MachI (Invitrogen) was used as a recipient for transformations during plasmid construction and for plasmid propagation and storage. PCR was performed with Phusion DNA polymerase (New England Biolabs) per the manufacturer's instructions. DNA oligonucleotides were ordered from IDT DNA. Site-directed mutagenesis was performed by a standard PCR protocol using PfuTurbo DNA polymerase per the manufacturer's instructions (Agilent) and DpnI (New England Biolabs) to digest the methylated parental DNA prior to transformation.

Site-directed mutagenesis was performed on the provided plasmid to introduce a 6xHisTag at the C-terminus of the αS-EGFP fusion protein. The primers used for mutagenesis were: 5'-GGC ATG GAC GAG CTG TAC AAG CAC CAT CAC CAC CAT CAC-3' and 5'-CTA GAG TCG CGG CCG CTT TAG TGA TGG TGG TGA TGG TGC TT-3'. After transformation, colonies were screened for the presence of the HisTag by PCR using the following primer pair: 5'-GGG ATC CAT CGC CAC CAT GG-3' and 5'-CGC GGC CGC TTT AGT GAT GG-3'. A plasmid which screened correctly was verified by sequencing. The final construct was based on the cloning vector EGFP-N3, with αS fused to the N-terminus of EGFP and a 6xHisTag fused to the C-terminus of EGFP.

The fusion construct described above was moved into a vector for *E. coli* expression by using the following primer pair: 5'-GGG TAG CAT ATG GAT GTA TTC ATG AAA GGA CTT TC-3' and 5'-CCC TAC TCG AGT TAG TGA TGG TGG TGA TGG TGC-3'. Following amplification, the PCR product was digested with *Nde*I and *Xho*I and ligated into a similarly digested pTHT vector, resulting in an additional 6xHisTag added to the N-terminus of the total fusion construct. pTHT is a homemade vector which is equivalent to pET-28 (Novagen) with a TEV protease recognition site in place of the thrombin recognition site.

Plasmids were transformed into BL21Star (DE3) cells (Stratagene) harboring the pRARE2 plasmid (Novagen) and selected on kanamycin/chloramphenicol media at all stages. Protein expression in shake flasks was performed as described in the pET-system manual, with induction by IPTG (1mM) at reduced temperature (15 °C) and overnight incubation post-induction. Cells were harvested by centrifugation, lysed by sonication and HisTagged protein was purified on 5 mL HisTrap HP columns (GE) using an AKTA FPLC. Buffers used for purification were A) Binding: 20 mM Tris, pH 8.0, 500 mM NaCl, 30 mM Imidazole. B) Elution: 20 mM Tris, pH 8.0, 500 mM NaCl, 500 mM imidazole. The column was washed with A until the A280 had returned to baseline and was then washed with 10% B in A and 15% B in A. For both washes, the wash was continued until the baseline had stabilized (several column volumes). The protein was then eluted in 100% B.

αS-EGFP Dialysis and Buffer Exchange: To prepare the samples shown in Figure D.4, which were buffered with Tris containing 100 mM NaCl or PBS (10 mM pH 7.5 NaPhos with 154 mM NaCl), the eluted protein was dialyzed into the buffer using 10,000 MWCO Slide-A-Lyzer casettes (Pierce).When dialyzed into PBS, the protein partially precipitated, and visible white material was removed from these solutions by centrifugation for 30 minutes at 13,000 x g. The pellet was collected and

used to "seed" some samples (e.g. Figure D.4G-I). Some aliquots of the dialyzed protein solutions were spin filtered using YM-100 Microcon filters (Millipore) in order to obtain mostly monomeric stock solutions. When necessary, filtered solutions were concentrated using Amicon YM-10 filters (Millipore).

For the samples shown in Figure D.6, filtering was performed using a 0.22 μm syringe filter (Millex-GV, Millipore), followed by filtering with YM-100 Microcon filters (Millipore). Buffer exchange into water was performed using Amicon YM-10 filters (Millipore), and the αS-EGFP stocks were diluted into buffer or acid prior to incubation.

Spectroscopy: Fluorescence emission and absorbance spectra were collected following the procedures described in Chapter 4. All fluorescence emission signals were normalized to the emission from EGFP in PBS at room temperature.

Determination of Protein Concentrations: UV or visible light absorbance measurements via a double-beam a Cary-300 spectrophotometer (Varian) were used to quantify the amount of protein in the stock solutions. Table D.1 shows the peak wavelengths and extinction coefficients for the fluorophores examined in this Appendix. The protein concentration was assumed to be the same as the fluorophore concentration in all cases.

Transmission Electron Microscopy Imaging: The general procedure for the TEM sample preparation and imaging is described in (Anderson, et al., 2010). Slight variations of these techniques were employed to obtain some of the images, including the occasional use of homemade butvar grids (both carbon-coated and uncoated butvar grids were employed), and the rare use of 1% (w/v) uranyl acetate, rather than 2% (w/v) phosphotungstic acid, stain. These differences in methodology did not significantly affect the imaging results.

Table D.1. Wavelengths (λ) of the absorbance peaks and the molar extinction coefficients (ε) at the peaks for the fluorescent tags examined in this Appendix. The EGFP value is from Lybarger, et al. (Lybarger, et al., 1998). For the extrinsic small molecule tags, the extinction coefficients were provided by the manufactures of the tags and/or the labeled peptides (Anaspec for Hilyte Fluor 488, AMCA, and TAMRA, and Molecular Probes for Alexa Fluor 488).

Fluorophore	λ (nm)	ε (M^{-1} cm^{-1})
EGFP	488	55,000
Alexa Fluor 488	492	72,000
Hilyte Fluor 488	502	85,000
AMCA	350	19,000
TAMRA	554	65,000

Two-Photon Action Cross Section Measurements: A pulsed titanium sapphire Mai Tai laser (Spectra Physics) was used to excite the fluorophores over the wavelength range of 760-1000 nm. The excitation and emission light were focused through a 63x, 1.2 NA water immersion C-Apochromat objective lens (Zeiss) into ~100 nM peptide samples, which were mounted on an inverted microscope (IX71, Olympus). The intensity of the excitation beam was measured using a photodiode, while the intensity of the emitted fluorescence was detected using a gallium arsenide phosphide photomultiplier tube (Hamamatsu). Linear fitting to the emitted light vs. incident intensity squared curves were performed at each measured wavelength and the resultant slopes were normalized to the values for a pH 11 fluorescein standard (Xu, et al., 1996) in order to determine the two photon action cross section for the unknown fluorophores.

Extrinsic Dye-Labeled Aβ40 Aggregates

After incubation in aggregation-promoting conditions, fluorescent clumps are often apparent by eye in the bottom of solutions containing Aβ40 constructs that are tagged with TAMRA or Hilyte Fluor 488 at the N terminus of the peptide. The supernatants of these solutions are fluorescent prior to aggregation, and become clear or nearly clear after incubation. The fluorophore AMCA emits in the UV, but similar aggregation behavior for Aβ40 labeled with this dye were observed when the peptide solutions were placed in a spectrophotometer. Therefore, Aβ40 aggregates grown in these solutions are fluorescent, and I used TEM to examine their ultrastructures.

Figure D.1 shows TEM images of aggregates grown from labeled Aβ40. Various fibril types are apparent, including thin flexible “protofibrils,” standard amyloid fibrils 9-12 nm in diameter, and wider, multi-stranded fibrils. Thus, labeling with these fluorophores does not prevent the formation of many types of amyloid

Figure D.1. TEM images of protofibrils and fibrils grown from Aβ40 labeled with three extrinsic fluorescent dyes. Each column shows aggregates for one fluorophore, and the images are arranged to show a rough progression from flexible protofibril-like species (top rows) to thicker rigid aggregates (bottom rows). The scale bar is 200 nm wide and all images are shown at the same magnification. Unless otherwise noted, the samples were incubated at room temperature under quiescent conditions. (A) Protofibrils in a sample containing ~200 μM Hilyte Fluor 488-Aβ40 in water, after 7 days' incubation. (B) Rigid fibrils and flexible protofibrils grown in a solution containing 16 μm Hilyte Fluor 488-Aβ40 in 50 mM pH 7 NaPhos buffer with 40 mM NaCl, after incubation for 1 month. (C) Fibrils grown from a solution containing 15 μM Aβ40 in 100 mM, pH 7 NaPhos buffer after 8 weeks. (D) Twisted fibrils grown from 10μM Aβ40 after 1 month incubation in 50 mM pH 6 NaPhos buffer. (E) Rigid fibrils with various widths and helicities present in a solution containing Hilyte Fluor 488-Aβ40 in 50 mM, pH 7 NaPhos buffer with 5% TFE, after ~2.5 months' incubation. (F)-(G) A combination of flexible protofibrils and rigid amyloid fibrils grown from 25 μM TAMRA-Aβ40 incubated for 14 days at 37 °C with 200 RPM shaking in 50 mM pH 7 NaPhos buffer with 10% TFE. (H) Twisted fibrils present in solutions containing 50 μM TAMRA-Aβ40 in 100 mM pH 7 NaPhos buffer after 8 weeks' incubation. (I) Twisted fibrils present in solutions containing 53 μM TAMRA-Aβ40 in 50 mM pH 7 NaPhos buffer with 5 % TFE after ~3 months incubation. (J) Wide fibrils grown from 50 μM TAMRA-Aβ40 in 50 mM pH 6 NaPhos after 5 months' incubation. (K) Flexible protofibrils grown from 25 μM AMCA-Aβ40 incubated for 14 days at 37 °C with 200 RPM shaking in 50 mM pH 7 NaPhos buffer containing 10% TFE. (L) Straight fibrils grown in identical solutions as K, except the samples were incubated overnight at 37 °C with 200 RPM shaking, followed by 37 days at room temperature under quiescent conditions. (M) Twisted fibrils present in solutions containing 10 μM AMCA-Aβ40 in 50 mM, pH 6 NaPhos buffer, after incubation for 1 month. (N) Twisted fibrils grown from 20 μM AMCA-Aβ40 in 50 mM, pH 7 NaPhos buffer with 100 mM NaCl, after 1 month. (O) Same as N, but without NaCl.

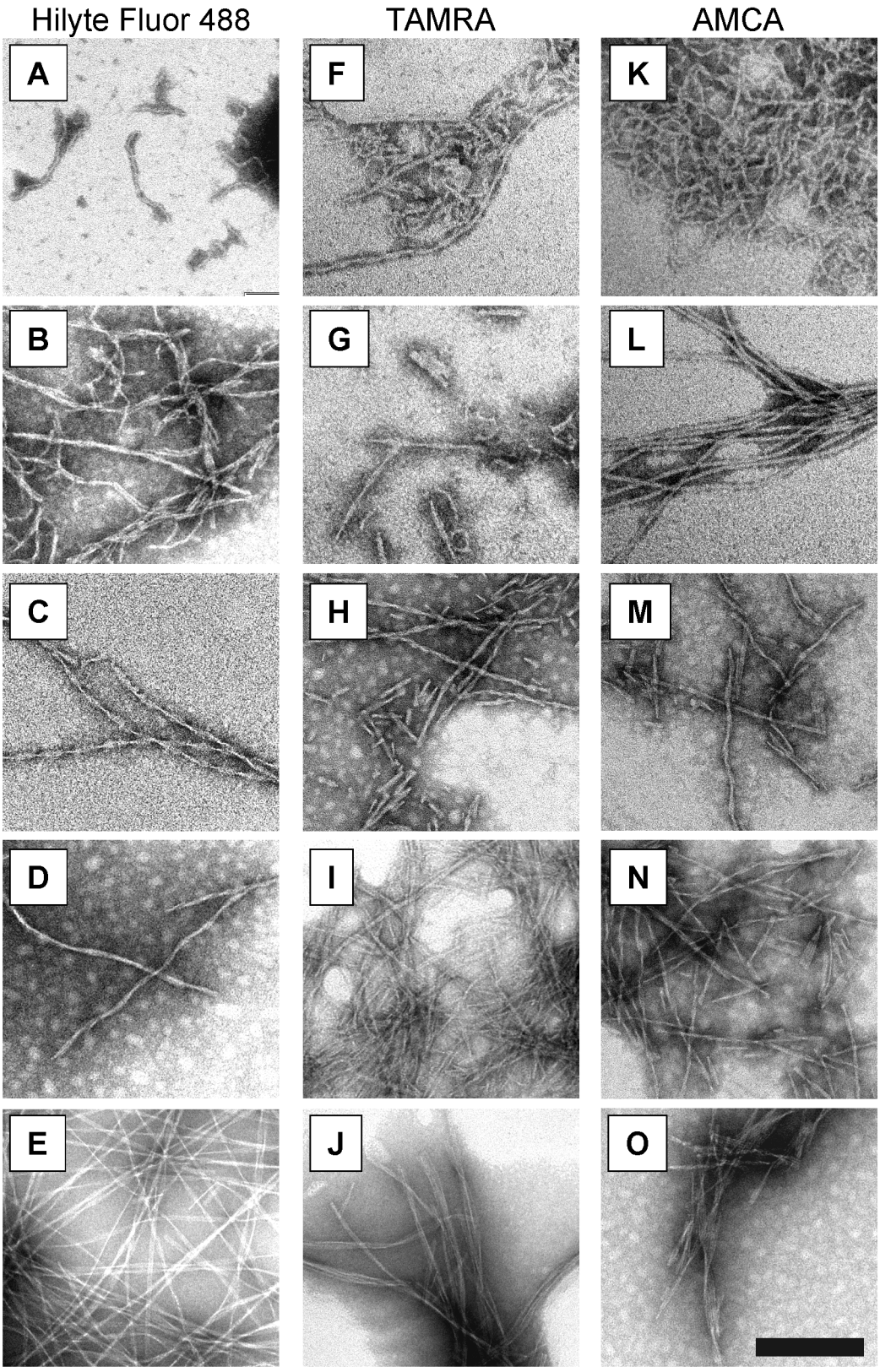
Hilyte Fluor 488
TAMRA
AMCA
A
F
K
B
G
L
C
H
M
D
I
N
E
J
O

aggregates. In general, samples with higher concentrations of peptide and lower ionic strengths are more likely to form protofibrils, while wider fibrils are prevalent at high ionic strengths. However, details of the solution preparations cause variations in fibril types and morphologies are not wholly reproducible.

Potential applications of these labeled peptides include two-photon imaging and two-photon fluorescence correlation spectroscopy. The two-photon action cross sections of AMCA and TAMRA are sufficient for these applications (Makarov, et al., 2008; Neu, et al., 2002; Wang, et al., 2010), but the cross section for Hilyte Fluor 488, which is an analogue of Alexa Fluor 488, had not been previously determined, as far as I know. Therefore, I measured the two photon action cross section for Hilyte Fluor 488-Aβ40, and compared this curve to the free Alexa Fluor 488 dye cross section (Figure D.2). Although the absorption peaks are shifted for the two fluorophores, Hilyte Fluor 488 is a good two-photon probe at ~660-820 nm and ~940-1000 nm. In sum, these observations indicate that AMCA, TAMRA and Hilyte Fluor 488 are reasonable tags for use in Aβ40 aggregation studies that involve single- and two-photon fluorescence techniques.

Alexa-488-αS Aggregates

Aggregates grown from αS variant proteins labeled with Alexa Fluor 488 are also visible by eye, especially when TFE is present in the solutions. When these fluorescent aggregates are imaged using TEM, both classic amyloid and "TFE fibrils" (see Chapter 2) are detected (Figure D.3).

In addition, Figure D.3 reveals that the Alexa Fluor 488 labeled αS variants form aggregates with diverse ultrastructures, including TFE fibrils, rigid strands with no apparent twist, and fibrils that appear to consist of pairs of strands wrapped around each other. Therefore, the Alexa Fluor 488 label does not prevent the formation of

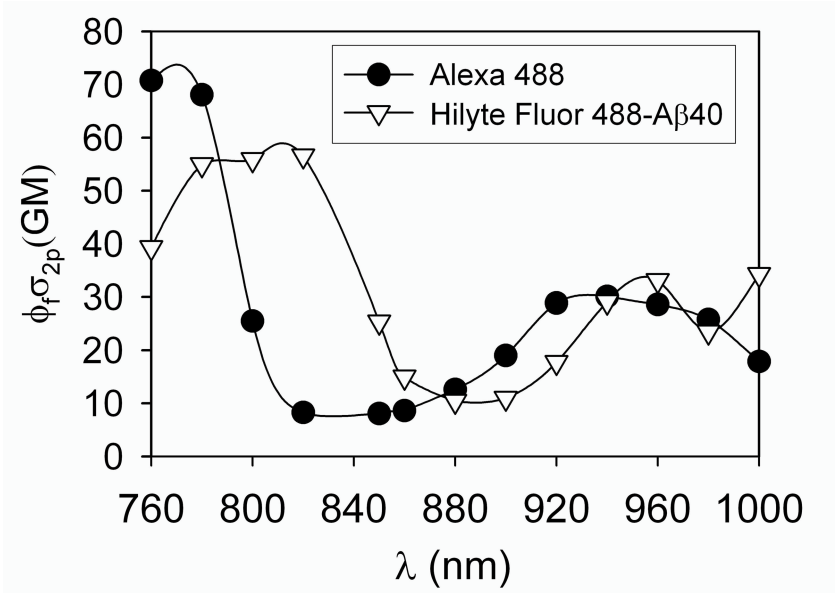

Figure D.2. Two-photon action cross section ($\phi_f\sigma_{2p}$) of Hilyte Fluor 488-labeled Aβ40, compared to the curve for Alexa Fluor 488 free dye. The units for the cross section are Goeppert-Mayer (GM), where 1 GM = 10^{-50} cm^4 s $photon^{-1}$.

Figure D.3. TEM images of aggregates grown in various solution conditions from αS variants labeled with Alexa Fluor 488. The scale bar is 200 nm wide and all images are shown at the same magnification. All samples were incubated in the presence of 10 mM Naphos, pH 7.5, but some samples contained additional TFE and/or NaCl, as noted. (A) Thin, rigid fibrils grown from 43 μM WT/E130C-Al488 αS in the presence of 154 mM NaCl after incubation for 8 days at 37 °C with shaking. (B) Thin, rigid fibrils grown from 43 μM WT/S9C-Al488 αS in the presence of 154 mM NaCl and 5% TFE after incubation for 8 days at 37 °C with shaking. (C) Thin, rigid fibrils grown from 50 μM A30P/E130C-Al488 in the presence of 154 mM NaCl after incubation for 2 weeks at 37 °C with shaking. (D) Similar to C, except fibrils were grown from A53T/S9C-Al488 αS. (E) Similar to C, except 5% TFE was added to the solution. (F) Fibrils of varying helicities grown from A53T/S9C-Al488 αS incubated in the presence of 154 mM NaCl and 5% TFE. (G-I) TFE fibrils, twisted, rigid fibrils and straight, rigid fibrils grown from 50 μM A30P/ E130C-Al488 αS with 5% TFE, after incubation for 10 days at 37 °C with shaking. (J) TFE fibrils and rigid fibrils grown from 43 μM WT/E130C-Al488 αS in the presence of 154 mM NaCl and 5% TFE after incubation for 8 days at 37 °C with shaking. (K) TFE fibrils grown from 43 μM WT/S9C-Al488 αS in the presence of 154 mM NaCl and 15% TFE after incubation for 36 days at 25 °C under quiescent conditions. (L) TFE fibrils grown from 50 μM WT/E130C-Al488 αS in the presence of 154 mM NaCl and 10% TFE after 2 weeks' incubation at 25 °C under quiescent conditions. (M) TFE fibrils grown from 50 μM WT/E130C-Al488 αS with 5% TFE after incubation for 1 week at 25 °C under quiescent conditions. (N) TFE fibrils grown from 50 μM A30P/S9C-Al488 αS with 10% TFE after 10 days' incubation at 37 °C with shaking. (O) TFE fibrils grown from 50 μM A30P/E130C-Al488 αS after 10 days' incubation at 37 °C with shaking.

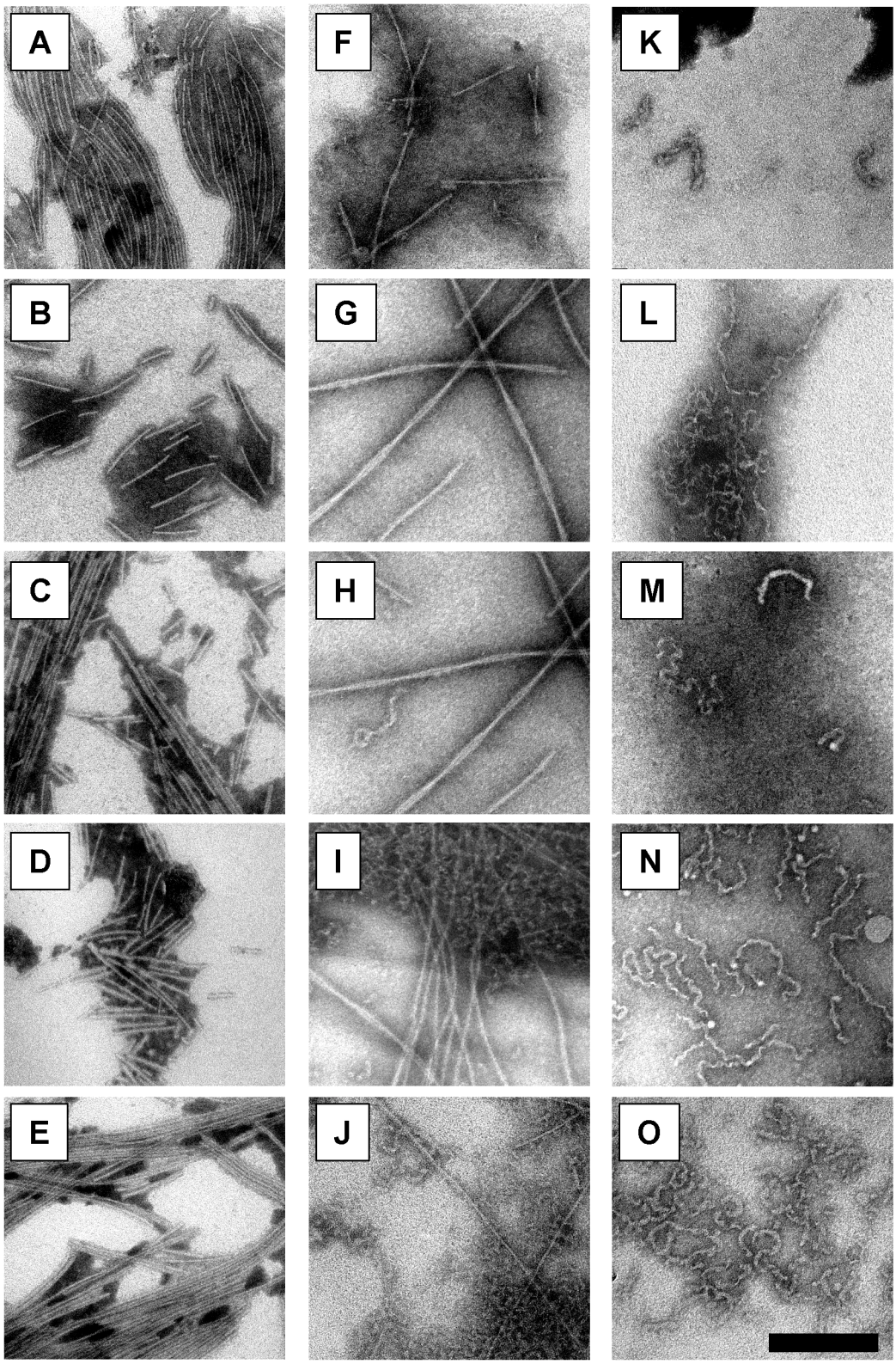
A
F
K
B
G
L
C
H
M
D
I
N
E
J
O

multiple types of αS aggregates. However, these images do not enable direct comparisons of the aggregation properties because of variability in solution conditions and incubation times, as well as the possible presence of pre-aggregated material or oligomeric species in the stock solutions. Therefore, more detailed studies are necessary to determine whether labeling or label location has any subtle effects on aggregation pathway selection.

EGFP-αS Aggregates

When solutions containing 75 μM and 150 μM αS-EGFP in PBS were prepared using unfiltered αS-EGFP stock solutions, fibrils were apparent and plentiful (Figure D.4A-C). However, fibrils were not found for filtered (100 kDa cutoff) stock solutions when all other solution conditions, including incubation time and protein concentration as measured by UV absorbance at 488 nm, were held constant. Similar results were obtained for αS-EGFP in Tris buffer with 100 mM NaCl. When the Tris stock solution was filtered, fibrils were not observed via TEM for a 34 μM sample incubated for 30 days at 37 °C. However, the addition of a small amount (~4 μM out of 34 μM total) of dialyzed, unfiltered protein to the sample resulted in the formation of αS-EGFP fibrils (Figure D.4D-E).

Additional images of αS-EGFP fibrils gown from seeded or unfiltered solutions at pH ~7.5 in various buffer conditions are shown in Figure D.4E-I. Interestingly, these fibrils appear to have a thin, straight core (~5-7 nm in diameter) around which winds a somewhat indistinct or blurry helix. The total fibril diameter is ~22 nm, and the helical period is variable, ranging from ~140 nm to over 300 nm. In some samples (Figure D.4B,C,E), shorter, untwisted, multi-stranded rigid fibrils were also observed.

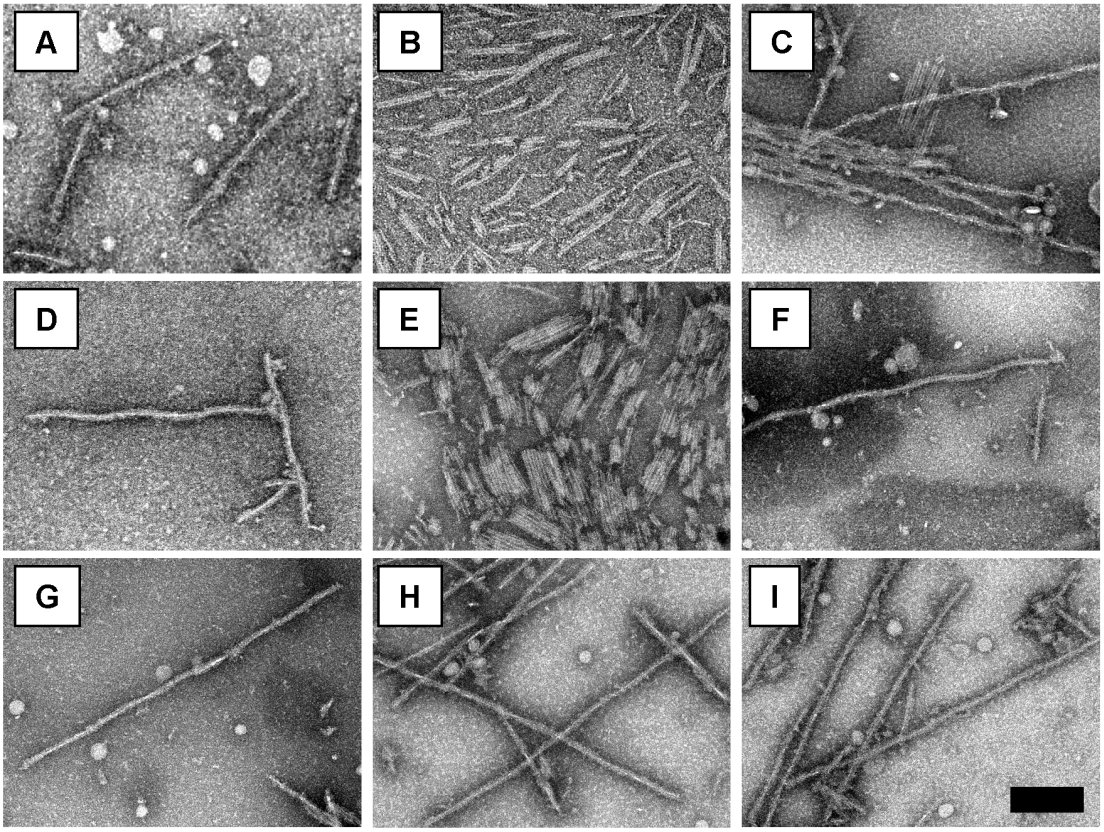

Figure D.4. TEM images of aggregates found in solutions that were prepared using unfiltered or seeded αS-EGFP stocks. The scale bar is 200 nm wide and all images are shown at the same magnification. (A-B) Aggregates grown from 75 μM unfiltered αS-EGFP in pH 7.5 PBS incubated for 3 weeks with shaking at 37 °C. (C) Same as A, but the solution contained 150 μM αS-EGFP. (D-E) Fibrils grown in a solution containing 30 μM filtered αS-EGFP, plus ~4 μM unfiltered αS-EGFP "seed", in pH 7.4 Tris buffer with 100 mM NaCl, incubated at 37 °C with shaking for one month. (F) Fibrils grown from 20 μM unfiltered αS-EGFP in pH 7.4 Tris buffer with 100 mM NaCl, after one month incubation at 37 °C with shaking. (G-I) Fibrils grown from 150 μM filtered αS-EGFP plus ~ 8 μM unfiltered αS-EGFP "seed", in pH 7.5 PBS buffer, after incubation for one month at 37 °C with shaking.

Although TEM imaging is not a quantitative technique, these preliminary results suggest that "seeding" samples with unfiltered or pre-aggregated material may promote fibril formation. However, additional experiments must be done to verify this result.

When αS-EGFP solutions containing fibrils are examined by eye, they appear uniformly fluorescent, unlike the extrinsic fluorophore-labeled samples in which fluorescent aggregated material is clearly visible at the bottom of the tubes. This may be a result of αS-EGFP fibrils remaining suspended in solution, or the fibril fraction may be a minor component of the sample. Alternatively, the EGFP tag may be quenched or altered in the αS-EGFP fibrils. Interestingly, van Ham, et al. observed a reduction in fluroescence for fibrils formed from YFP-labeled αS, which they attribute to energy migration Förster resonant energy transfer (also known as homoFRET), rather than disruption of the YFP tertiary structure (Van Ham, et al., 2010). It is currently unclear whether the αS-EGFP fibrils preserve the EGFP tertiary structure or involve unfolding of the EGFP tag prior to fibrillization.

Fluorescent protein tertiary structure can be disrupted by extremes of pH (Bokman and Ward, 1981) and by the addition of moderate-to-high concentrations of TFE (Chapter 4). Loss of native tertiary structure results in loss of green fluorescence and a shift in the absorbance peak (Bokman and Ward, 1981; Ward and Bokman, 1982). In Figure D.5A, I show that the spectral features of acid-denatured αS-EGFP are similar to those of EGFP alone. In addition, the presence of $\geq\approx$10% TFE results in loss of fluorescence for the αS-EGFP construct (Figure D.5B), as was previously observed for EGFP (Chapter 4). Note that, although loss of green fluorescence reflects disruption of EGFP tertiary structure, the acid-denatured state of αS-EGFP is likely to be significantly different from the TFE-denatured state. In particular, acidic conditions

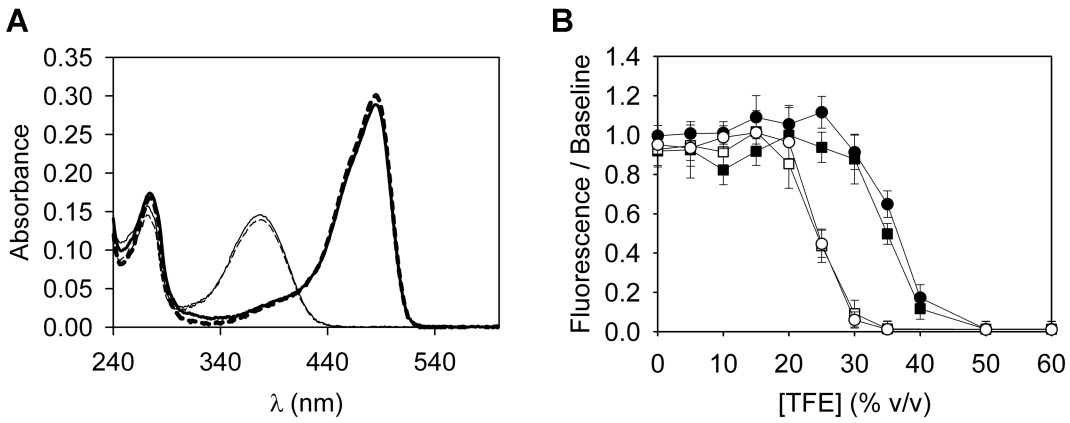

Figure D.5. Spectral properties of the αS-EGFP construct. (A) Absorbance spectra of αS-EGFP (dashed lines) and EGFP (solid lines). Spectra are shown for 5 μM protein in 10 mM phosphoric acid (pH 2.4, thin lines) and 10 mM, pH 7.5 NaPhos buffer (thick lines). (B) The normalized fluorescence emission from αS-EGFP (squares) and EGFP (circles) as a function of TFE concentration (in % v/v for samples mixed at room temperature). The signal from 0.3 μM protein is measured after a 2.0 ± 0.5 minute incubation at room temperature (~22 °C, solid symbols) or 37°C (open symbols). The error bars show the standard deviations of measurements of three identical samples.

populate a "statistical coil" or disordered conformation, while ≥ 15% TFE likely promotes the formation of non-native α-helical secondary structure (Chapter 4).

Figure D.6 shows TEM images of aggregates grown from αS-EGFP in conditions in which the EGFP tag is likely to be denatured. In low ionic strength, pH 2.4 solutions, rigid, amyloid-like fibrils ~12 nm in diameter were observed (Figure D.6A-B). However, the inclusion of 154 mM NaCl in these solutions resulted in the formation of thin, flexible fibrils (Figure D.6C). Notably, these aggregates are similar to those observed for EGFP alone at pH 2.4 (Chapter 4 and Appendix C).

αS-EGFP solutions appear clear or cloudy-white after incubation for > 24 hours in the presence of 15% TFE. TEM examination of these samples reveals a combination of amorphous aggregates, thin, flexible, fibrillar aggregates, and rigid fibrils that resemble classical amyloid (Figure D.6D). Prolonged, room-temperature incubation of αS-EGFP in the presence of 10-15% TFE resulted in the formation of short, flexible aggregates (Figure D.6E-G). When a combination of acidic conditions and TFE were employed, both short, disordered, fibrillar aggregates and rigid fibrils were observed (Figure D.6H-I). The diameters of the flexible species grown in the presence of TFE appear to vary, and these structures bear some resemblance both to "TFE fibrils" (Chapter 2) and to the flexible aggregates observed for EGFP alone (Chapter 4).

In sum, TEM images of αS-EGFP solutions reveal that this construct forms rigid fibrils that resemble classic amyloid at neutral pH, and preliminary results indicate that the aggregation pathway may be nucleation-dependent. In addition, conditions in which the EGFP label is disrupted result in the formation of amyloid-like fibrils and shorter, flexible fibrillar species. The relationship between the aggregates observed for the αS-EGFP construct and fibrils formed from αS and EGFP separately

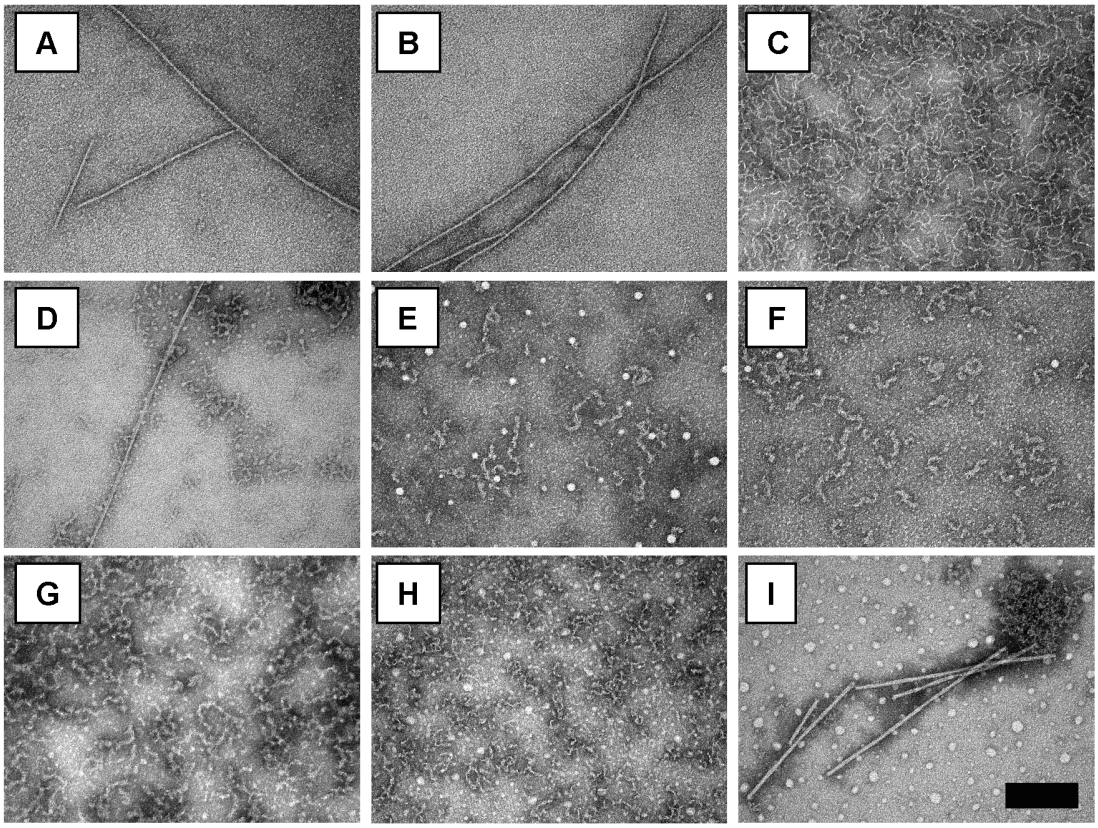

Figure D.6. TEM images of αS-EGFP aggregates grown in conditions in which the EGFP tag is likely to be disrupted or denatured. The scale bar is 200 nm wide and all images are shown at the same magnification. (A-B) Aggregates grown from 50 μM αS-EGFP at pH 2.4, incubated for 3 weeks with shaking at 37 °C. (C) Same as A, but the solution also contained 150 mM NaCl. (D) A rigid, amyloid-like fibril and thinner, flexible fibrils observed in a solution containing 50 μM αS-EGFP in pH 7.5 NaPhos with 15% TFE, after incubation for 3 weeks with shaking at 37 °C. (E) Flexible, irregular fibrils grown from 50 μM αS-EGFP in pH 7.5 NaPhos with 10% TFE, after incubation for 3 weeks at room temperature under quiescent conditions. (F) Same as E, but the solution contained 75 μM αS-EGFP. (G) Same as E, but the solution contained 15% TFE. (H) Aggregates grown from 50 μM αS-EGFP at pH 2.4 with 15% TFE, incubated for 3 weeks with shaking at 37 °C. (I) Same as G, but the solution also contained 150 mM NaCl.

remains unclear. Further experiments must be performed to determine whether the EGFP tertiary structure remains intact in any of the αS-EGFP fibrils.

REFERENCES

Abedini, A., and Raleigh, D.P. (2009a). A critical assessment of the role of helical intermediates in amyloid formation by natively unfolded proteins and polypeptides. Protein Eng. Des. Sel. 22, 453-459.

Abedini, A., and Raleigh, D.P. (2009b). A role for helical intermediates in amyloid formation by natively unfolded polypeptides? Phys. Biol. 6, 015005.

Adzhubei, A.A., and Sternberg, M.J. (1993). Left-handed polyproline II helices commonly occur in globular proteins. J. Mol. Biol. 229, 472-493.

Ahmad, A. (2010). DnaK/DnaJ/GrpE of Hsp70 system have differing effects on alpha-synuclein fibrillation involved in Parkinson's disease. Int. J. Biol. Macromol. 46, 275-279.

Ahmad, M.F., Ramakrishna, T., Raman, B., and Rao, C. (2006). Fibrillogenic and non-fibrillogenic ensembles of SDS-bound human alpha-synuclein. J. Mol. Biol 364, 1061-1072.

Andersen, N.H., Cort, J.R., Liu, Z., Sjoberg, S.J., and Tong, H. (1996). Cold denaturation of monomeric peptide helices. J. Am. Chem. Soc. 118, 10309-10310.

Anderson, V.L., Ramlall, T.F., Rospigliosi, C.C., Webb, W.W., and Eliezer, D. (2010). Identification of a helical intermediate in trifluoroethanol-induced alpha-synuclein aggregation. Proc. Natl. Acad. Sci. U. S. A. 107, 18850-18855.

Andrade, M.A., Chacon, P., Merelo, J.J., and Moran, F. (1993). Evaluation of secondary structure of proteins from UV circular dichroism spectra using an unsupervised learning neural network. Protein Eng. 6, 383-390.

Balbirnie, M., Grothe, R., and Eisenberg, D.S. (2001). An amyloid-forming peptide from the yeast prion Sup35 reveals a dehydrated beta-sheet structure for amyloid. Proc. Natl. Acad. Sci. U. S. A. 98, 2375-2380.

Bertoncini, C.W., Jung, Y.S., Fernandez, C.O., Hoyer, W., Griesinger, C., Jovin, T.M., and Zweckstetter, M. (2005). Release of long-range tertiary interactions potentiates aggregation of natively unstructured alpha-synuclein. Proc. Natl. Acad. Sci. U. S. A. 102, 1430-1435.

Beyer, K. (2007). Mechanistic aspects of Parkinson's disease: alpha-synuclein and the biomembrane. Cell Biochem. Biophys. 47, 285-299.

Bitan, G., and Teplow, D.B. (2005). Preparation of aggregate-free, low molecular weight amyloid-beta for assembly and toxicity assays. Methods Mol. Biol. 299, 3-9.

Blanch, E.W., Morozova-Roche, L.A., Cochran, D.A.E., Doig, A.J., Hecht, L., and Barron, L.D. (2000). Is polyproline II helix the killer conformation? A Raman optical activity study of the amyloidogenic prefibrillar intermediate of human lysozyme. J. Mol. Biol. 301, 553-563.

Bochicchio, B., and Tamburro, A.M. (2002). Polyproline II structure in proteins: identification by chiroptical spectroscopies, stability, and functions. Chirality 14, 782-792.

Bodner, C.R., Dobson, C.M., and Bax, A. (2009). Multiple tight phospholipid-binding modes of alpha-synuclein revealed by solution NMR spectroscopy. J. Mol. Biol. 390, 775-790.

Bokman, S.H., and Ward, W.W. (1981). Renaturation of Aequorea green-fluorescent protein. Biochem. Biophys. Res. Commun. 101, 1372-1380.

Booth, D.R., Sunde, M., Bellotti, V., Robinson, C.V., Hutchinson, W.L., Fraser, P.E., Hawkins, P.N., Dobson, C.M., Radford, S.E., Blake, C.C., and Pepys, M.B. (1997). Instability, unfolding and aggregation of human lysozyme variants underlying amyloid fibrillogenesis. Nature 385, 787-793.

Brahms, S., and Brahms, J. (1980). Determination of protein secondary structure in solution by vacuum ultraviolet circular dichroism. J. Mol. Biol. 138, 149-178.

Broersen, K., van den Brink, D., Fraser, G., Goedert, M., and Davletov, B. (2006). Alpha-synuclein adopts an alpha-helical conformation in the presence of polyunsaturated fatty acids to hinder micelle formation. Biochemistry 45, 15610-15616.

Brown, D.R. (2010). Oligomeric alpha-synuclein and its role in neuronal death. IUBMB Life 62, 334-339.

Bucciantini, M., Giannoni, E., Chiti, F., Baroni, F., Formigli, L., Zurdo, J., Taddei, N., Ramponi, G., Dobson, C.M., and Stefani, M. (2002). Inherent toxicity of aggregates implies a common mechanism for protein misfolding diseases. Nature 416, 507-511.

Bussell, R.,Jr, and Eliezer, D. (2004). Effects of Parkinson's disease-linked mutations on the structure of lipid-associated alpha-synuclein. Biochemistry 43, 4810-4818.

Bussell, R.,Jr, and Eliezer, D. (2003). A structural and functional role for 11-mer repeats in alpha-synuclein and other exchangeable lipid binding proteins. J. Mol. Biol. 329, 763-778.

Bussell, R.,Jr, and Eliezer, D. (2001). Residual structure and dynamics in Parkinson's disease-associated mutants of alpha-synuclein. J. Biol. Chem. 276, 45996-46003.

Bychkova, V.E., Dujsekina, A.E., Klenin, S.I., Tiktopulo, E.I., Uversky, V.N., and Ptitsyn, O.B. (1996). Molten globule-like state of cytochrome c under conditions simulating those near the membrane surface. Biochemistry 35, 6058-6063.

Calamai, M., Chiti, F., and Dobson, C.M. (2005). Amyloid fibril formation can proceed from different conformations of a partially unfolded protein. Biophys. J. 89, 4201-4210.

Cammers-Goodwin, A., Allen, T.J., Oslick, S.L., McClure, K.F., Lee, J.H., and Kemp, D.S. (1996). Mechanism of stabilization of helical conformations of polypeptides by water containing trifluoroethanol. J. Am. Chem. Soc. 118, 3082-3090.

Cattell, R. (1966). The scree test for the number of factors. Multivar. Behav. Res. 1, 245-276.

Chafekar, S.M., Baas, F., and Scheper, W. (2008). Oligomer-specific Abeta toxicity in cell models is mediated by selective uptake. Biochim. Biophys. Acta 1782, 523-531.

Chandra, S., Chen, X., Rizo, J., Jahn, R., and Sudhof, T.C. (2003). A broken alphahelix in folded alpha-synuclein. J. Biol. Chem. 278, 15313-15318.

Chatterjee, C., and Gerig, J.T. (2007). Interactions of trifluroethanol with the Trp-cage peptide. Biopolymers 87, 115-123.

Chatterjee, C., and Gerig, J.T. (2006). Interactions of hexafluoro-2-propanol with the Trp-cage peptide. Biochemistry 45, 14665-14674.

Chaudhary, N., Singh, S., and Nagaraj, R. (2009). Morphology of self-assembled structures formed by short peptides from the amyloidogenic protein tau depends on the solvent in which the peptides are dissolved. J. Pept. Sci. 15, 675-684.

Chen, H., Rhoades, E., Butler, J.S., Loh, S.N., and Webb, W.W. (2007). Dynamics of equilibrium structural fluctuations of apomyoglobin measured by fluorescence correlation spectroscopy. Proc. Natl. Acad. Sci. U. S. A. 104, 10459-10464.

Chin, J.T., Wheeler, S.L., and Klibanov, A.M. (1994). On protein solubility in organic solvent. Biotechnol. Bioeng. 44, 140-145.

Chiti, F., and Dobson, C.M. (2006). Protein misfolding, functional amyloid, and human disease. Annu. Rev. Biochem. 75, 333-366.

Chiti, F., Taddei, N., Bucciantini, M., White, P., Ramponi, G., and Dobson, C.M. (2000). Mutational analysis of the propensity for amyloid formation by a globular protein. EMBO J. 19, 1441-1449.

Chiti, F., Webster, P., Taddei, N., Clark, A., Stefani, M., Ramponi, G., and Dobson, C.M. (1999). Designing conditions for in vitro formation of amyloid protofilaments and fibrils. Proc. Natl. Acad. Sci. U. S. A. 96, 3590-3594.

Chitra, R., and Smith, P.E. (2002). Molecular association in solution: A Kirkwood-Buff analysis of sodium chloride, ammonium sulfate, guanidinium chloride, urea, and 2,2,2-trifluoroethanol in water. J. Phys. Chem. B 106, 1491-1500.

Cho, M.K., Nodet, G., Kim, H.Y., Jensen, M.R., Bernado, P., Fernandez, C.O., Becker, S., Blackledge, M., and Zweckstetter, M. (2009). Structural characterization of alpha-synuclein in an aggregation prone state. Protein Sci. 18, 1840-1846.

Compton, L.A., and Johnson, W.C.,Jr. (1986). Analysis of protein circular dichroism spectra for secondary structure using a simple matrix multiplication. Anal. Biochem. 155, 155-167.

Conio, G., Patrone, E., and Brighetti, S. (1970). The effect of aliphatic alcohols on the helix-coil transition of poly-L-ornithine and poly-L-glutamic acid. J. Biol. Chem. 245, 3335-3340.

Conway, K.A., Lee, S.J., Rochet, J.C., Ding, T.T., Williamson, R.E., and Lansbury, P.T.,Jr. (2000). Acceleration of oligomerization, not fibrillization, is a shared property of both alpha-synuclein mutations linked to early-onset Parkinson's disease: implications for pathogenesis and therapy. Proc. Natl. Acad. Sci. U. S. A. 97, 571-576.

Cooney, A., and Morcom, K.W. (1988). Thermodynamic behaviour of mixtures containing fluoroalcohols I. (Water + 2,2,2-trifluoroethanol). J. Chem. Thermodyn. 20, 735-741.

Cormack, B.P., Valdivia, R.H., and Falkow, S. (1996). FACS-optimized mutants of the green fluorescent protein (GFP). Gene 173, 33-38.

Craggs, T.D. (2009). Green fluorescent protein: structure, folding and chromophore maturation. Chem. Soc. Rev. 38, 2865-2875.

Creighton, T.E., Darby, N.J., and Kemmink, J. (1996). The roles of partly folded intermediates in protein folding. FASEB J. 10, 110-118.

Crowther, R.A., Jakes, R., Spillantini, M.G., and Goedert, M. (1998). Synthetic filaments assembled from C-terminally truncated alpha-synuclein. FEBS Lett. 436, 309-312.

Falsone, S.F., Kungl, A.J., Rek, A., Cappai, R., and Zangger, K. (2009). The molecular chaperone Hsp90 modulates intermediate steps of amyloid assembly of the Parkinson-related protein alpha-synuclein. J. Biol. Chem. 284, 31190-31199.

Fan, F., and Mayo, K.H. (1995). Effect of pH on the conformation and backbone dynamics of a 27-residue peptide in trifluoroethanol. J. Biol. Chem. 270, 24693-24701.

Ferreon, A.C., and Deniz, A.A. (2007). Alpha-synuclein multistate folding thermodynamics: implications for protein misfolding and aggregation. Biochemistry 46, 4499-4509.

Fezoui, Y., and Teplow, D.B. (2002). Kinetic studies of amyloid β-protein fibril assembly. J. Biol. Chem. 277, 36948-36954.

Fioroni, M., Diaz, M.D., Burger, K., and Berger, S. (2002). Solvation phenomena of a tetrapeptide in water/trifluoroethanol and water/ethanol mixtures: a diffusion NMR, intermolecular NOE, and molecular dynamics study. J. Am. Chem. Soc. 124, 7737-7744.

Fredenburg, R.A., Rospigliosi, C., Meray, R.K., Kessler, J.C., Lashuel, H.A., Eliezer, D., and Lansbury, P.T.,Jr. (2007). The impact of the E46K mutation on the properties of alpha-synuclein in its monomeric and oligomeric states. Biochemistry 46, 7107-7118.

Gast, K., Siemer, A., Zirwer, D., and Damaschun, G. (2001). Fluoroalcohol-induced structural changes of proteins: some aspects of cosolvent-protein interactions. Eur. Biophys. J. 30, 273-283.

Gast, K., Zirwer, D., Muller-Frohne, M., and Damaschun, G. (1999). Trifluoroethanol-induced conformational transitions of proteins: insights gained from the differences between alpha-lactalbumin and ribonuclease A. Protein Sci. 8, 625-634.

Gente, G., and La Mesa, C. (2000). Water-trifluoroethanol mixtures: some physicochemical properties. J. Solution Chem. 29, 1159-1172.

Georgieva, E.R., Ramlall, T.F., Borbat, P.P., Freed, J.H., and Eliezer, D. (2008). Membrane-bound alpha-synuclein forms an extended helix: long-distance pulsed ESR measurements using vesicles, bicelles, and rodlike micelles. J. Am. Chem. Soc. 130, 12856-12857.

Giasson, B.I., Uryu, K., Trojanowski, J.Q., and Lee, V.M. (1999). Mutant and wild type human alpha-synucleins assemble into elongated filaments with distinct morphologies in vitro. J. Biol. Chem. 274, 7619-7622.

Davidson, W.S., Jonas, A., Clayton, D.F., and George, J.M. (1998). Stabilization of alpha-synuclein secondary structure upon binding to synthetic membranes. J. Biol. Chem. 273, 9443-9449.

Dedmon, M.M., Christodoulou, J., Wilson, M.R., and Dobson, C.M. (2005). Heat shock protein 70 inhibits alpha-synuclein fibril formation via preferential binding to prefibrillar species. J. Biol. Chem. 280, 14733-14740.

Del Vecchio, P., Graziano, G., Granata, V., Barone, G., Mandrich, L., Rossi, M., and Manco, G. (2003). Effect of trifluoroethanol on the conformational stability of a hyperthermophilic esterase: a CD study. Biophys. Chem. 104, 407-415.

Diaz, M.D., Fioroni, M., Burger, K., and Berger, S. (2002). Evidence of complete hydrophobic coating of bombesin by trifluoroethanol in aqueous solution: an NMR spectroscopic and molecular dynamics study. Chemistry 8, 1663-1669.

Drake, A.F., Siligardi, G., and Gibbons, W.A. (1988). Reassessment of the electronic circular dichroism criteria for random coil conformations of poly(L-lysine) and the implications for protein folding and denaturation studies. Biophys. Chem. 31, 143-146.

Drescher, M., Godschalk, F., Veldhuis, G., van Rooijen, B.D., Subramaniam, V., and Huber, M. (2008). Spin-label EPR on alpha-synuclein reveals differences in the membrane binding affinity of the two antiparallel helices. Chembiochem 9, 2411-2416.

Drozdov, A.N., Grossfield, A., and Pappu, R.V. (2004). Role of solvent in determining conformational preferences of alanine dipeptide in water. J. Am. Chem. Soc. 126, 2574-2581.

Eggers, D.K. (2011). A bulk water-dependent desolvation energy model for analyzing the effects of secondary solutes on biological equilibria. Biochemistry 50, 2004-2012.

El-Agnaf, O.M., Jakes, R., Curran, M.D., and Wallace, A. (1998). Effects of the mutations Ala30 to Pro and Ala53 to Thr on the physical and morphological properties of alpha-synuclein protein implicated in Parkinson's disease. FEBS Lett. 440, 67-70.

Eliezer, D., Kutluay, E., Bussell, R.,Jr, and Browne, G. (2001). Conformational properties of alpha-synuclein in its free and lipid-associated states. J. Mol. Biol. 307, 1061-1073.

Espinosa, S., Bosch, E., Roses, M., and Valko, K. (2002). Change of mobile phase pH during gradient reversed-phase chromatography with 2,2,2-trifluoroethanol-water as mobile phase and its effect on the chromatographic hydrophobicity index determination. J. Chromatogr. A 954, 77-87.

Giehm, L., Oliveira, C.L., Christiansen, G., Pedersen, J.S., and Otzen, D.E. (2010). SDS-induced fibrillation of alpha-synuclein: an alternative fibrillation pathway. J. Mol. Biol. 401, 115-133.

Glabe, C.G. (2006). Common mechanisms of amyloid oligomer pathogenesis in degenerative disease. Neurobiol. Aging 27, 570-575.

Greenfield, N.J. (1996). Methods to estimate the conformation of proteins and polypeptides from circular dichroism data. Anal. Biochem. 235, 1-10.

Grudzielanek, S., Jansen, R., and Winter, R. (2005). Solvational tuning of the unfolding, aggregation and amyloidogenesis of insulin. J. Mol. Biol. 351, 879-894.

Hegyi, H., and Tompa, P. (2008). Intrinsically disordered proteins display no preference for chaperone binding in vivo. PLoS Comput. Biol. 4, e1000017.

Hillson, N., Onuchic, J.N., and Garcia, A.E. (1999). Pressure-induced protein-folding/unfolding kinetics. Proc. Natl. Acad. Sci. U. S. A. 96, 14848-14853.

Hinault, M.P., Cuendet, A.F., Mattoo, R.U., Mensi, M., Dietler, G., Lashuel, H.A., and Goloubinoff, P. (2010). Stable alpha-synuclein oligomers strongly inhibit chaperone activity of the Hsp70 system by weak interactions with J-domain co-chaperones. J. Biol. Chem. 285, 38173-38182.

Hirota, N., Mizuno, K., and Goto, Y. (1997). Cooperative alpha-helix formation of beta-lactoglobulin and melittin induced by hexafluoroisopropanol. Protein. Sci. 6, 416-421.

Hong, D., Hoshino, M., Kuboi, R., and Goto, Y. (1999). Clustering of fluorine-substituted alcohols as a factor responsible for their marked effects on proteins and peptides. J. Am. Chem. Soc. 121, 8427-8433.

Hsu, S.T., Blaser, G., and Jackson, S.E. (2009). The folding, stability and conformational dynamics of beta-barrel fluorescent proteins. Chem. Soc. Rev. 38, 2951-2965.

Hwang, W., Zhang, S., Kamm, R.D., and Karplus, M. (2004). Kinetic control of dimer structure formation in amyloid fibrillogenesis. Proc. Natl. Acad. Sci. U. S. A. 101, 12916-12921.

Iovino, M., Falconi, M., Marcellini, A., and Desideri, A. (2001). Molecular dynamics simulation of the antimicrobial salivary peptide histatin-5 in water and in trifluoroethanol: a microscopic description of the water destructuring effect. J. Pept. Res. 58, 45-55.

Jasanoff, A., and Fersht, A.R. (1994). Quantitative determination of helical propensities from trifluoroethanol titration curves. Biochemistry 33, 2129-2135.

Jungbauer, L.M., Yu, C., Laxton, K.J., and LaDu, M.J. (2009). Preparation of fluorescently-labeled amyloid-beta peptide assemblies: the effect of fluorophore conjugation on structure and function. J. Mol. Recognit. 22, 403-413.

Kakinoki, S., Hirano, Y., and Oka, M. (2005). On the stability of polyproline-I and II structures of proline oligopeptides. Polym. Bull. 53, 109-115.

Kauzmann, W., and Eyring, H. (1941). The effect of the rotation of groups about bonds on optical rotatory power. J. Chem. Phys. 9, 41-53.

Kelly, M.A., Chellgren, B.W., Rucker, A.L., Troutman, J.M., Fried, M.G., Miller, A.F., and Creamer, T.P. (2001). Host-guest study of left-handed polyproline II helix formation. Biochemistry 40, 14376-14383.

Kentsis, A., and Sosnick, T.R. (1998). Trifluoroethanol promotes helix formation by destabilizing backbone exposure: desolvation rather than native hydrogen bonding defines the kinetic pathway of dimeric coiled coil folding. Biochemistry 37, 14613-14622.

Kinoshita, M., Okamoto, Y., and Hirata, F. (2000). Peptide conformations in alcohol and water: Analyses by the reference interaction site model theory. J. Am. Chem. Soc. 122, 2773-2779.

Kjaergaard, M., Norholm, A.B., Hendus-Altenburger, R., Pedersen, S.F., Poulsen, F.M., and Kragelund, B.B. (2010). Temperature-dependent structural changes in intrinsically disordered proteins: formation of alpha-helices or loss of polyproline II? Protein Sci. 19, 1555-1564.

Kodali, R., and Wetzel, R. (2007). Polymorphism in the intermediates and products of amyloid assembly. Curr. Opin. Struct. Biol. 17, 48-57.

Kruger, R., Kuhn, W., Muller, T., Woitalla, D., Graeber, M., Kosel, S., Przuntek, H., Epplen, J.T., Schols, L., and Riess, O. (1998). Ala30Pro mutation in the gene encoding alpha-synuclein in Parkinson's disease. Nat. Genet. 18, 106-108.

Kumar, S., Modig, K., and Halle, B. (2003). Trifluoroethanol-induced beta --> alpha transition in beta-lactoglobulin: hydration and cosolvent binding studied by 2H, 17O, and 19F magnetic relaxation dispersion. Biochemistry 42, 13708-13716.

Kundu, A., and Kishore, N. (2004). Interaction of 2,2,2-trifluoroethanol with proteins: calorimetric, densimetric and surface tension approach. Biophys. Chem. 109, 427-442.

Kuznetsova, I.M., Turoverov, K.K., and Uversky, V.N. (2004). Use of the phase diagram method to analyze the protein unfolding-refolding reactions: fishing out the "invisible" intermediates. J. Proteome Res. 3, 485-494.

Lawrence, J.R., and Johnson, W.C. (2002). Lifson-Roig nucleation for alpha-helices in trifluoroethanol: context has a strong effect on the helical propensity of amino acids. Biophys. Chem. 101-102, 375-385.

Lees, J.G., Miles, A.J., Wien, F., and Wallace, B.A. (2006). A reference database for circular dichroism spectroscopy covering fold and secondary structure space. Bioinformatics 22, 1955-1962.

Li, H.T., Du, H.N., Tang, L., Hu, J., and Hu, H.Y. (2002). Structural transformation and aggregation of human alpha-synuclein in trifluoroethanol: non-amyloid component sequence is essential and beta-sheet formation is prerequisite to aggregation. Biopolymers 64, 221-226.

Li, J., Uversky, V.N., and Fink, A.L. (2001). Effect of familial Parkinson's disease point mutations A30P and A53T on the structural properties, aggregation, and fibrillation of human alpha-synuclein. Biochemistry 40, 11604-11613.

Li, W., West, N., Colla, E., Pletnikova, O., Troncoso, J.C., Marsh, L., Dawson, T.M., Jakala, P., Hartmann, T., Price, D.L., and Lee, M.K. (2005). Aggregation promoting C-terminal truncation of alpha-synuclein is a normal cellular process and is enhanced by the familial Parkinson's disease-linked mutations. Proc. Natl. Acad. Sci. U. S. A. 102, 2162-2167.

Lim, K.H., Le, Y.T., Collver, H.H., Putnam-Evans, C., and Kenney, J.M. (2010). Characterization of amyloidogenic intermediate states through a combined use of CD and NMR spectroscopy. Biophys. Chem. 151, 155-159.

Liu, W., Prausnitz, J.M., and Blanch, H.W. (2004). Amyloid fibril formation by peptide LYS (11-36) in aqueous trifluoroethanol. Biomacromolecules 5, 1818-1823.

Liu, Z., and Chan, H.S. (2005). Solvation and desolvation effects in protein folding: native flexibility, kinetic cooperativity and enthalpic barriers under isostability conditions. Phys. Biol. 2, S75-85.

Luo, P., and Baldwin, R.L. (1997). Mechanism of helix induction by trifluoroethanol: a framework for extrapolating the helix-forming properties of peptides from trifluoroethanol/water mixtures back to water. Biochemistry 36, 8413-8421.

Lybarger, L., Dempsey, D., Patterson, G.H., Piston, D.W., Kain, S.R., and Chervenak, R. (1998). Dual-color flow cytometric detection of fluorescent proteins using single-laser (488-nm) excitation. Cytometry 31, 147-152.

Ma, K., and Wang, K. (2003). Malleable conformation of the elastic PEVK segment of titin: non-co-operative interconversion of polyproline II helix, beta-turn and unordered structures. Biochem. J. 374, 687-695.

MacCallum, J.L., Moghaddam, M.S., Chan, H.S., and Tieleman, D.P. (2007). Hydrophobic association of alpha-helices, steric dewetting, and enthalpic barriers to protein folding. Proc. Natl. Acad. Sci. U. S. A. 104, 6206-6210.

Makarov, N.S., Drobizhev, M., and Rebane, A. (2008). Two-photon absorption standards in the 550-1600 nm excitation wavelength range. Opt. Express 16, 4029-4047.

Malavolta, L., Pinto, M.R., Cuvero, J.H., and Nakaie, C.R. (2006). Interpretation of the dissolution of insoluble peptide sequences based on the acid-base properties of the solvent. Protein Sci. 15, 1476-1488.

Malhotra, R., and Woolf, L. (1991). Thermodynamic properties of 2,2,2-trifluoroethanol. Int. J. Thermophys. 12, 397-407.

Mancinelli, R., Botti, A., Bruni, F., Ricci, M.A., and Soper, A.K. (2007). Hydration of sodium, potassium, and chloride ions in solution and the concept of structure maker/breaker. J. Phys. Chem. B 111, 13570-13577.

Mao, D., Wachter, E., and Wallace, B.A. (1982). Folding of the mitochondrial proton adenosinetriphosphatase proteolipid channel in phospholipid vesicles. Biochemistry 21, 4960-4968.

Marcus, Y. (2001). Preferential solvation in mixed solvents X. Completely miscible aqueous co-solvent binary mixtures at 298.15 K. Monatsh. Chem. 132, 1387-1411.

Marcus, Y. (1988). Preferential solvation of ions in mixed solvents. Part 2.-The solvent composition near the ion. J. Chem. Soc. Farad. T. 1 84, 1465-1473.

McClendon, S., Rospigliosi, C.C., and Eliezer, D. (2009). Charge neutralization and collapse of the C-terminal tail of alpha-synuclein at low pH. Protein Sci. 18, 1531-1540.

McLean, P.J., Kawamata, H., and Hyman, B.T. (2001). Alpha-synuclein-enhanced green fluorescent protein fusion proteins form proteasome sensitive inclusions in primary neurons. Neuroscience 104, 901-912.

Michell, A.W., Tofaris, G.K., Gossage, H., Tyers, P., Spillantini, M.G., and Barker, R.A. (2007). The effect of truncated human alpha-synuclein (1-120) on dopaminergic cells in a transgenic mouse model of Parkinson's disease. Cell Transplant. 16, 461-474.

Miles, A.J., Whitmore, L., and Wallace, B.A. (2005). Spectral magnitude effects on the analyses of secondary structure from circular dichroism spectroscopic data. Protein Sci. 14, 368-374.

Milla, M.E., and Sauer, R.T. (1994). p22 Arc repressor: folding kinetics of a single-domain, dimeric protein. Biochemistry 33, 1125-1133.

Minamihonoki, T., Ogawa, H., Nomura, H., and Murakami, S. (2007). Thermodynamic properties of binary mixtures of 2,2,2-trifluoroethanol with water or alkanols at T = 298.15 K. Thermochim. Acta 459, 80-86.

Moelbert, S., Normand, B., and De Los Rios, P. (2004). Kosmotropes and chaotropes: modelling preferential exclusion, binding and aggregate stability. Biophys. Chem. 112, 45-57.

Monsellier, E., and Chiti, F. (2007). Prevention of amyloid-like aggregation as a driving force of protein evolution. EMBO Rep. 8, 737-742.

Mukherjee, S., Chowdhury, P., and Gai, F. (2009). Effect of dehydration on the aggregation kinetics of two amyloid peptides. J. Phys. Chem. B 113, 531-535.

Munishkina, L.A., Phelan, C., Uversky, V.N., and Fink, A.L. (2003). Conformational behavior and aggregation of alpha-synuclein in organic solvents: Modeling the effects of membranes. Biochemistry 42, 2720-2730.

Ndao, M., Dutta, K., Bromley, K.M., Lakshminarayanan, R., Sun, Z., Rewari, G., Moradian-Oldak, J., and Evans, J.S. (2011). Probing the self-association, intermolecular contacts, and folding propensity of amelogenin. Protein Sci. 20, 724-734.

Necula, M., Chirita, C.N., and Kuret, J. (2003). Rapid anionic micelle-mediated alpha-synuclein fibrillization in vitro. J. Biol. Chem. 278, 46674-46680.

Nelson, J.W., and Kallenbach, N.R. (1986). Stabilization of the ribonuclease S-peptide alpha-helix by trifluoroethanol. Proteins 1, 211-217.

Nettels, D., Müller-Späth, S., Küster, F., Hofmann, H., Haenni, D., Rüegger, S., Reymond, L., Hoffmann, A., Kubelka, J., Heinz, B., Gast, K., Best, R.B., and Schuler, B. (2009). Single-molecule spectroscopy of the temperature-induced collapse of unfolded proteins. Proc. Natl. Acad. Sci. U. S. A. 106, 20740-20745.

Neu, T.R., Kuhlicke, U., and Lawrence, J.R. (2002). Assessment of fluorochromes for two-photon laser scanning microscopy of biofilms. Appl. Environ. Microbiol. 68, 901-909.

Othon, C.M., Kwon, O.H., Lin, M.M., and Zewail, A.H. (2009). Solvation in protein (un)folding of melittin tetramer-monomer transition. Proc. Natl. Acad. Sci. U. S. A. 106, 12593-12598.

Otzen, D.E. (2010). Amyloid formation in surfactants and alcohols: membrane mimetics or structural switchers? Curr. Protein Pept. Sci. 11, 355-371.

Palepu, R., and Clarke, J. (1989). Viscosities and densities of 2,2,2-trifluoroethanol + water at various temperatures. Thermochim. Acta 156, 359-363.

Pallarès, I., Vendrell, J., Avilés, F.X., and Ventura, S. (2004). Amyloid fibril formation by a partially structured intermediate state of α-chymotrypsin. J. Mol. Biol. 342, 321-331.

Patterson, G.H., Knobel, S.M., Sharif, W.D., Kain, S.R., and Piston, D.W. (1997). Use of the green fluorescent protein and its mutants in quantitative fluorescence microscopy. Biophys. J. 73, 2782-2790.

Pedersen, J.S., and Otzen, D.E. (2008). Amyloid-a state in many guises: survival of the fittest fibril fold. Protein Sci. 17, 2-10.

Pellarin, R., Schuetz, P., Guarnera, E., and Caflisch, A. (2010). Amyloid fibril polymorphism is under kinetic control. J. Am. Chem. Soc. 132, 14960-14970.

Perez-Iratxeta, C., and Andrade-Navarro, M.A. (2008). K2D2: estimation of protein secondary structure from circular dichroism spectra. BMC Struct. Biol. 8, 25.

Plakoutsi, G., Taddei, N., Stefani, M., and Chiti, F. (2004). Aggregation of the acylphosphatase from Sulfolobus solfataricus. J. Biol. Chem. 279, 14111-14119.

Polymeropoulos, M.H., Lavedan, C., Leroy, E., Ide, S.E., Dehejia, A., Dutra, A., Pike, B., Root, H., Rubenstein, J., Boyer, R., Stenroos, E.S., Chandrasekharappa, S., Athanassiadou, A., Papapetropoulos, T., Johnson, W.G., Lazzarini, A.M., Duvoisin, R.C., Di Iorio, G., Golbe, L.I., and Nussbaum, R.L. (1997). Mutation in the alpha-synuclein gene identified in families with Parkinson's disease. Science 276, 2045-2047.

Poon, C., Samulski, E.T., Weise, C.F., and Weisshaar, J.C. (2000). Do bridging water molecules dictate the structure of a model dipeptide in aqueous solution? J. Am. Chem. Soc. 122, 5642-5643.

Pountney, D.L., Lowe, R., Quilty, M., Vickers, J.C., Voelcker, N.H., and Gai, W.P. (2004). Annular alpha-synuclein species from purified multiple system atrophy inclusions. J. Neurochem. 90, 502-512.

Pribic, R. (1994). Principal component analysis of Fourier transform infrared and/or circular dichroism spectra of proteins applied in a calibration of protein secondary structure. Anal. Biochem. 223, 26-34.

Provencher, S.W., and Glockner, J. (1981). Estimation of globular protein secondary structure from circular dichroism. Biochemistry 20, 33-37.

Putnam, C.D. (2006). Protein calculator v.3.3.
http://www.scripps.edu/~cdputnam/protcalc.html

Rabanal, F., Ludevid, M.D., Pons, M., and Giralt, E. (1993). CD of proline-rich polypeptides: application to the study of the repetitive domain of maize glutelin-2. Biopolymers 33, 1019-1028.

Rajan, R., and Balaram, P. (1996). A model for the interaction of trifluoroethanol with peptides and proteins. Int. J. Pept. Protein Res. 48, 328-336.

Rauscher, S., Baud, S., Miao, M., Keeley, F.W., and Pomes, R. (2006). Proline and glycine control protein self-organization into elastomeric or amyloid fibrils. Structure 14, 1667-1676.

Reid, B.G., and Flynn, G.C. (1997). Chromophore formation in green fluorescent protein. Biochemistry 36, 6786-6791.

Reiersen, H., and Rees, A.R. (2000). Trifluoroethanol may form a solvent matrix for assisted hydrophobic interactions between peptide side chains. Protein. Eng. 13, 739-743.

Rezaei-Ghaleh, N., Ebrahim-Habibi, A., Moosavi-Movahedi, A.A., and Nemat-Gorgani, M. (2007). Role of electrostatic interactions in 2,2,2-trifluoroethanol-induced structural changes and aggregation of alpha-chymotrypsin. Arch. Biochem. Biophys. 457, 160-169.

Rhoades, E., Ramlall, T.F., Webb, W.W., and Eliezer, D. (2006). Quantification of alpha-synuclein binding to lipid vesicles using fluorescence correlation spectroscopy. Biophys. J. 90, 4692-4700.

Roccatano, D., Colombo, G., Fioroni, M., and Mark, A.E. (2002). Mechanism by which 2,2,2-trifluoroethanol/water mixtures stabilize secondary-structure formation in peptides: a molecular dynamics study. Proc. Natl. Acad. Sci. U. S. A. 99, 12179-12184.

Rochester, C.H., and Symonds, J.R. (1974). Densities of solutions of four fluoroalcohols in water. J. Fluorine Chem. 4, 141-148.

Rohl, C.A., Chakrabartty, A., and Baldwin, R.L. (1996). Helix propagation and N-cap propensities of the amino acids measured in alanine-based peptides in 40 volume percent trifluoroethanol. Protein Sci. 5, 2623-2637.

Rospigliosi, C.C., McClendon, S., Schmid, A.W., Ramlall, T.F., Barre, P., Lashuel, H.A., and Eliezer, D. (2009). E46K Parkinson's-linked mutation enhances C-terminal-to-N-terminal contacts in alpha-synuclein. J. Mol. Biol. 388, 1022-1032.

Rothemund, S., Weisshoff, H., Beyermann, M., Krause, E., Bienert, M., Mügge, C., Sykes, B.D., and Sönnichsen, F.D. (1996). Temperature coefficients of amide proton NMR resonance frequencies in trifluoroethanol: A monitor of intramolecular hydrogen bonds in helical peptides? J. Biomol. NMR 8, 93-97.

Rucker, A.L., Pager, C.T., Campbell, M.N., Qualls, J.E., and Creamer, T.P. (2003). Host-guest scale of left-handed polyproline II helix formation. Proteins 53, 68-75.

Saavedra, L., Mohamed, A., Ma, V., Kar, S., and de Chaves, E.P. (2007). Internalization of beta-amyloid peptide by primary neurons in the absence of apolipoprotein E. J. Biol. Chem. 282, 35722-35732.

Sassi, M., and Atik, Z. (2003). Excess molar volumes of binary mixtures of 2,2,2-trifluoroethanol with water, or acetone, or 1,4-difluorobenzene, or 4-fluorotoluene, or α,α,α, trifluorotoluene or 1-alcohols at a temperature of 298.15 K and pressure of 101 kPa. J. Chem. Thermodyn. 35, 1161-1169.

Sen, P., Ahmad, B., Rabbani, G., and Khan, R.H. (2010). 2,2,2-Trifluroethanol induces simultaneous increase in alpha-helicity and aggregation in alkaline unfolded state of bovine serum albumin. Int. J. Biol. Macromol. 46, 250-254.

Serpell, L.C., Berriman, J., Jakes, R., Goedert, M., and Crowther, R.A. (2000). Fiber diffraction of synthetic alpha-synuclein filaments shows amyloid-like cross-beta conformation. Proc. Natl. Acad. Sci. U. S. A. 97, 4897-4902.

Shi, Z., Chen, K., Liu, Z., and Kallenbach, N.R. (2006). Conformation of the backbone in unfolded proteins. Chem. Rev. 106, 1877-1897.

Shi, Z., Olson, C.A., Rose, G.D., Baldwin, R.L., and Kallenbach, N.R. (2002). Polyproline II structure in a sequence of seven alanine residues. Proc. Natl. Acad. Sci. U. S. A. 99, 9190-9195.

Soldi, G., Bemporad, F., Torrassa, S., Relini, A., Ramazzotti, M., Taddei, N., and Chiti, F. (2005). Amyloid formation of a protein in the absence of initial unfolding and destabilization of the native state. Biophys. J. 89, 4234-4244.

Spillantini, M.G. (1999). Parkinson's disease, dementia with Lewy bodies and multiple system atrophy are alpha-synucleinopathies. Parkinsonism Relat. Disord. 5, 157-162.

Sreerama, N. (2004). CDPro: a software package for analyzing protein spectra. http://lamar.colostate.edu/~sreeram/CDPro/main.html

Sreerama, N., Venyaminov, S.Y., and Woody, R.W. (2000). Estimation of protein secondary structure from circular dichroism spectra: inclusion of denatured proteins with native proteins in the analysis. Anal. Biochem. 287, 243-251.

Sreerama, N., and Woody, R.W. (2000). Estimation of protein secondary structure from circular dichroism spectra: comparison of CONTIN, SELCON, and CDSSTR methods with an expanded reference set. Anal. Biochem. 287, 252-260.

Srisailam, S., Kumar, T.K.S., Rajalingam, D., Kathir, K.M., Sheu, H., Jan, F., Chao, P., and Yu, C. (2003). Amyloid-like fibril formation in an all β-barrel protein. J. Biol. Chem. 278, 17701-17709.

Starzyk, A., Barber-Armstrong, W., Sridharan, M., and Decatur, S.M. (2005). Spectroscopic evidence for backbone desolvation of helical peptides by 2,2,2-trifluoroethanol: an isotope-edited FTIR study. Biochemistry 44, 369-376.

Storrs, R.W., Truckses, D., and Wemmer, D.E. (1992). Helix propagation in trifluoroethanol solutions. Biopolymers 32, 1695-1702.

Strassmair, H., Engel, J., and Zundel, G. (1969). Binding of alcohols to the peptide CO-group of poly-L-proline in the I and II conformation. I. Demonstration of the binding by infrared spectroscopy and optical rotatory dispersion. Biopolymers 8, 237-246.

Tiffany, M.L., and Krimm, S. (1972). Effect of temperature on the circular dichroism spectra of polypeptides in the extended state. Biopolymers 11, 2309-2316.

Ulmer, T.S., and Bax, A. (2005). Comparison of structure and dynamics of micelle-bound human alpha-synuclein and Parkinson disease variants. J. Biol. Chem. 280, 43179-43187.

Ulmer, T.S., Bax, A., Cole, N.B., and Nussbaum, R.L. (2005). Structure and dynamics of micelle-bound human alpha-synuclein. J. Biol. Chem. 280, 9595-9603.

Upadhyay, S.K. (2006). Chemical Kinetics and Reaction Dynamics (Dordrecht, Netherlands: Springer).

Uversky, V.N., Gillespie, J.R., and Fink, A.L. (2000). Why are "natively unfolded" proteins unstructured under physiologic conditions? Proteins 41, 415-427.

Uversky, V.N., Li, J., and Fink, A.L. (2001). Evidence for a partially folded intermediate in alpha-synuclein fibril formation. J. Biol. Chem. 276, 10737-10744.

Valerio, M., Porcelli, F., Zbilut, J.P., Giuliani, A., Manetti, C., and Conti, F. (2008). pH effects on the conformational preferences of amyloid beta-peptide (1-40) in HFIP aqueous solution by NMR spectroscopy. ChemMedChem 3, 833-843.

Van Buuren, A.R., and Berendsen, H.J.C. (1993). Molecular dynamics simulation of the stability of a 22-residue α-helix in water and 30% trifluoroethanol. Biopolymers 33, 1159-1166.

Van Ham, T.J., Esposito, A., Kumita, J.R., Hsu, S.T., Kaminski Schierle, G.S., Kaminski, C.F., Dobson, C.M., Nollen, E.A., and Bertoncini, C.W. (2010). Towards multiparametric fluorescent imaging of amyloid formation: studies of a YFP model of alpha-synuclein aggregation. J. Mol. Biol. 395, 627-642.

Van Stokkum, I.H., Spoelder, H.J., Bloemendal, M., van Grondelle, R., and Groen, F.C. (1990). Estimation of protein secondary structure and error analysis from circular dichroism spectra. Anal. Biochem. 191, 110-118.

Vila, J.A., Ripoll, D.R., and Scheraga, H.A. (2000). Physical reasons for the unusual α-helix stabilization afforded by charged or neutral polar residues in alanine-rich peptides. Proc. Natl. Acad. Sci. U. S. A. 97, 13075-13079.

Vilar, M., Chou, H.T., Luhrs, T., Maji, S.K., Riek-Loher, D., Verel, R., Manning, G., Stahlberg, H., and Riek, R. (2008). The fold of alpha-synuclein fibrils. Proc. Natl. Acad. Sci. U. S. A. 105, 8637-8642.

Visser, N.V., Hink, M.A., Borst, J.W., van der Krogt, G.N., and Visser, A.J. (2002). Circular dichroism spectroscopy of fluorescent proteins. FEBS Lett. 521, 31-35.

Wakamatsu, M., Ishii, A., Iwata, S., Sakagami, J., Ukai, Y., Ono, M., Kanbe, D., Muramatsu, S., Kobayashi, K., Iwatsubo, T., and Yoshimoto, M. (2008). Selective loss of nigral dopamine neurons induced by overexpression of truncated human alpha-synuclein in mice. Neurobiol. Aging 29, 574-585.

Walgers, R., Lee, T.C., and Cammers-Goodwin, A. (1998). An indirect chaotropic mechanism for the stabilization of helix conformation of peptides in aqueous trifluoroethanol and hexafluoro-2-propanol. J. Am. Chem. Soc. 120, 5073-5079.

Wallimann, P., Kennedy, R.J., Miller, J.S., Shalongo, W., and Kemp, D.S. (2003). Dual wavelength parametric test of two-state models for circular dichroism spectra of helical polypeptides: anomalous dichroic properties of alanine-rich peptides. J. Am. Chem. Soc. 125, 1203-1220.

Wang, Y., Clark, T.B., and Goodson, T.,3rd. (2010). Two-photon and time-resolved fluorescence conformational studies of aggregation in amyloid peptides. J. Phys. Chem. B 114, 7112-7120.

Ward, W.W., and Bokman, S.H. (1982). Reversible denaturation of Aequorea green-fluorescent protein: physical separation and characterization of the renatured protein. Biochemistry 21, 4535-4540.

Weast, R.C. (1988). CRC Handbook of Chemistry and Physics (Boca Raton, Florida: CRC Press).

Webster, S.D., Galvan, M.D., Ferran, E., Garzon-Rodriguez, W., Glabe, C.G., and Tenner, A.J. (2001). Antibody-mediated phagocytosis of the amyloid beta-peptide in microglia is differentially modulated by C1q. J. Immunol. 166, 7496-7503.

Wetzel, R., Shivaprasad, S., and Williams, A.D. (2007). Plasticity of amyloid fibrils. Biochemistry 46, 1-10.

Whitmore, L., and Wallace, B.A. (2011). DichroWeb. http://dichroweb.cryst.bbk.ac.uk/html/home.shtml

Whitmore, L., and Wallace, B.A. (2008). Protein secondary structure analyses from circular dichroism spectroscopy: methods and reference databases. Biopolymers 89, 392-400.

Whitmore, L., and Wallace, B.A. (2004). DICHROWEB, an online server for protein secondary structure analyses from circular dichroism spectroscopic data. Nucleic Acids Res. 32, W668-73.

Williamson, J.A., Loria, J.P., and Miranker, A.D. (2009). Helix stabilization precedes aqueous and bilayer-catalyzed fiber formation in islet amyloid polypeptide. J. Mol. Biol. 393, 383-396.

Wu, K.P., Weinstock, D.S., Narayanan, C., Levy, R.M., and Baum, J. (2009). Structural reorganization of alpha-synuclein at low pH observed by NMR and REMD simulations. J. Mol. Biol. 391, 784-796.

Xu, C., Williams, R.M., Zipfel, W., and Webb, W.W. (1996). Multiphoton excitation cross-sections of molecular fluorophores. Bioimaging 4, 198-207.

Yamaguchi, K., Naiki, H., and Goto, Y. (2006). Mechanism by which the amyloid-like fibrils of a beta 2-microglobulin fragment are induced by fluorine-substituted alcohols. J. Mol. Biol. 363, 279-288.

Yanagi, K., Ashizaki, M., Yagi, H., Sakurai, K., Lee, Y.H., and Goto, Y. (2011). Hexafluoroisopropanol induces amyloid fibrils of islet amyloid polypeptide by enhancing both hydrophobic and electrostatic interactions. J. Biol. Chem. 286, 23959-23966.

Yang, W.Y., Larios, E., and Gruebele, M. (2003). On the extended beta-conformation propensity of polypeptides at high temperature. J. Am. Chem. Soc. 125, 16220-16227.

Yang, Y., Barker, S., Chen, M.J., and Mayo, K.H. (1993). Effect of low molecular weight aliphatic alcohols and related compounds on platelet factor 4 subunit association. J. Biol. Chem. 268, 9223-9229.

Zagorski, M.G., and Barrow, C.J. (1992). NMR studies of amyloid beta-peptides: proton assignments, secondary structure, and mechanism of an alpha-helix - beta-sheet conversion for a homologous, 28-residue, N-terminal fragment. Biochemistry 31, 5621-5631.

Zarranz, J.J., Alegre, J., Gomez-Esteban, J.C., Lezcano, E., Ros, R., Ampuero, I., Vidal, L., Hoenicka, J., Rodriguez, O., Atares, B., Llorens, V., Gomez Tortosa, E., del Ser, T., Munoz, D.G., and de Yebenes, J.G. (2004). The new mutation, E46K, of alpha-synuclein causes Parkinson and Lewy body dementia. Ann. Neurol. 55, 164-173.

Zerovnik, E., Skarabot, M., Skerget, K., Giannini, S., Stoka, V., Jenko-Kokalj, S., and Staniforth, R.A. (2007). Amyloid fibril formation by human stefin B: influence of pH and TFE on fibril growth and morphology. Amyloid 14, 237-247.

Zhang, J., and Yan, Y.B. (2008). Oligomerization and aggregation of bovine pancreatic ribonuclease A: backbone hydration probed by infrared band-shift. Protein Pept. Lett. 15, 650-657.

Zhang, Y., Furyk, S., Bergbreiter, D.E., and Cremer, P.S. (2005). Specific ion effects on the water solubility of macromolecules: PNIPAM and the Hofmeister series. J. Am. Chem. Soc. 127, 14505-14510.